

HIGH-QUALITY LASER MACHINING OF ALUMINA CERAMICS

A thesis submitted to

The University of Manchester

For the degree of

Doctor of Philosophy (PhD)

in the Faculty of Engineering and Physical Sciences

2012

Yinzhou Yan

School of Mechanical, Aerospace and Civil Engineering

(This page is intentionally left blank)

Abstract

Name of the University: The University of Manchester
Submitted by: Yinzhou Yan
Degree Title: Doctor of Philosophy (PhD)
Thesis Title: High-Quality Laser Machining of Alumina Ceramics
Date: 11th May 2012

Alumina is one of the most commonly used engineering ceramics for a variety of applications ranging from microelectronics to prosthetics due to its desirable properties. Unfortunately, conventional machining techniques generally lead to fracture, tool failure, low surface integrity, high energy consumption, low material removal rate, and high tool wear during machining due to high hardness and brittleness of the ceramic material. Laser machining offers an alternative for rapid processing of brittle and hard engineering ceramics. However, the material properties, especially the high thermal expansion coefficient and low thermal conductivity, may cause ceramic fracture due to thermal damage. Striation formation is another defect in laser cutting. These drawbacks limit advanced ceramics in engineering applications.

In this work, various lasers and machining techniques are investigated to explore the feasibility of high-quality laser machining different thicknesses of alumina. The main contributions include: (i) Fibre laser crack-free cutting of thick-section alumina (up to 6-mm-thickness). A three-dimensional numerical model considering the material removal was developed to study the effects of process parameters on temperature, thermal-stress distribution, fracture initiation and propagation in laser cutting. A rapid parameters optimisation procedure for crack-free cutting of thick-section ceramics was proposed. (ii) Low power CW CO₂ laser underwater machining of closed cavities (up to 2-mm depth) in alumina was demonstrated with high-quality in terms of surface finish and integrity. A three-dimensional thermal-stress model and a two-dimensional fluid smooth particle hydrodynamic model (SPH) were developed to investigate the physical processes during CO₂ laser underwater machining. SPH modelling has been applied for the first time to studying laser processing of ceramics. (iii) Striation-free cutting of alumina sheets (1-mm thickness) is realised using a nano-second pulsed DPSS Nd: YAG laser, which demonstrates the capability of high average power short pulsed lasers in high-quality macro-machining. A mechanism of pulsed laser striation-free cutting was also proposed. The present work opens up new opportunities for applying lasers for high-quality machining of engineering ceramics.

Table of Contents

Abstract	3
Table of Contents	4
List of Figures	9
List of Tables	24
Declaration	25
Copyright Statement	26
List of Publications	27
Dedication	28
Acknowledgement	29
Nomenclature	30
Acronyms	33
Chapter 1	35
Introduction	
1.1 Overview	35
1.2 Aim and Objectives of the Project	37
1.3 Thesis Structure.....	39
Chapter 2	41
Review of Laser Cutting/Machining of Engineering Ceramics	
2.1 Introduction to Ceramic Materials	41
2.2 Alumina Ceramics.....	44
2.3 Fabrication Techniques	47

2.3.1	Green body shaping techniques	49
2.3.2	Post-sintering-machining techniques	54
2.4	State-of-The-Art in Laser Cutting/Machining of Engineering Ceramics	59
2.4.1	Laser Conventional cutting techniques	62
2.4.2	Laser multi-pass cutting/machining techniques	87
2.4.3	Laser controlled fracture cutting/machining techniques	102
2.4.4	Laser hybrid cutting/machining techniques	125
2.5	Summary	135
Chapter 3	139
Fibre Laser Crack-Free Cutting of Thick-Section Alumina		
3.1	Introduction.....	139
3.2	Experimental Procedure	139
3.2.1	Laser cutting system setup and process parameters selection.....	139
3.2.2	Material properties	142
3.3	FE Modelling	144
3.3.1	FE geometric model	144
3.3.2	Material properties and laser heat load for FE modelling.....	145
3.3.3	Thermal analysis and thermal-stress analysis in FE model	147
3.3.4	Fracture criterion and crack prediction in FE model	148
3.3.5	Assumptions.....	149
3.4	Results and Discussion.....	149
3.4.1	Initial results.....	149

3.4.2	Laser peak power effect	152
3.4.3	Pulse duration effect.....	154
3.4.4	Pulse repetition rate effect.....	156
3.4.5	Feed rate effect.....	158
3.4.6	Optimisation of process parameters	160
3.5	Conclusions.....	162
Chapter 4		163
CO₂ Laser Underwater Machining of Deep Cavities in Alumina		
4.1	Introduction.....	163
4.2	Experimental Procedure	163
4.3	Modelling Approaches	165
4.4	Results and Discussion.....	169
4.4.1	Effect of water cooling.....	169
4.4.2	Effect of fluid dynamics.....	174
4.4.3	Effect of scanning pass number and water layer thickness.....	182
4.4.4	Laser underwater machining of polygon cavities	185
4.4.5	Potential improvements for high machining rate and quality	186
4.5	Conclusions.....	188
Chapter 5		189
Nano-Second Pulsed Laser Striation-Free Cutting of Alumina Sheets		
5.1	Introduction.....	189
5.2	Experimental Procedure	190

5.3	Results	193
5.3.1	Demonstration of striation-free cutting	193
5.3.2	Effect of assist gas type	196
5.3.3	Effect of assist gas pressure and nozzle standoff distance	202
5.3.4	Effect of laser power, pulse repetition rate and cutting speed	203
5.4	Discussion	205
5.4.1	Selection of operating conditions	205
5.4.2	Prediction of striation-free laser cutting parameters theoretically	206
5.4.3	Potential methods for prevention of dross formation	213
5.5	Conclusions	214
Chapter 6	216
Conclusions and Future Recommendations		
6.1	Conclusions	216
6.1.1	Fibre laser crack-free cutting of thick-section alumina	216
6.1.2	CO ₂ laser underwater machining of deep cavities in alumina	217
6.1.3	Nano-second pulsed laser striation-free cutting of alumina sheets	219
6.2	Future Recommendations	221
6.2.1	Laser controlled fracture polishing of cut surface	221
6.2.2	High power pico-second pulsed laser machining	223
6.2.3	Multi-physical numerical simulation of laser cutting/machining	224
References	225
Appendix A	242

A.1 FE Geometric Model and Mesh Strategy	242
A.2 FE Time-Step Criterion.....	245
A.3 Solution Strategy	247
A.4 Measurement strategy in Extracted FE Model.....	249
A.5 Effect of Process Parameters on Temporal Temperature Distribution	250
A.6 Optimisation Procedure for Process Parameters	253

Word count: [52,901](#)

List of Figures

<i>Figure 2.1</i>	North American engineering ceramics market in 2007 and predicted size by 2012 [6]	44
<i>Figure 2.2</i>	The rhombohedral crystal structure of α -Al ₂ O ₃ [10]	45
<i>Figure 2.3</i>	The typical microstructure of alumina ceramic	46
<i>Figure 2.4</i>	A typical route for forming engineering ceramics and the most commonly used machining techniques	48
<i>Figure 2.5</i>	Schematics of (a) dry pressing, (b) isostatic pressing, (c) hot pressing, and (d) hot isostatic pressing processes [16, 17]	50
<i>Figure 2.6</i>	Two schemes of the extrusion process [16]	51
<i>Figure 2.7</i>	Schematic of the injection moulding process [16]	52
<i>Figure 2.8</i>	Schematic of the tape casting process [19]	52
<i>Figure 2.9</i>	Schematic of laser conventional cutting [41]	62
<i>Figure 2.10</i>	The major cut quality factors in laser conventional cutting [42]	63
<i>Figure 2.11</i>	Fractural line of CW CO ₂ laser cutting of alumina [43]	64
<i>Figure 2.12</i>	(a) Schematic of cutting front and (b) fracture line during laser cutting of alumina [45]	65
<i>Figure 2.13</i>	Limited cutting speed as a function of the employed average laser power and assist gas pressure [49]	67
<i>Figure 2.14</i>	Optical images of a 2D cut piece at different magnifications [49]	67
<i>Figure 2.15</i>	The schematic and optical images of recast layer on the cut surface [58]	69

<i>Figure 2.16</i>	Aerodynamic interactions between molten materials and assist gas flow jetted from a coaxial nozzle [58, 59]	69
<i>Figure 2.17</i>	Setup of the supersonic off-axial assist gas injection system [58]	70
<i>Figure 2.18</i>	(a) Schematic of interaction of the off-axial gas jet with the cut front and (b) the cut edges obtained by the supersonic off-axial assist gas injection cutting head. Optical graphs of the cut surface at side view (left) and cross-section view (right) [58]	71
<i>Figure 2.19</i>	Schematic of the transparent model of the cut kerf and the setup of the off-axial nozzle for flow visualisation by Schlieren Photography [59]	72
<i>Figure 2.20</i>	(a)-(d) Images of the gas flow inside the cut kerf captured by Schlieren Photography and (e)-(h) photographs of the cut surfaces at different distances between the gas nozzle and the cut front [59]	73
<i>Figure 2.21</i>	The CNC controlled off-axial nozzle laser cutting head [65]	74
<i>Figure 2.22</i>	Schematic of two different laser cutting techniques [68]	75
<i>Figure 2.23</i>	Photographs of crack-free curve and sharp angle cuts in alumina by the CPL technique [68]	75
<i>Figure 2.24</i>	Striation-free cutting of 1-mm thick alumina sheets using a 1 kW CW fibre laser [83]	77
<i>Figure 2.25</i>	Various physical phenomena during laser-ceramic interaction with laser power density increasing [84]	78
<i>Figure 2.26</i>	(a) Absorptance versus temperature of alumina for 1.06 μm wavelength laser and (b) typical temperature signal of alumina during heating process [85]	79

<i>Figure 2.27</i>	Variation of surface absorptivity with temperature for engineering ceramics at 1.06 μm wavelength [88]	80
<i>Figure 2.28</i>	Schematic of the geometry of the cutting model and cross section of the cut front [93]	81
<i>Figure 2.29</i>	Simulated results for a pulse length of 0.5 ms with pulse energy of 0.75 J [93]	82
<i>Figure 2.30</i>	Simulated results for a pulse length of 10 ms with pulse energy of 15 J [93]	83
<i>Figure 2.31</i>	Optical micrographs of the cut surfaces by the laser operating at different pulse lengths and energies [93]	83
<i>Figure 2.32</i>	The variation of machining depth per pulse with laser fluence for short pulsed laser drilling of alumina [98]	84
<i>Figure 2.33</i>	Typical photographs of HAZ around a laser drilled hole in ZrO_2 ceramic [101]	86
<i>Figure 2.34</i>	Surface microstructures of the alumina substrate [102]	86
<i>Figure 2.35</i>	Schematic of multi-pass cutting/machining [103]	87
<i>Figure 2.36</i>	The relationship of crack length and crack number per cut length with cutting speed [105]	88
<i>Figure 2.37</i>	Optical images showing a typical cross-section view of the cut kerf [106]	89
<i>Figure 2.38</i>	Optical images of Si-SiC ceramic 2D cuts by the multi-pass cutting technique [106]	89
<i>Figure 2.39</i>	Schematic of 3D laser machining by a single laser beam [107]	90
<i>Figure 2.40</i>	Schematic of 3D laser machining by a dual laser beam [42]	91
<i>Figure 2.41</i>	3D laser machining of a star shape in alumina ceramic [108]	92

<i>Figure 2.42</i>	Laser machining model [108]	92
<i>Figure 2.43</i>	Top view of non-optimised machining [109]	93
<i>Figure 2-44</i>	(a) Cross-section and (b) top view of a trough machined by repeated laser scanning with optimised process parameters [109]	93
<i>Figure 2.45</i>	A demonstration component made from Y-TZP ceramics by nano-second pulsed Nd: YAG laser machining [109]	93
<i>Figure 2.46</i>	Cross-section view of machined Y-TZP [111]	94
<i>Figure 2.47</i>	Cross-section view of (a) picosecond-laser-machined Y-TZP surface and (b) femtosecond-laser-machined alumina surface [9, 112]	95
<i>Figure 2.48</i>	Variation of groove cross-section with scanning speed and laser power [95]	96
<i>Figure 2.49</i>	Temperature profiles at the laser power of 1500 W with the scanning speed of 50 mm/s and 200 mm/s [95]	96
<i>Figure 2.50</i>	Variation of groove cross-section with laser power and scanning speed [113]	97
<i>Figure 2.51</i>	(a) Simplified 2D cutting model and (b) the predicted shape of the cut front in pulsed CO ₂ laser multi-pass cutting [114]	98
<i>Figure 2.52</i>	(a) Cross-section and top view of the machined cavities in alumina by various numbers of pulses and (b) temporal evolution of machined depth by the developed model [115]	99
<i>Figure 2.53</i>	(a) Variation of temperature with depth and (b) cross-sections and top view of the machined grooves in alumina at various cutting speeds [116]	100

<i>Figure 2.54</i>	Comparison of predicted and measured (a) depths and (b) widths of machined cavities in alumina at various numbers of passes [117]	100
<i>Figure 2.55</i>	The machined 3D cavities in (a) Al ₂ O ₃ , (b) Si ₃ N ₄ , (c) SiC and (d) MgO ceramics [107]	101
<i>Figure 2.56</i>	Schematic of the pulse overlap in x and y directions and the cylindrical volume machined per spot area in pulsed laser machining [107]	101
<i>Figure 2.57</i>	Schematic of laser controlled fracture cutting and the system [118]	102
<i>Figure 2.58</i>	Stress distribution of (a) the first stage – fracture initiation, (b) the second stage – stable fracture, and (c) the third stage – unstable fracture. (d) Stress states between the crack tip and the laser spot [129]	104
<i>Figure 2.59</i>	Stress distribution in the second stage for dimensional samples [129]	105
<i>Figure 2.60</i>	Variation of the maximum cutting speed with laser spot size [129]	105
<i>Figure 2.61</i>	The cut surface of the alumina ceramic substrate cut by (a) controlled fracture cutting, (b) laser scribing, and (c) laser fusion cutting [129]	105
<i>Figure 2. 62</i>	Fracture trajectory deviation from the laser moving path in (a) straight line, (b) curved line cut and (c) right angle cuts [129]	106
<i>Figure 2.63</i>	Unstable fracture due to the main crack linking with a small hole existing in alumina [129]	107
<i>Figure 2.64</i>	SEM photograph of the fracture surface in alumina substrate [118]	108

<i>Figure 2.65</i>	Magnification of the fracture surface in alumina substrate [118]	108
<i>Figure 2.66</i>	Formation of (a) a laser evaporation groove, (b) columnar grains and intergranular fracture cracks and (c) transgranular fracture cracks [118]	108
<i>Figure 2.67</i>	Top view of the alumina substrate surface after laser beam passing [118]	109
<i>Figure 2.68</i>	The minor cracks at the fracture surface [118]	109
<i>Figure 2.69</i>	The fracture surfaces of the alumina substrate by the laser spot diameter of (a) 0.27 mm and (b) 0.80 mm [118]	110
<i>Figure 2.70</i>	Photograph of dual-beam controlled fracture cutting of 10-mm-thick mullite-alumina [131]	111
<i>Figure 2.71</i>	Configuration of the dual-beam controlled fracture cutting system [131]	111
<i>Figure 2.72</i>	CO ₂ laser power versus the maximum cutting speed for various specimen widths under a constant Nd: YAG laser power of 60 W and 80 W [131]	112
<i>Figure 2.73</i>	The required groove-crack depth versus the maximum cutting speed for through cutting of 2-mm-thick and 108-mm-wide substrates [131]	112
<i>Figure 2.74</i>	Photographs of asymmetrical cutting [131]	112
<i>Figure 2.75</i>	Compensation of applied laser paths for right-angle and circular arc cutting [130]	113
<i>Figure 2.76</i>	Algorithm of the iterative path revision technique [132]	113
<i>Figure 2.77</i>	The dual-beam delivery system on the left side and schematic of prescoring process on the right side [134, 136]	114

<i>Figure 2.78</i>	(a) Mixed-mode fracture at the trailing edge of the alumina substrate without prescore and (b) markedly improved fracture quality after a 4 W (12.7 μm net depth) simultaneous prescore [134]	114
<i>Figure 2.79</i>	Stress distribution and evolution along the cutting direction [134]	115
<i>Figure 2.80</i>	Comparison of maximum allowable damage-free cutting speeds for single-beam and dual-beam laser controlled fracture cutting [136]	116
<i>Figure 2.81</i>	Cross-sectional view of the prescore limit and the planar fracture surface (arrows) [136]	116
<i>Figure 2.82</i>	(a) Typical fractures deviating from the cutting path after rapid cutting using a single beam with a duty cycle of 40% and a feed rate of 3.30 mm/s and (b) micro-damages [136]	117
<i>Figure 2.83</i>	Cross-section view of the specimen where the cracks propagate along the path preordained by the prescore and the transition region with the unfocused (diving) beam to the prescore [133]	117
<i>Figure 2-84</i>	Results of controlled-fracture experiments for a semicircular fracture path [133]	118
<i>Figure 2.85</i>	Experimental setup showing cantilevered beam, offset beams, and corner weight to induce mixed-mode fracture in dual-beam controlled-fracture cutting [137]	118
<i>Figure 2.86</i>	Illustration of the 90 angled precore and weight added to exaggerate the mixed-mode loading [137]	119

<i>Figure 2.87</i>	(a) Risk of rupture intensities on the surface, (b) surface zone with failure probability greater than 0.01, (c) the first principal stress (SI) in the surface zone, and (d) the principal stress directions in the surface zone [138]	120
<i>Figure 2.88</i>	Profile cutting of 13-mm-thick Y-TZP ceramic [139]	121
<i>Figure 2.89</i>	A corner cut [139]	121
<i>Figure 2.90</i>	Calculated thermal stress fields in drilling during controlled crack propagation cutting [139]	121
<i>Figure 2.91</i>	Schematic of laser controlled fracture machining [140]	122
<i>Figure 2.92</i>	Crack network and the cross-section view [140]	123
<i>Figure 2.93</i>	Laser controlled fracture milling of alumina [141]	123
<i>Figure 2.94</i>	(a) Schematic of the dual laser shaping system and (b) a typical procedure of shaping a bevel face [142]	124
<i>Figure 2.95</i>	Photographs of the shaped bevel face and step at the edge of alumina substrates [142]	124
<i>Figure 2.96</i>	(a) Laser-assisted turning system and (b) the chip formation in machining of ceramics [153]	125
<i>Figure 2.97</i>	(a) Laser-assisted milling system and (b) the schematic of the milling process [149]	126
<i>Figure 2.98</i>	Schematic of underwater/water-assisted laser cutting techniques [156]	127
<i>Figure 2-99</i>	Methods for providing water in the processing zone during laser machining [156]	128
<i>Figure 2.100</i>	Laser induced (a) fluid motion and (b) bubble motion during underwater laser machining [156]	128

<i>Figure 2.101</i>	Schematic of the CO ₂ laser underwater machining system [160]	129
<i>Figure 2.102</i>	Photos of (a) array-holes and (b) cut pattern in air machining and in underwater machining [162]	130
<i>Figure 2.103</i>	Schematic of the water-assisted laser shock cutting technique [163]	131
<i>Figure 2.104</i>	Process maps related to the laser power and the feed rate for (a) dry laser shock cutting and (b) water-assisted laser shock cutting of alumina [163]	131
<i>Figure 2.105</i>	Schematic of the hybrid CO ₂ laser/waterjet (LWJ) machining system [164]	132
<i>Figure 2.106</i>	Relationship of fracture characteristics with process parameters [164]	132
<i>Figure 2.107</i>	Process of the unstable fracture cutting technique [165]	133
<i>Figure 2.108</i>	Stress states of (a) stable fracture growth and (b) unstable fracture extension [165]	134
<i>Figure 2.109</i>	The breaking surface of the alumina substrate using the unstable fracture cutting technique [165]	134
<i>Figure 2.110</i>	Failure in asymmetric cutting [165]	135
<i>Figure 3.1</i>	The IPG YLP-1000-SM fibre laser system	140
<i>Figure 3.2</i>	Experimental setup incorporating a fibre laser, focusing optics, gas and a high speed linear motor stage	141
<i>Figure 3.3</i>	Laser cut surfaces using (a) N ₂ and (b) O ₂ assist gas	142
<i>Figure 3.4</i>	Transmittance and reflectance curves of alumina for near infrared wavelength light (750–1400 nm)	144

<i>Figure 3.5</i>	Overview of the FE semi-model for numerical simulation	145
<i>Figure 3.6</i>	Temperature and stress distribution during laser cutting of 6-mm-thick alumina	150
<i>Figure 3.7</i>	Component stress distributions during laser cutting of 6-mm-thick alumina	150
<i>Figure 3.8</i>	Crack formation and propagation from cut front in laser cutting of 6-mm-thick alumina	151
<i>Figure 3.9</i>	The experimental result of 6-mm-thick alumina cut by 800 W CW laser with feed rate of 1 mm/s	152
<i>Figure 3.10</i>	Temperature and resulting stress distributions at the cut front on the top surface of the workpiece at various laser peak powers	153
<i>Figure 3.11</i>	Optical photographs of the cutting edge (a) at middle point and (b) at trailing edge of cut path by various laser peak powers	154
<i>Figure 3.12</i>	Temperature and resulting stress distributions at the cut front on the top surface of the workpiece at various pulse durations	155
<i>Figure 3.13</i>	Optical photographs of the cutting edge (a) at middle point and (b) at trailing edge of cut path by various pulse durations	156
<i>Figure 3.14</i>	Temperature and resulting stress distributions at the cut front on the top surface of the workpiece at various pulse repetition rates	157
<i>Figure 3.15</i>	Optical photographs of the cutting edge (a) at middle point and (b) at trailing edge of cut path by various pulse repetition rates	158
<i>Figure 3.16</i>	Temperature and corresponding stress distributions at the cut front on the top surface of the workpiece at various feed rates	159

<i>Figure 3.17</i>	Optical photographs of the cutting edge (a) at middle point and (b) at trailing edge of cut path by various feed rates	160
<i>Figure 3.18</i>	6-mm-thick alumina cut by the optimised process parameters	161
<i>Figure 4.1</i>	Schematic diagram of experimental setup for underwater machining of alumina	164
<i>Figure 4.2</i>	Machining modes employed in this work	165
<i>Figure 4.3</i>	The optical micrographs of the alumina cavity machined in air	169
<i>Figure 4.4</i>	The SEM micrographs of the alumina cavity machined in air	170
<i>Figure 4.5</i>	The optical micrographs of the alumina cavity machined under water	171
<i>Figure 4.6</i>	The SEM micrographs of the alumina cavity machined under water	172
<i>Figure 4.7</i>	Temperature fields and resulting stress distributions during laser machining in different ambient conditions	173
<i>Figure 4.8</i>	(a) Temperature fields and (b) 1 st principle stress distributions along machining path during laser machining of alumina in air and in water	174
<i>Figure 4.9</i>	Schematic diagram of interaction between the CO ₂ laser beam, water, and alumina substrate	175
<i>Figure 4.10</i>	Capture of (a) water wave and (b) bubble formation during the interaction between CO ₂ laser beam and water	175
<i>Figure 4.11</i>	Histogram of the size distribution of the particles generated in laser underwater machining	176
<i>Figure 4.12</i>	Side wall surface of the groove machined (a) in air and (b) in water	177

<i>Figure 4.13</i>	Microstructure of dross on the side wall surface of the groove machined (a) in air and (b) in water and cross-section microstructure of recast layer on the bottom of the groove machined (c) in air and (d) in water	178
<i>Figure 4.14</i>	Roughness plot of the side wall surface of the groove machined (a) in air ($R_a = 13.16 \mu\text{m}$, $R_z = 43.68 \mu\text{m}$) and (b) in water ($R_a = 5.12 \mu\text{m}$, $R_z = 23.02 \mu\text{m}$)	179
<i>Figure 4.15</i>	Cross-section of the groove machined (a) in air at a power of 60 W and a scanning speed of 10 mm/s for 4 passes and (b) under water at a power of 60 W and a scanning speed of 10 mm/s for 80 passes	179
<i>Figure 4.16</i>	Time history of melt ejection during underwater machining at (a) 0 μs , (b) 22.1 μs , (c) 51.6 μs and (d) 110 μs	180
<i>Figure 4.17</i>	Vector plot (a) of water flow during underwater machining and detailed view at the region (b) near the water surface, (c) at the middle of water depth, and (d) near the machined region	182
<i>Figure 4.18</i>	The effect of water layer thickness on machining (a) depth and (b) width in alumina substrate at a fixed 60 W laser power and 10 mm/s scanning speed for 1 to 100 passes	183
<i>Figure 4.19</i>	The effect of water layer thickness on machining rate for alumina substrate at a fixed 60 W laser power and 10 mm/s scanning speed for 1 to 100 passes	184
<i>Figure 4.20</i>	Optical micrographs of the CO ₂ laser underwater machined polygon cavities	185
<i>Figure 4.21</i>	Schematic diagram of the change of water layer thickness with increasing of the machining depth	186
<i>Figure 4.22</i>	Schematic diagram of forced water layer formation technique with substrate position correction	187

<i>Figure 5.1</i>	Schematic diagram of the experimental setup for nano-second pulsed DPSS Nd:YAG laser cutting of alumina sheets	190
<i>Figure 5.2</i>	Curves of nominal laser average power versus pump voltage at different pulse repetition rates	191
<i>Figure 5.3</i>	Surface profile of a cut with major striations at an average laser power of 415 W, pulse repetition rate of 15 kHz, cutting speed of 360 mm/min, and nozzle stand-off distance of 0.5 mm with 1 bar N ₂ assist gas	193
<i>Figure 5.4</i>	Surface profile of a cut with minor striations at an average laser power of 415 W, pulse repetition rate of 15 kHz, cutting speed of 60 mm/min, and nozzle stand-off distance of 0.5 mm with 1 bar N ₂ assist gas	194
<i>Figure 5.5</i>	Surface profile of a cut with striation free at an average laser power of 415 W, pulse repetition rate of 15 kHz, cutting speed of 186 mm/min, and nozzle stand-off distance of 0.5 mm with 1 bar N ₂ assist gas	195
<i>Figure 5.6</i>	Surface profile of a cut with major striations at an average laser power of 415 W, pulse repetition rate of 15 kHz, cutting speed of 186 mm/min, and nozzle stand-off distance of 0.5 mm with 1 bar He assist gas	198
<i>Figure 5.7</i>	Surface profile of a cut with minor striations at an average laser power of 415 W, pulse repetition rate of 15 kHz, cutting speed of 186 mm/min, and nozzle stand-off distance of 0.5 mm with 1 bar Ar assist gas	199
<i>Figure 5.8</i>	Surface profile of a blind cut at an average laser power of 415 W, pulse repetition rate of 15 kHz, cutting speed of 186 mm/min, and nozzle stand-off distance of 0.5 mm with 1 bar O ₂ assist gas	200

<i>Figure 5.9</i>	Surface profile of a cut with major striations at an average laser power of 415 W, pulse repetition rate of 15 kHz, cutting speed of 186 mm/min, and nozzle stand-off distance of 0.5 mm with 1 bar compressed air assist gas	201
<i>Figure 5.10</i>	Effect of nozzle stand-off distance and gas pressure on striation characteristics at a laser average power of 415 W, pulse repetition rate of 15 kHz, and cutting speed of 186 mm/min with N ₂ assist gas	203
<i>Figure 5.11</i>	Effect of laser average power and cutting speed on striation characteristics at a pulse repetition rate of 15 kHz and nozzle stand-off distance of 0.5 mm with 1 bar N ₂ gas pressure	204
<i>Figure 5.12</i>	Effect of pulse repetition rate and cutting speed on striation characteristics at a diode laser pump voltage of 10 V and nozzle stand-off distance of 0.5 mm with 1 bar N ₂ gas pressure	205
<i>Figure 5.13</i>	Time history for drilling a through hole in a 1-mm alumina sheet using 415 W average laser power, 15 kHz pulse repetition rate, and 0.5 mm nozzle standoff distance with 1 bar N ₂ assist gas	208
<i>Figure 5.14</i>	Cross-section of the cut front under the optimal operating conditions	210
<i>Figure 6.1</i>	Laser controlled fracture polishing of alumina surface	222
<i>Figure 6.2</i>	The micrograph of a micro-chip peeled off from the polished surface	222
<i>Figure 6.3</i>	(a) An overview of the partially polished 6-mm-thick alumina cut surface and (b) a close-up view of the boundary between unpolished area (left) and polished area (right)	223

<i>Figure A.1</i>	Error of FE simulated temperature for different mesh sizes at the fixed time-step of 25 ms	244
<i>Figure A.2</i>	Mesh strategy for the extracted symmetric semi-model	245
<i>Figure A.3</i>	Continuous laser beam and discrete laser beam sweeping the same length	246
<i>Figure A.4</i>	Error of swept area and simulated temperature in FE model for different time-step sizes at the fixed mesh size of 25 μm	246
<i>Figure A.5</i>	The thermal-stress concentration on rough cut surface	248
<i>Figure A.6</i>	The thermal-stress on smooth cut surface	249
<i>Figure A.7</i>	Measurement strategy for temperatures and resulting stresses in the FE model	250
<i>Figure A.8</i>	Temporal distribution of temperature at the middle point of the cut kerf under various laser peak powers	251
<i>Figure A.9</i>	Temporal distribution of temperature at the middle point of the cut kerf under various pulse durations	251
<i>Figure A.10</i>	Temporal distribution of temperature at the middle point of the cut kerf under various pulse repetition rates	252
<i>Figure A.11</i>	Temporal distribution of temperature at the middle point of the cut kerf under various feed rates	253
<i>Figure A.12</i>	Stepwise procedure for optimisation of process parameters for crack-free cutting of thick-section ceramics	254

List of Tables

<i>Table 2.1</i>	Products using advanced ceramics [2]	42
<i>Table 2.2</i>	Applications of some commonly used engineering ceramics [1]	43
<i>Table 2.3</i>	Engineering alumina ceramics and their characteristics [11]	46
<i>Table 2.4</i>	Typical compositions of alumina green body [13]	47
<i>Table 2.5</i>	Typical shrinkages of some ceramics [26]	53
<i>Table 2.6</i>	Economic comparisons of different machining techniques [36]	58
<i>Table 2.7</i>	Major physical phenomena in laser machining of some typical engineering ceramics [56]	68
<i>Table 2.8</i>	Underwater/water-assisted laser cutting of materials [156]	127
<i>Table 2.9</i>	Features of various laser cutting/machining techniques for engineering ceramics	138
<i>Table 3.1</i>	Laser cutting parameters employed in this work	141
<i>Table 3.2</i>	Material's properties of 95% alumina used in the work	142
<i>Table 3.3</i>	Alumina material properties used for FE analysis [12, 170]	146
<i>Table 3.4</i>	The optimal parameters for crack-free cutting of 6-mm-thick alumina	161
<i>Table 4.1</i>	Material properties of 95% alumina used in the work [12]	164
<i>Table 5.1</i>	Laser cutting conditions used in this work	191
<i>Table 5.2</i>	Material properties of 99.6% alumina used in the work [12]	192
<i>Table 5.3</i>	Comparison between standard laser cutting, CW laser striation-free cutting, and pulsed laser striation-free cutting conditions for alumina sheets	206

Declaration

I hereby declare that no portion of the work referred to in the thesis has been submitted in support of an application for another degree or qualification of this or any other university or other institute of learning.

Copyright Statement

- i.** The author of this thesis (including any appendices and/or schedules to this thesis) owns certain copyright or related rights in it (the “Copyright”) and s/he has given The University of Manchester certain rights to use such Copyright, including for administrative purposes.
- ii.** Copies of this thesis, either in full or in extracts and whether in hard or electronic copy, may be made **only** in accordance with the Copyright, Designs and Patents Act 1988 (as amended) and regulations issued under it or, where appropriate, in accordance with licensing agreements which the University has from time to time. This page must form part of any such copies made.
- iii.** The ownership of certain Copyright, patent, designs, trade marks and other intellectual property (the “Intellectual Property”) and any reproductions of copyright works in the thesis, for example graphs and tables (“Reproductions”), which may be described in this thesis, may not be owned by the author and may be owned by third parties. Such Intellectual Property and Reproductions cannot and must not be made available for use without the prior written permission of the owner(s) of the relevant Intellectual Property and/or Reproductions.
- iv.** Further information on the conditions under which disclosure, publication and commercialisation of this thesis, the Copyright and any Intellectual Property and/or Reproductions described in it may take place is available in the University IP Policy (see <http://documents.manchester.ac.uk/DocuInfo.aspx?DocID=487>), in any relevant Thesis restriction declarations deposited in the University Library, The University Library’s regulations (see <http://www.manchester.ac.uk/library/aboutus/regulations>) and in The University’s policy on Presentation of Theses.

List of Publications

Journal publications

1. Yinzhou Yan, Lin Li, Kursad Sezer, David Whitehead, Lingfei Ji, Yong Bao, Yijian Jiang. *Experimental and theoretical investigation of fibre laser crack-free cutting of thick-section alumina*. **International Journal of Machine Tools and Manufacture**, 51 (2011) 859-870.
2. Yinzhou Yan, Lin Li, Kursad Sezer, Wei Wang, David Whitehead, Lingfei Ji, Yong Bao, Yijian Jiang. *CO₂ laser underwater machining of deep cavities in alumina*. **Journal of the European Ceramic Society**, 31 (2011) 2793-2807.
3. Yinzhou Yan, Lin Li, Kursad Sezer, David Whitehead, Lingfei Ji, Yong Bao, Yijian Jiang. *Nano-second pulsed DPSS Nd: YAG laser striation-free cutting of alumina sheets*. **International Journal of Machine Tools and Manufacture**, 53 (2012) 15-26.

Dedication

Dedicated to

My Parents

and

My Wife

for their continuous support and endless love

Acknowledgement

I wish to thank all those who helped me successfully accomplish this work for my PhD degree. Firstly, I would like to convey my profound thanks to my supervisor, Professor Lin Li, for his consistent guidance and support throughout this project. His enthusiastic advice and key suggestions were very important to the project. Most importantly, he taught me how to become a qualified researcher and his positive and serious attitude toward work influenced me deeply. I would also like to extend my gratitude to Professor Yijian Jiang, Professor Lingfei Ji, and Dr. Yong Bao from Beijing University of Technology for their guidance and support in the early stages of my study.

I am extremely grateful to my parents and wife, for their love and understanding. Their suggestions and motivation encouraged me to successfully finish this work.

I would also like to thank all of my friends and colleagues within the University and the Laser Processing Research Centre (LPRC). I am very pleased to know them and thank their kind support and friendship. Particularly, I thank Dr. Kursad Sezer, Dr. Wei Wang and Dr. Wei Guo for their patient and generous help on the project. I am thankful to Dr. David Whitehead, the Senior Experimental Officer of LPRC, for his cooperation and very useful suggestions on equipment. My thanks are also conveyed to my annual report examiner Dr. Paul Mativenga for his very useful advice on this work.

Lastly, I acknowledge the financial support from Institute of Laser Engineering (ILE), Beijing University of Technology, P.R. China, for the first year of my PhD's program at The University of Manchester.

Nomenclature

Notation	Description (Units)
α	Light attenuation coefficient (m^{-1})
α'	Proportional contribution of the enthalpy of reaction to the total energy density
α_T	Material thermal diffusivity (m^2/s)
λ	Laser wavelength (m)
ρ	Material's mass density (kg/m^3)
σ_{xx}	x -component stress distribution (MPa)
σ_{yy}	y -component stress distribution (MPa)
φ_{in}	The angle of light incidence
$A_{coupled}$	Percentage of coupled beam energy into cut kerf
A_f	Equivalent absorptance of the material with respect to a specific wavelength
A_{front}	Absorptance at cut front with respect to a specific wavelength
C_p	Thermal capacity ($\text{J}/\text{kg}\cdot\text{K}$)
$c(T)$	Temperature-dependent specific heat ($\text{J}/\text{kg}\cdot\text{K}$)
D	Average laser spot diameter across the thickness of workpiece (m)
D_b	Cut kerf width on the bottom surface of workpiece (m)
D_{cut}	Average cut kerf width across the thickness of workpiece (m)
D_{drill}	Average drilled hole diameter across the thickness of workpiece (m)
D_t	Cut kerf width on the top surface of workpiece (m)
D_{t-spot}	Laser spot diameter on the top surface of workpiece (m)
d	Laser spot diameter (m)
F	Laser power density (W/m^2)
f	Pulse repetition rate (Hz)
$f.p.p$	Focal plane position (m)
h	Heat transfer coefficient ($\text{W}/(\text{m}^2\cdot\text{K})$)
$I(x, y)$	Surface heat flux distribution (W/m^2)
K_m	Thermal conductivity of the melt ($\text{W}/\text{m}\cdot\text{K}$)
$k(T)$	Temperature-dependent thermal conductivity ($\text{W}/(\text{m}\cdot\text{K})$)
L_m	Latent heat of fusion (J/kg)

L_{mesh}	Mesh size (m)
L_p	Beam energy loss from the exit cut kerf
$L_{time-step}$	Time-step length (m)
L_v	Latent heat of vaporisation (J/kg)
l	Characteristic length of heat conduction (m)
M^2	Beam quality factor
n'	Normal vector pointing outward from the surface
P	Laser power (W)
P_0	Light power arriving at the workpiece surface (W)
P_{in}	Light power incident into the workpiece (W)
P_{out}	Light power transmitted through the t -thickness-workpiece (W)
$Q(x,y,z)$	Heat generation rate (W/m ³)
R	Reflectance of the material with respect to a specific wavelength
R_a	Arithmetic mean roughness (μm)
R_q	Root mean square roughness (μm)
R_t	Maximum height of profile (μm)
R_z	Average maximum height of the profile (μm)
r	Laser spot radius (m)
r_0	Laser spot radius at focal plane position (m)
$r(z)$	Laser spot radius at position z (m)
$S1$	The 1 st principal stress (MPa)
T	Temperature (K)
T_0, T_∞	Room temperature (K)
T_b	Boiling temperature (K)
T_{light}	Transmittance of material with respect to a specific wavelength
T_m	Melting temperature (K)
T_s	Melt surface temperature (K)
$T_{time-step}$	Time-step (s)
T_x	Temperature along x -direction (K)
T_y	Temperature along y -direction (K)
t	Workpiece thickness (m)
t'	Time (s)
t_{drill}	Threshold time for drilling a through hole (s)

t_p	Pulse duration (s)
v	Feed rate/Cutting speed (m/s)
v_c	Critical cutting speed for striation-free cutting (m/s)

Acronyms

2D	Two-dimensional
3D	Three-dimensional
AC	Alternating current
ALE	Arbitrary Lagrange-Euler
Al	Aluminium
Al ₂ O	Aluminium(I) oxide
Al ₂ O ₃	Aluminium oxide
AlN	Aluminium nitride
AlO	Aluminium(II) oxide
AlO ₂	Aluminium peroxide oxide
AlON	Aluminium oxynitride
Ar	Argon
ASCC	Anti-spatter composite coating
B ₄ C	Boron carbide
CAD	Computer-aided design
CCC	Carbon-carbon composite
CFD	Computational fluid dynamics
CMC	Ceramic matrix composite
CNC	Computer numerical control
CO ₂	Carbon dioxide
CPL	Close-piercing lapping
CW	Continuous wave
DC	Direct current
DPSS	Diode-pumped solid-state
FBG	Fibre Bragg Gratings
FE	Finite element
FEA	Finite element analysis
FEM	Finite element method
HAZ	Heat-affected zone
He	Helium
HPSN	Hot Pressed Silicon Nitride

IC	Integrated circuit
IR	Infrared
LAM	Laser-assisted machining
LCD	Liquid crystal display
LWJ	Laser/Waterjet machining
MEMS	Micro-electro-mechanical systems
MgO	Magnesium oxide
MMC	Metal matrix composite
N ₂	Nitrogen
Na	Natrium
Nd	Neodymium
NIR	Near-infrared
O ₂	Oxygen
PM	Pulsed mode
PMC	Polymer matrix composite
RBSN	Reaction bonded silicon nitride
SEM	Scanning electron microscope
Si	Silicon
Si ₃ N ₄	Silicon nitride
SiC	Silicon carbide
SPH	Smoothed-particle hydrodynamics
TEM ₀₀	The lowest transverse mode (i.e. ideal Gaussian beam)
Y-TZP	Yttria-stabilized tetragonal zirconia polycrystal ceramic
Y ₃ Al ₅ O ₁₂	Yttrium-aluminium garnet chemical composition
YAG	Yttrium-aluminium garnet
YVO ₄	Yttrium vanadate
ZrO ₂	Zirconia

Chapter 1

Introduction

1.1 Overview

During the past few decades, interest in ceramics has grown dramatically due to their outstanding properties such as high-temperature strength, superior wear resistance, high hardness, high thermal and electrical resistance and chemical stability that make them desirable for a wide range of industrial applications in mechanical, aerospace, automotive, electrical, biological and chemical engineering [1, 2]. Retention of these material's outstanding properties at elevated temperatures and in chemically aggressive environments presents them as an exclusive solution for engineering challenges [3]. On the other hand, these unique features of ceramic materials certainly have several limitations, such as difficulty in fabrication, high cost, and poor reproducibility for practical applications [1].

As varieties of ceramic materials that hold their own remarkable properties able to meet the need for high-end applications have appeared, the search of efficient machining techniques for them becomes more urgent. Pre-forming processes for ceramic green bodies are commonly used before sintering. However, the level of end-product accuracy is low, due to the shrinkage of the green body in the subsequent sintering process. Further machining after sintering is inevitable for tight dimensional accuracy. Mechanical machining (such as grinding) processes are generally considered as the most desirable and reliable techniques, which fulfil the necessities for dimensional accuracy and surface finish [4]. Unfortunately, most of the mechanical machining techniques are precluded for hard and brittle ceramics or the cost of producing component shapes is extremely high due to the use of expensive and time-consuming diamond grinding [3].

Developing a cost-effective machining technique is one of the key challenges to apply advanced ceramics in engineering areas. Laser machining represents an alternative technique for processing brittle and hard materials such as ceramics by

means of melting, evaporation, and ablation, etc., which potentially provides a rapid and flexible machining without tool wear, vibrations and cutting forces. In addition, lasers can be easily automated with CNC tables to achieve 3D machining. Over the past two decades, many studies have been carried out to demonstrate the feasibility of applying lasers to machining ceramics. However, the basic limitations have not been completely solved, such as cracks and low material removal rate in cutting of thick-section ceramics (>2 mm thickness), striation formation on cut surfaces, heat affected zones, poor surface finish, fracture and molten material re-deposition, etc., caused by the intense thermal effect and inherent defects of laser machining. These obstacles limit the application of laser cutting/machining techniques in ceramics processing.

Over the last few years, the availability of high power and high beam quality fibre lasers with linear motor stages and fine modulated short/ultra-short pulsed lasers with precision stages or galvanometer mirror scanners have opened up new opportunities to achieve laser cutting and even remote machining with high finish quality and accuracy. Some unique advantages employing these lasers for ceramic processing have been demonstrated.

Unfortunately, some scientific challenges in laser cutting/machining of ceramic materials have not been resolved by previous studies and techniques. The major challenges are listed as follows:

- 1) Cracking is the major challenge in laser processing of ceramics. Thermal damage in IR laser cutting/machining was considered to be inevitable in previous studies. There could cause catastrophic breakdown of workpiece.
- 2) Material removal rate in laser cutting/machining of thick-section ceramics is still very low although it is higher than mechanical machining. For high power lasers, the machining rate cannot be dramatically improved due to the significant thermal damage, which could induce crack formation.
- 3) Surface finish quality of laser cutting/machining is much lower than mechanical machining. Rough surface finish is another challenge for laser macro-machining. The low surface finish quality was attributed to inherent characteristics of laser

processing (e.g. melt oscillation and re-deposition). Mechanical post-processing is still necessary for high surface finish quality. Although short/ultrashort pulsed lasers (e.g. pico-second and femto-second) have demonstrated the capability for high surface finish quality machining, the low machining rate (typically, $2.2\text{mm}^3/\text{min}$ for pico-second lasers and $0.054\text{mm}^3/\text{min}$ for femto-second lasers) limits their applications to the micro-machining field.

- 4) To date, the mechanisms of laser cutting/machining of ceramic materials have not been revealed completely due to the complicated multi-physical phenomena occurring during laser processing. Therefore, it is difficult to significantly control the laser cutting/machining process for high finish quality.

Considering the above mentioned scientific challenges, it is essential to further study the effects of process parameters on process quality and machining rate, investigate the unrevealed mechanisms, and explore the potential new techniques, in order to achieve high-quality laser cutting/machining of engineering ceramics.

1.2 Aim and Objectives of the Project

The aim of the project is to explore the feasibility, characteristics and potential improvement of high-quality and damage-free laser cutting/machining of ceramics by various laser processing systems, process conditions and techniques, and numerical simulations.

Cracking is the major challenge in laser cutting of thick-section ceramics. In order to solve the problem, the following objectives were set in the investigation.

- 1) To develop suitable Finite Element (FE) modelling for accurate and reliable simulation of laser cutting, in order to obtain temperature and thermal-stress distributions.
- 2) To understand the crack initiation and propagation mechanisms in ceramics during laser cutting by means of FE simulation.

- 3) To evaluate the effect of process parameters on crack formation in laser cutting by FE analyses and corresponding experiments.
- 4) To develop a method to optimise process parameters for crack-free laser cutting of thick-section ceramics.

In order to further achieve crack-free and high-quality laser macro-machining of ceramics, alternative laser machining techniques should be employed to compensate the inherent defects of laser processing, such as thermal damage, recast layer formation, etc. Therefore, a special study was performed following fibre laser crack-free cutting in this project. It is CO₂ laser high-quality machining of deep cavities in ceramics. The investigation objectives included:

- a) To explore the feasibility of laser high-quality machining of ceramic in fluid.
- b) To study the mechanism of fluid-assisted laser machining by experiments and numerical simulation techniques.
- c) To optimise the process parameters for achieving high-quality laser machining of ceramics in practice.

In addition, striation formation is another major quality defect during short/ultrashort pulsed laser cutting of ceramics. Elimination of striation formation is critical to further improve the cut quality in pulsed laser cutting. Therefore, the following objectives were set in this work to achieve pulsed laser striation-free cutting:

- 5) To explore the feasibility of pulsed laser striation-free cutting of ceramic sheets.
- 6) To understand the mechanism of pulsed laser striation-free cutting based on an empirical model.
- 7) To develop a theoretical model and predict operating conditions for pulsed laser striation-free cutting of ceramic materials in practice.

1.3 Thesis Structure

The thesis is comprised of six chapters described as follows:

Chapter 1. Introduction. This chapter gives a brief overview, aim, objectives and structure of the thesis. The major challenges of laser cutting/machining of ceramics are also proposed in this chapter.

Chapter 2. Literature Review. This chapter gives a review on the current techniques and the challenges in cutting/machining of ceramics. Particularly, the major research work and milestones on laser cutting/machining of ceramics are reviewed, where the fundamentals, advantages and drawbacks of different laser processing techniques are compiled and discussed in details.

Chapter 3. Experimental and Numerical Investigation of Fibre Laser Crack-Free Cutting of Thick-Section Alumina. This chapter includes an investigation into laser crack-free cutting of thick-section alumina (6-mm thickness) using a 1 kW single mode fibre laser (1075-nm). The thermal behaviours of alumina and crack formation during fibre laser cutting were investigated by Finite Element Analysis (FEA) and validated by experiments. The criteria of FEM modelling for laser cutting were presented in this chapter. The crack formation in laser cutting alumina ceramic was simulated by ANSYS FEA software for the first time. Based on the numerical and experimental study, the mechanism of crack formation during laser cutting of thick-section alumina was proposed and a procedure for rapid optimisation of process conditions was also developed. Crack-free cutting of thick-section alumina was achieved in experiments.

Chapter 4. CO₂ Laser Underwater Machining of Deep Cavities in Alumina. A method for crack-free machining of deep cavity in alumina was demonstrated using a low-cost CO₂ continuous wave (CW) laser. CO₂ laser underwater machining was found to be beneficial in reducing the substrate defects such as recast layer, dross, cracking and thermal damage that typically occur during machining in air. Finite element method (FEM) modelling and Smooth Particle Hydrodynamic (SPH) modelling techniques were both employed to understand the effect of water on crack

resistance and debris removal during CO₂ laser underwater machining. The machining rate in underwater machining was also discussed here.

Chapter 5. Nano-Second Pulsed DPSS Nd: YAG Laser Striation-Free Cutting of Alumina Sheets. An investigation into pulsed laser striation-free cutting of alumina sheets is presented in this chapter. The study demonstrates striation-free cutting of 1 mm alumina sheets using a 400 W high repetition rate nano-second DPSS Nd: YAG laser. The specific operating conditions for nano-second pulsed laser striation-free cutting are presented. A mechanism of pulsed laser striation-free cutting was proposed, by which the existing theory of continuous wave (CW) laser striation-free cutting of metallic materials was extended to the pulsed laser striation-free cutting of ceramic materials.

Chapter 6. Conclusions and Future Recommendations. This chapter consists of the conclusions of this work as well as the recommendations for future studies. A short discussion linking crack-free cutting and striation-free cutting as part of the overall thesis to reduce defects in laser cutting of ceramics is also included in this chapter.

Chapter 2

Review of Laser Cutting/Machining of Engineering Ceramics

2.1 Introduction to Ceramic Materials

Ceramics are defined as inorganic and non-metallic materials that have hard, brittle, corrosion and heat resistant properties. They consist of one or more metals or non-metals in combination with one or more non-metals. After a high temperature firing and compaction process well known as sintering, ceramic materials generally have a crystalline or partly crystalline structure with glassy phases known as crystal grains and crystal boundary. The definition of ceramic materials is therefore often restricted to inorganic crystalline or partly crystalline materials. The earliest ceramics were pottery objects made from clay and then glazed and fired to create a coloured surface. These are generally used as domestic and art products.

In the 20th century, advanced ceramic materials were developed, which found far wider applications in engineering than traditional porcelain and pottery. Table 2.1 shows several products using advanced ceramics. The advanced ceramics are classified as structural ceramics (i.e. engineering ceramics) and functional ceramics. Functional ceramics are generally employed as a part of electronic components due to their inherent physical features, such as electric, magnetic, dielectric, ferroelectric, optical or other properties, which play an active role in the electronic industries. Engineering ceramics are applied as structural components in most engineering industries. Compared with other engineering materials (e.g. metals or polymers), engineering ceramics offer numerous enhancements in performance, durability, reliability, chemical stability, hardness, mechanical strength at elevated temperatures, wear resistance and thermal resistance [2].

Table 2.1 Products using advanced ceramics [2]

Mechanical Engineering	Aerospace	Automotive	Defence industry
Cutting tools and dies	Fuel systems and valves	Heat engines, Turbines	Tank power trains
Abrasives	Power units	Catalytic converters	Submarine shaft seals
Precise instrument parts	Low weight components	Drivetrain components	Improved armours
Molten metal filter	Fuel cells	Fixed boundary recuperators	Propulsion systems
Turbine engine components	Thermal protection systems	Fuel injection components	Ground support vehicles
Low weight components for rotary equipment	Turbine engine components	Turbocharger rotors	Military weapon systems
Wearing parts	Combustors	Low heat rejection diesels	Military aircraft (airframe and engine)
Bearings, Seals	Bearings, Seals and Structures	Waterpump seals	Wear-resistant precision bearings
Biological, Chemical Processing Engineering	Electrical, Magnetic Engineering	Nuclear industry	
Artificial teeth, Bones and joints	Memory element , Varistor sensor	Nuclear fuel	
Catalysts and igniters	Resistance heating element	Nuclear fuel cladding	
Heart valves, Heat exchanger, Reformers	Integrated circuit substrate	Control materials	
Recuperators, Refractories and Nozzle	Multilayer capacitors	Moderating materials	
Oil industry	Electric power generation	Optical Engineering	Thermal Engineering
Bearings	Bearings	Laser diode	Electrode materials
Flow control valves	Ceramic gas turbines	Optical communication cable	Heat sink for electronic parts
Pumps	High temperature components	Heat resistant translucent	High-temperature industrial furnace lining
Refinery heater	Fuel cells (solid oxide)	Porcelain	
Blast sleeves	Filters	Light emitting diode	

The family of engineering ceramics spans many compounds, including oxides, carbides, nitrides, borides, silicates, and glass ceramics and composite materials such as polymer matrix (PMC), metal matrix (MMC), ceramic matrix (CMC), and carbon-carbon (CCC) ceramics [2]. The most commonly used engineering ceramics are: Alumina (Al_2O_3), Zirconia (ZrO_2), Aluminium Nitride (AlN), Silicon Nitride (Si_3N_4), Silicon Carbide (SiC), Reaction Bonded Silicon Nitride (RBSN), and Hot Pressed Silicon Nitride (HPSN). Some of their applications are listed in Table 2.2.

Table 2.2 Applications of some commonly used engineering ceramics [1]

Application	Performance advantages	Ceramics
Wear Parts: Seals, bearing, valves, nozzle	High hardness, low friction	SiC, Al_2O_3
Cutting tools	High strength, hardness	Si_3N_4
Heat Engines: Diesel components, gas turbines	Thermal insulation, high temperature strength, fuel economy	ZrO_2 , SiC, Si_3N_4
Medical Implants: Hips, teeth, joints	Biocompatibility, surface bond to tissue, corrosion resistance	Hydroxyapatite, Bioglass, Al_2O_3 , ZrO_2
Construction: Highways, bridges, buildings	Improved durability, low overall cost	Advanced cements and concrete

In 1987, a research by the USA National Research Council investigated eight major US industries that employed seven million employees and had sales of 1.4 trillion US dollars. These showed a generic need for lighter, stronger, more corrosion-resistant materials capable of withstanding high temperatures in future technology strategies [5]. Engineering ceramics are the leading candidates for meeting these requirements. A report from BCC Research in 2008 reported the North American market for structural ceramics to be \$2.7 billion in 2007 and predicted it would grow to \$3.7 billion in 2012 [6]. Figure 2.1 shows the predicted growth of the top three largest market shares, involving bioceramics, armour and military, and wear and corrosion segment in North American. BCC's report also stresses that the advanced engineering ceramics market would be renewed when the fabrication and synthesis of ceramics were innovated [7].

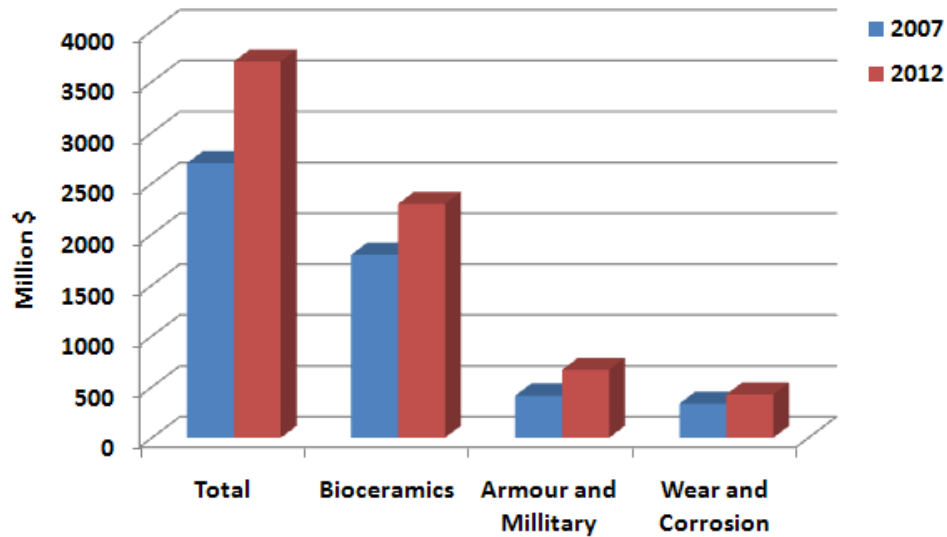


Figure 2.1 North American engineering ceramics market in 2007 and predicted size by 2012 [6]

2.2 Alumina Ceramics

Alumina (Al_2O_3) is one of the most commonly used engineering ceramics in various industrial applications owing to its good mechanical strength, good heat and fire resistance, high corrosion and wear resistance, and high electric insulation. It is generally used in making machine tools, heat-resistant packings, electrical and electronic components, attachments to melting ducts, and refractory linings [8]. Alumina substrates further possess several unique features, such as excellent dielectric strength, thermal stability and conductivity, good surface with high smoothness/flatness and less porosity, high thermal shock resistance, low warpage and camber, high temperature and chemical stability, and very stable breaking strength as well as shape/dimension variance. Therefore, they are widely applied in the electronics industry as chip resistor substrates, hybrid integrated circuit (IC) substrates, electrical isolations, etc [9]. Considering the wide use of the ceramic, alumina (Al_2O_3) was selected as the major experimental sample in this programme.

There are several crystalline forms of alumina, namely α , β , γ , δ - Al_2O_3 , etc. The most thermodynamically stable form is α - Al_2O_3 known as corundum or sapphire in its crystalline form. It has an internal crystal structure where the oxygen ions are

packed in a close-packed hexagonal arrangement with aluminium ions in two-thirds of the octahedral sites, as shown in Figure 2.2.

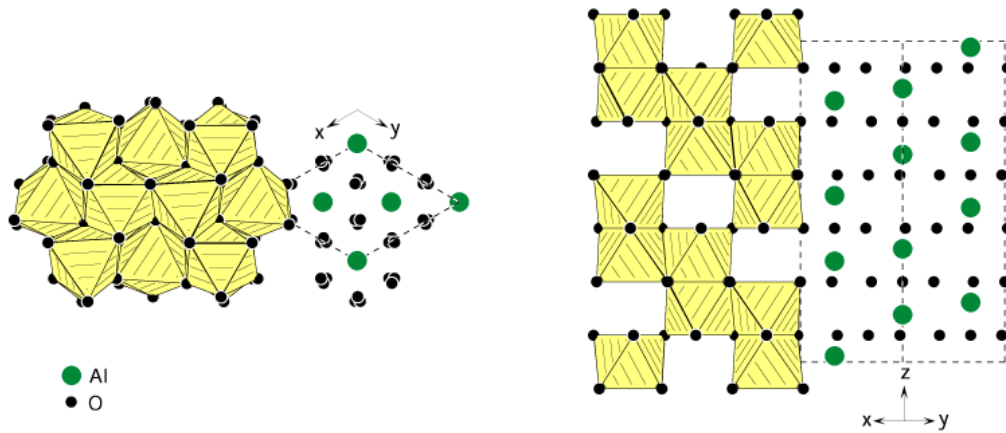


Figure 2.2 The rhombohedral crystal structure of α - Al_2O_3 (space group $R3, -c$). At right-hand side such a layer is projected along $[110]$ direction [10]

Engineering grade polycrystalline alumina ceramics are usually sintered from α - Al_2O_3 powder at a high temperature (>1300 °C). The typical microstructure of alumina ceramics is shown in Figure 2.3. In general, alumina is graded into two main groups, i.e. high-alumina grades with at least 99% Al_2O_3 and alumina grades between 80% and 99% Al_2O_3 [11]. Table 2.3 lists the characteristics of alumina ceramics at different subclasses. The high purity alumina is characterised by high density (>3.75 g/cm^3), high sintering temperatures (1500-1900 °C) and relatively good mechanical and other performances, whereas the lower grades are cheaper and therefore attractive for purposes where these properties are sufficient [12].

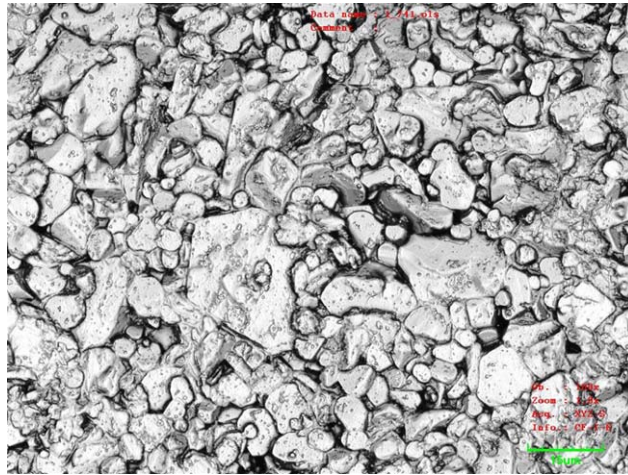


Figure 2.3 The typical microstructure of alumina ceramic.

Table 2.3 Engineering alumina ceramics and their characteristics [11]

Grade	Al ₂ O ₃ (%)	Type	Porosity (%)	Density (g/cm ³)	Applications
A1	99.6	Electrical & engineering	0.2-3	3.75-3.95	Structural
A2	99.8	Translucent	<1	3.97-3.99	Na lamps
A3	99.5	Hot-pressed	<1	3.90-3.99	Machine tools
A4	99.6	Sintered recrystallised	3-6	3.75-3.85	Refractory
A5	99.0	Low dielectric loss	1-5	3.76-3.94	Microwave
A6	96.5-99.0	Electrical & engineering	1-5	3.71-3.92	Mechanical & electrical
A7	94.5-96.5	Electrical & engineering	2-5	3.60-3.90	Insulators, wear parts
A8	86.0-94.5	Electrical & engineering	2-5	3.40-3.90	Insulators, wear parts, refractory
A9	80.0-86.0	Electrical & engineering	3-6	3.30-3.60	Insulators, wear parts, refractory

Although alumina has been widely used in engineering areas, the major drawback for its further applications, as most advanced ceramics, is the difficulty in fabrication, high processing cost, and poor reproducibility. In the next section, various fabrication techniques for engineering ceramics (e.g. Al₂O₃) are reviewed.

2.3 Fabrication Techniques

The high-performance material properties of ceramics make them attractive for uses but also make them difficult to fabricate. Moreover, the damage caused by machining may affect the performance of the final ceramic components. Therefore, cost-effective machining without significant reduction of the outstanding material properties is a crucial step for ceramic components manufacturing. High quality ceramic components can be realised once this fundamental challenge is overcome. Over the past few decades, numerous efforts have been performed to improve the process quality and several advanced machining techniques with reduced deleterious effects on material properties have been developed [3].

Figure 2.4 shows a typical route of forming engineering ceramics. There are three basic steps in this route (and each of these may incorporate some sub-processes). The first step is powder synthesis and treatment. The second step involves the consolidation of the treated powder into an expected shape that is known as “Green Body”. The green body typically contains about 50 vol % porosity and is extremely weak, which is a machinable form. The typical composition of alumina green body is listed in Table 2.4. The last step utilises heat, or heat and pressure combined, to bond the individual powder particles, remove the free space and porosity in the compact via mass diffusion, and create a fully dense and well-bounded ceramic component [14]. This process is known as sintering or firing. The sintered ceramics can be machined but it is very difficult. Figure 2.4 also summarises the most commonly used techniques for machining of engineering ceramics in the green body form and in the sintered form.

Table 2.4 Typical compositions of alumina green body [13]

Function	Composition	Volume (%)
Powder	Alumina (Al_2O_3)	27
Solvent	1,1,1-trichloroethane/ethanol	58
Deflocculant	Menhaden oil	1.8
Binder	Poly (vinyl butyrol)	4.4
Plasticiser	Poly (ethylene glycol)/octyl phthalate	8.8

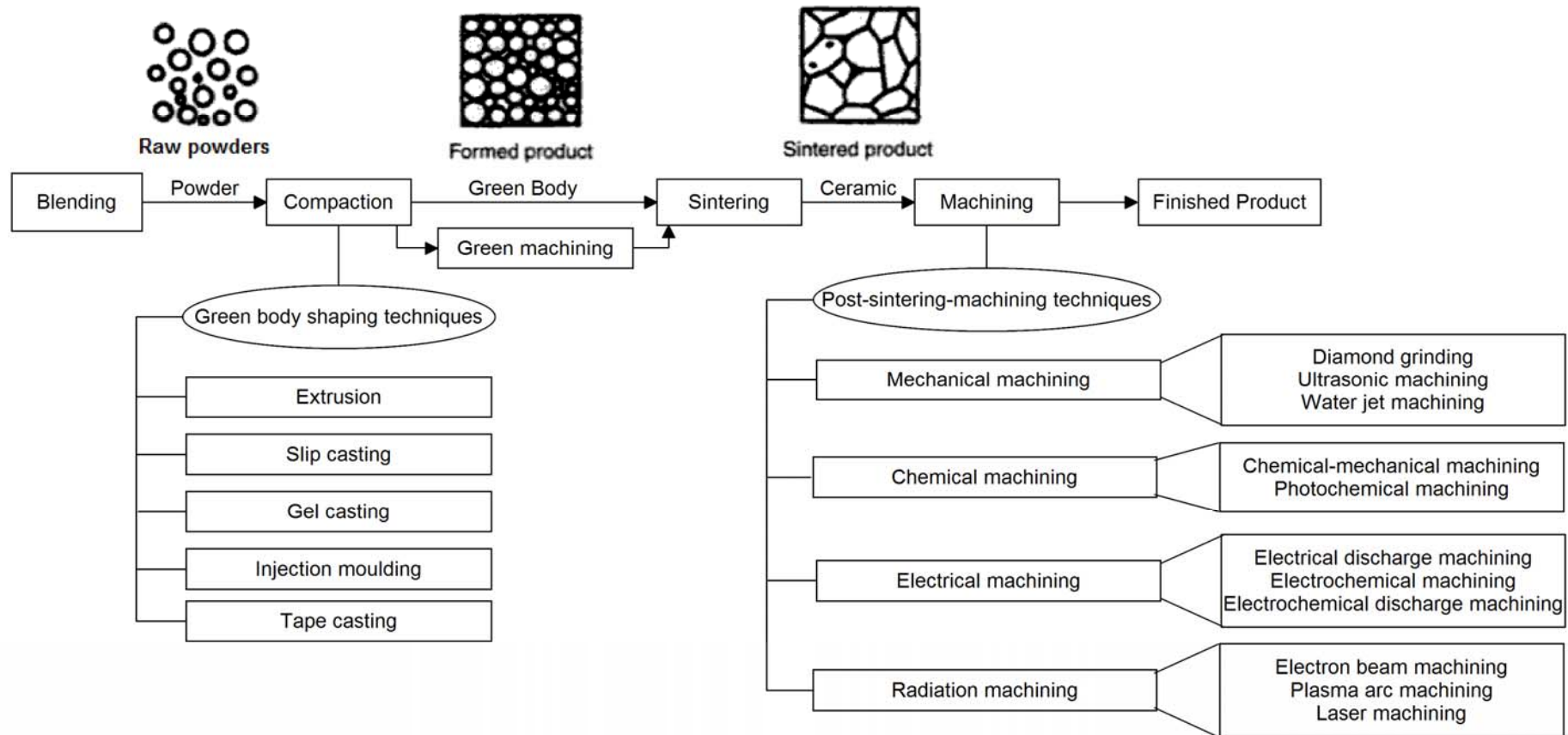


Figure 2.4 A typical route for forming engineering ceramics and the most commonly used machining techniques

2.3.1 Green body shaping techniques

The ceramic green body can be directly fabricated to the final shape before sintering. The desired shapes can be easily formed due to the low mechanical strength of weakly bonded ceramic powders in 'green body' phase. The fabrication techniques under this category include: Pressing, Extrusion, Slip Casting and Gel Casting, Injection Moulding, Tape Casting, and Green Machining.

2.3.1.1 Pressing

Pressing is the most widely used shaping technique for advanced ceramics, by which ceramic powders are under uniaxial or isostatic pressure into a desired shape. The external heat may be applied at the same time, in order to further enhance densification. The binder sticks powders and stabilises the ceramic slip without overly increasing the viscosity. Lubricants can also be used as one of the mixtures to enable powder flow and better packing density. This process is primarily used for substrates that have sharp edges, plastic and non-plastic masses and used for highly automated conditions. The green bodies generally have lower moisture content than other processing methods. Therefore, the lower shrinkage and higher accuracy after sintering can be achieved [15]. The subclass of the pressing technique involves: Dry pressing, Isostatic pressing, Hot pressing, and Hot isostatic pressing. Figure 2.5 shows the schematics of these pressing processes. The Pressing technique is generally used for manufacturing insulating parts, magnetic ceramics, capacitors and substrates. Compared with dry pressing, isostatic pressing further possess some advantages, such as better uniformity of compaction and more complex forms.

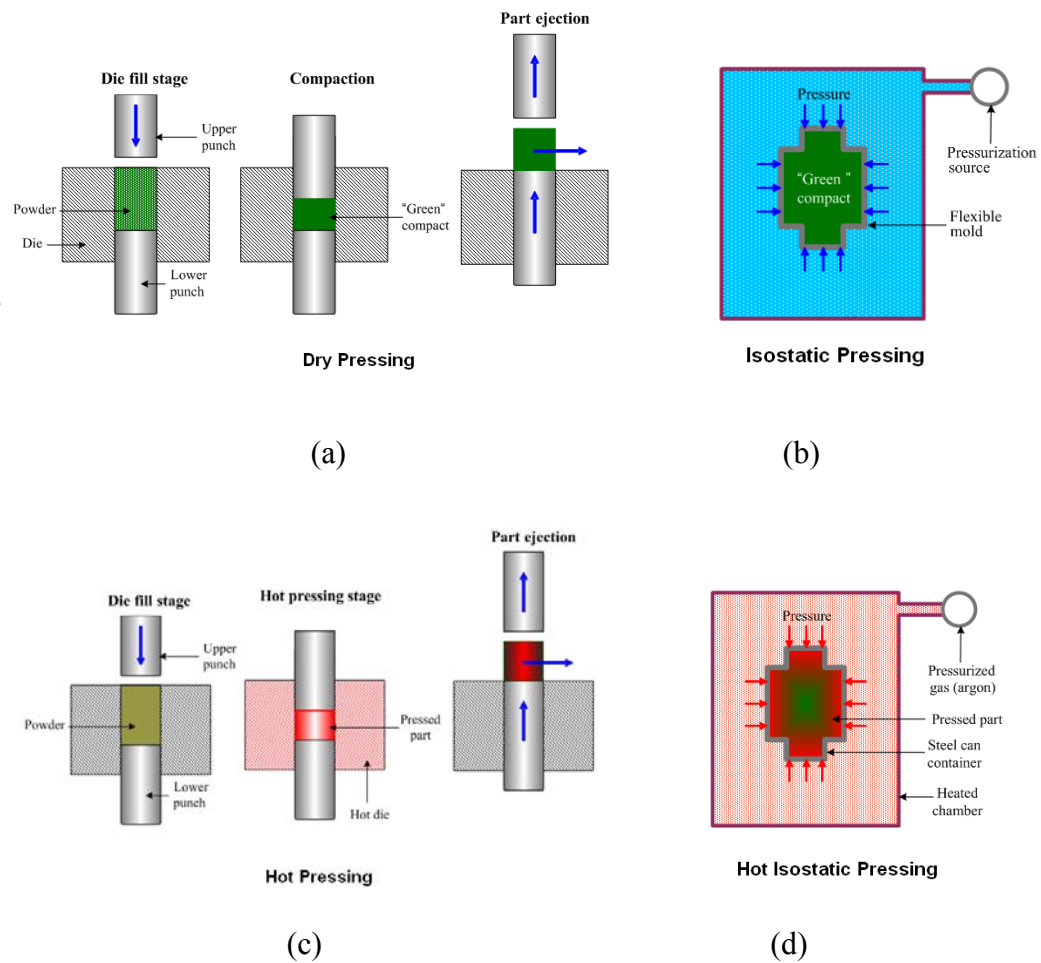


Figure 2.5 Schematics of (a) dry pressing, (b) isostatic pressing, (c) hot pressing, and (d) hot isostatic pressing processes [16, 17]

2.3.1.2 Extrusion

The extrusion process consists of forcing the ceramic paste through a constricting die to produce an elongated shape with regular cross-section (such as rods, bars, long plates, pipes, or honeycombs for automobile catalytic converters), which may be cut into pieces of required length. The binder provides plasticity to the green body in addition to strength [18]. The external heat may be applied at the same time, in order to enhance densification during forming. Figure 2.6 shows two schemes of the extrusion technique. Extrusion is used for manufacturing furnace tubes, thermocouple components, and heat exchanger tubes, etc [16].

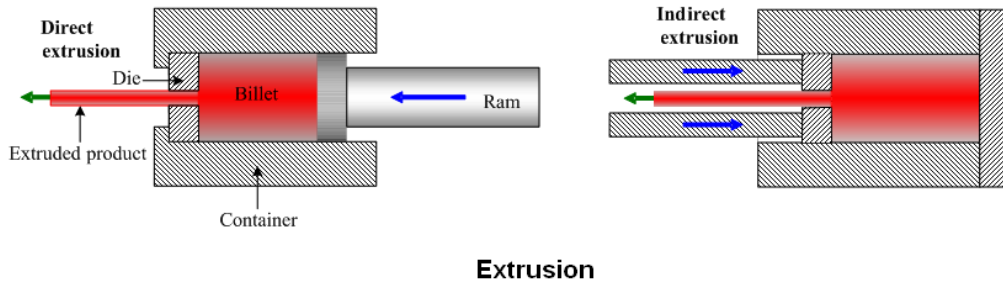


Figure 2.6 Two schematics of the extrusion process [16]

2.3.1.3 Slip and gel casting

Slip and gel casting techniques both need a negative mould of the desired shape. Slip casting is the process by which the ceramic suspension (slurry) is poured into a porous mould that is capable to soak the liquid from the slurry and then consolidate the ceramic part. Slip casting is used for manufacturing thermal insulation parts, sinks, sanitary ware, etc [16].

Gel casting is a process of forming slurry prepared from ceramic powder mixed with a solution of organic monomer. When the slurry is poured into a mould, the monomer polymerises and forms a gel that binds ceramic powder particles into the strong complex-shaped part. The part may be further machined before sintering. The process is economical and used for manufacturing large complex shape parts such as turbine rotors [16].

2.3.1.4 Injection moulding

This technique is comprised of four steps. (1) Mixing the ceramic powder with 30-40% of a binder, (b) Injection of the warm powder with molten binder into a mould cavity using a screw rotating in cylinder, (c) Removal of the part from the mould after cooling down, and (d) Debinding the binder (including solvent debinding and thermal debinding) by sintering. A schematic of the injection moulding technique is shown as Figure 2.7. This method is widely used for manufacturing small parts with complex shapes [16].

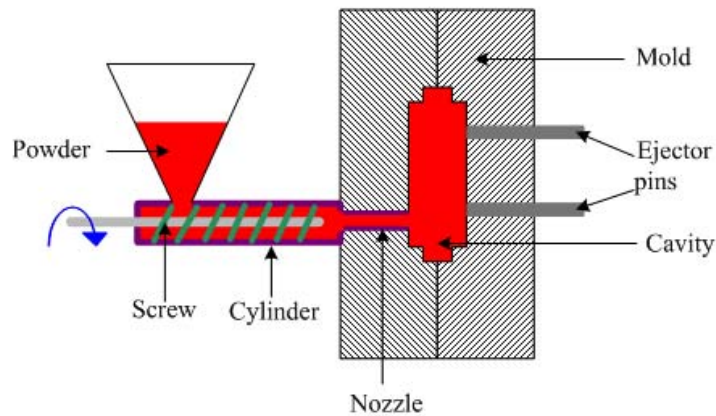


Figure 2.7 Schematic of the injection moulding process [16]

2.3.1.5 Tape casting

The tape casting process forms a thin film of ceramic slurry spread over a flat surface (as Figure 2.8). The slurry film thickness is controlled by a knife edge located above the moving carrier surface. Then the slurry film is heated and the solvent evaporates to leave a relatively dense flexible sheet, which can be stored on rolls or stripped from the carrier in a continuous process. Tape casting is used to manufacture multilayer ceramics such as capacitors and dielectric insulators [16].

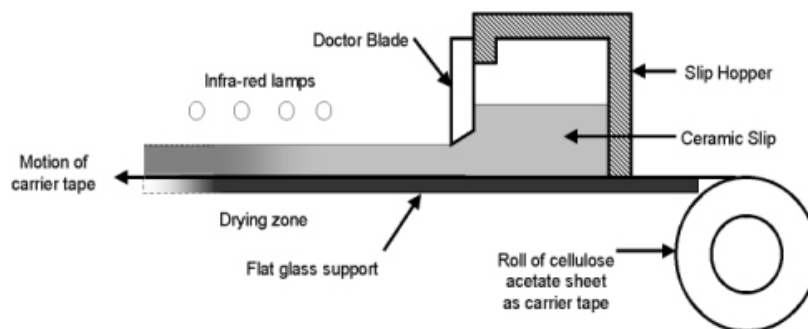


Figure 2.8 Schematic of the tape casting process [19]

2.3.1.6 Green machining

Ceramic machining in unsintered states is called Green Machining. It is generally employed to fabricate the shapes that cannot be directly realised by above-mentioned shaping processes. The low mechanical strength of a green body makes green machining an extremely high material removal rate with relatively low tool wear. Many machine tools have been used in green machining, such as computer numerical control (CNC) milling, lathes and drilling equipment, cut-off saws, surface grinders, and rotary finders [20]. Laser beams have also been applied to drill micro-through-holes in green electronic substrates. The spatter deposition and micro-cracks can be suppressed [21, 22]. Moreover, electron beams have been employed as machine tools in green machining [23-25].

2.3.1.7 Dimensions and shrinkage

The primary goal, when forming a green body, is to come as close as possible to the final dimensions and shapes, since it is costly to post-machine hard and brittle sintered ceramics. Basically, the green body is formed larger than the final dimensions due to a reduction in volume (known as shrinkage) during binder removal, drying, pre-sintering and sintering. In sintering, the high temperature leads to a reduction of the specific surface area of the powder particles (e.g. diffusion processes, creation of liquid phases, and phase transitions) and hence compaction of the microstructure causing the dimension shrinkage after sintering. Table 2.5 lists the typical shrinkage percentages of some advanced ceramics.

Therefore, moulds are usually over-dimensioned with respect to the desired geometries, in order to compensate the shrinkages. However, the tolerances of sintered ceramic parts via industrial standard processes are approximately $\pm 2\%$ [26].

Table 2.5 Typical shrinkages of some advanced ceramics [26]

Ceramic	Shrinkage Vol %
Sintered silicon carbide (SiC)	18-20
Alumina (Al ₂ O ₃)	17-20
Zirconia (ZrO ₂)	25-32

2.3.2 Post-sintering-machining techniques

In order to meet the tighter requirement of dimensional precision and surface finish quality as well as the variety of geometries, post-sintering-machining techniques should be employed. However, the extremely high hardness of sintered ceramics makes this process slow and costly (hence called Hard Machining). The commonly used machining techniques in industries in hard machining include: Mechanical machining, Chemical machining, Electrical machining, and Radiation machining.

2.3.2.1 Mechanical machining

Mechanical machining employs some mechanical forces or impingements of abrasive particles to remove material. The most used techniques in this subcategory include Diamond grinding, Ultrasonic machining and Water jet machining.

2.3.2.1.1 Diamond grinding

Diamond grinding is considered to be the most desirable and reliable technique for ceramic machining [4]. This technique is capable of producing complex profiles and fine surface finish. Unfortunately, the major drawbacks of the technique are the extremely long machining time and the high machining cost (amounting to 60-90% of final costs [1]). Plastic deformation and surface residual stresses after machining also degrade the final quality [27]. However, it still cannot be completely superseded by any other techniques for fine machining of ceramic materials. In most situations, it has to be employed as the final-grinding step for good surface finish and high dimensional precision [3].

2.3.2.1.2 Ultrasonic machining

Ultrasonic machining removes material by ultrasonically vibrated abrasive particles with a relatively low material removal rate. The basic element of ultrasonic machining head is a transducer/booster combination that converts electrical energy

into mechanical vibration and causes the tool to vibrate along the longitudinal axis at a high frequency with amplitude of 5-50 μm . The vibration causes the abrasive particles held in the suspension to microchip the ceramic surface [28]. The surface finish and machining resolution depends on to the used tool whereas the machining rate is directly related to the size of abrasive particles. In drilling, minimal hole diameter is 76 μm but the depth to diameter ratio is limited to about 3:1 [28]. Ultrasonic machining could reduce the damage in machining due to the low normal forces compared with diamond grinding. However, the mechanism of the material removal process is not well understood due to the complexity of this technique. Therefore, the process parameters are difficult to be optimised effectively [29].

2.3.2.1.3 Water jet machining

Water jet machining employs a high pressure water jet seeded with abrasive particles impinging on the surface of workpiece to remove material. The main advantage of this technique is the relatively high cut quality, low heat affected zone, and low tool wear. However, the machining rate is relatively low since ceramics have similar hardness as the seeded particles. The typical cutting speed is lower than 50mm/min for ceramic matrixes and plastic deformation cannot be avoided [30].

2.3.2.2 Chemical machining

Chemical machining utilises etchants to attack the material and remove small amounts from the surface. This technique has been developed to chemical-mechanical machining, photochemical machining, etc. Sharp corners, deep cavities and porous workpieces cannot be easily machined by this technique. Also, the material removal rate is relatively low. For photochemical machining of alumina ceramic, the etching depth can be lower than 200 μm and the etching rate can be 3.2 $\mu\text{m}/\text{min}$ [31]. Chemical-mechanical machining is generally used in surface patterning in semi-conductor (silicon) and micro-electro-mechanical systems (MEMS), in which a softened layer on the material surface is produced under a chemical reaction and then the mechanical machining is used to generate the desired

pattern on the surface. However, high costs, low machining rate and the multi-step limit this technique within the micro-machining field [32].

2.3.2.3 Electrical machining

Electrical machining technique employs electrical energy in the form of pulses or continuation in isolation or in combination with chemicals to achieve material removal. Generally, it is highly effective for machining electrically conductive or semi-conductive materials. The commonly used techniques in this catalogue are electrical discharge machining, electrochemical machining, and electrochemical discharge machining.

2.3.2.3.1 Electrical discharge machining

Electrical discharge machining is a non-abrasion process, which keeps a gap between the tool-piece electrode and the workpiece surface at approximately 40 μm . The material is removed by high energy plasma produced by the electrical discharge. This technique is not affected by material hardness but restricted to conductive material which should have an electrical resistivity of less than 100 Ωcm . Therefore, this technique is only suitable for conductive ceramics, such as boron carbide (B_4C) and silicon carbide (SiC) [3]. The surface roughness (central line average, CLA) is typically 4 μm and the material removal rate is 0.6 mm^3/min . The damage on ceramic surface may be caused due to heat generation in discharging [33].

2.3.2.3.2 Electrochemical machining

Electrochemical machining is characterised as reverse electroplating. This method is limited to electrically conductive materials only. Therefore, it is commonly used for machining metals with excellent electrical conductivity. The low heat and stress mean that little damage is caused. However, the high power costs and the unsuitability to generate sharp corners are two major drawbacks of this technique [1].

2.3.2.3.3 Electrochemical discharge machining

This technique involves a complex combination of electrical discharge machining and electrochemical machining. It is capable of machining high hardness electrically non-conductive ceramics [34]. However, the maximum machined depth is lower than 2 mm and the mass removal rate could not exceed 2.5 mg/min. Most importantly, the machined material shows tendency to crack due to the thermal shocks caused by the heat generated at high voltages [35].

2.3.2.4 Radiation machining

Radiation machining is a non-contact machining process, which generates a localised energy with high intensity, provided by electron beam, plasma arc or laser, onto the workpiece to melt, evaporate, and/or ablate the materials. This technique is independent of the hardness and electrical conductivity of the materials being machined. The commonly used techniques in this catalogue include Electron beam machining, Plasma arc machining, and Laser machining.

2.3.2.4.1 Electron beam machining

In electron beam machining, high-velocity electrons are directed toward the workpiece, heating or melting/vaporising the material. It can be used for fine cutting of a wide variety of materials, with a high cut quality. Unfortunately, the need of a vacuum chamber and the beam defocusing at high speeds are two major drawbacks of this technique [24]. Hence this technique is not suitable for large scale and high speed machining.

2.3.2.4.2 Plasma arc machining

Plasma arcs induced by ionised gas can be used for machining. The generated high intensity plasma provides sufficiently high temperatures leading to melting/vaporising the material and ejects molten material away from the processed

region. The narrow cut kerf and good surface finish are two significant advantages of this technique [1]. However, similar to the electron beam machining, the need of vacuum ambient limits the application of plasma arc to large-scale machining.

2.3.2.4.3 Laser machining

In laser machining, high power light energy is focused onto the workpiece surface and the local material is hence heated, melted, dissociated, decomposed, evaporated, and/or ablated from the surface. The machining quality is jointly governed by the laser parameters employed and inherent material properties. But it is almost independent of material hardness and brittleness properties. The technique represents a possible alternative for processing ceramic materials due to a number of advantages, such as no tool wear and cutting forces, high machining quality, as well as high flexibility and automation, etc. The economic comparison of laser machining with other machining techniques is listed in Table 2.6.

Table 2.6 Economic comparisons of different machining techniques [36]

Machining process	Capital investment	Tooling/ fixtures	Power requirements	Tool wear
Conventional machining	Low	Low	Low	Low
Ultrasonic machining	Low	Low	Low	Medium
Electrochemical machining	Very high	Medium	Medium	Very low
Chemical machining	Medium	Low	High	Very low
Electrical-discharge machining	Medium	High	Low	High
Plasma arc machining	Very low	Low	Very low	N/A
Laser machining	Medium	Low	Very low	N/A

In the next section, laser cutting/machining techniques for engineering ceramics (especially alumina) are reviewed in detail. Meanwhile, the major developments and challenges in laser cutting/machining of ceramic materials are summarised.

2.4 State-of-The-Art in Laser Cutting/Machining of Engineering Ceramics

To date, several lasers have been used in machining of engineering ceramics, including CO₂, Nd: YAG, Nd: YVO₄, Excimer, Fibre, diode, and ultrashort (i.e. picosecond and femtosecond) pulsed lasers. Each laser has its own emitting wavelength and machining applications. Although some of these lasers can be operated in both continuous wave (CW) and pulsed mode (PM), PM lasers are considered to be preferred for ceramic machining due to the more effective control of process parameters [37]. For macro-machining in industrial applications, infrared (IR) lasers are more suitable than ultrashort and ultraviolet lasers due to their high average power output causing a high material removal rate. Ultrashort and ultraviolet lasers are generally used in micro-machining and surface treatment. Basically, CO₂, Nd: YAG and fibre lasers have been widely employed in ceramic macro-machining.

CO₂ Lasers. CO₂ lasers are molecular lasers that use gas molecules (combination of carbon dioxide, nitrogen, helium, etc.) as the gain medium. The vibrational energy of carbon dioxide molecule is excited by AC or DC electrical discharge (known as the pump source) and then the stimulated radiation takes place in the oscillator. The CO₂ laser emits the light at a wavelength of 10.6 μm in the far infrared spectrum. CO₂ lasers have contributed to over 40% of industrial lasers [38]. The overall efficiency of electrical-optical energy conversion is in the range of 10%-30% and a beam power greater than 10 kW can be achieved. However, the beam quality degrades with increasing output power. Using the “SLAB” technique developed by Rofin-Sinar Technologies Inc., the high beam quality ($M^2 < 1.1$) can be kept up to 8 kW output power. Furthermore, CO₂ lasers are usually operated in CW mode, but PM can also be achieved by modulating the pump source up to 5 kHz. Therefore, CO₂ lasers are generally considered as one of general-purpose lasers for most material processing, such as heat treatment, cutting, welding, cladding, etc.

Fast axial gas flow, slow axial gas flow, perpendicular direction of gas flow to the laser optical path, and perpendicular direction of electrical discharge to the optical path, sealed-off are five techniques applied in CO₂ laser systems. Sealed-off CO₂

lasers are the lowest cost lasers in the CO₂ laser family but their output powers are also limited and lower by some hundred watts. Periodic maintenance is required (i.e. refilling pre-mixed gas) in order to hold the laser output power. This is the major drawback of CO₂ lasers. In addition, the wavelength emitted by CO₂ lasers cannot be delivered by optical fibres, which limits the combination with robots in industrial applications.

Nd: YAG Lasers. They are solid-state lasers that use 1-2% dopants (i.e. Neodymium (Nd³⁺)) dispersed in a crystalline matrix (i.e. Yttrium-Aluminium-Garnet (YAG) with the chemical composition Y₃Al₅O₁₂) as the gain medium. Pump sources are krypton or xenon flash lamps, or recently laser diodes. The wavelength of an Nd: YAG laser is emitted at 1.06 μm in the near-infrared spectrum. The power output of CW Nd: YAG lasers are lower by some kilowatts. But the Q-switch Nd: YAG lasers can generate short pulses with peak power in megawatts, repetition rates up to 100 kHz and pulse durations between 15-400 ns. The average output power of a pulsed Nd: YAG laser is generally lower than 1 kW. The output laser beam (at 1.06 μm wavelength) can be coupled into an optical fibre for delivery. Therefore, it is suitable to combine with robots for more flexible processing in industries. Nd: YAG lasers have been widely used for cutting, welding, cladding, and drilling of metal or non-metal materials. The drawback of Nd: YAG lasers is the relatively low beam quality at high output powers ($M^2 < 6$), causing a large spot size, low power density and short focal depth. Therefore, high power Nd: YAG lasers are not very suitable in precision processing and thick-section machining applications. Furthermore, maintenance is also essential to Nd: YAG lasers.

Fibre lasers. Although the first fibre laser was proposed in early 1960's, their practical applications were limited in laboratory demonstrations until the late 1990's. In the late decade, they appear some unique advantages in material processing when the advanced and commercial double-clad high power fibre lasers are available. In high power fibre lasers, a multi-clad silica-based optical fibre is used as the gain medium, which is doped with rare-earth ions, such as erbium (emitted laser at 1.55 μm wavelength), ytterbium (emitted laser at 1.07 μm wavelength), neodymium (emitted laser at 1.06 μm wavelength), praseodymium (emitted laser at 1.3 μm wavelength), and thulium (emitted laser at 1.45 μm wavelength). The fibre core

confines the majority of the laser energy, in which the laser is generated. The inner cladding layer is of a lower refraction index than the core region to prevent laser attenuation and confine the most diode pump beam energy to be absorbed by the fibre core for stimulated radiations. The outer cladding layer keeps the pump light confined. The light is transmitted along the fibre by total reflection. Fibre Bragg Gratings (FBG) inside the fibre provides an oscillator for the generated laser wavelength and filters other wavelength lights. The laser transverse modes are controlled by the waveguide characteristics of the fibre core. The beam quality of fibre lasers is perfect ($M^2 < 1.1$), even at high powers (up to some kilowatts). The leader of high power fibre laser manufactures – IPG Photonics Corp. – provides kilowatt class fibre lasers up to 50 kW, operating in CW or modulated modes up to 20 kHz, with wall-pump efficiencies greater than 30% [39]. High power fibre laser has been widely used in cutting and welding fields. The distinctive advantages, such as high power, high brightness, high efficiency, high flexibility (fibre-delivered beam and robot manipulation), small spot size, high beam quality, maintenance-free, high compactness, and high durability, make fibre lasers more attractive in future laser industrial applications.

All the wavelengths of above mentioned lasers are in the IR spectrum. Nowadays, IR lasers can partially replace mechanical material removal techniques in several engineering applications due to their unique feature, i.e. the non-contact, photo-thermal and flexible process [40]. Generally, the material removal rate and the finish quality mainly depend on the employed laser parameters, such as laser power, spot size, focal plane position (*f.p.p*), feed rate, pulse repetition rate, pulse duration, etc., and relay on the thermal and optical properties of the material as well. This makes hard and brittle materials with low thermal conductivity, such as engineering ceramics, suitable to be machined by IR lasers. Although the laser cutting/machining techniques have been employed in industrial applications for many years and become mature, laser cutting/machining of engineering ceramic still faces some challenges. The major challenge is to achieve high quality (without crack and rough surface finish) and high speed cutting/machining. Therefore, many studies were performed and several techniques were developed in past decades, in order to

improve the process quality and machining rate of laser cutting/machining of engineering ceramics. The following sections review the most studied laser cutting/machining techniques for engineering ceramics (especially for alumina). The techniques include: Laser conventional cutting, Laser multi-pass cutting/machining, Laser controlled fracture cutting/machining, and Laser hybrid cutting/machining.

2.4.1 Laser Conventional cutting techniques

In laser conventional cutting, a cut front is formed when the laser beam melts/vaporises the localised workpiece throughout the thickness. A cut kerf is then formed when the laser beam is in relative motion with respect to the workpiece. The material removal in laser cutting is by means of melting and/or evaporation. The coaxial high pressure gas jet is used to enhance material removal and probably generate chemical exothermic reactions. Plasma may also appear during high power laser cutting, which attenuate the laser power arriving on the workpiece. The basic schematic of the laser conventional cutting process is shown in Figure 2.9. The major cut quality factors, such as cut kerf width (at top surface and bottom surface), recast layer, heat-affected zone (HAZ), crack, bur, dross, and cut surface roughness (i.e. striation formation and droplet re-deposition), are illustrated in Figure 2.10.

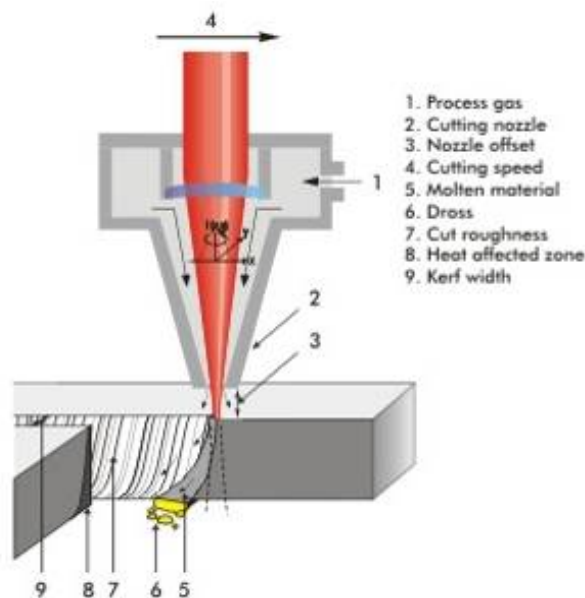


Figure 2.9 Schematic of the laser conventional cutting process [41]

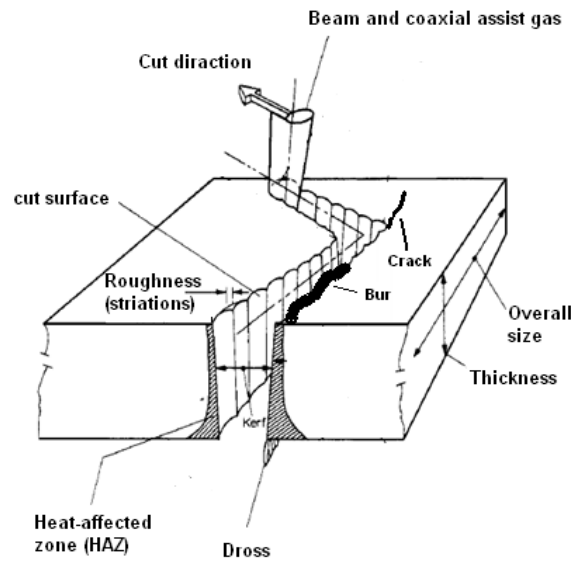


Figure 2.10 The major cut quality factors in laser conventional cutting [42]

Crack is the most critical quality factor since it may cause fracture and catastrophic failure in brittle ceramic materials. Therefore, most of studies were first focused on crack-free cutting. Previous studies indicated that high laser power with a low cutting speed can reduce the thermal-stress level and subsequently, reduce the possibility of fracture in CW laser cutting (Figure 2.11) [43]. Lu et al specified an empirical equation to identify the boundary of operating conditions on fracture initiations in CW CO₂ laser cutting of alumina up to 2-mm thickness [44]:

$$P \geq 1.78 \times 10^{11} t^{2.41} v \quad (2-1)$$

Where P is the minimum laser power to avoid crack formation (in W), t' is the workpiece thickness (in m), and v is the feed rate (in m/s).

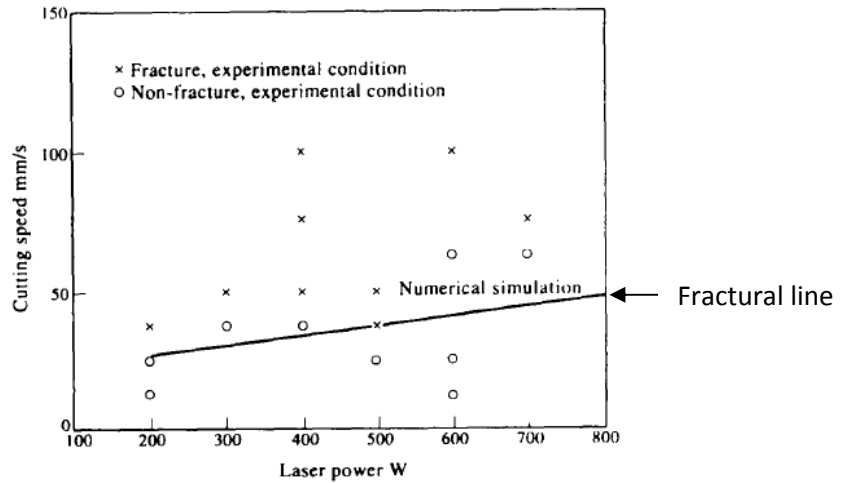


Figure 2.11 Fractural line of CW CO₂ laser cutting of alumina [43]

Lee et al pointed out that although the critical crack formation boundary can be determined by the laser power and cutting speed, the occurrence of cracks is still uncertain at the critical conditions due to the undulations of the cutting front angle affected by the operating conditions such as materials, inert gas and laser focusing. They proposed a lower bound of the crack-forming cutting front angle δ , which is defined as the angle between the vertical line (z -axis) and the normal vector n' (Figure 2.12(a)). Under some uncertain conditions, when cut front angle becomes smaller, the amount of absorbed energy will be increased (no cracking), but if the cut front angle becomes larger, the probability of crack formation will be increased (Figure 2.12(b)). It means that crack forms if $\delta > \delta^*$ and no crack forms otherwise, where δ^* is the critical lower bound of the cut front angle for crack formation [45].

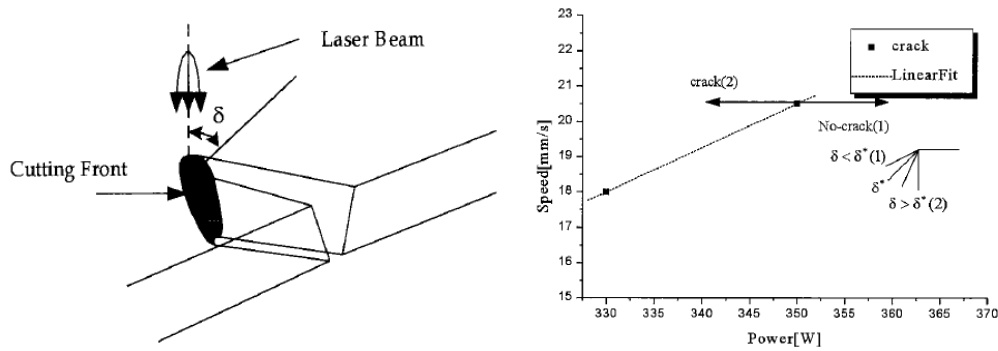


Figure 2.12 (a) Schematic of cutting front and (b) fracture line during laser cutting of alumina [45]

However, continuous wave (CW) lasers are not recommended for cutting brittle materials owing to the large amount of heat that is accumulated and conducted into the bulk inducing heat overload and crack growth [46]. Pulsed mode (PM) lasers are therefore more suitable for ceramic cutting due to the significant reduction in heat accumulation [47, 48]. Some studies have been carried out to demonstrate the feasibility of applying millisecond lasers [49], nanosecond lasers [50], picosecond lasers [51] and femtosecond lasers [52] in ceramic cutting/machining. On the other hand, PM cutting leads to a low machining rate and cutting speed due to the low average power [46-52].

In addition to the input energy effect, Black et al further studied the effect of assist gas on cut quality and indicated that [53]:

- (i) The gas parameter has a significant effect on cut quality. High quality cuts can be achieved in the thinner tiles ($< 6\text{mm}$) at gas pressures of 2 bars but cannot be achieved in thicker tiles unless >3 bars gas pressure is used. At low pressures (< 2.5 bars), the maximum cutting speeds for full through-cutting dropped drastically as the gas failed in its role of dress cleaner. Moreover, the assist gas was acting as a coolant and helping to minimise the large thermal gradient produced by the laser beam. Cutting ceramics using the inert gases argon and nitrogen produced better results, especially with the latter due to the high cooling efficiency.

- (ii) Nozzle size was directly related to pressure jetted from the nozzle (i.e. the smaller is the nozzle size the higher is the obtainable pressure). The nozzle should be always smaller than 1.5 mm diameter with a gas pressure greater than 3 bars to effectively remove molten material. The smaller nozzle diameters produced better cuts at high cutting speeds.
- (iii) By lowering the *f.p.p* into the workpiece the 'dross' adherence decreased but in raising the *f.p.p* away from the workpiece full through-cutting failed as the beam defocused.
- (iv) The ability of the assist gas through the cut dictated the pattern of dross. At the top of the cut edge where the gas pressure was high and the gas flow was directed, there was little or no dross adherence. More dross adhered to the bottom of the cut edge since the gas pressure reduced due to more turbulent gas flows with the cut depth increasing.

Considering the significance of assist gases, Quintero et al performed a series of investigations into the effect of assist gases in laser cutting of mullite-alumina ceramics ($3\text{Al}_2\text{O}_3 \cdot 2\text{SiO}_2$). They used a 500 W pulsed Nd: YAG laser guided by an optical fibre to cut mullite-alumina plates with 4-mm thickness. They found the limitation of maximum cutting speed as a function of average power and assist gas pressure. A linear relation of the limited cutting speed with the employed laser power is shown in Figure 2.13, which indicates the shallow influence of the heat conduction losses on the overall heat balance during cutting of low heat conductive materials. They also found that when the gas pressure was raised from 5 to 8 bars, there was no significant increase of the limited cutting speed since a strong normal shock wave diminishes the effectiveness of the assist gas jet capability. Based on their study, some two-dimensional (2D) complex cuts were demonstrated in Figure 2.14, showing the suitability and versatility of the Nd: YAG laser cutting of mullite-alumina ceramics. The employed cutting conditions were cutting speed of 5 mm/s, assist gas pressure of 5 bars, average laser power of 430 W, pulse frequency of 120 Hz, and pulse duration of 1 ms [49, 54, 55].

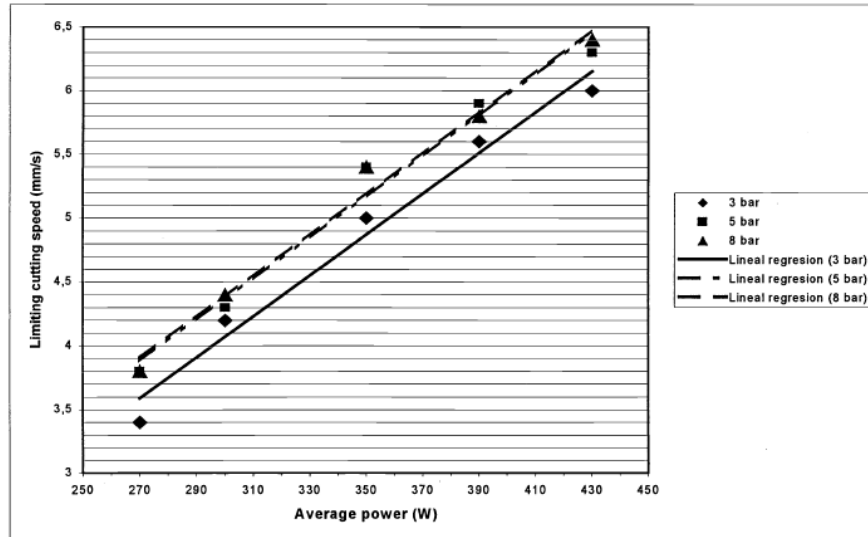


Figure 2.13 Limited cutting speed as a function of the employed average laser power and assist gas pressure [49]

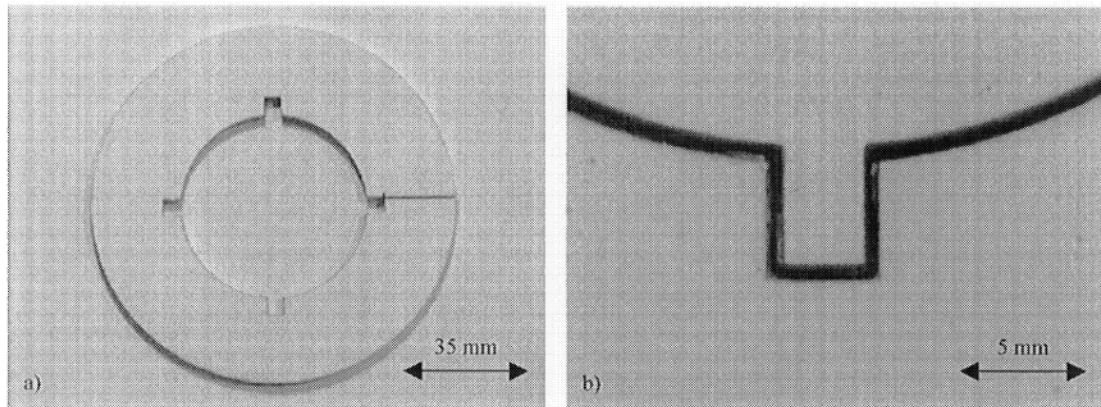


Figure 2.14 Optical images of a 2D cut piece at different magnifications: (a) overview of the sample (outside part), (b) detail of the cut (outside and inside parts of the piece) [49]

For various ceramic materials, the physical processes governing material removal are varied depending on their thermal properties. Table 2.7 lists the major physical phenomena during laser machining of some typical engineering ceramics.

Table 2.7 Major physical phenomena in laser machining of some typical engineering ceramics [56]

Material	Melting	Dissociation	Evaporation
Al ₂ O ₃	Yes	Yes	Yes
SiC	Yes	Yes	Yes
Si ₃ N ₄	Yes	Yes	Yes
MgO	No	Yes	Yes

Due to the inevitable melting in laser cutting/machining alumina, even using femtosecond lasers [57], a significant process in cutting/machining alumina is the aerodynamic interaction between the assist gas and molten materials. The above mentioned studies have indicated that the recast layer and dross cannot be eliminated by coaxial gas jets. This deterioration becomes more significant in laser cutting of thick-section ceramics [52]. A typical view of cut surface via a coaxial nozzle is shown in Figure 2.15, where the most significant feature is the critical recast layer which appears as a white area in the border of the cut kerf. The upper face of the kerf edge appears completely free of recast layer whereas below this area the recast layer appears. This outcome can be explained by the aerodynamic interactions of the assist gas jet and molten materials. A schematic drawing of the coaxial assist gas aerodynamic performance in laser cutting is shown in Figure 2.16. It explains the formation of the two different zones observed in Figure 2.15. (1) In the upper area of the kerf edge, the gas jet is able to drag out the molten material with a laminar flow. Below this area, eddies and slipstreams of the gas flow reduce its ability to remove the molten materials. Therefore, a recast layer is formed and the dross resolidifies onto the cut edge. (2) The dross attached to the edge of the kerf releases a great quantity of heat into the workpiece during its cooling and hence resolidification led to a thicker recast layer at the lower face of the kerf edge (as Figure 2.15(b)) [58].

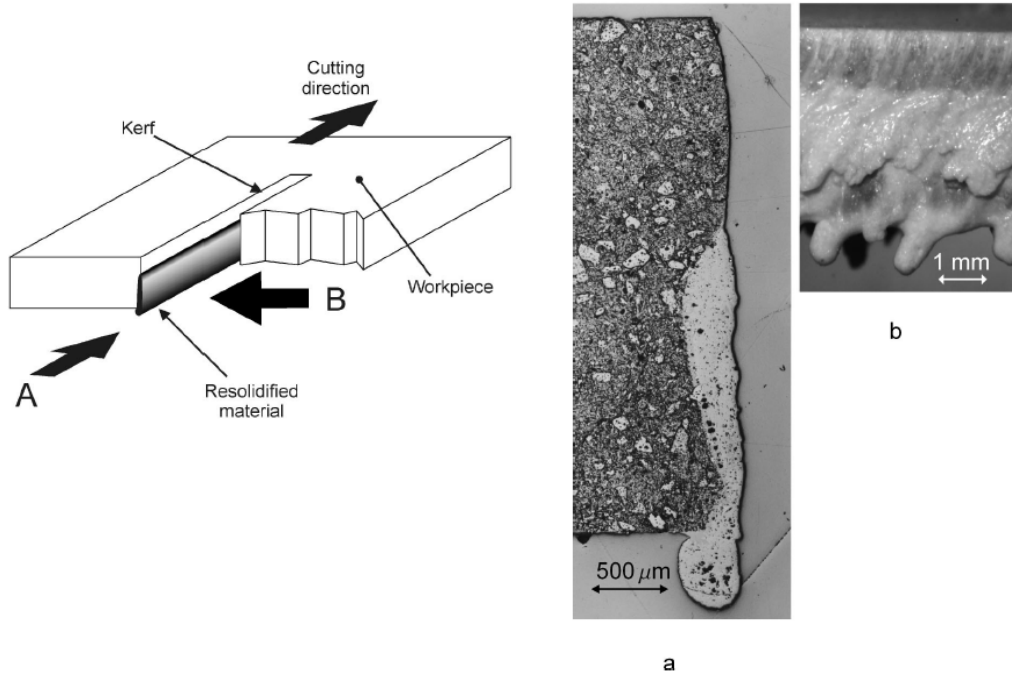


Figure 2.15 Schematic (left side) and optical images (right side) of recast layer on the cut surface. (a) A typical cross-section. (b) A side view of the cut surface [58].

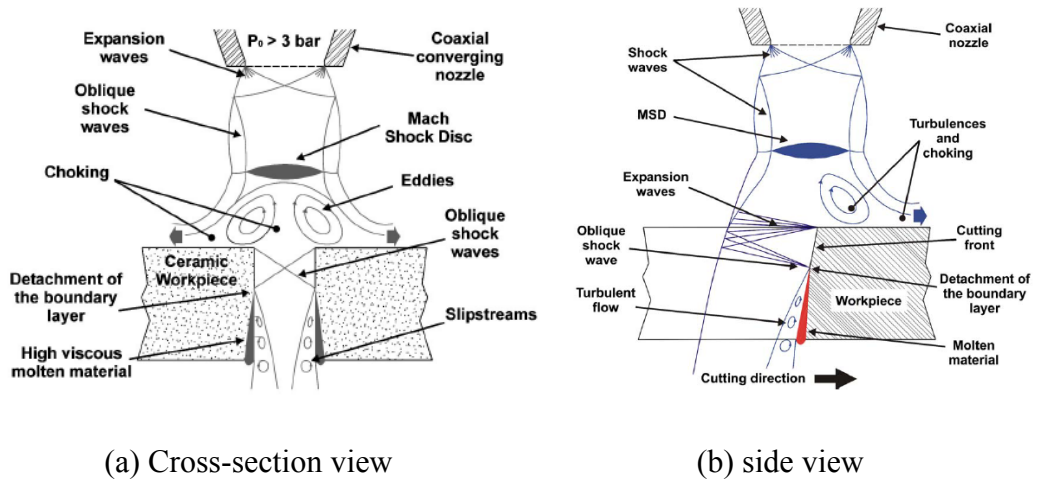


Figure 2.16 Aerodynamic interactions between molten materials and assist gas flow jetted from a coaxial nozzle [58, 59]

During laser cutting, the assist gas jet with high kinetic energy is injected in the cut front to remove the molten material. This process has great influence on the resultant cutting characteristics, affecting the cutting speed and the cut quality as mentioned above [58]. These consequences have a more significant effect on cutting of thick-section alumina, since the viscosity of molten alumina is 1-2 orders of magnitude higher than steels and aluminium [60-62].

In order to improve the efficiency and capability of assist gas injection, Quintero et al developed a new cutting head with an off-axial supersonic nozzle as shown in Figure 2.17. Two adjustable parameters for the off-axial nozzle setup are the distance X behind the laser beam and the angle of gas jet axis θ with respect to the laser beam axis. Under this configuration, a laminar boundary layer that flows along the entire depth of the cutting front keeps two driving forces removing the molten material (shear stresses and pressure gradient) effectively [58]. Figure 2.18 shows a cut edge obtained by the off-axial nozzle cutting head with the best settings. The thin recast layer and free of dross indicates the less disrupted gas flow jetted from the off-axial nozzle and shows the capability of off-axial gas flow in cutting of 4-mm thick mullite-alumina plates.

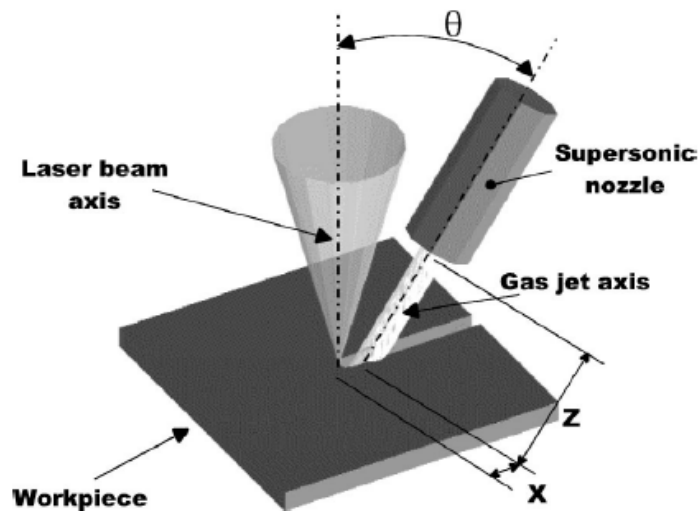


Figure 2.17 Setup of the supersonic off-axial assist gas injection system [58]

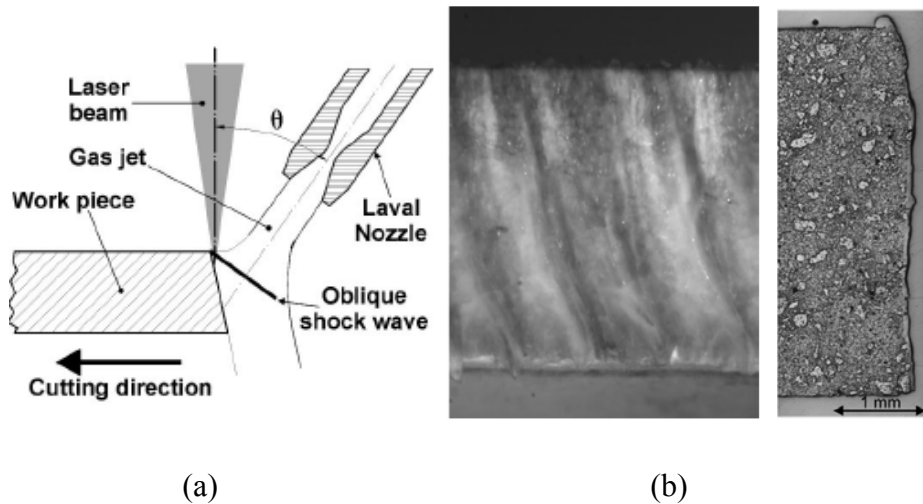


Figure 2.18 (a) Schematic of interaction of the off-axial gas jet with the cut front and (b) the cut edges obtained by the supersonic off-axial assist gas injection cutting head. Optical graphs of the cut surface at side view (left) and cross-section view (right) [58].

Quintero et al [63, 64] further carried out a series of investigations into the effects of different cutting parameters and different gas nozzle setups on the pulsed Nd: YAG laser cut quality for mullite-alumina ceramics with 4-mm thickness or greater. Their studies indicated that the characteristic of HAZ was a function of laser average power, cutting speed, and assist gas pressure and pulse frequency (with 1 ms fixed pulse duration), whereas the maximum cutting speed was determined as a function of the laser average power and the gas pressure. The coaxial assist gas pressure was found to affect the HAZ at the upper face of the cut kerf but no affect on the HAZ at lower face due to the detachment of the gas flow from the kerf edge. The pulse repetition rate had a clear influence on the extension and intensity of the HAZ [63]. A study of the CO₂ CW and PM laser cutting mullite-alumina with 5-mm thickness was also performed. It was found that the best cut quality in CW mode can be achieved using a laser power below 1000 W, a cutting speed close to the maximum (>14 mm/s) and an off-axial gas nozzle. Meanwhile, the pulsed mode at low frequencies (<20 Hz) with a coaxial gas nozzle can also achieve a high efficient material removal rate. However, the cutting speed of the PM mode is lower (<11 mm/s) due to the lower laser average power output [64].

In 2006, the aerodynamic characteristics of the off-axial supersonic gas flow inside the cut kerf were validated by means of flow visualisation using the Schlieren technique [59]. The cut kerf was made with two plates of glass parallel to each other arranged at a distance of 0.5 mm to simulate the cut kerf. A solid sheet with the precise thickness of the gap between the glass plates was placed occupying half of their area in order to simulate the cut front (Figure 2.19). The angle of 15° of the sheet edge with respect to the vertical was set as the typical angle of the cut front. Figure 2.20 shows the captured pictures of gas flows inside the cut kerf at various distances between the off-axial gas nozzle and the cut front. It was seen that a very uniform distribution of the gas flow along the cut front in Figure 2.20(d). This gas flow should be the most effective to remove molten material as shown in Figure 2.20(h), where the thinnest recast layer with typical cut ripples was achieved. This work validated the significance of assist gas flow in molten material removal during laser fusion cutting of ceramic materials.

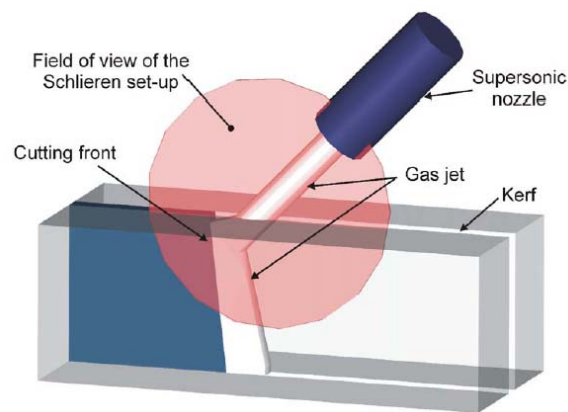


Figure 2.19 Schematic of the transparent model of the cut kerf and the setup of the off-axial nozzle for flow visualisation using Schlieren Photography [59]

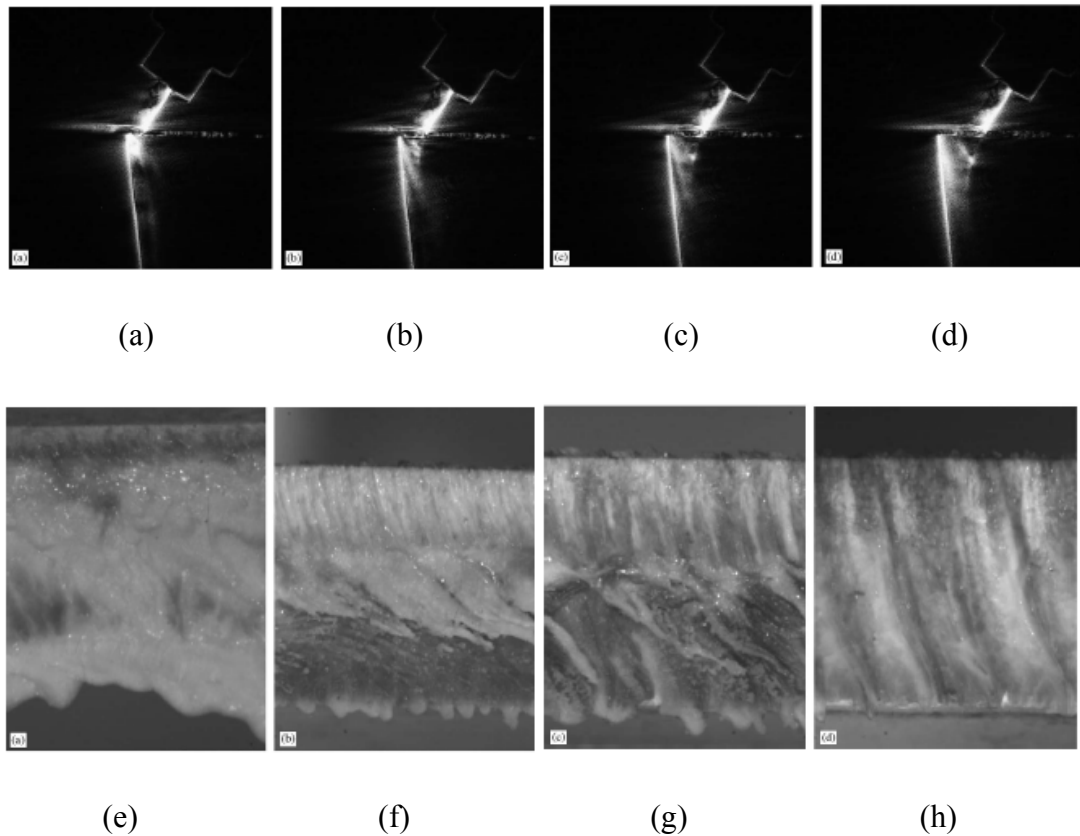


Figure 2.20 (a)-(d) Images of the gas flow inside the cut kerf captured by Schlieren Photography and (e)-(h) photographs of the cut surfaces at different distances between the gas nozzle and the cut front: (a) and (e) $X=0$, (b) and (f) $X=1$, (c) and (g) $X=2$, (d) and (h) $X=3$ mm [59]

Unfortunately, profile cutting is the major challenge using the off-axial nozzle cutting head since the direction of nozzle has to be adjusted in real time in order to aim the gas flow normal to the cut front. In 2008, a new concept of off-axial nozzle cutting head controlled by CNC for profile cutting was released (as Figure 2.21). It removes the obstacle to application of the off-axial nozzle cutting head in profile cutting in industrial applications. However, the complicated mechanical structure of the cutting head makes it unsuitable to three-dimensional (3D) and/or high-speed cutting.

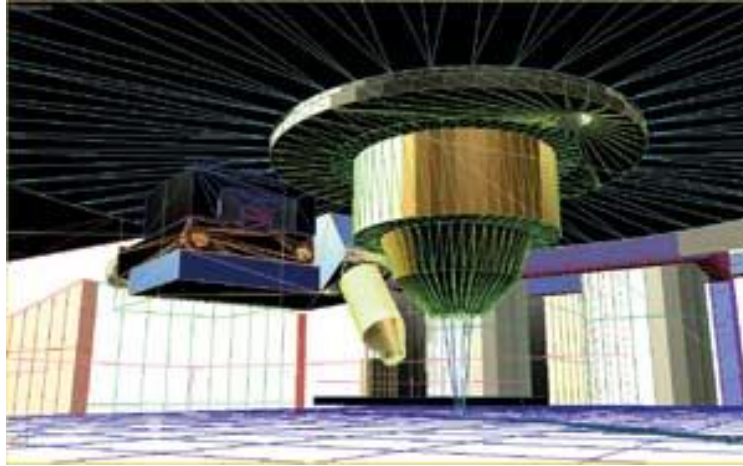


Figure 2.21 The CNC controlled off-axial nozzle laser cutting head [65]

Quintero's research did not focus on cracks in laser cutting, due to the low thermal expansion coefficient and Young's modulus of the mullite-alumina (a weight of 80% of alumina and 20% silica) in comparison with 95-99% alumina ceramics [12, 66]. Moreover, cracking can be trapped by the creep of soften glassy phases in mullite-alumina at high temperatures. Therefore, mullite-alumina has a relatively high resistance to thermal-stress-caused fracture in laser cutting. For high performance engineering ceramics (e.g. 95-99% alumina ceramics), less glassy phases make cracking and fracture take place more easily. Therefore, laser process parameters should be chosen more carefully for crack-free cutting of the engineering ceramics.

Kacar et al demonstrated Nd: YAG laser crack-free percussion drilling of 95% alumina ceramic up to 10 mm thickness [67]. From their work, it can be deduced that the crack-free cutting could be achieved when the crack-free drilling is repeated along a desired path. Based on this hypothesis, Ji et al developed a close-piercing lapping (CPL) laser cutting technique for crack-free cutting of 99% alumina ceramics up to 10-mm thickness using a 3.5 kW CO₂ laser [68]. The cutting process of the technique is a series of percussion drilling instead of conventional pulsed laser cutting (as Figure 2.22). Serious thermal accumulation is therefore suppressed via sufficient cooling between adjacent piercing processes. Using the technique, crack-free curve and sharp angle cuts were demonstrated (as Figure 2.23). However, the

cutting speed of the CPL technique was only 0.23-0.42 mm/s for 10 mm thick alumina ceramics, which presents a critical obstacle to industrial applications.

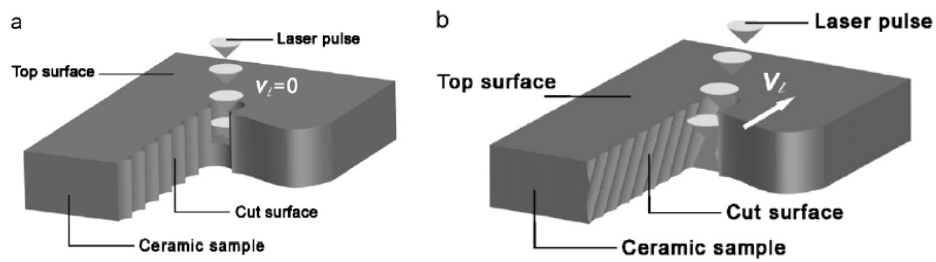


Figure 2.22 Schematic of two different laser cutting techniques: (a) close-piercing lapping (CPL) laser cutting technique and (b) pulsed laser conventional cutting techniques [68].

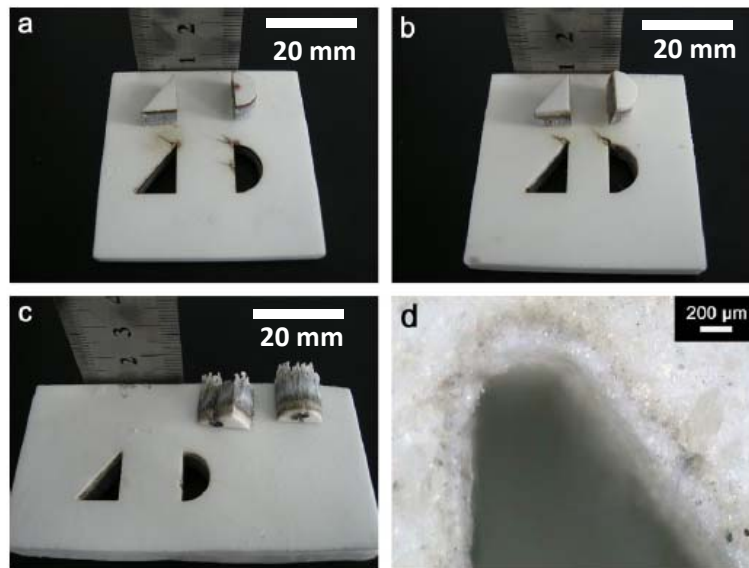


Figure 2.23 Photographs of crack-free curve and sharp angle cuts in alumina by the CPL technique. (a) 4-mm thickness, (b) 6-mm thickness, (c) 10-mm thickness, and (d) a close-up view of the cut sharp angle on the top surface of 10-mm-thick alumina [68]

In order to achieve high-quality cutting, other quality factors in addition to crack should also be considered. As mentioned above, Quintero's studies have involved some cut quality improvements, such as lower dross, thinner recast layer and HAZ, as well as smoother cut surface [64]. However, striation formation in laser cutting is

always found on all laser cut surfaces, even in femto-second laser cutting [52]. Striations are some relatively regular periodic straight lines with a slight inclination from the laser beam axis. It influences the quality (i.e. roughness of cut surface) and precision (i.e. kerf width variation) of laser cutting [69]. Generally, the roughness (R_a) of alumina sheet (< 1 mm thickness) cut surface by laser cutting is 10-50 μm , which poses a major challenge for denser circuit patterns and device miniaturisation. Furthermore, for thick-section ceramics, the cut surface roughness dramatically increases [64].

Although many studies have been performed to explore the mechanisms of striation formation, most of them are focused on oxygen-assisted laser cutting of metals, in which the energy matching between exothermic reaction and laser beam was most studied [70-74]. However, during laser cutting of ceramics, striations still appear although no reaction takes place between assist gas and material. Therefore, some other mechanisms of striation formation should exist. Schuocker proposed a mechanism of striation formation as a result of small fluctuations in laser power and gas flow, which can initiate hydrodynamic instabilities of the molten front [75]. Vicanek et al proposed a striation formation mechanism based on the instabilities in the melt removal process induced by the pressure gradient driven melt flow [76]. Makashev proposed that striation formation was caused by the melt droplet formation for materials with a thickness much greater than the kerf width during laser cutting with inert gases, where the changing melt droplet size within the cut kerf could cause imbalance between the capillary forces and the gas pressure [77]. Olsen observed via spark shower experiments that the melt flow moved from one dimensional to two dimensional when the cutting speed increased, which supported the liquid layer oscillation theory for striation formation [78]. The increase of striation depth with increasing gas pressure was further observed by Kaebernick et al [79].

Based on these theoretical and experimental investigations into understanding of striation formation mechanisms and characteristics, several efforts to eliminate striations in laser cutting were attempted over the last few years. Li et al demonstrated striation-free laser oxygen-assisted cutting of mild steel sheets up to 2-mm thickness using 1 kW CW fibre laser [69]. The minimum arithmetic mean

roughness (R_a) of striation-free cut surfaces was $0.88 \mu\text{m}$ [80], by which post-process-free laser net shape cutting could be achieved. They also found that two conditions are necessary to overcome striation formation. One is that the cutting speed must be higher than a threshold in order to achieve a steady state reaction and prevent the oxidation front escaping from the laser beam. This condition overcomes possible striations resulting from the cyclic nature of the oxidation front [81]. The other condition is the advancement time of the vaporisation front through the depth of the workpiece should be equal to the time of laser/material interaction within the beam spot, by which the melting rate equals to the melt removal rate. Under this condition and assuming melting to be a continuous process (i.e. CW laser beam), melt oscillation can be prevented [69]. For ceramics, only the second condition is viable, as generally no reaction between material and assist gas takes place. Wee et al used statistical analysis to study striation formation characteristics for 1 kW CW fibre laser cutting of 7 mm thick alumina ceramics under different operating conditions. They indicated that the striation formation could not be eliminated completely even though the cut quality can be improved by the statistical model [82]. Ji et al recently demonstrated striation-free cutting of 1 mm thick alumina substrates using a 1 kW CW fibre laser as shown in Figure 2.24 [83]. This work supports the theory developed by Li et al [69].

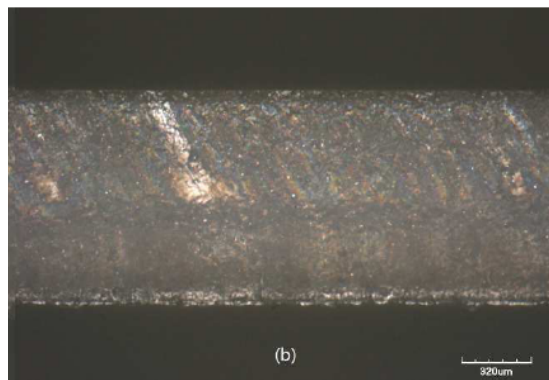


Figure 2.24 Striation-free cutting of 1-mm thick alumina sheets using a 1 kW CW fibre laser [83]

Despite many studies on the elimination of striation formation for CW laser cutting, no work has shown striation-free cutting by pulsed lasers. In previous studies, pulsed

lasers were considered as the most suitable laser mode for cutting of ceramics since fracture and catastrophic breakdown were easily caused by the serious heat shocks in CW laser cutting [46]. Recent studies further found that short and ultra-short pulsed lasers (e.g. ns-fs) could obtain higher cut quality than CW or millisecond pulsed lasers [52]. However, elimination of striation is still a challenge in pulsed laser cutting even employing short or ultra-short pulses.

In next part of this section, the significant phenomena associated with laser cutting of ceramics are discussed. In laser-material interaction, the magnitude of temperature rise governs the different physical phenomena, such as melting, vaporisation, plasma formation and ablation, depending on the applied power density and thermal properties of the material. Figure 2.25 shows the various physical phenomena during laser-ceramic interaction with laser power density increasing from (a) to (e).

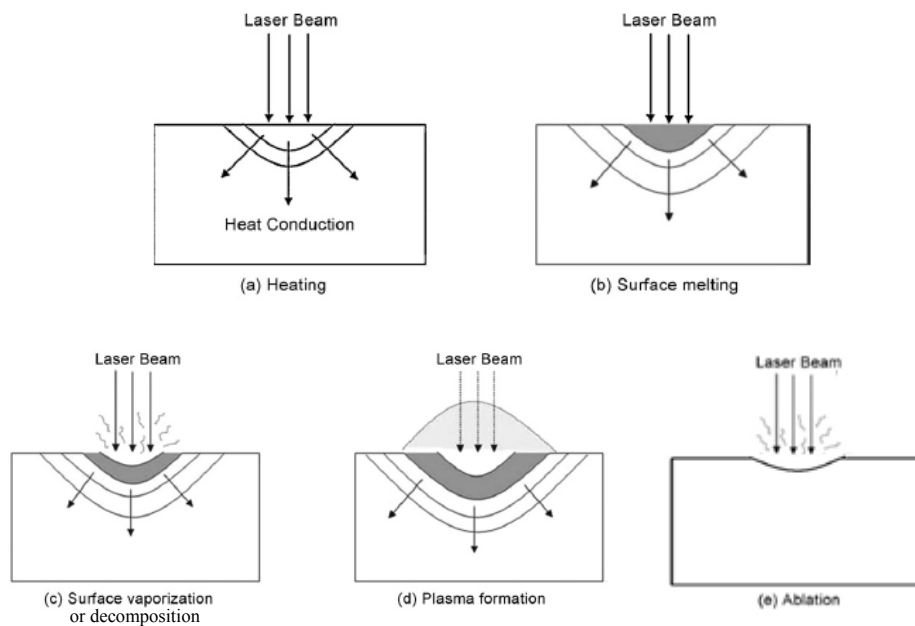


Figure 2.25 Various physical phenomena during laser-ceramic interaction with laser power density increasing [84]

The laser-ceramic interaction is in relation to the absorptance of ceramics with respect to a given laser wavelength. Having an insight into the absorptance would be more efficient to control the laser process parameters. Modest et al studied the temperature-dependent absorptance of 99% alumina for 1.06 μm wavelength Nd:

YAG lasers [85]. Alumina melts at around 2315 K under equilibrium conditions [86]. The results of Modest's work (as Figure 2.26(a)) indicated that alumina is more likely scattering until about 1800 K, and its absorptance starts to increase sharply thereafter, reaching 0.95 at 2800 K. Figure 2.26(b) shows the ceramic superheats to about 2600 K before starting to melt. Due to the superheating, melting takes place over a range of temperatures and internal melting is possibly continuing after the laser was turned off at a surface temperature of about 3350 K [85]. The results verified that fusion is a primary material removal mechanism in laser cutting of alumina. For 10.6 μm wavelength CO₂ lasers, alumina generally has a relatively high absorptance (> 90%) at whole temperature range [87].

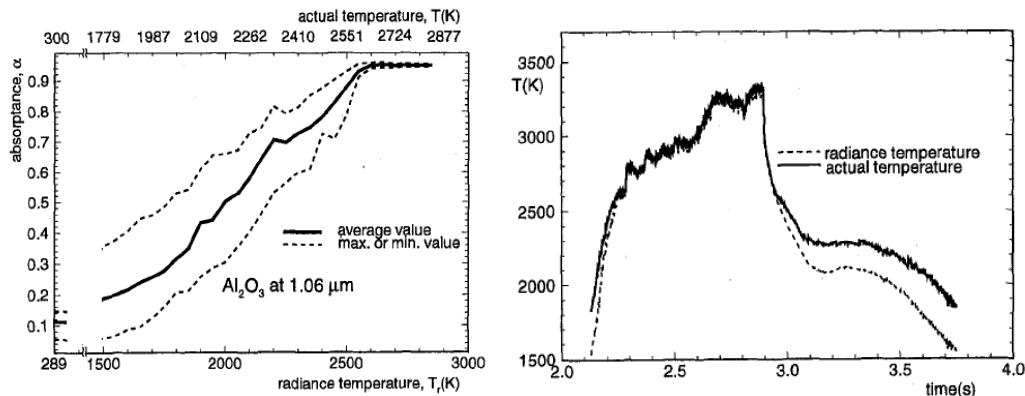


Figure 2.26 (a) Absorptance versus temperature of alumina for 1.06 μm wavelength laser and (b) typical temperature signal of alumina during heating process [85]

Dahoter et al studied the variation of surface absorptivity with temperature for engineering ceramics. The in-situ temperatures reached during pulsed Nd: YAG laser low-aspect-ratio-cavity (< 1) machining of the ceramics under various pulse numbers were measured [88]. The measured absorptivities are shown in Figure 2.27. For the temperature ranging from 1040 K to 1100 K, it can be seen that the maximum absorptivity of Al₂O₃ with respect to 1.06 μm wavelength was about 25%. When the cut kerf was formed, the absorptivity is increased due to the multi-reflection [89, 90] and it is expected to instantaneously reach the value of 100% in some processes such as high aspect ratio laser machining and laser cutting of thick-section workpiece [91, 92].

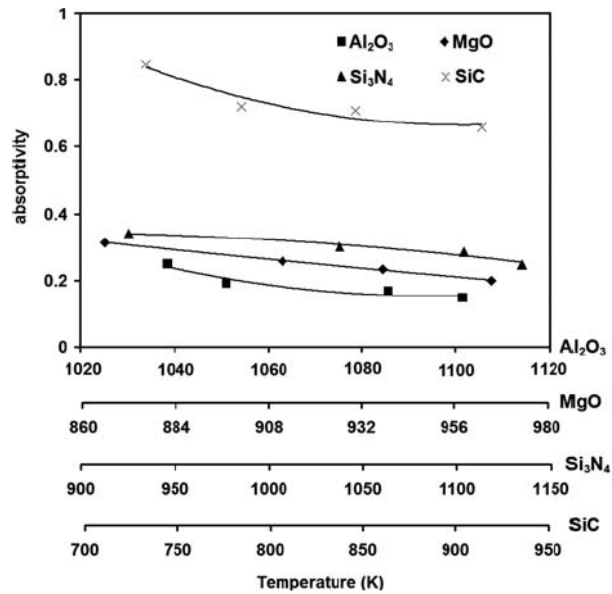


Figure 2.27 Variation of surface absorptivity with temperature for engineering ceramics at 1.06 μm wavelength [88]

When the surface temperature reaches the melting point, material removal occurs by melt ejection. When the surface temperature further increases and reaches the vaporisation point, material removal takes place by means of evaporation and melt ejection. During laser fusion cutting of ceramics, material removal should be melt ejection and evaporation together. Considering multi-physical processes occurring simultaneously, theoretical analyses of laser cutting processes are very difficult. Although the theoretical models are not practical in selecting the proper working conditions in quantitative manner [93], information on the behaviours of some important physical parameters from the theoretical analysis, such as the temperature at the cutting front, the ratio of molten and evaporated material, energy losses by heat conduction, radiation or convection, etc., is still useful for improvement of the knowledge about the physical processes involved in laser fusion cutting since these parameters are difficult to determine by experimental measurement.

Modest et al developed a theoretical model for laser cutting of Si₃N₄ and SiC ceramics [94, 95]. Kim et al also developed a FE model on evaporative cutting with a moving high energy pulsed laser [96]. However, these models solve the problem on vaporisation cutting where the effect of assist gas on material removal was

ignored. In laser fusion cutting of alumina, three major mechanisms of molten material removal simultaneously exist: melt shearing by the assist gas, melt evaporation, and melt ejection by the recoil pressure induced by vaporisation [93]. Quintero et al presented a theoretical model for pulsed laser fusion cutting of ceramics [93]. The three material removal mechanisms were all considered according to the solution of the balances of mass, momentum and energy at the cut front (as Figure 2.28). The simulated results for a pulse length of 10 ms with pulse energy of 15 J and a pulse length of 0.5 ms with pulse energy of 0.75 J are listed in Figures 2.29 and 2.30. It was found that the molten material ejected mainly by the assist gas at low pulse energy of 0.75 J, whereas the predominant removal mechanism contributes to the melt ejection by recoil pressure at high pulse energy of 15 J. The corresponding experimental results (Figure 2.31) validated the simulated results. Compared with the Figures 2.29(d) and 2.30(d), it can also be found that the power consumed to evaporate the melt with regard to the corresponding mass flow is proportionally much higher than that in the melting process.

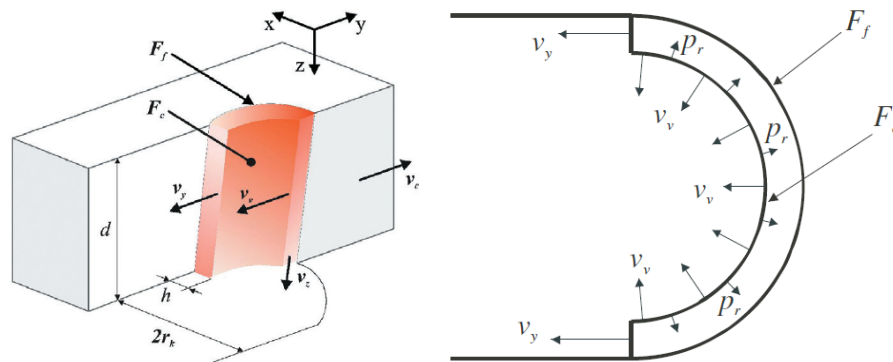


Figure 2.28 Schematic of the geometry of the cutting model and cross section of the cut front, where F_f is the fusion front, F_c is the cutting front, v_v is the evaporation velocity, p_r is the recoil pressure, v_y is the velocity of the flow promoted by the recoil pressure, v_z is velocity of the mass flow in the direction of the cut front axis governed by the assist gas, v_c is cutting speed, h is thickness of molten layer, $2r_k$ is kerf width and d is workpiece thickness[93]

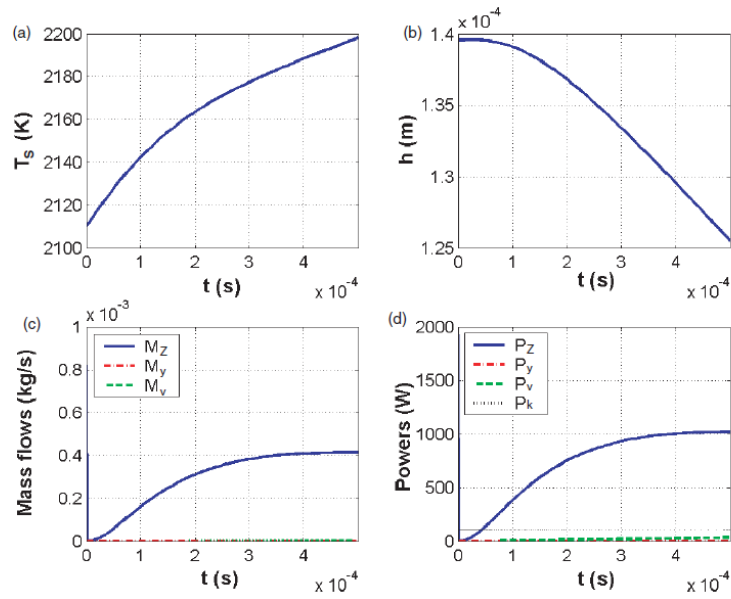


Figure 2.29 Simulated results for a pulse length of 0.5 ms with pulse energy of 0.75 J, representing the temporal evolution of several process parameters in a pulse length:

- (a) temperature of the molten layer; (b) thickness of the molten layer; (c) instantaneous value of the ejected mass flows, M_Z being the flow ejected by the assist gas, M_V being the evaporated mass flow and M_Y being the melt ejected by the recoil pressure; (d) energy flows carried away by the corresponding mass flows and heat conduction losses (P_K) [93]

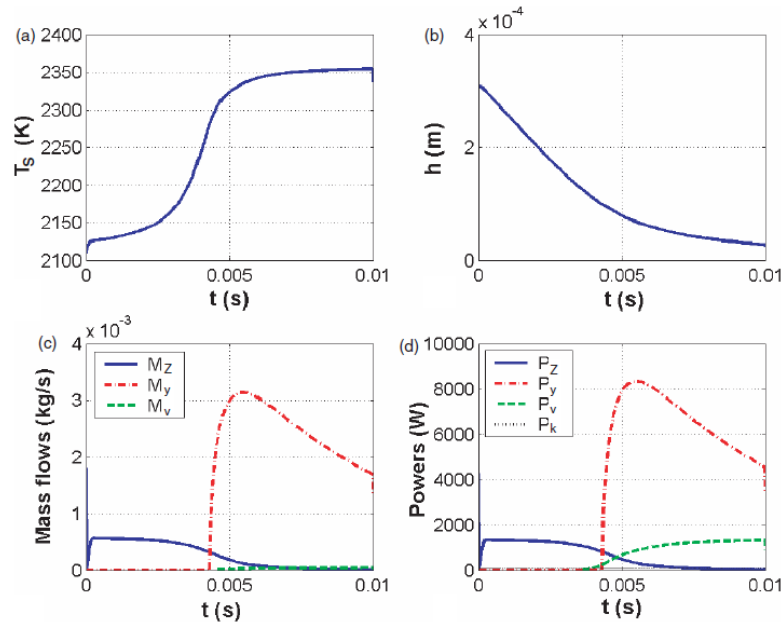


Figure 2.30 Simulated results for a pulse length of 10 ms with pulse energy of 15 J, representing the temporal evolution of several process parameters in a pulse length:

(a) temperature of the molten layer; (b) thickness of the molten layer; (c) instantaneous value of the ejected mass flows, M_Z being the flow ejected by the assist gas, M_V being the evaporated mass flow and M_Y being the melt ejected by the recoil pressure; (d) energy flows carried away by the corresponding mass flows and heat conduction losses (P_K) [93]

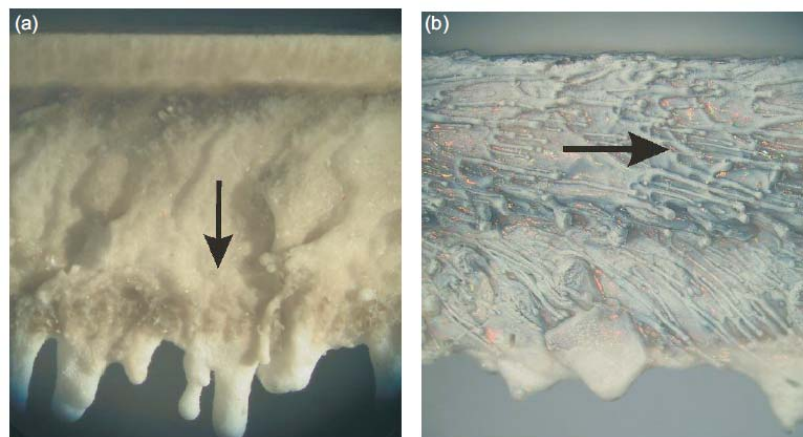


Figure 2.31 Optical micrographs of the cut surfaces by the laser operating at different pulse lengths and energies: (a) 0.5 ms – 0.75 J; (b) 10 ms – 15 J [93]

When the laser intensity passes a certain threshold limit, the vapour gets ionized and forms a plasma having electron temperature as high as 50,000 °C and pressure up to 500 Mpa [97]. The plasma forms a shield over the machined area and reduces the energy arriving onto the workpiece. Ho et al proposed a one-dimensional thermal model considering the absorption of plasma to represent the short pulsed laser drilling process. They indicated that it was essential to take the plasma absorption into account for short pulsed laser (< 10 ns) drilling of SiC and Al₂O₃ (as Figure 2.32) [98]. Beyer et al studied the interaction between CO₂ laser pulses with microsecond duration and Al₂O₃ ceramic substrates. They found that the plasma oscillated with a characteristic period of 5-10 μs between states with low and high absorption. Therefore, a short pulse (< 5us) with low energy and high repetition frequency (>10 kHz) should be employed to achieve a high machining rate without significant energy loss in plasma [99].

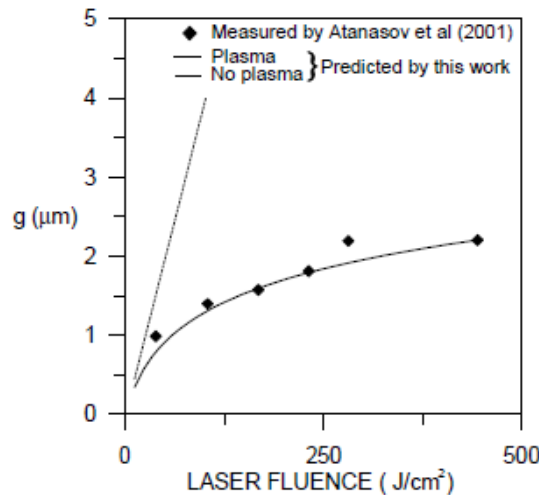


Figure 2-32 Variation of machining depth per pulse with laser fluence in short pulsed laser drilling of alumina [98]

In addition to melt and evaporation, some of species such as AlO(g), Al(l), Al(g), Al₂O(g) and AlO₂(g) can also be formed above 3250 K due to the dissociation of Al₂O₃ by reactions in Eqs. (2-2)-(2-4). At the temperature above 5000 K, dissociation is complete and aluminium vapour and oxygen are formed according to Eq. (2-5) [56]. Moreover under ambient nitrogen, other reactions may take place as

Eq. (2-6). The formation of AlON species increases the hardness and ductility of the cut surface [100]. The produced species directly influence the process quality and performance of the end product. Depending on different applications, these reactions may be expected or not. In order to maintain the alumina composition on the cut surface, it is necessary to control the temperature of the cut surface below 3250 K by setting proper process parameters and employ proper assist gas for cutting.



Where g means the gas phase and l is the liquid phase.

Although ceramics generally have low thermal conductivities, HAZ cannot be avoided during laser machining even for ZrO₂ ceramics, of which the thermal conductivity is about 30% of alumina. Figure 2.33 shows a typical HAZ around a pulsed Nd: YAG laser drilled hole in ZrO₂. The ceramic micro-structure in HAZ is varied from the base material. Generally, the ceramic in HAZ is redensified due to the high temperature history. It is most likely a re-sintering process (as Figure 2.34). Therefore, HAZ makes ceramics harder and trend to fracture during laser cutting.

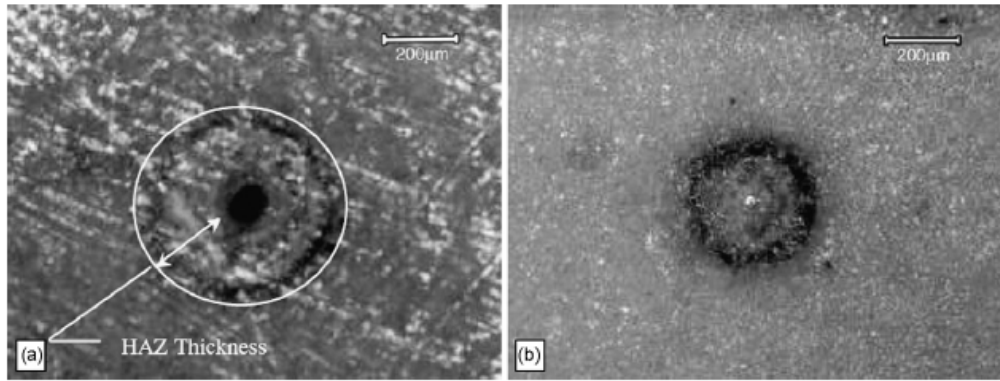


Figure 2.33 Typical photographs of HAZ around a laser drilled hole in ZrO_2 ceramic [101]

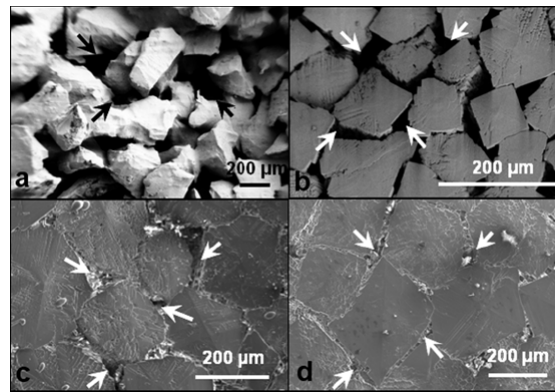


Figure 2.34 Surface microstructures of the alumina substrate (a) before laser treatment; and after laser treatment with fluence of (b) 420 J/cm^2 , (c) 535 J/cm^2 , and (d) 649 J/cm^2 [102]

From the above mentioned studies, it can be found that laser conventional cutting of ceramics is a combined effect of melting, evaporation, dissociation, reaction and re-sintering. Therefore, the control of process parameters is the key point to achieve high quality and crack-free laser conventional cutting of ceramic materials.

2.4.2 Laser multi-pass cutting/machining techniques

Multi-pass cutting employs a laser beam successively passing forward and backward along the same path to finish a through-cut in workpiece. Every pass only removes material to a prescribed depth that is always smaller than the thickness of workpiece (as Figure 2.35).

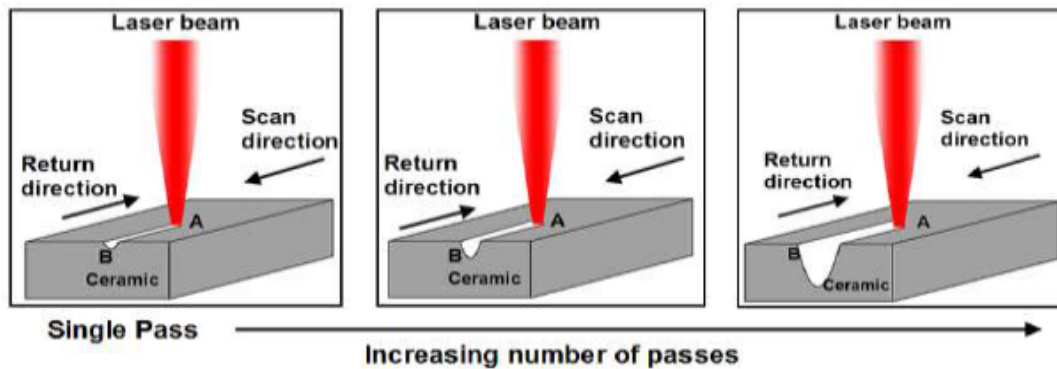


Figure 2.35 Schematic of multi-pass cutting/machining [103]

Black et al indicated that the temperature gradient in multi-pass cutting was greatly reduced due to the low laser power input per pass, the thermal damage was hence minimised [46]. Although it is suitable to cut thick-section ceramics without any fracture, the low process speed is the major drawback of this technique. In order to solve this problem, an improved technique was developed by Black et al. In the technique, the multi-pass cutting was begun with a low laser power (100 W) to produce a well defined blind kerf. This process was repeated until the kerf was about 2 mm and then the laser power was switched to 500 W and finished the full-through cutting for 9.2-mm-thick ceramic tiles. This technique improved the process efficiency and significantly reduced the thermal overload during CW laser cutting [53].

In addition, similar to the laser conventional cutting, pulsed lasers are recommended since the lengths of thermal-shock-induced cracks could be restricted below the grain size, by which crack-free cutting/machining of ceramics would be achieved [104]. Lei et al used a Q-Switched CO₂ pulsed laser with a high peak power (12.5 kW), short pulse duration (1 μ s), high pulse repetition frequency (20 kHz) and moderate

average power (250 W) to study multi-pass cutting of hot pressed Si_3N_4 ceramics with a cutting speed ranging from 8 mm/s to 220 mm/s. For each cutting speed, the cutting process was repeated several times until line-energy (laser energy input per cutting length) reached the same value of 240 J/mm [105]. The relationship of crack length and crack number per cut length with cutting speed is shown in Figure 2.36. It was found that the short pulse duration and low pulse duration ratio should be employed in order to reduce the thermal overload. A high cutting speed can further reduce the thermal effect to trap the length of micro-cracks within the grain size, by which the crack-free cutting can be achieved.

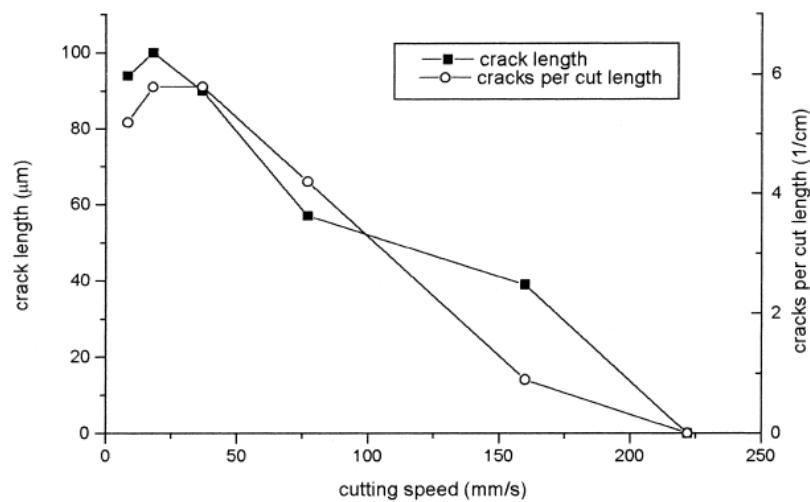


Figure 2.36 The relationship of crack length and crack number per cut length with cutting speed [105]

Quintero et al studied the quality of different laser cutting techniques (single- and multi-pass) for silicon infiltrated silicon carbide (Si-SiC) with 6-mm thickness. A quantitative method was employed to assess the HAZ and effectively compare the cut results using different parameters and techniques. It was found that the utilisation of compressed air as the assist gas and the multi-pass cutting technique is the most important factor to obtain the best cut quality in crack-free cutting of Si-SiC [106]. The optical images (as Figure 2.37) show a typical view of the cutting edge via single-pass and multi-pass cutting. Figure 2.38(a) shows the capabilities of the multi-pass cutting technique for 2D cutting of Si-SiC tubes. The cut result was crack-free

and to strict dimensions. The ceramic tube can be inserted tightly into the other one (as Figure 2.38(b)). Furthermore, mechanical testing at high temperatures proved that multi-pass cutting is an acceptable profile cutting technique for some special applications, such as kiln furniture production [106].

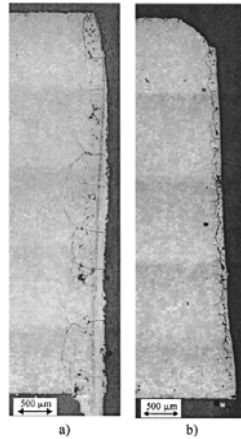


Figure 2.37 Optical images showing a typical cross-section view of the cut kerf via (a) single-pass cutting and (b) multi-pass cutting [106]

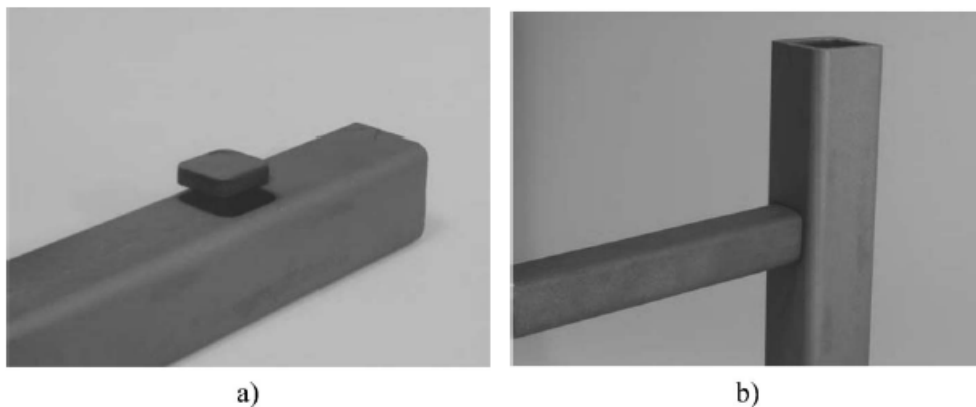


Figure 2.38 Optical images of Si-SiC ceramic 2D cuts by the multi-pass cutting technique [106]

According to the above mentioned studies, it can be found that multi-pass cutting of ceramics such as SiC and Si_3N_4 were most investigated due to their dissociation/decomposition properties (i.e. without melt points). However, during laser cutting/machining of alumina or zirconia ceramics, melting ejection is the

primary material removal mechanisms [93]. Therefore, melting deposition and resolidification raise a major challenge in laser multi-pass cutting/machining.

Compared with laser cutting, the 3D structures involving controllable z -depth in workpiece can be obtained by multi-pass laser machining techniques. Laser machining is generally performed by a single laser beam (Figure 2.39). However, two or more laser beams may also be used for 3D machining (Figure 2.40). For the ceramics having a melting point (such as alumina and zirconia), high peak power pulsed lasers are usually employed in order to achieve ablation without melting. Furthermore, continuous wave (CW) lasers were rarely directly used for machining ceramics at room temperatures in air atmosphere without forced cooling, since the serious heat accumulation in machining may cause catastrophic breakdown of the workpiece.

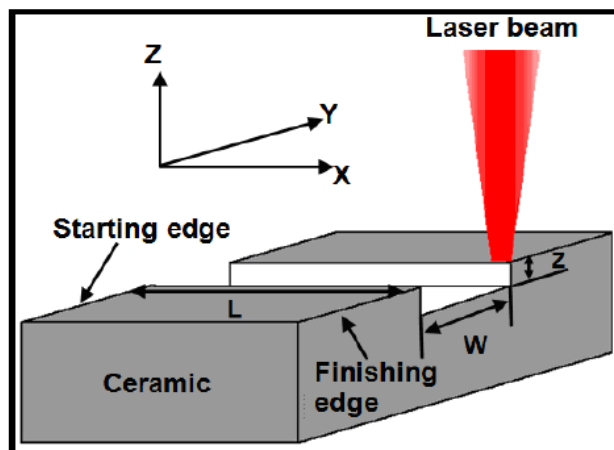


Figure 2.39 Schematic of 3D laser machining by a single laser beam [107]

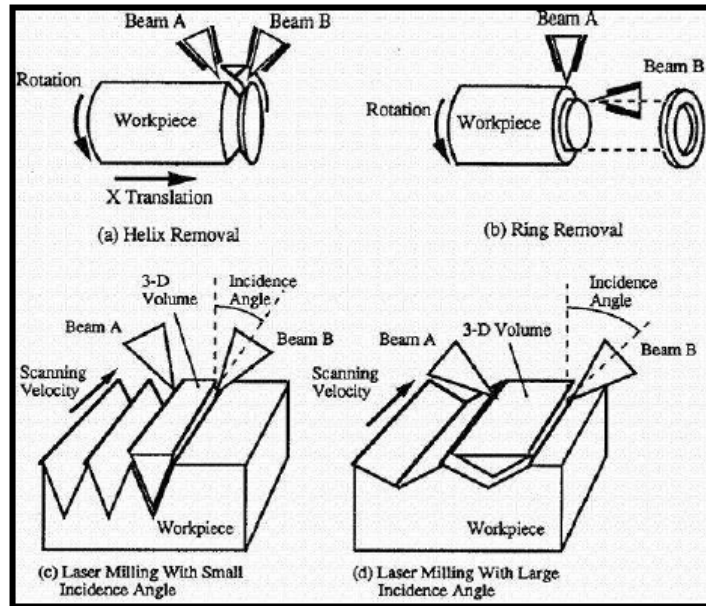


Figure 2.40 Schematic of 3D laser machining by a dual laser beam [42]

Zeng et al reported laser carving of 3D structures in alumina substrates using a short pulsed CO₂ laser. A 3D CAD model is first sliced in a particular direction to obtain profile information of the slice. Then a focused laser beam is used for scanning and engraving the ceramic surface based on profile per slice, producing 2D layer patterns. Finally, the z-axis is lowered to a designated height to locate the carving surface at the focal plane. This process is cycled until the whole model is finished. Figure 2.41 shows a 15 mm×14.27 mm×2.5 mm cavity obtained by this machining technique. The machining time was 50 minutes. They also presented a machining model as Figure 2.42 and found that the process quality mainly depended on the parameters of pulse repetition rate, scanning speed, pulse energy, interval of scanning lines and slicing thickness [108].



Figure 2.41 3D laser machining of a star shape in alumina ceramic [108]

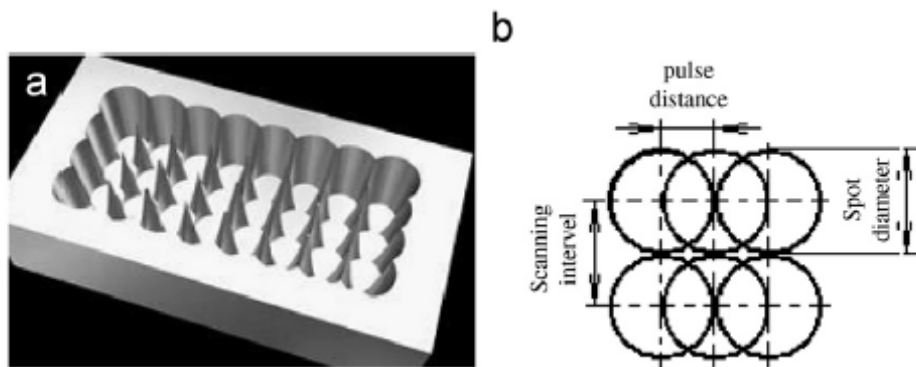


Figure 2.42 Laser machining model. (a) Overlapping drilled holes and (b) spot diameter, pulse distance and scanning interval during machining [108]

Hand et al examined the parameters of nanosecond pulsed (60 ns) Nd: YAG laser crack-free machining of yttria-stabilized tetragonal zirconia polycrystal (Y-TZP) ceramics. They found that the combination of processing variables (at an average power of 11.3 W, a repetition rate of 30 kHz and a scan speed of 50 mm/s) provided the optimum material removal rate up to $\sim 2 \text{ mm}^3/\text{min}$. Additionally, it was found that the pulse overlap has a significant influence on the material removal rate and hence, the combination of scan speed and repetition rate should be carefully considered. Their experimental results showed that too much pulse overlap or insufficient pulse overlap could create a lower quality machined surface (as Figure 2.43). Figure 2.44 shows the crack-free machined cavity using the optimised parameters. They also demonstrated the power of the nano-second pulsed Nd: YAG laser in high-quality machining of complex 3D structures (as Figure 2.45) [109].

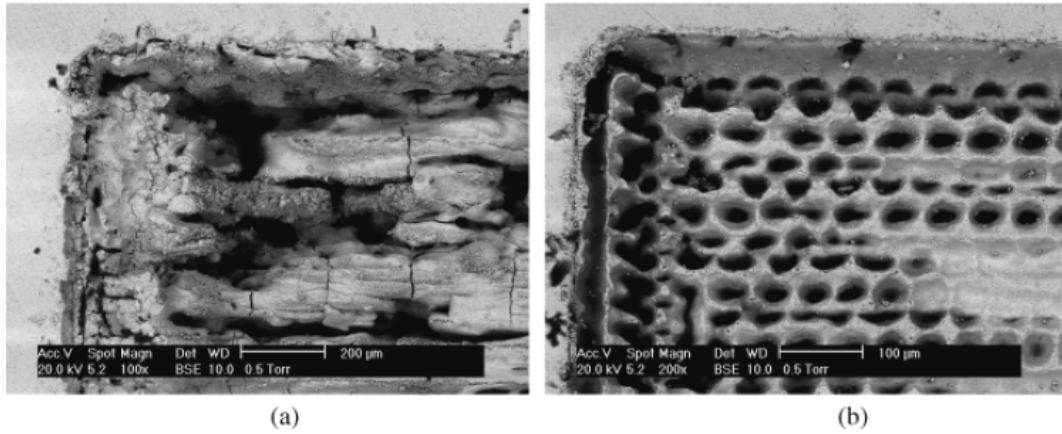


Figure 2.43 Top view of non-optimised machining: (a) too much pulse overlap and (b) insufficient pulse overlap [109]

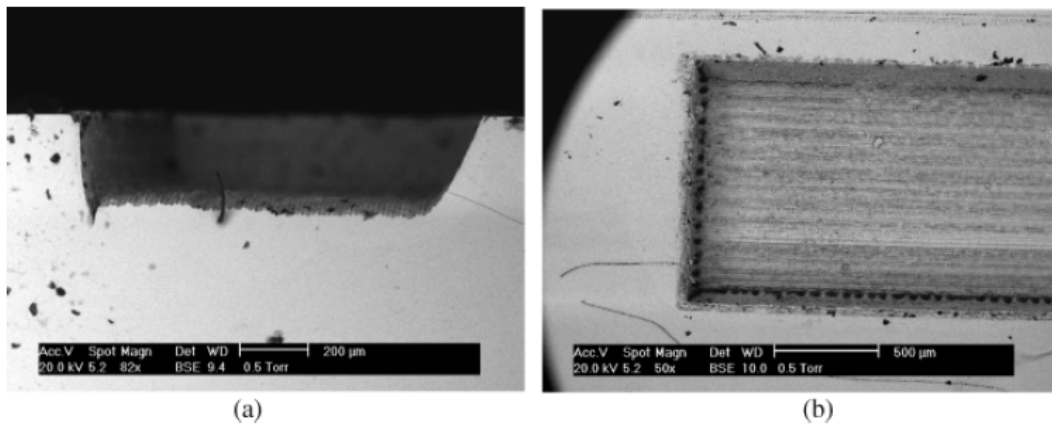


Figure 2.44 (a) Cross-section and (b) top view of a trough machined by repeated laser scanning with optimised process parameters [109]

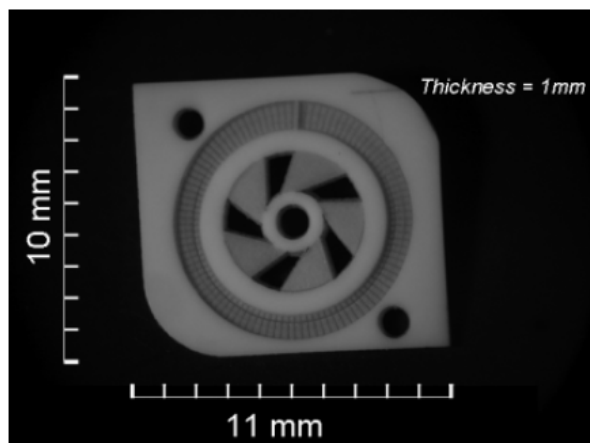


Figure 2.45 A demonstration component made from Y-TZP ceramics by nano-second pulsed Nd: YAG laser machining [109]

However, the material removal rate using the nano-second pulsed laser is relatively low ($\sim 2 \text{ mm}^3/\text{min}$). In order to improve the removal rate, Hand et al presented a method of nanosecond-laser post-processing of millisecond-laser machined Y-TZP surfaces. The millisecond laser (0.3-5 ms) process was used first to provide a ‘rough machining’ process with a high-speed material removal due to the high average power available, in which the material removal rate was up to $2.5 \text{ mm}^3/\text{s}$ without significant cracking. The quality of the initially finished surface was limited by recast layer formation, HAZ, and in particular the surface micro-cracks (as Figure 2.46(a)-left). Then, a nanosecond laser (50-100 ns) system was used to finish the ‘fine machining’ process in a relatively short time [110]. The nanosecond laser post-processing of millisecond laser machined surface used two different sets of parameters to combine an optimal material removal rate at 15 kHz for the removal of the recast layers with a lower thermal impact machining (as Figure 2.46(a)-right) and at 60 kHz to further reduce the cracking extent (as Figure 2.46(b)) [111]. The high-quality laser machining of Y-TZP ceramics is therefore achieved.

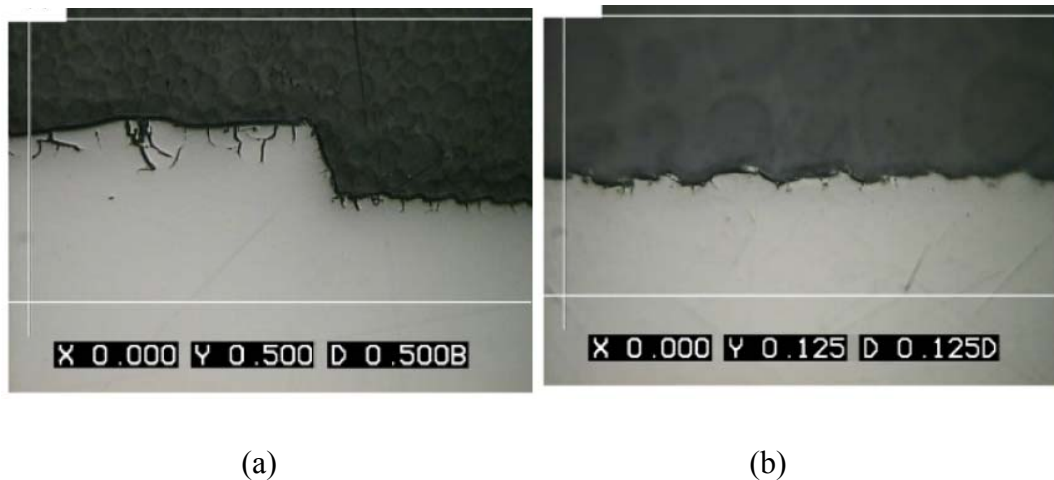


Figure 2.46 Cross-section view of machined Y-TZP. (a) Boundary between the millisecond-machined surface on the left side and the nanosecond-machined (15 kHz) surface on the right side. (b) Further machined (60 kHz) surface [111]

For a higher process quality, picosecond and femtosecond lasers were applied in previous studies and have demonstrated their unique advantages, such as elimination of thermal damage, low roughness of machined surfaces, etc. (as Figure 2.47).

However, the low material removal rates (e.g. $2.2 \text{ mm}^3/\text{min}$ and $0.054 \text{ mm}^3/\text{min}$, respectively) due to the low average laser power output and the expensive systems make them only suitable for micro-machining [9, 112].

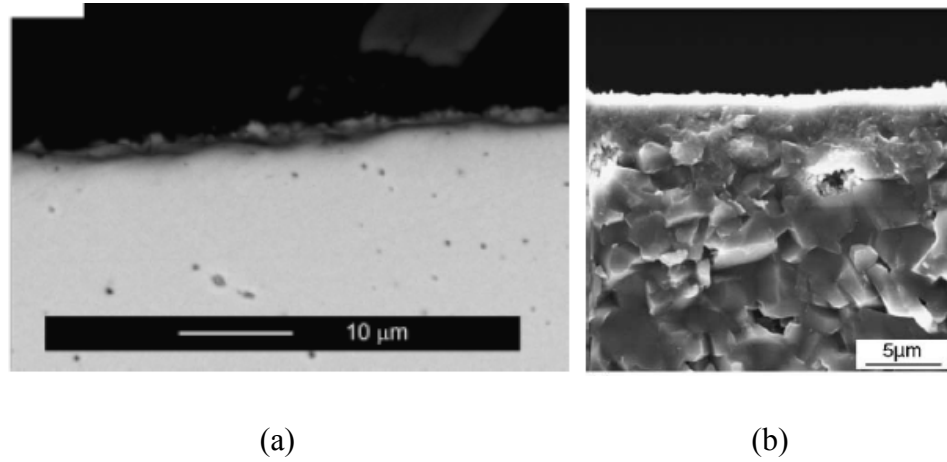


Figure 2.47 Cross-section view of (a) picosecond-laser-machined Y-TZP surface and (b) femtosecond-laser-machined alumina surface [9, 112]

Theoretical analyses of multi-pass cutting and machining are both based on the laser machining models, due to the similar fundamentals. Modest et al developed a 3D conduction model to predict the temperature distribution in the solid and the shape of a groove formed by partial evaporation of a semi-infinite body using a moving CW Gaussian laser beam. The model can be applied where the material is removed by repeated scanning with a focused beam on the workpiece surface. The effects of laser power, scanning speed and beam profile were investigated by this model. An estimate of the 3D conduction losses revealed that heat losses by conduction were between 25-45 % of the absorbed laser power and the losses were lower at the highest power of 1500 W. If variable properties are considered, the material removal rate drops another 5-15 %. For shallow grooves, the theoretical prediction was in agreement with experimental measurement. The predicted groove shapes for hot-pressed Si_3N_4 was within the bounds of experimental error. For deep grooves, the model could not predict the grooved depth accurately since the multi-reflection was not considered in this model. The comparison of theoretical results with experimental results is shown in Figure 2.48. Figure 2.49 shows the theoretical

computation on temperature profiles at 1500 W laser power with the scanning speed of 50 mm/s and 200 mm/s, respectively [95].

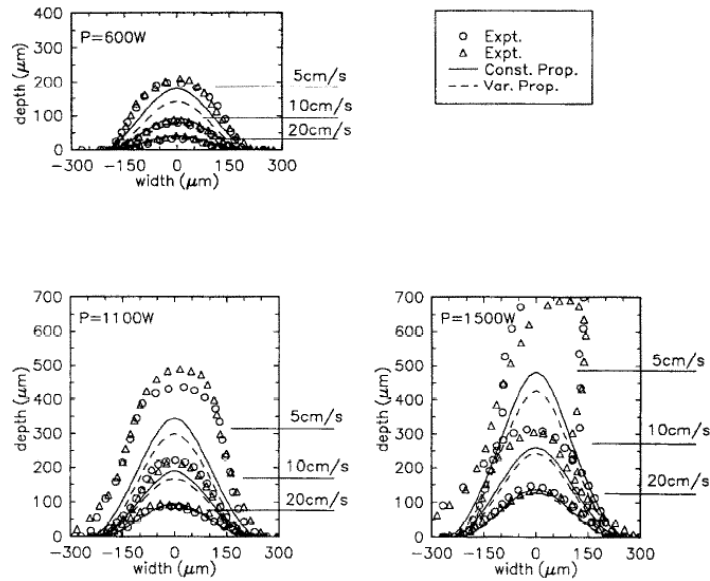


Figure 2.48 Variation of groove cross-section with scanning speed and laser power [95]

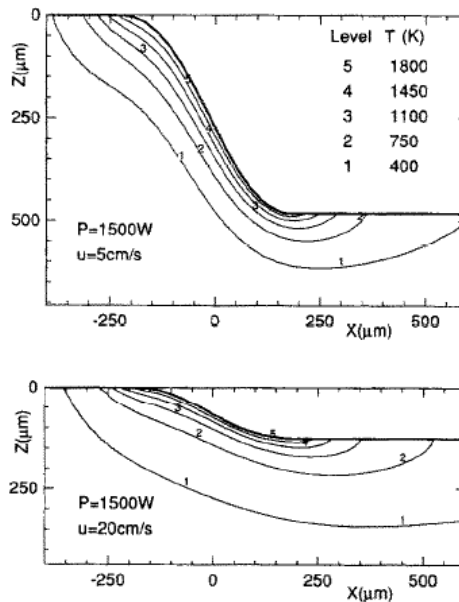


Figure 2.49 Temperature profiles at the laser power of 1500 W with the scanning speed of 50 mm/s and 200 mm/s [95]

In order to solve the multi-reflection effect, Modest et al further developed the theoretical model considering the multi-reflection effect including purely specular and purely diffuse reflections. They found that the beam reflection plays an important role in forming a groove and resulting in an increased effective absorptivity. Due to the effect of beam channelling from the upstream wall and the side walls, the specularly-reflected irradiation produces a strong peak for downstream extending the evaporation zone, while diffusely reflected irradiation shows a smooth variation at a mild peak (as Figure 2.50). Multiple specular reflections also produce flatter profiles near the centreline and steeper slopes in the groove cross-sections than no reflection, and similar behaviour is also observed for diffuse reflections (Figure 2.50). Moreover, the computation showed that the effective absorptivity is increased by 15-30% in the 3D specular reflection model, while the 3D diffuse reflections produce an increase of up to 50-70% for the same set of parameters [113]. From Figure 2.50, it can be found that the prediction using the beam guiding model is consistent with the experimental observations for deep engraving of Si_3N_4 . Especially, the diffuse reflection model gives better agreement with the experimental data. Therefore, it can be concluded that the multi-reflection effect is a vital process in laser deep machining.

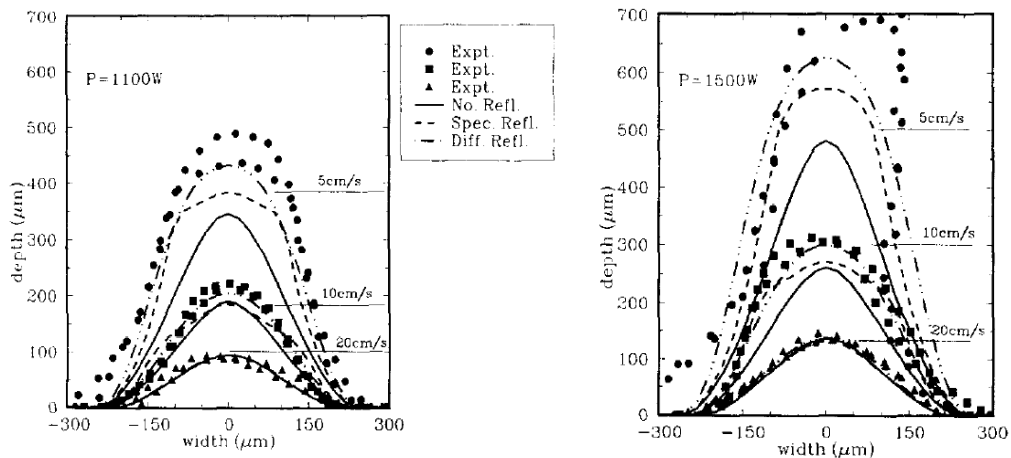


Figure 2.50 Variation of groove cross-section with laser power and scanning speed

[113]

Lei et al studied laser multi-pass cutting of Si_3N_4 ceramics via a Q-switched pulse CO_2 laser [114]. Considering the influence of the cut front shape on the absorption of the laser beam, they developed a simplified 2D mathematical model according to the pulsed laser vaporisation process and the conservation of energy as Figure 2.51(a). Their study indicated that cutting Si_3N_4 by a CW or long pulse laser would induce cracking due to the great temperature gradient in the cut-off station. The Q-switched pulsed laser with short pulse duration and high peak power can dominate the vaporisation and reduce the temperature gradient. The predicted cut front shape in pulsed CO_2 laser multi-pass cutting is shown in Figure 2.51(b).

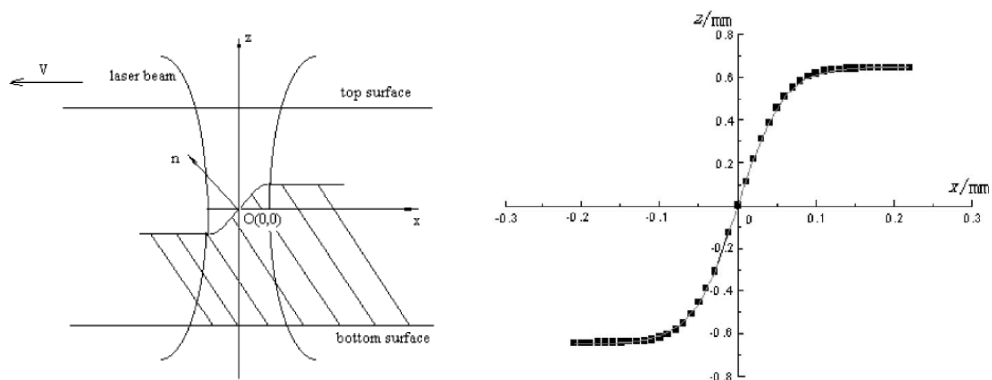


Figure 2.51 (a) Simplified 2D cutting model and (b) the predicted shape of the cut front in pulsed CO_2 laser multi-pass cutting [114]

Dahotre et al did a series of work on Nd: YAG pulsed laser (20 Hz pulse repetition rate with 4 J pulse energy in 0.5 ms pulse duration) machining of alumina ceramics and modelling of laser machining [107, 115-117]. For laser drilling, a hydrodynamic machining model was developed. The model incorporated the effect of multi-reflection on the amount of laser energy absorbed, the thermal effects for melting the materials, vapour pressure effect on expelling out the molten material, the material losses due to evaporation and the inverse effect of surface tension on the expelled depth. The model also incorporated the transient laser beam defocusing effect according to the change in machined depth. They indicated that the multi-reflection within the high aspect ratio machined cavities was responsible for increasing the amount of energy absorbed ($\sim 100\%$). The thermal effects were responsible for melting and evaporating the material whereas the recoil pressure and surface tension

were responsible to expelling of the molten material. The predicted machined depth by the developed computational model was in agreement with the experimental results as Figure 2.52. Their work validated the importance of melt expulsion and evaporation processes in laser machining of alumina ceramics [115].

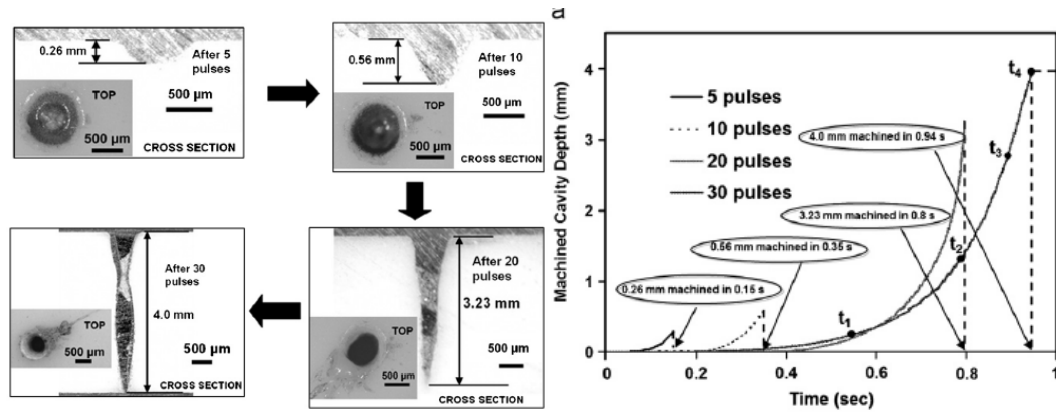


Figure 2.52 (a) Cross-section and top view of the machined cavities in alumina by various numbers of pulses and (b) temporal evolution of machined depth by the developed model [115]

For 2D laser machining of alumina, Dahotre et al presented a thermal model to obtain the trend in absorptivity below the phase transition temperature within the low aspect ratio machined-groove. Figure 2.53 shows the predicted depths via the thermal model at various machining speeds, which are in agreement with the experimental results [116]. Having an insight into the absorptivity transitions would be useful to more proficiently control the laser machining process. Therefore, they further enhanced the thermal model, incorporating several additional effects, such as substrate heating due to multiple tracks and defocusing of laser beam with groove depth increasing, in order to accurately predict the depth and width of the machined cavity under a given set of process conditions. Figure 2.54 shows the variation of predicted depths and widths with number of laser passes, which are in decent match with the experimental results [117].

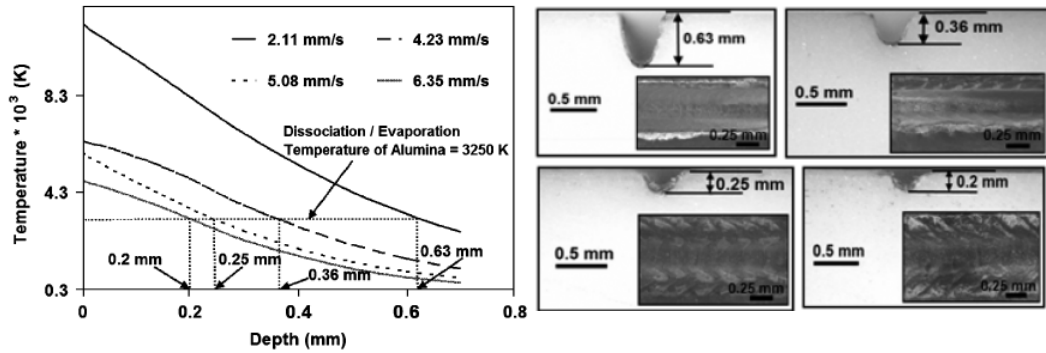


Figure 2.53 (a) Variation of temperature with depth and (b) cross-sections and top view of the machined grooves in alumina at various cutting speeds [116]

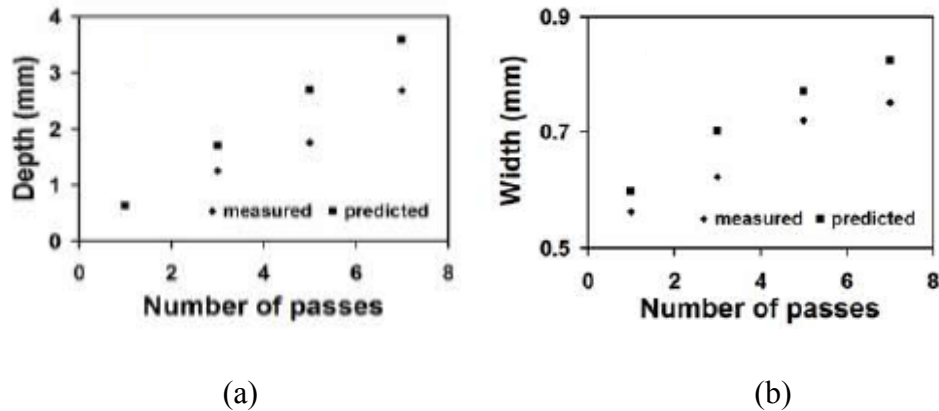


Figure 2.54 Comparison of predicted and measured (a) depths and (b) widths of machined cavities in alumina at various numbers of passes [117]

The 3D laser machining of engineering ceramics such as Al_2O_3 , Si_3N_4 , SiC and MgO was also demonstrated (as Figure 2.55) by Dahotre et al using the pulsed Nd: YAG laser [107]. The above mentioned 2D machining model was further developed considering pulse overlapping effect in order to predict the material removal rate in 3D laser machining (as Figure 2.56). The predicted material removal rates were compared with measured values, which showed reasonable match. They also found that the machining rate increased with an increase in heating rate within the process region. Dahotre's studies demonstrated the feasibility of laser machining in engineering ceramics with melt points (such as alumina) and provided a starting

point to solve some of challenging problems, such as cracks, thermal damage and molten material redeposition.

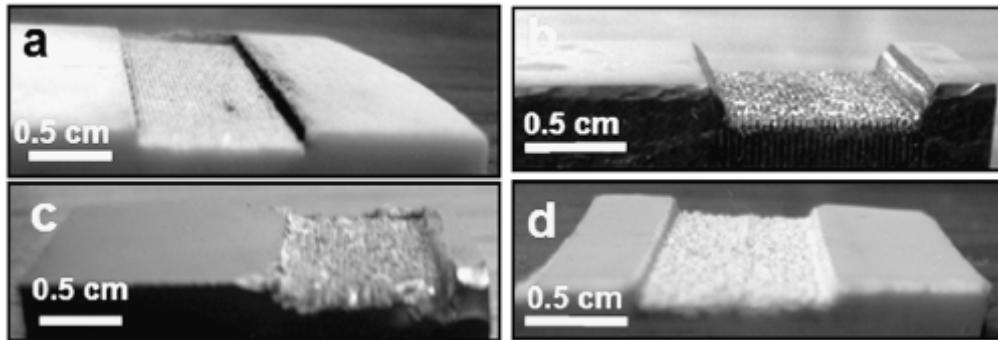


Figure 2.55 The machined 3D cavities in (a) Al_2O_3 , (b) Si_3N_4 , (c) SiC and (d) MgO ceramics [107]

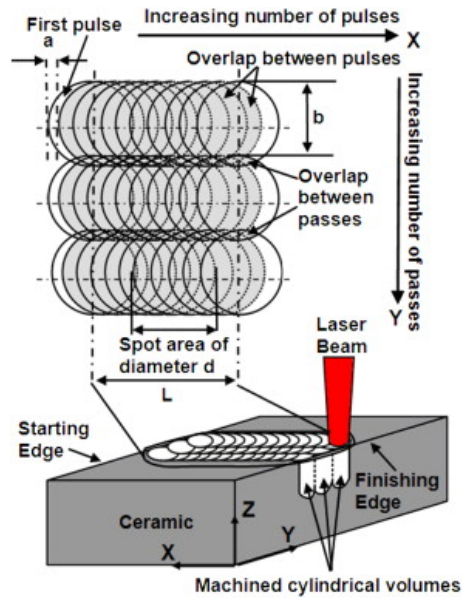


Figure 2.56 Schematic of the pulse overlap in x and y directions and the cylindrical volume machined per spot area in pulsed laser machining [107]

2.4.3 Laser controlled fracture cutting/machining techniques

In order to separate brittle materials (e.g. ceramic or glass), a controlled fracture technique was developed where the incident laser energy generates localised mechanical stresses that separate the material by controllable crack extension [118]. This technique requires much lower laser power output than other laser cutting/machining techniques as mentioned above for the same workpiece thickness. Laser controlled fracture cutting was first proposed by Lumley in 1969 [119] and now has become the major technique to separate flat glass in the LCD industry. Massive investigations into controlled fracture cutting of glass have been performed since 1969. The energy absorption either by the surface (for 10.6 μm wavelength) or by the volume (for 810, 940, and 1064 nm wavelength) is considered as an important boundary condition in modelling [120-126]. The early investigations generally focused on the fracture technique with a coolant jet [127, 128], by which the crack propagation is unstable and the fracture control is very difficult due to the completely tensile stress at the crack tip. The later studies paid more attention to laser controlled fracture without coolant jet (as Figure 2.57) since it can produce a compressive stress dominated region between the crack tip and the laser spot, by which the fracture extension was stabilised [129].

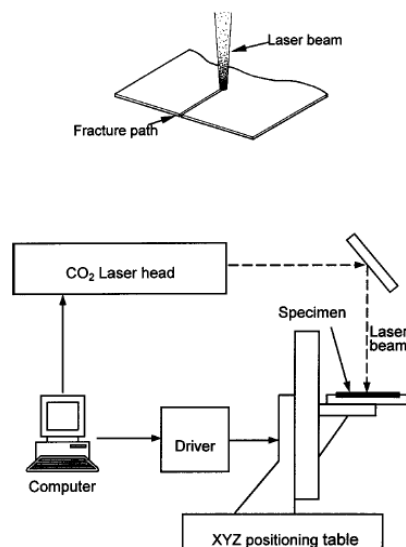


Figure 2.57 Schematic of laser controlled fracture cutting and the system [118]

Tsai et al carried out a series of research on controlled fracture cutting of alumina ceramics. They studied the fracture mechanism in laser controlled fracture cutting by theoretical analyses and experiments. The temperature and stress distributions were obtained by FEA. They found that the cutting process can be divided into three stages: The first is the initiation stage. The initiation of the fracture occurs due to the tensile stress at the edge of the specimen, which will make the crack penetrate through the specimen (as Figure 2.58(a)). The second is the stable growth stage. The stress near the laser spot behaves highly compressive. After the laser passing, the plastic compressive stress will be relaxed and then induce a residual tensile stress near the upper surface of the substrate. The residual tensile stress will make the fracture grow from upper surface to lower surface of the substrate (as Figure 2.58(b) and (d)). The final stage is the unstable fracture. The stress near the crack tip is totally a tensile stress through the thickness direction and hence, the cracks extend unstably and finish the cut through the workpiece thickness (as Figure 2.58(c) and (d)). The distance between the crack tip and laser spot will affect the stress near the crack tip. If the distance is too long, the compressive stress will become small or change to tensile stress, by which the fracture cannot be effectively controlled. Furthermore, the cutting speed is greatly affected by the specimen size. The release of the compressive stress around the crack tip for the wide specimen is less than the narrow specimen. Therefore the crack propagation speed of wide specimen is slower than the narrow specimen (as Figure 2.59). They also indicated that the maximum cutting speed for the same specimen is determined by the laser spot size, where a larger spot size causes a higher cutting speed (as Figure 2.60). Most importantly, Tsai's work demonstrates a significant advantage of laser controlled fracture cutting of ceramics, i.e. the very smooth cut surface ($R_f=26\ \mu\text{m}$) and the fewer defects (as Figure 2-61) [129].

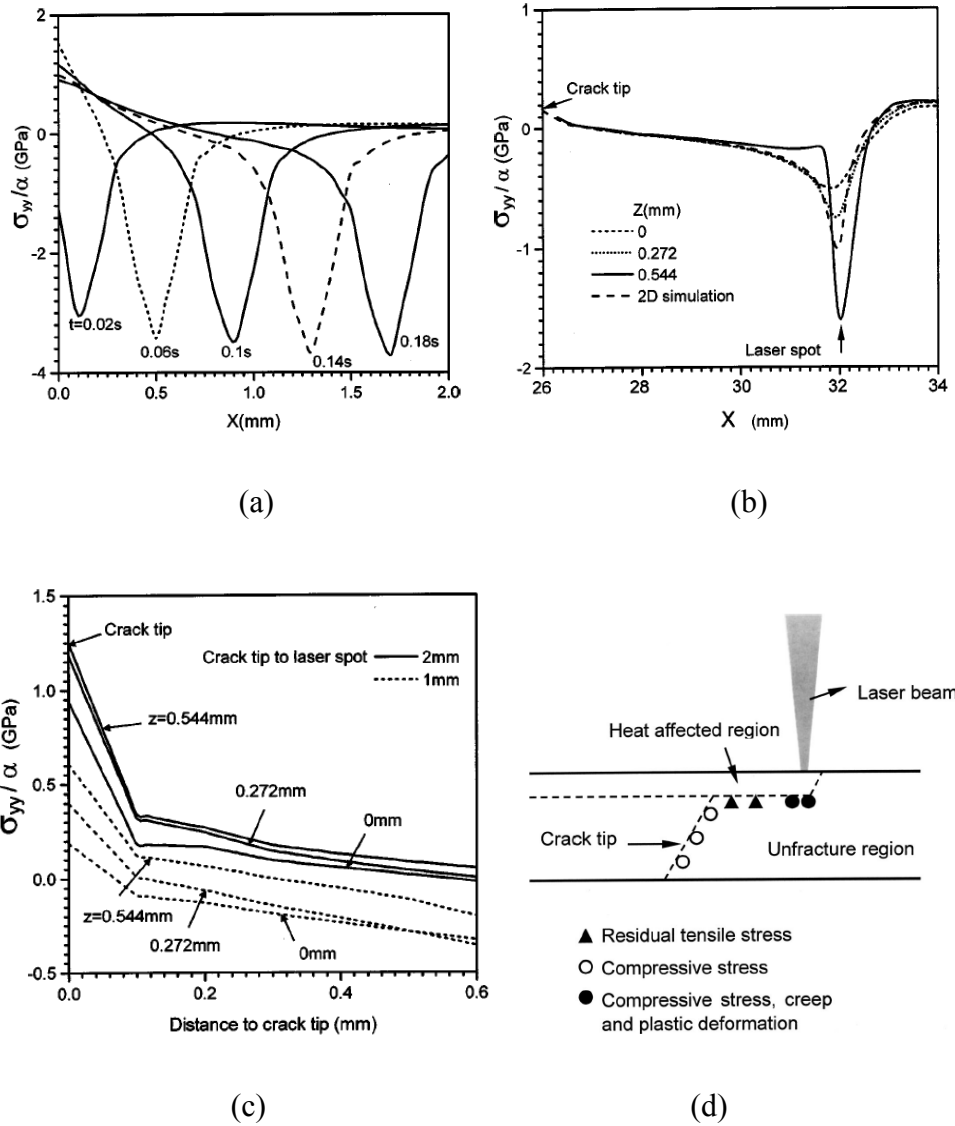


Figure 2.58 Stress distribution of (a) the first stage – fracture initiation, (b) the second stage – stable fracture, in which the crack tip lags behind the laser spot by 6 mm, and (c) the third stage – unstable fracture, in which the distance from the laser spot to specimen edge is 9.6 mm. (d) Stress states between the crack tip and the laser spot [129]

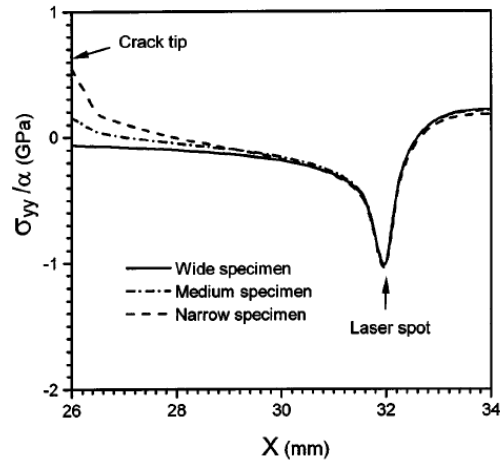


Figure 2.59 Stress distribution in the second stage for dimensional samples [129]

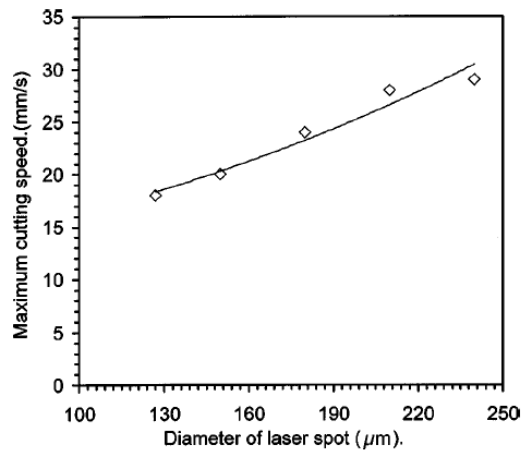


Figure 2.60 Variation of the maximum cutting speed with laser spot size [129]

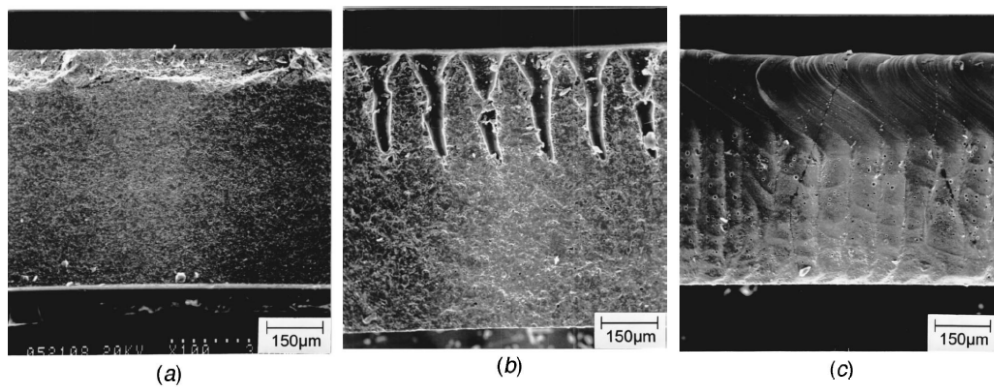


Figure 2.61 The cut surface of the alumina ceramic substrate cut by (a) controlled fracture cutting, (b) laser scribing, and (c) laser fusion cutting [129]

However, the fracture trajectory deviation occurring in curve and right angle cuts is the major challenge in laser controlled fracture profile cutting. For symmetrical straight line cuts, the stress at the crack tip is pure mode I, the crack propagation is hence exactly follow the laser moving path and the fracture trajectory is consistent with the desired cutting path. However for curve or right angle cuts, the geometrical asymmetry makes the stress field near the crack tip behave in a mixed mode condition [130]. Therefore, the crack extension deviates from the linear extension line and the extension trajectory cannot exactly consist with the desired cutting path (as Figure 2.62). Moreover, in some special situations when the thermal-stress was disturbed, the material separation may also fail. Figure 2.63 shows a specimen containing a small hole (regarded as a defect in workpiece), where the main crack extension is influenced by the small hole and subsequently, becomes uncontrollable to link with the hole and suddenly ruptured during cutting [129].

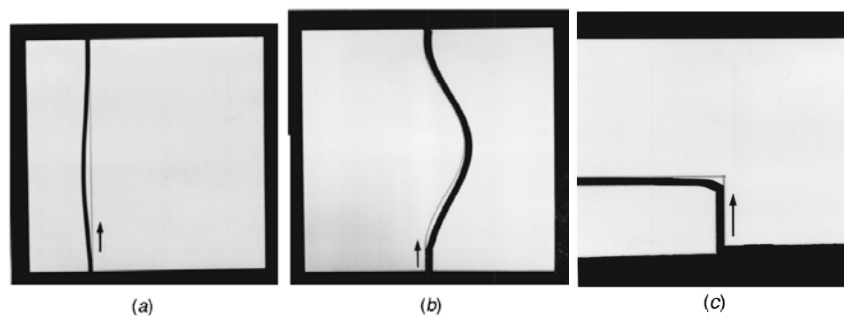


Figure 2.62 Fracture trajectory deviation from the laser moving path in (a) straight line, (b) curved line cut and (c) right angle cuts [129]

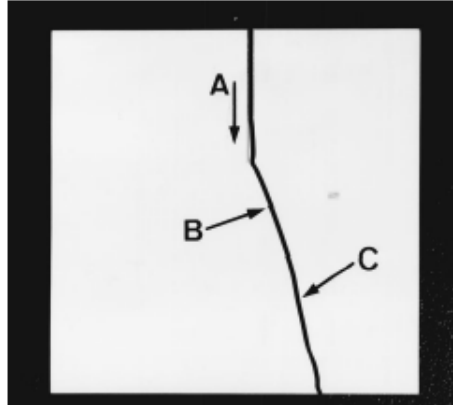


Figure 2.63 Unstable fracture due to the main crack linking with a small hole existing in alumina (A: Cutting direction, B: Small hole, C: Unstable fracture) [129]

Tsai et al also found that the breaking surface by laser controlled fracture cutting can be divided into four regions (as Figures 2.64 to 2.66) [118]. The first region is the laser evaporation region. The second region is the columnar grain region produced by resolidification of the melted material. The third region is the intergranular fracture region produced by controlled fracture. The fourth region is the transgranular fracture region characterised by unstable fractures. The four regions are shown in Figure 2.64. The columnar grain grows from a separate nucleus in the interface of molten layer and solid region. The columnar grain stays parallel to the direction of temperature gradient (as Figure 2.65(a)). When the molten material is solidified, main crack is formed at the columnar grain boundary along the thickness direction (as Figure 2.67). Minor cracks are generated at the edge of the breaking surface (as Figure 2.68). Based on stress analysis, the tensile stress is produced after laser passing. The tensile stress makes the main crack induced in the intergranular region stable and makes transgranular regions extend unstably. The unstable breaking forms the transgranular fracture region (as Figure 2.66(c)). For a large laser spot, the transgranular fracture region occupies the main part and the intergranular fracture region is very small, whereas the evaporation region and the columnar grain region nearly vanish. Meanwhile, the minor cracks generated at the columnar region and intergranular fracture region also disappear. Therefore the good cutting quality can be achieved as shown in Figure 2.69.

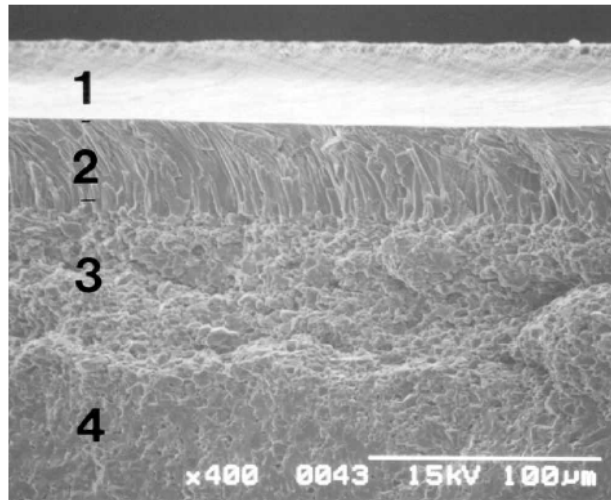


Figure 2.64 SEM photograph of the fracture surface in alumina substrate. The laser evaporation, columnar grain, intergranular fracture and transgranular fracture regions are labelled by 1, 2, 3 and 4, respectively [118]

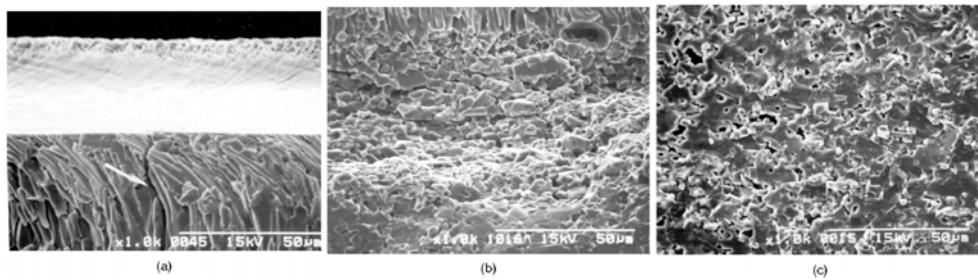


Figure 2.65 Magnification of the fracture surface in alumina substrate: (a) laser evaporation and columnar grain regions (the white arrow indicates the minor crack); (b) intergranular fracture region; (c) transgranular fracture region [118]

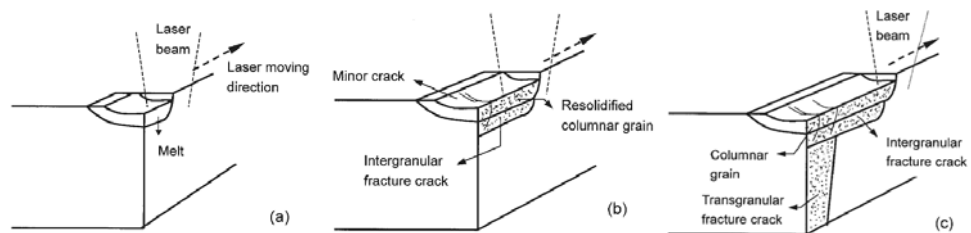


Figure 2.66 Formation of (a) a laser evaporation groove, (b) columnar grains and intergranular fracture cracks and (c) transgranular fracture cracks. Dotted areas indicate the separated surface [118]

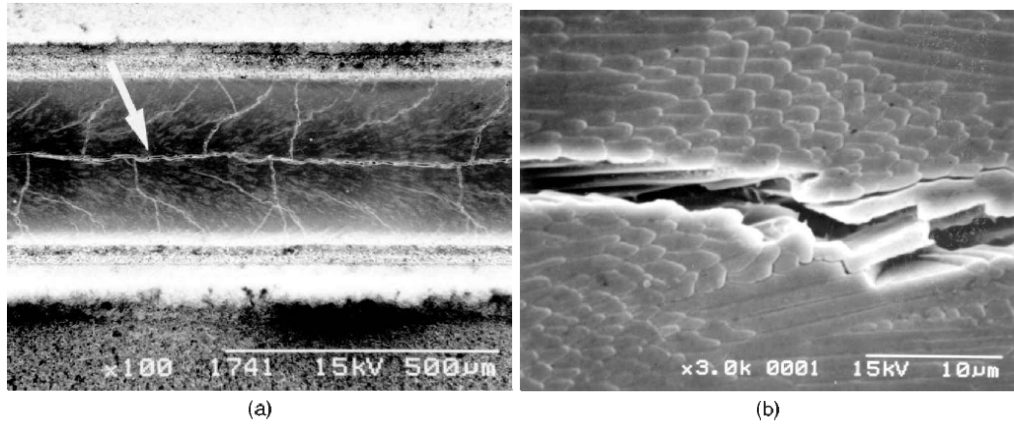


Figure 2.67 Top view of the alumina substrate surface after laser beam passing: (a) the main crack and the branch minor cracks; (b) the magnified main crack [118]

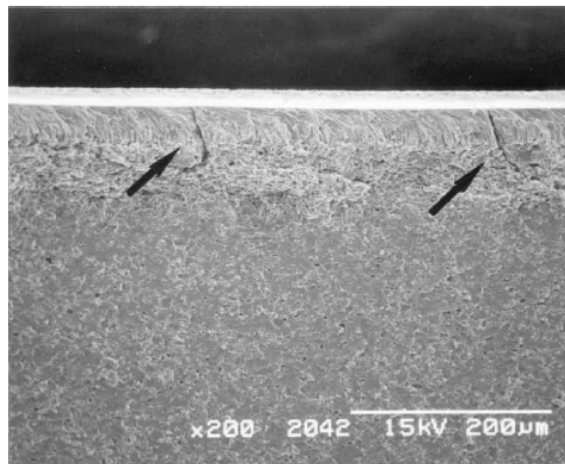


Figure 2.68 The minor cracks at the fracture surface. The arrows indicate the minor cracks that extend from the columnar grain region to the intergranular fracture region [118]

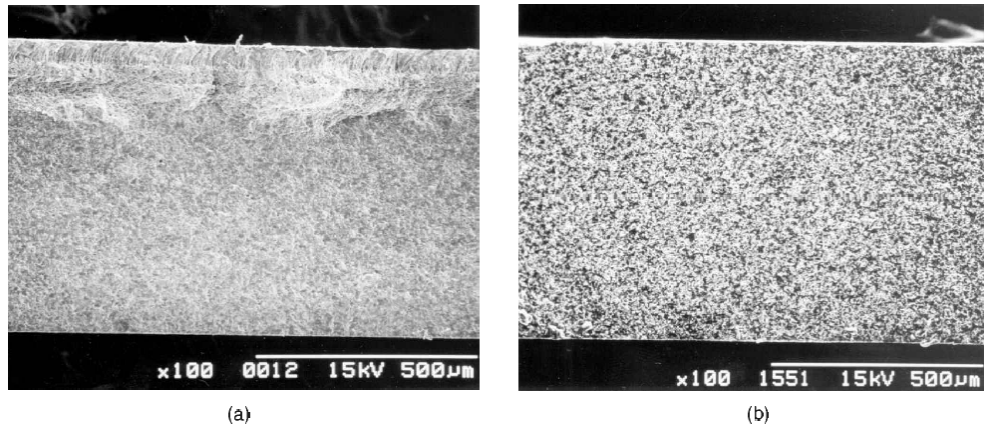


Figure 2.69 The fracture surfaces of the alumina substrate by the laser spot diameter of (a) 0.27 mm and (b) 0.80 mm [118]

Tsai et al further achieved controlled fracture cutting of 10-mm-thick mullite-alumina (as Figure 2.70) by synchronously applying an Nd: YAG laser and a CO₂ laser [131]. The focused Nd: YAG laser was used to scribe a groove-crack on the substrate surface and then the defocused CO₂ laser was employed to generate the thermal stress (as Figure 2.71). The thermal-stress concentrates on the tip of the groove-crack and makes it extend through the substrate with the defocused laser beam moving along the path scribed by the previous focused laser beam. The tensile stress was induced at the groove-crack edge so that the crack unstably propagated along the thickness direction (z -direction). But the fracture extension in the transverse direction (x -direction) was stable due to the compressive stress between the laser beam and the crack tip. They found that the maximum cutting speed was higher for the narrow specimen than for the wide specimen (as Figure 2.72). The maximum cutting speed could be further improved for the deeper groove-crack scribed by the higher power of the Nd: YAG laser (as Figure 2.73). For the narrow specimen with 10 mm thickness and 27 mm width, the maximum cutting speed was 3 mm/s under the 60 W Nd: YAG and 44 W CO₂ laser output. The fracture surfaces were very smooth ($R_a = 2 \mu\text{m}$) and curve cuts could be achieved due to the cracking trapping by the scribed groove. Although the dual beam can control the fracture trajectory along the cutting path more accurately than the single beam, the deviation

was still not completely eliminated especially at the right angle and the trailing edge (as Figure 2.74).

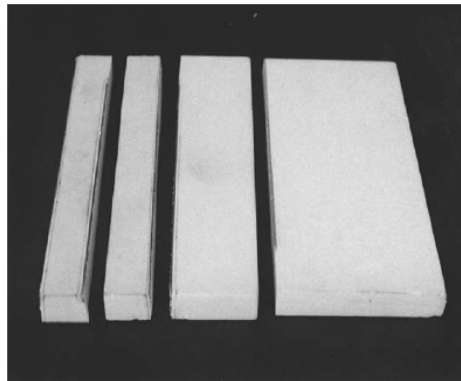


Figure 2.70 Photograph of dual-beam controlled fracture cutting of 10-mm-thick mullite-alumina [131]

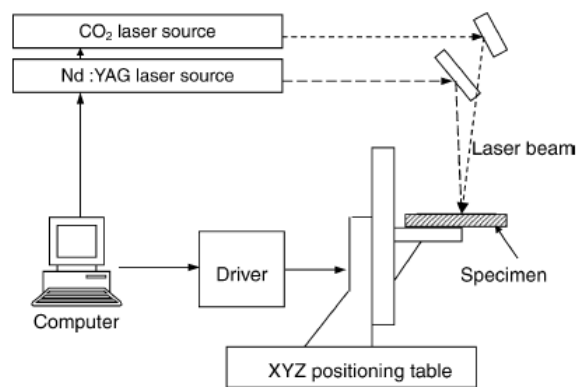


Figure 2.71 Configuration of the dual-beam controlled fracture cutting system [131]

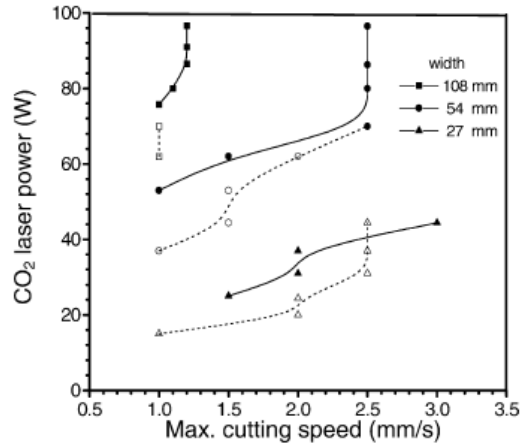


Figure 2.72 CO₂ laser power versus the maximum cutting speed for various specimen widths under a constant Nd: YAG laser power of 60 W (solid lines) and 80 W (dashed lines). Substrate thickness is 10 mm [131]

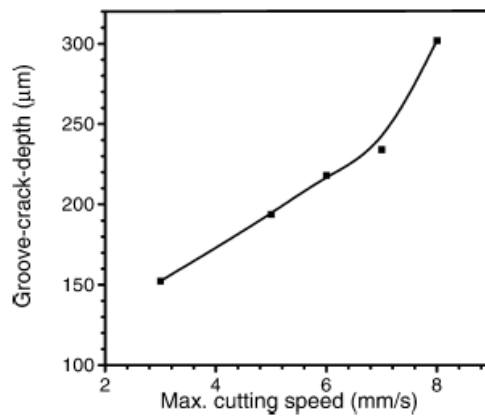


Figure 2.73 The required groove-crack depth versus the maximum cutting speed for through cutting of 2-mm-thick and 108-mm-wide substrates. CO₂ laser power is 37 W [131]

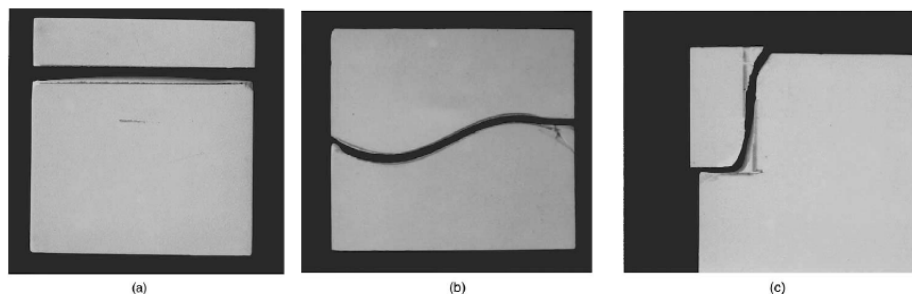


Figure 2.74 Photographs of asymmetrical cutting. (a) The straight line cut, (b) the curved line cut and (c) the right angle cut [131]

In order to resolve the fracture trajectory deviation in curve and right angle cuts, Tsai et al proposed an on-line laser moving path compensation technique (as Figure 2.75) [130] and an iterative path revision technique (as Figure 2.76) [132]. Unfortunately, the deviation was still not completely compensated. The trajectory deviation was generally > 0.2 mm [132], which cannot meet the requirement of industrial applications.

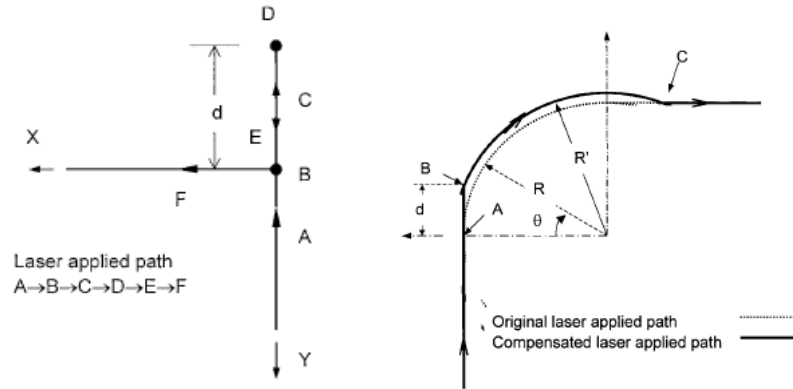


Figure 2.75 Compensation of applied laser paths for right-angle and circular arc cutting [130]

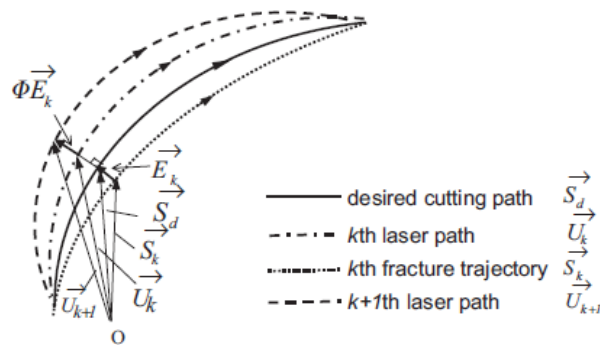


Figure 2.76 Algorithm of the iterative path revision technique [132]

Segall et al investigated the controlled fracture cutting technique using a dual-beam CO₂ laser. Employing a beam delivery system, a lower-power focused beam simultaneously created a shallow groove (namely prescore) directly ahead of the higher-power unfocused cutting beam (as Figure 2.77). Experiments verified that the dual-beam approach was successful in controlling the fracture of linear trajectories,

especially with high cutting speeds and low input power levels [133]. Results for 0.59-mm-thick alumina plates under mixed-mode conditions (i.e. near the trailing edge) indicted that presoring did work with markedly improved fracture control compared to the single-beam controlled fracture cuts (as Figure 2.78). This was attributed to the reduction of the mixed-mode fracture by the net prescore. A complete elimination of the mixed-mode fracture can be achieved with the net prescore as shallow as $14.6\ \mu\text{m}$ [134]. The method solved one of the major challenges, i.e. the cut path deviation at the trailing edge, which is impossible to eliminate using single-beam cutting regardless of CW or PM lasers with any beam geometries [124-126, 135].

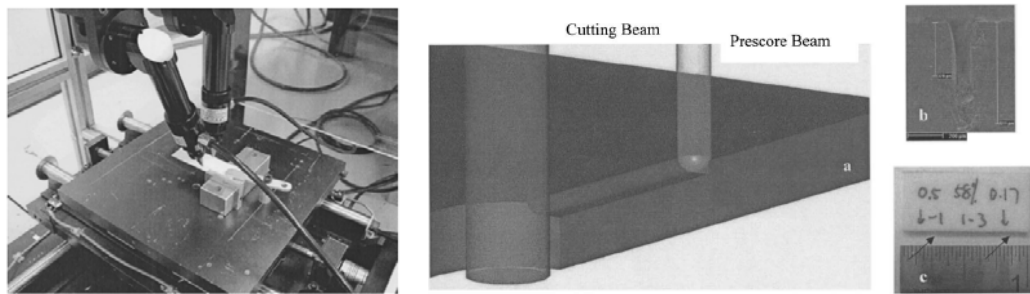


Figure 2.77 The dual-beam delivery system on the left side and schematic of prescoring process on the right side. (a) Schematic of dual-beam controlled fracture cutting, (b) the cross-section the groove, and (c) the finish of the Al_2O_3 substrate cut by the dual-beam controlled fracture technique [134, 136]

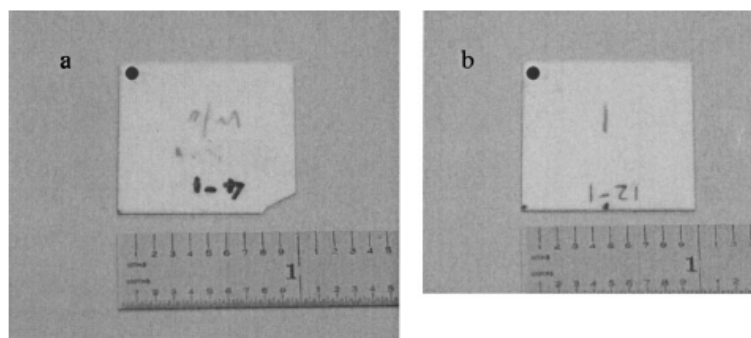


Figure 2.78 (a) Mixed-mode fracture at the trailing edge of the alumina substrate without prescore and (b) markedly improved fracture quality after a 4 W ($12.7\ \mu\text{m}$ net depth) simultaneous prescore [134]

FE modelling was further employed to show the difference of thermal stress between single-beam and dual-beam controlled fracture cutting. Figure 2.79(a) shows the cutting-direction stress induced by a single-beam laser. Results for the dual-beam configuration spaced at 0.5 mm shown in Figure 2.79(b) indicated that the dual-beam configuration caused higher tensile and compressive stresses than the single-beam laser but relatively mild net changes in the tensile stress. Therefore, the fracture cutting is more controllable. However, a greater separation of two beams showed an increasing isolation of the evolving stress fields by the two laser beams (as Figure 2.79(c)). The results showed that a proper dual-beam arrangement is important to reduce the development of deleterious thermal stresses [134].

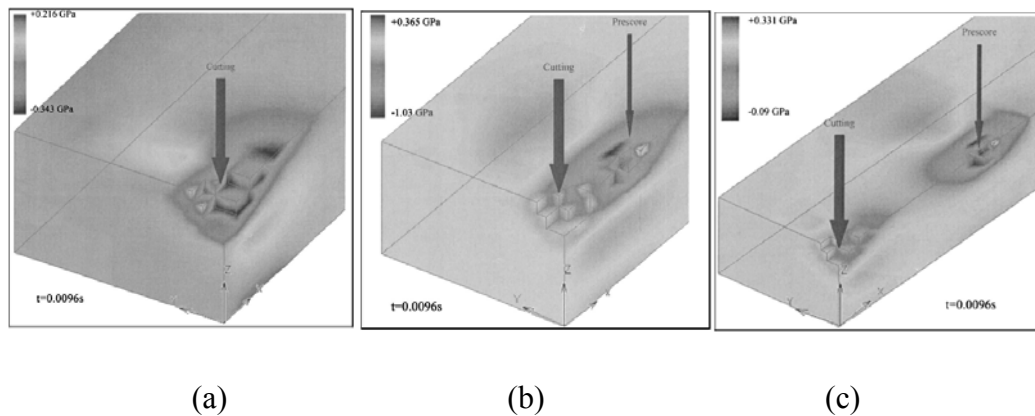


Figure 2.79 Stress distribution and evolution along the cutting direction, x , in (a) single-beam, (b) dual-beam spaced at 0.5 mm and (c) dual-beam spaced at 1 mm controlled fracture cutting [134]

Segall et al also investigated the simultaneous prescore approach on cutting thicker alumina ceramics (2.54 mm) [136]. It was found that, compared to the maximum single-beam feed rate of 4.57 mm/s, the dual-beam technique can be much faster (as Figure 2.80). The fracture path had no deviation from the prescoring path due to reinforcing control by the prescore limit (as Figure 2.81). Their study also proposed that the spacing of the two beams can affect the cut quality, such as the premature fractures when spacing was increased. In addition, cutting speeds, prescore power levels and the resulting groove depths were found to be the key variables to control the fracture path. In single-beam cutting of thick-section ceramics, the groove depth

is too deep due to need relatively high energy. Hence micro-cracks generally form in the recast layer and fracture could prematurely occur leading to relatively severe damage (as Figure 2.82). In dual-beam cutting, the fracture surface appeared to stay in plane with the prescore. Cracks are extended in both the forward and backward directions following the prescore by the unfocused beam irradiation. Figure 2.83 demonstrates the clean fracture surface without significant micro-crack formation.

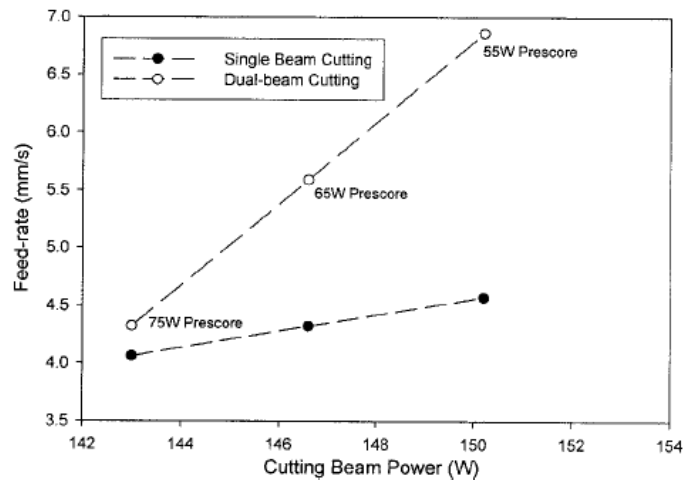


Figure 2.80 Comparison of maximum allowable damage-free cutting speeds for single-beam and dual-beam laser controlled fracture cutting [136]

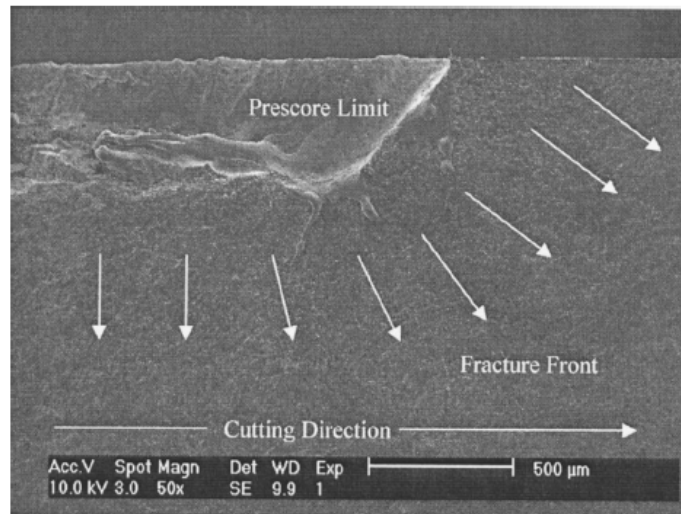


Figure 2.81 Cross-sectional view of the prescore limit and the planar fracture surface (arrows) [136]

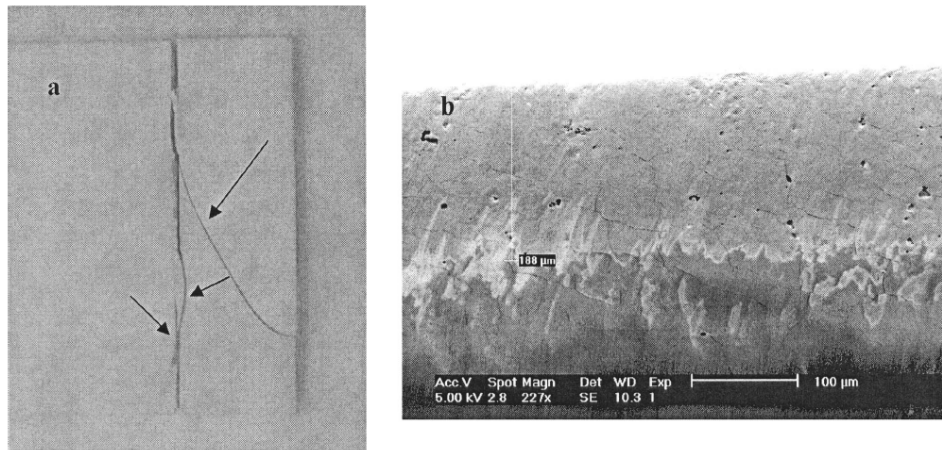


Figure 2.82 (a) Typical fractures deviating from the cutting path after rapid cutting using a single beam with a duty cycle of 40% and a feed rate of 3.30 mm/s and (b) micro-damages [136]

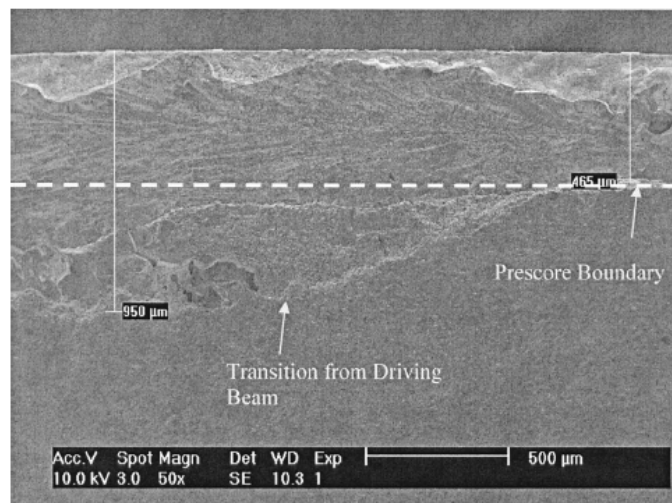


Figure 2.83 Cross-section view of the specimen where the cracks propagate along the path preordained by the prescore and the transition region with the unfocused (diving) beam to the prescore [133]

Experiments on curve cutting were performed as well by Segall et al. Unfortunately, the results showed the dual-beam cutting technique was not suitable for curve cutting. Despite the presence of the prescore, cracking was still observed at the cut curve, particularly in concave parts (as Figure 2.84). But the corresponding convex sections were relatively damage-free except for some easily removed burrs [133]. In 2006,

the practice of prescoring was extended to include both offset and angled prescores to investigate possible improvements (as Figures 2.85 and 2.86). The results showed that offset or angled prescores did not improve the quality of the cut. However, the study demonstrated the relative insensitivity of the cut quality to the alignment of the grooves up to 50 % of the beam diameter and the slight angles up to 9° off the surface [137].

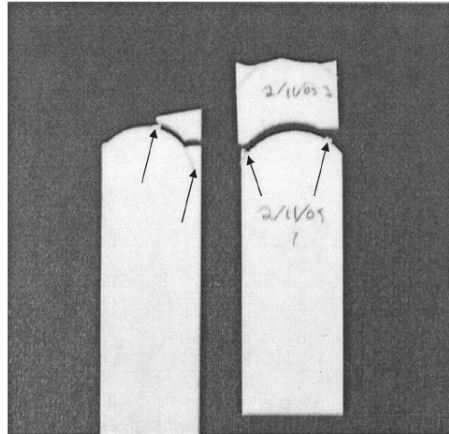


Figure 2.84 Results of controlled-fracture experiments for a semicircular fracture path; the burrs indicated by the arrows can be easily removed from the convex side while the damage to the concave side is irreparable [133]

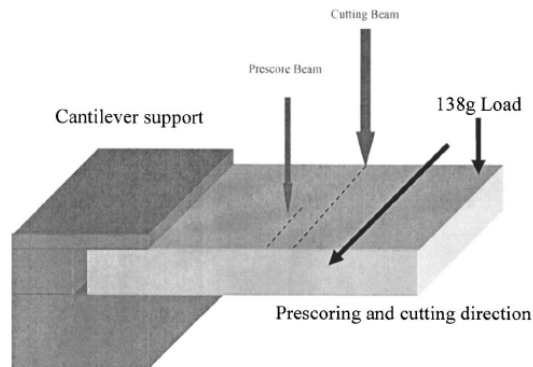


Figure 2.85 Experimental setup showing cantilevered beam, offset beams, and corner weight to induce mixed-mode fracture in dual-beam controlled-fracture cutting [137]

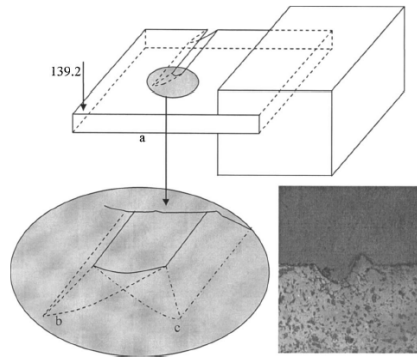


Figure 2.86 Illustration of the 90° angled precore and weight added to exaggerate the mixed-mode loading [137]

Segall et al also simulated the possibility of the delaying fracture by introducing compressive stresses via laser surface heating using a 3D FE model. Based on these numerical simulations, it was found that there was an optimum power for a defocused laser with a fixed beam diameter and location. The Low power could not produce sufficiently strong compressive-stresses to reduce the overall failure probability. At the high laser power, significant deleterious tensile-stresses were developed at the cut front that actually increased the failure probability. Thus, there are a favourable effect due to the compressive-stresses and an unfavourable contribution due to the tensile-stresses. The cutting parameters thereby must be carefully considered to balance them. Furthermore, the size of the failure zone is relatively small. Thus, the location and beam diameter of the defocused laser must be precisely controlled (as Figure 2.87). The simulated results also showed the possibility to change the fracture path by modifying the principal stress directions (as Figure 2.87(d)) when the inappropriate parameters were employed. Therefore, the selection of parameters (power, beam diameter and location of the laser beam) is critical for a reduction of failure probability in dual-beam controlled-fracture cutting [138].

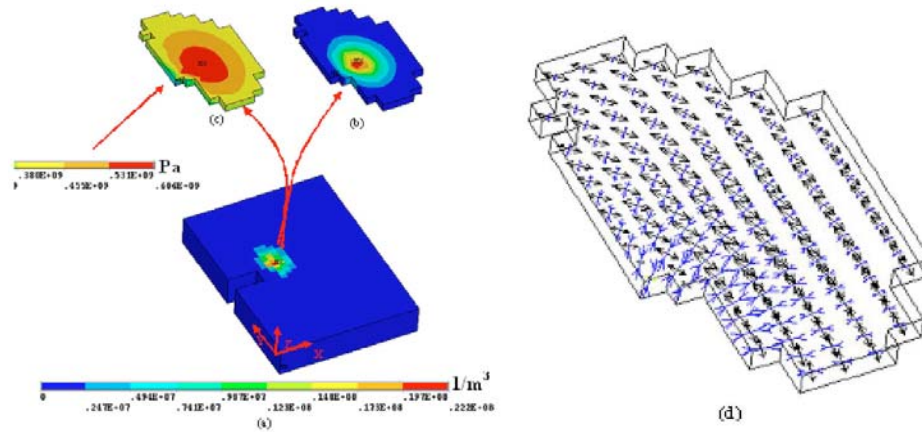


Figure 2.87 (a) Risk of rupture intensities on the surface, (b) surface zone with failure probability greater than 0.01, (c) the first principal stress ($S1$) in the surface zone, and (d) the principal stress directions in the surface zone [138]

Hand et al presented a novel controlled crack propagation technique demonstrating full thickness cutting of Y-TZP ceramics (up to 13-mm thickness) using a 1 kW fibre laser with cutting speed of 1.3 mm/s (as Figure 2.88) [139]. In this technique, a series of discrete holes were drilled and then controlled crack propagation occurred between the adjacent drilled holes to achieve material separation (as Figure 2.89). Based on the experimental evidence and FEM simulations, they indicated that the cracks aroused in the HAZ surrounding the hole and then were driven by the large shear stress occurring near the bottom of the hole in drilling (as Figure 2.90). The distribution of the tensile stresses in the surrounding materials determined that the driving cracks only propagated in the forward direction and connected with the next adjacent hole (as Figure 2.90). However, the deviation in corner cut was still not eliminated by this technique and the cut quality (especially the roughness of cut surface) was relatively low due to the discrete drilled-holes (as Figure 2.89).

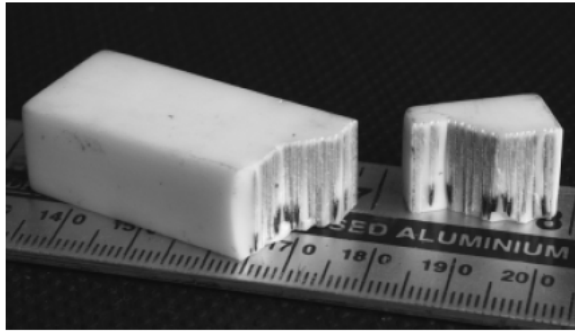


Figure 2.88 Profile cutting of 13-mm-thick Y-TZP ceramic [139]

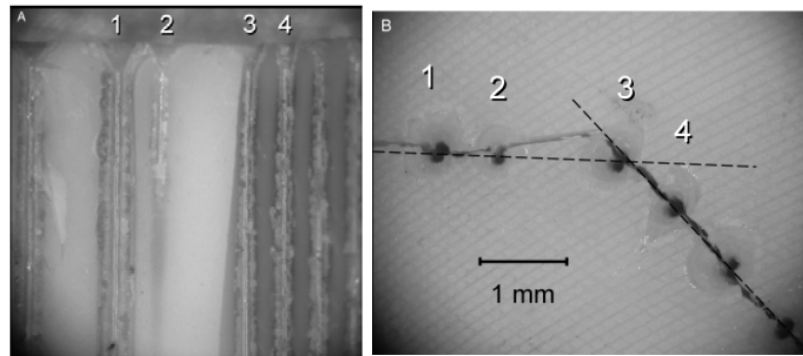


Figure 2.89 A corner cut. (a) Image of the cut surface (b) Top view of the corner cut [139]

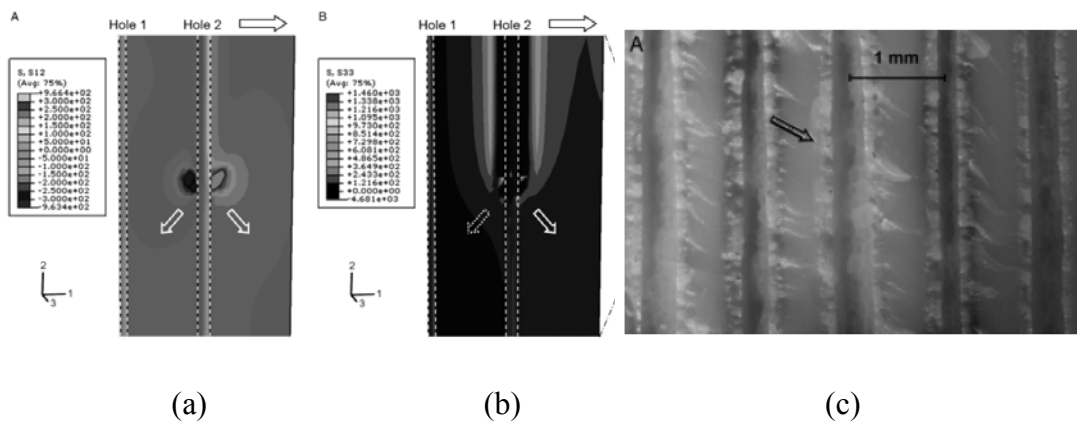


Figure 2.90 Calculated thermal stress fields in drilling during controlled crack propagation cutting. (a) the shear stress distribution (S12), (b) the tensile distribution (S33) and (c) cross-section view of fractured surface. Solid white arrows indicate direction where cracks are driven by tensile stress. The broken arrow indicates that the crack propagation is inhibited in that direction due to the compressive stress. The black arrow indicates the crack propagation in practice [139].

Tsai et al applied a controlled fracture technique to mill ceramics, which they called fracture-machining element technique. This technique employed a focused laser to scan and generate micro-cracks on the ceramic surface forming a fine crack network. A defocused laser is then scanned along the same area again. The laser generated tensile thermal-stresses are concentrated at the tip of cracks and extend the micro-cracks. Materials are thereby removed due to the linkage of the micro-cracks (as Figure 2.91). The minimum average length of the removed ‘chip-element’ was about 0.1 mm and the thickness was about 0.02 mm (as Figure 2.92). The roughness of machined surface was $1.1 \mu\text{m}$ (R_a). These features provide a solution to achieve high precision machining and grinding of ceramic materials [140]. Applying the machining process layer by layer, closed cavities with a specific depth could be obtained (as Figure 2.93). The material removal rate was up to $0.156 \text{ mm}^3/\text{s}$ whereas the roughness of machined surface was $65 \mu\text{m}$ (R_a) [141].

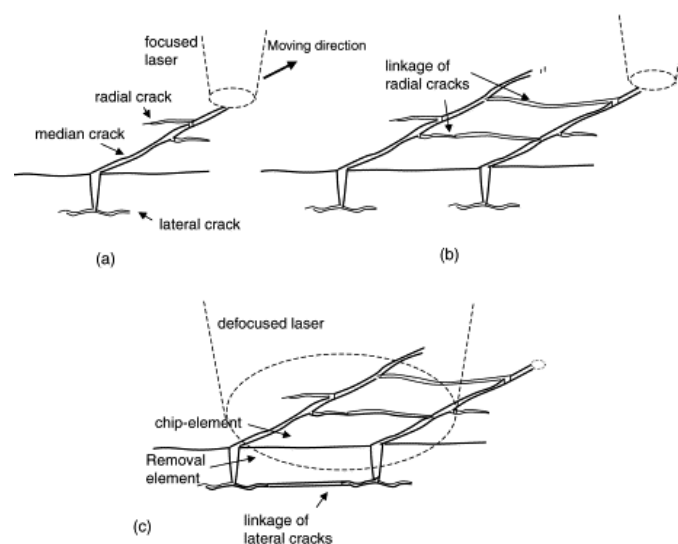


Figure 2.91 Schematic of laser controlled fracture machining (namely, the fracture-machining element technique). (a) laser scribing the first median crack line, (b) laser scribing the second median crack line, (c) thermal breaking [140]

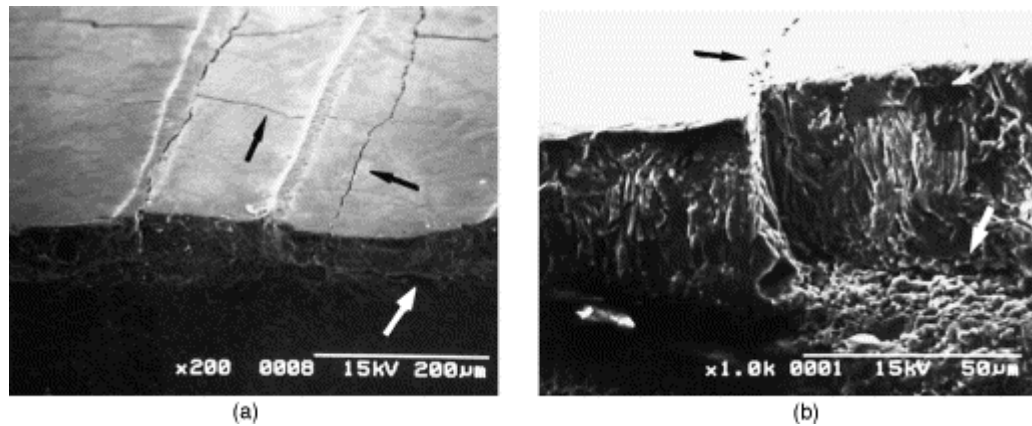


Figure 2.92 Crack network and the cross-section view. The black arrows indicate the median cracks and radial cracks, and the white arrows indicate the lateral cracks (at the boundary of the material removal surface) [140]

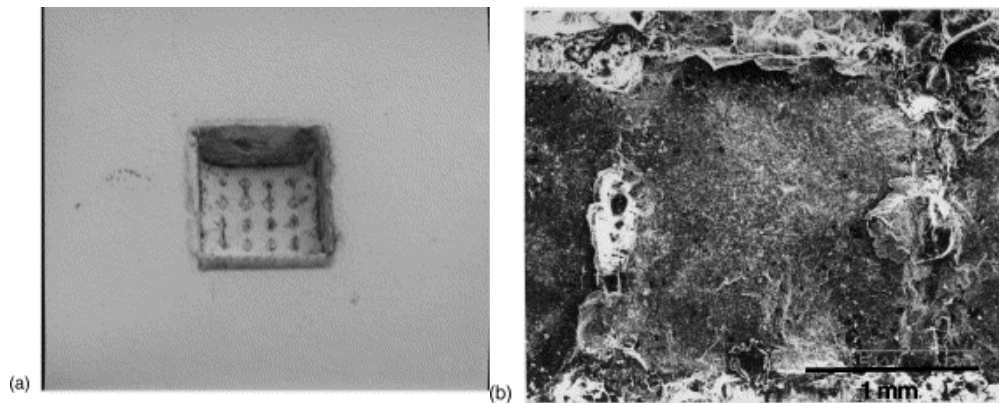


Figure 2.93 Laser controlled fracture milling of alumina. (a) Overview and (b) the SEM micrograph [141]

Tsai et al also employed a dual-laser system (with a CO₂ laser and a YAG laser) to shape bevel face and step at the edge in ceramic substrates (as Figures 2.94 and 2.95) [142]. The machining is fundamentally similar as the dual-beam laser controlled fracture cutting technique. The best roughness (R_a) of machined surface was 20 μm . However, the process procedure and the system of the technique are complicated. Meanwhile, it is only suitable to machining specific shapes in ceramics. These drawbacks restrict the technique to some specific applications.

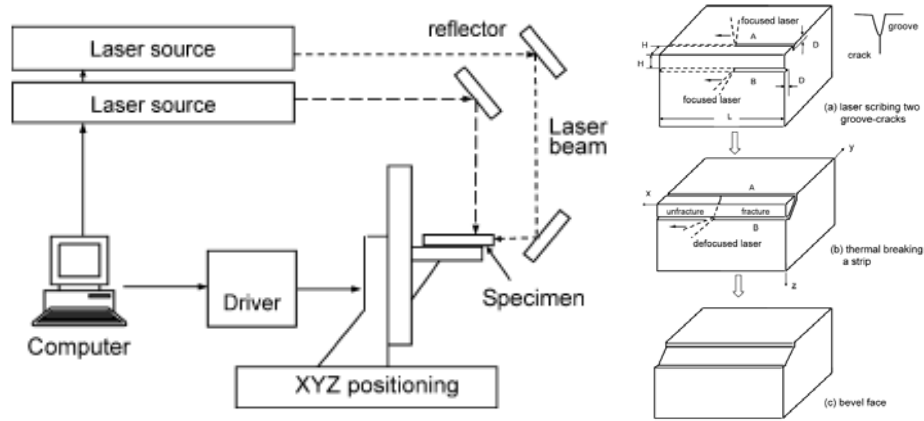


Figure 2.94 (a) Schematic of the dual laser shaping system and (b) a typical procedure of shaping a bevel face [142]

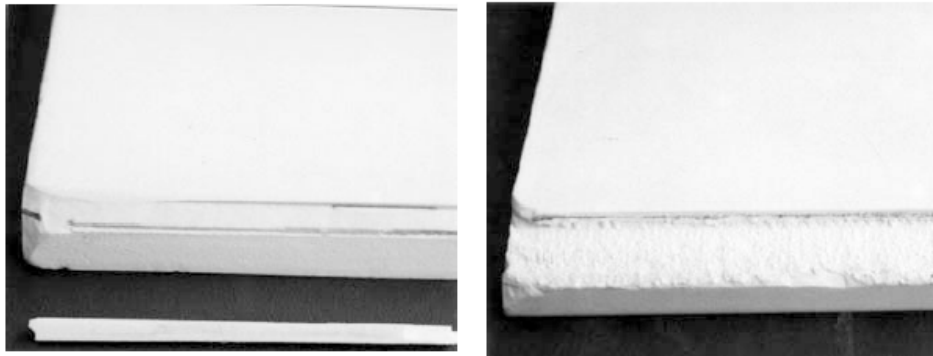


Figure 2.95 Photographs of the shaped bevel face and step at the edge of alumina substrates [142]

Although many studies on laser controlled fracture techniques have been carried out for cutting/machining of brittle ceramics for past decades, some major challenges (e.g. path deviation in right angle and trailing edge, relative low machining precision, and complex processing system and procedures) still limit the laser controlled fracture techniques to industrial applications.

2.4.4 Laser hybrid cutting/machining techniques

Laser hybrid cutting/machining techniques employ a combination of laser and another one or more techniques for ceramic cutting/machining.

Laser-assisted machining (LAM) has been studied for the past decades and partially used in manufacturing industry to machine hard and brittle materials [143]. In LAM, the workpiece is intensely and locally heated by a controllable laser beam, and then machined by a conventional cutting tool [144]. Due to the lowered hardness and brittleness of materials at elevated temperatures, LAM can achieve lower cutting forces, lower tool wear, higher material removal rates, and better surface quality for various engineering ceramics, such as alumina [145], silicon nitride [146-150], mullite [151], and magnesia-partially stabilized zirconia [152]. LAM includes laser-assisted turning and laser-assisted milling (as Figures 2.96 and 2.97). Unfortunately, effective cooling of the cutting tool, optimisation of the machining process and flexible control of the laser source to achieve complex pattern machining are challenging tasks for LAM processes [154], which limit LAM for further industrial applications. The role of laser beam used in LAM is a heat source to soften materials rather than remove materials. It belongs to another research branch in mechanical machining and therefore this technique is not discussed in detail in this work.

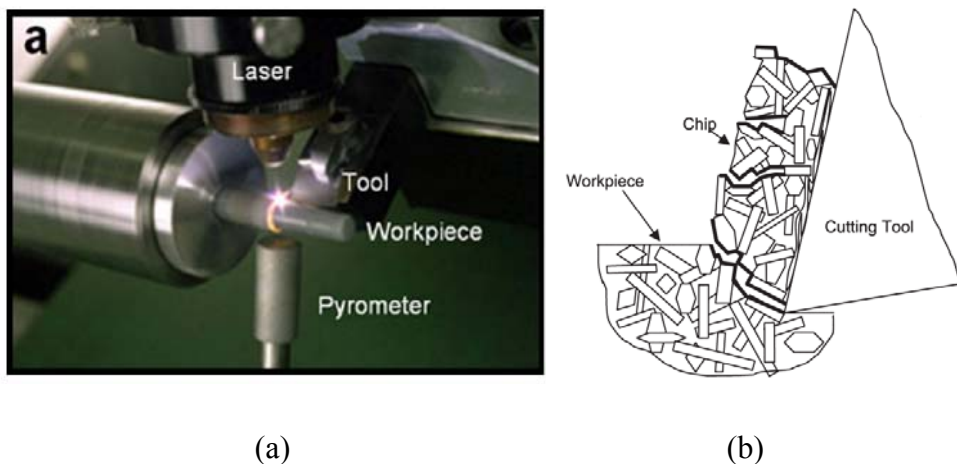


Figure 2.96 (a) Laser-assisted turning system and (b) the chip formation in machining of ceramics [153]

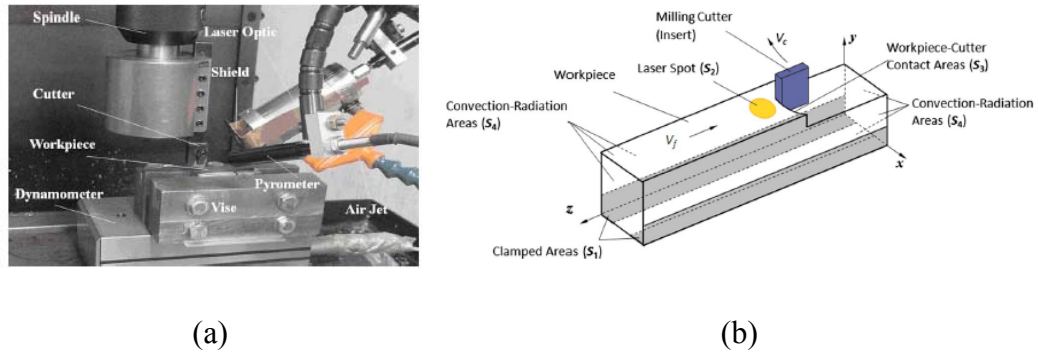


Figure 2.97 (a) Laser-assisted milling system and (b) the schematic of the milling process [149]

Underwater/water-assisted laser cutting/machining is one of the most studied laser hybrid processing techniques. Kruusing reviewed the advantages and disadvantages of water-assisted laser processing and concluded that the underwater machining techniques can be successfully applied for machining, cutting, surface cleaning, and shock processing [155, 156]. In underwater/water-assisted laser cutting, the laser beam, along with the shielding gas or water, is transmitted to the workpiece through a special cutting head (as Figure 2.98). The thickness of the materials for through-cutting may range up to 50 mm and the laser power, CW or millisecond-pulsed, can be used ranging up to 1 kW [156]. When using CO₂ lasers, a dry processing zone is necessary due to the high absorption of water with respect to the 10.6 μm wavelength laser. But for Nd: YAG lasers, of which the wavelength (1.06 μm) can transmit through water with minor losses, a wet zone is acceptable. As shown in Figure 2.98(a) to (d), water is used to chill the workpiece in addition to reducing the emission/liberation of waste gas and particles deposition. In Figure 2.98(e), water jet was used to conduct the YAG laser beam via total internal reflections, which enables a longer distance between the nozzle and the workpiece without defocusing. Some research results on the five underwater/water-assisted laser cutting techniques are listed in Table 2.8.

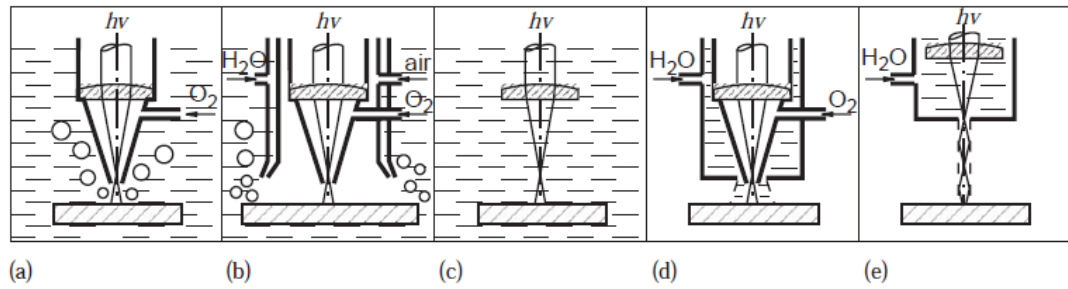


Figure 2.98 Schematic of underwater/water-assisted laser cutting techniques. When using CO₂ lasers, a dry zone at the workpiece surface is needed ((a), (b) and (d)) owing to the high absorption of water with respect to the 10.6 μm wavelength laser. However, YAG lasers (1.06 μm) can transmit through the water (c) or along with a water jet (e) [156]

Table 2.8 Underwater/water-assisted laser cutting of materials [156]

Lasers	Schematic Figure 2-97	Materials	Benefits and remarks
CO₂, 1 kW, CW and pulsed	(a), (d)	Steel C45 sheets; Steel 37-2 also EPO coated; X5CrNi1810; Reinforce plastics	Less burr, better tolerance; HAZ is 10-20% narrower at cutting in water; the plastic layer on the steel was not detached or burnt near the cut; the emission of gases was reduced by 10-30%
CO₂, 5 kW; Nd: YAG, 1.2kW, pulsed	(a)	304L stainless steel, 10-50 mm	Narrower and more regular kerf, 6 times less aerosols and 40% less dross in underwater cutting
CO₂, 530 W, pulsed	(a)	Ceramic tiles, 9 mm	Burnout was greatly reduced
CO₂, 5 kW	(b)	AISI 304 stainless steel, 10mm;	2 times less aerosols and debris, 15 times more H ₂ emission
CVL (511 nm), 500 W, 1-80 ns, 15-166 mJ/pulse	(c)	SUS 304 austenitic stainless steel, 20 mm	20 mm thick material was cuttable at 110 W laser beam power; power density is 15-75 TW/m ²
CO₂, 2-2.3 kW, pulsed	No water addition in cutting	Marble, granite	The materials were soaked with water for better cut quality
Nd: YAG 700 W, CW; 450 W, pulsed	(e)	Cu, Al, Ni, Au, Ag, stainless steel, Si, Ge, Al ₂ O ₃ , Si ₃ N ₄ , SiC	Diameter of the jet 65-100 μm; length of a stable jet up to 100 mm; typical kerf width 50 μm (Si); no focusing problems; suits for cutting of thin sheet materials or thick films

The major challenge in laser machining of ceramics in air is the heat-accumulation-caused cracking and molten material resolidification onto the machined surface. In 1988, Morita et al first reported the pulsed YAG laser drilling of silicon carbide, aluminium nitride and alumina ceramics in water [157]. They found that the recast layer and cracks that were always formed in air machining could be avoided in underwater machining. Kruusing summarised the commonly used methods for underwater/water-assisted laser machining (as Figure 2.99) as well as the potential laser-induced fluid and bubble motions (as Figure 2.100).

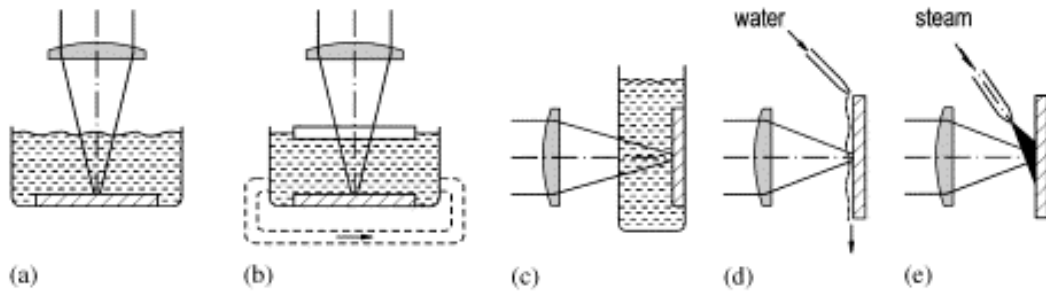


Figure 2.99 Methods for providing water in the processing zone during laser machining. The lasers not well transmitted through the water can use the case (d) and (e), in which the typical thickness of the liquid layer over the target is 1 mm [156]

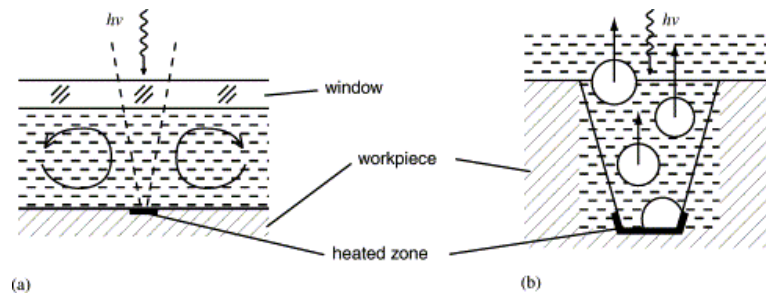


Figure 2.100 Laser induced (a) fluid motion and (b) bubble motion during underwater laser machining [156]

In the previous studies, Nd: YAG lasers emitted at $1.06 \mu\text{m}$ was considered as ideal IR lasers for underwater machining due to the low optical energy loss in water [158, 159]. On the other hand, alumina and glass also have a low absorption for YAG lasers compared with CO_2 lasers. Therefore, CO_2 laser underwater machining was

developed. The mechanism of CO₂ laser underwater machining is different from that by YAG lasers due to the high absorption of water with respect to the 10.6 μm wavelength lasers. During CO₂ laser underwater machining, a proportion of the laser energy vaporises the water and forms a conical keyhole in water allowing the residual laser energy to reach the workpiece. Black et al found that the thermal load during CO₂ laser underwater cutting of ceramic tiles was reduced by the intensive cooling effect of the water [46]. Chung et al employed a CO₂ laser with galvanometer mirrors (as Figure 2.101) achieving crack-free drilling and cutting of Pyrex glass. The defects of bugle, debris, cracks and scorch that often occurred in air machining were eliminated in underwater machining [160, 161]. Tsai et al performed a wide range of experiments on laser machining of thin glass and alumina substrates in air and in water. They found that the underwater machining quality is much better than that in air. The micro-cracking and the HAZ could be prevented by underwater machining (as Figure 2.102) [162].

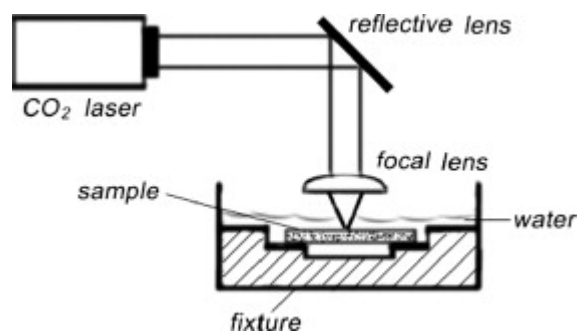


Figure 2.101 Schematic of the CO₂ laser underwater machining system [160]

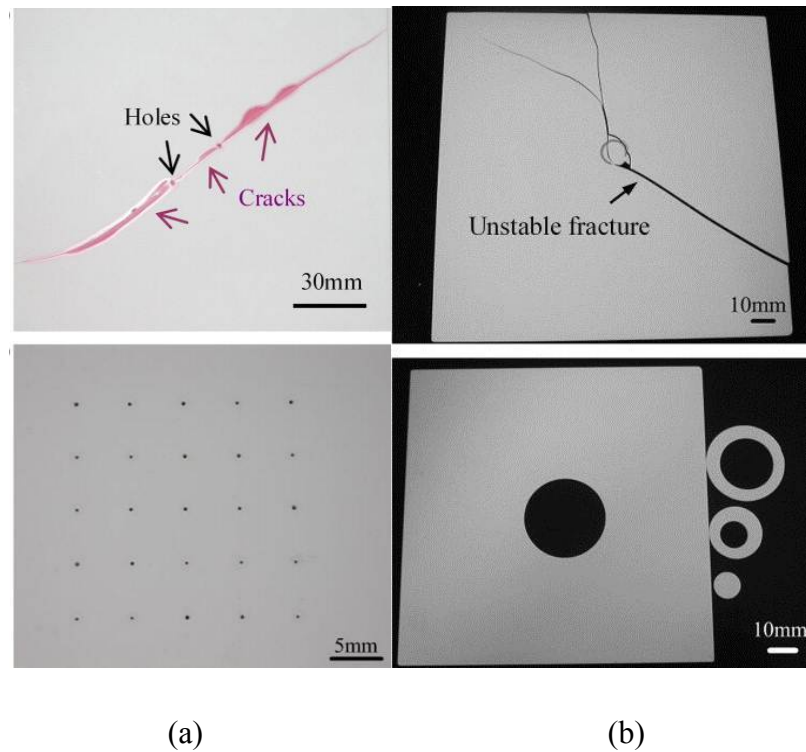


Figure 2.102 Photos of (a) array-holes and (b) cut pattern in air machining (top) and in underwater machining (bottom). The thickness of the alumina substrate is 0.635 mm [162]

Molian et al investigated water-assisted laser cutting of 96% alumina specimens (0.5-mm-thickness) through controlled thermal shock fracture mechanism. A low power CO₂ laser (< 300 W) was used for localised heating and scribing of alumina samples followed by water quenching to induce thermal stress cracking (as Figure 2.103) [163]. The data collected for the dry laser shock cutting of alumina does not seem to have any clear division between uncontrolled cracking and controlled cracking. While the data for the alumina that was cut by the water-assisted laser shocking displayed consistent results depending on the laser power (as Figure 2.104). Therefore, they concluded that laser controlled fracture in water was more controllable than in air. From Figure 2.104, it can also be found that at the same laser power, the feed rate for controlled cracking in water was higher than in air. During water-assisted laser cutting, laser-heated zone is rapidly quenched by water and thus only a small volume of the material is heated. Due to the restraint of the surrounding material, large compressive stresses developed in the heated zone while the sample is

subjected to tensile stress. When the laser-heated zone is quenched in water, the rapidly cooled sample surface induces more serious thermal shock, i.e. development of tensile radial stresses in the heated zone. The larger tensile stresses associated with rapid cooling are responsible for propagation of existing flaws into cracks and fracture of the workpiece. It was found that the feed rate in water-assisted laser shock cutting is approximately 500% faster than dry laser controlled fracture cutting [163]. Furthermore in dry laser cutting, the slow cooling rate precludes the development of tensile stresses and most of the surface damage could be induced due to melt and ablation of the surface material.

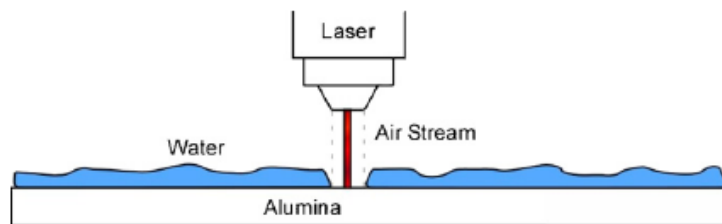


Figure 2.103 Schematic of the water-assisted laser shock cutting technique [163]

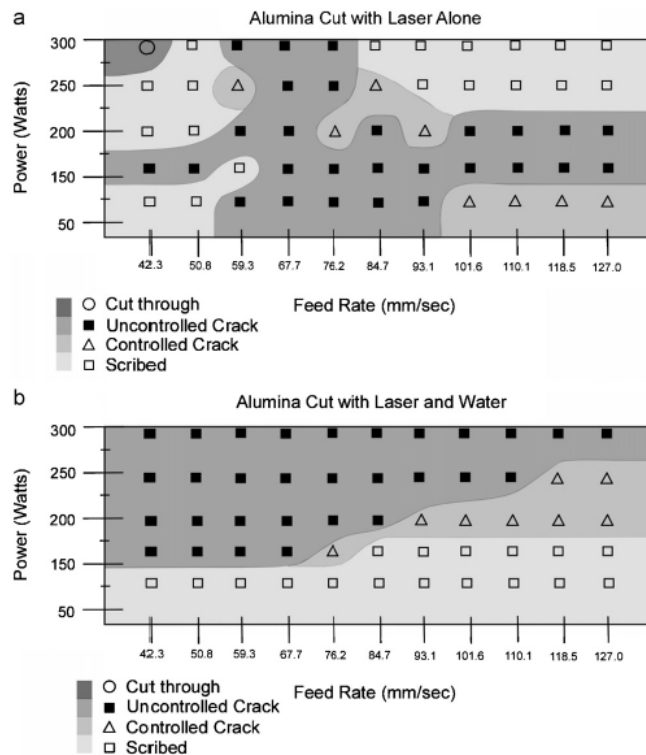


Figure 2.104 Process maps related to the laser power and the feed rate for (a) dry laser shock cutting and (b) water-assisted laser shock cutting of alumina [163]

Molian et al further developed the technique and studied the relationship between process parameters and fracture behaviour in cutting of 1 mm thick alumina samples by a hybrid CO₂ laser/waterjet (LWJ) machining system (as Figure 2.105) [164]. Figure 2.105 relates the process parameters to the expected fracture characteristics of alumina specimen in numerical simulation and experimental results. Minimum energy release rate (G) for cracking (as Figure 2.106) was used to identify the transition from scribing to fracture cutting.

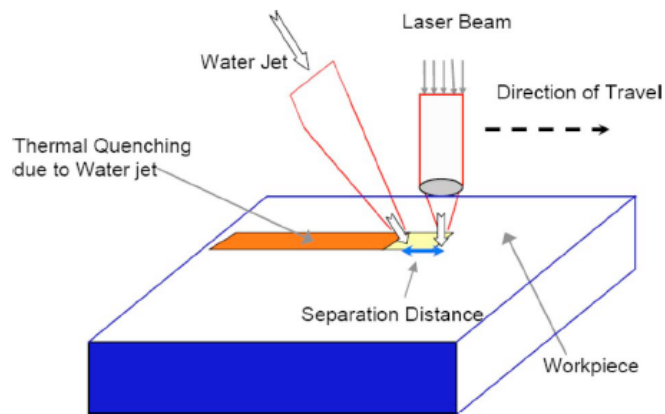


Figure 2.105 Schematic of the hybrid CO₂ laser/waterjet (LWJ) machining system [164]

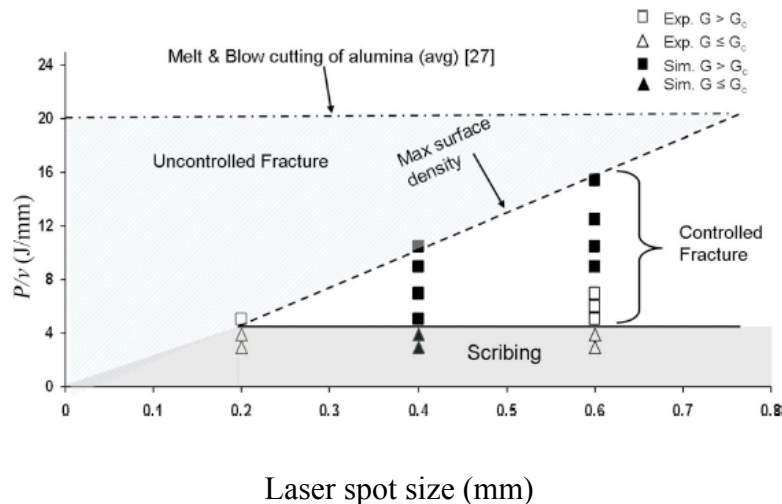


Figure 2.106 Relationship of fracture characteristics with process parameters [164]

Tsai et al proposed an unstable fracture laser cutting technique combined with a diamond blade used to scribe a groove along the desired cutting path in an alumina substrate. Then a defocused CO₂ laser (30 W) irradiates the substrate surface. As the laser moves a short distance, a short through-crack is generated from the edge of the substrate. When the laser direction is reversed, a great thermal tensile stress is induced at the crack tip and causes the substrate to break along the scribed line (as Figure 2.107). Unlike the controlled fracture method, this method is based on unstable fracture, in which the region near the crack tip always displays a tensile effect (as Figure 2.108). The laser scanning speed ranged from 5 to 20 mm/s for 0.635 mm thick alumina substrates. Figure 2.109 shows the breaking surface quality of the unstable fracture cutting. It is free from chips and cracks and the entire breaking surface is smoother than conventional mechanical bending [165]. Although the quality of the breaking surface by the technique is much better than other cutting techniques, the method cannot be applied to asymmetrical geometry cutting even the straight cutting not along the central line (as Figure 2.110), in which the crack always branches away from the desired cutting path as the uncontrollable tensile stress state at the crack tip is not purely mode I (i.e. the mixed mode stress concentration at the crack tip).

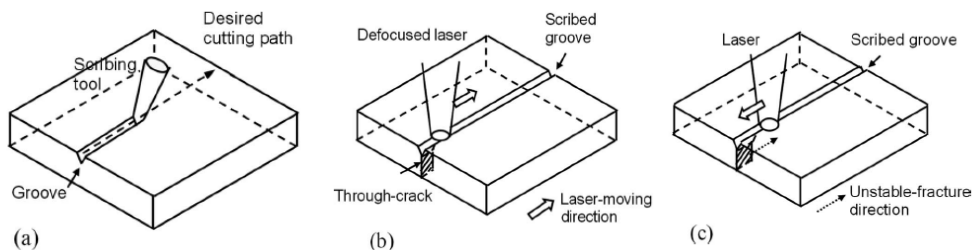


Figure 2.107 Process of the unstable fracture cutting technique: (a) scribe a groove, (b) produce a short through-crack, and (c) make the through-crack extend unstably

[165]

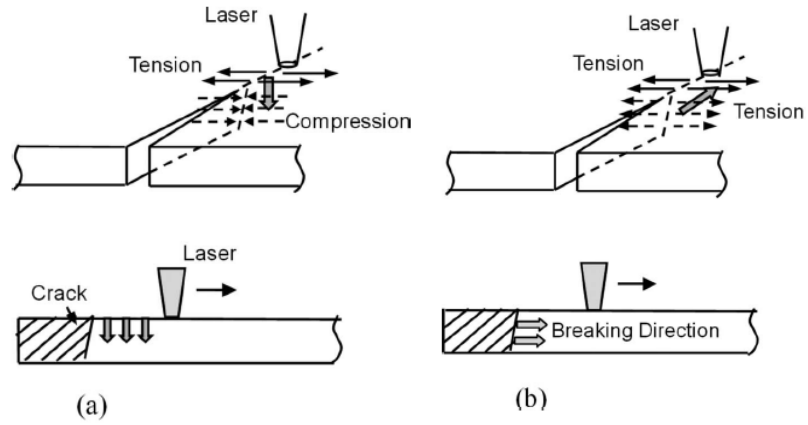


Figure 2.108 Stress states of (a) stable fracture growth and (b) unstable fracture extension [165]

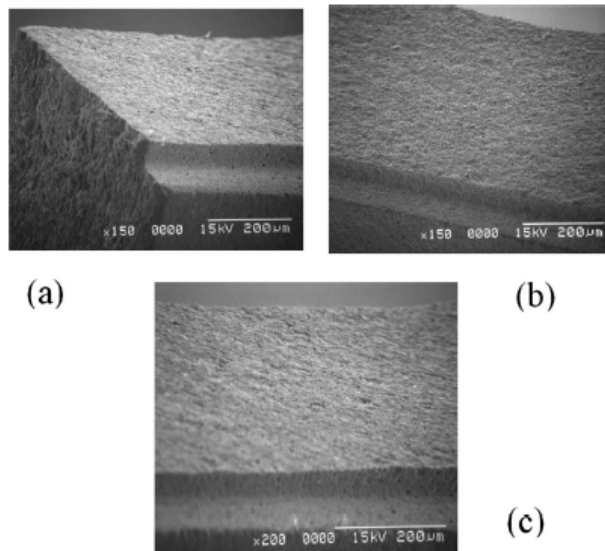


Figure 2.109 The breaking surface of the alumina substrate at (a) the frontier stage, (b) the middle stage, and (c) the latter stage using the unstable fracture cutting technique [165]

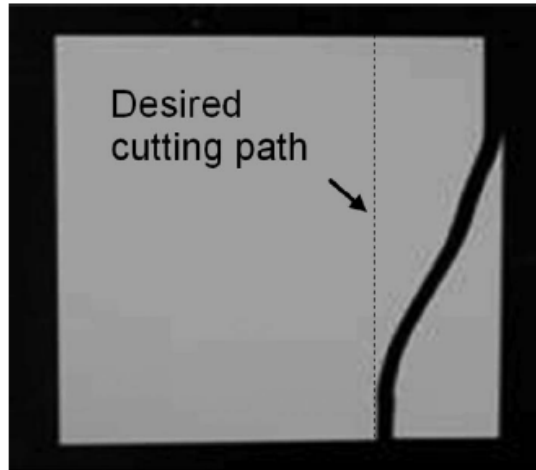


Figure 2.110 Failure in asymmetric cutting [165]

Laser cutting/machining of preheated ceramics is another method to reduce thermal damage. However, these studies showed that it was necessary to previously heat the ceramic at least above 1000°C to soften ceramics to reduce the thermal stress in cutting/machining [166-168]. The thermal damage can therefore be minimised and a good cut quality can be achieved. However, preheating ceramics and holding the reached temperatures are difficult during laser cutting/machining in practice. Especially in laser cutting, the assist gas could generate a reversed temperature gradient and hence induces the crack formation [166]. These drawbacks limit the application of the preheating method in ceramic cutting/machining.

2.5 Summary

Outstanding mechanical and physical properties such as high thermal resistance, high hardness and chemical stability have encouraged the use of engineering ceramics in many applications. Unfortunately, the brittle and hard natures make them difficult to be machined by conventional techniques and the damage on machined surfaces always affects the properties of the finished products. Laser cutting/machining has emerged as an alternative technique for high material removal rates and good process quality. It is considered as a rapid, non-contact and flexible machining process.

In this chapter, an attempt has been made to cover the laser cutting/machining techniques for engineering ceramics (especially for alumina). Four types of laser cutting/machining techniques associated with their mechanisms and features in cutting/machining of engineering ceramics are reviewed in this chapter after a brief introduction to ceramics, alumina ceramic and conventional fabrication techniques. For green body shaping, the low mechanical strength of the green body makes the desired shape formed easily and rapidly by conventional fabrication techniques. But green machining has a low level of end-product accuracy due to the shrinkage after sintering. For post-sintering machining, an economic comparison between laser machining and other machining techniques is listed in Table 2.6. It can be found that the laser machining is the most competitive technique for machining of hard and brittle sintered engineering ceramics.

In order to expand the applications of ceramics, laser cutting/machining techniques have to meet the high requirement of finish quality and machining rate for the end products. The features of the four representative laser cutting/machining techniques mentioned in this chapter are summarised in Table 2.9. Unfortunately, some scientific challenges in laser cutting/machining of ceramics have not been resolved by the previous studies and techniques. The major challenges are listed as follows:

- 1) Cracking is the big challenge in laser processing of ceramics. The thermal damage in IR laser cutting/machining was considered to be critical in previous studies and could cause the workpiece catastrophic breakdown.
- 2) Material removal rate in laser cutting/machining of thick-section ceramics is still very low although it is higher than mechanical machining. For high power lasers, the machining rate cannot be dramatically improved due to the significant thermal damage, which could induce crack formation.
- 3) Surface finish quality of laser cutting/machining is much lower than mechanical machining. Rough finish surface is another challenge for IR laser macro-machining in addition to cracking. The low surface finish quality was attributed to the inherent characteristic of laser processing (e.g. melting oscillation and re-deposition). Post-mechanical process is still necessary for high surface finish quality. Although short/ultrashort pulsed lasers (e.g. pico-second and femto-

second) have demonstrated the capability for high surface finish quality machining, the low machining rate limits their applications only in micro-machining field.

- 4) To date, the mechanisms of laser cutting/machining have not been revealed completely due to the complicated multi-physical phenomena occurring during laser cutting/machining of ceramic materials. Therefore, it is difficult to control the process of laser cutting/machining for high finish quality.

Considering the above mentioned scientific challenges, it is essential to further study the effects of process parameters on process quality and machining rate, investigate the unrevealed mechanisms, and explore the potential new techniques, in order to achieve high-quality laser cutting/machining of engineering ceramics. This work aims to contribute in the progress of high-quality laser cutting/machining of alumina ceramics.

Table 2.9 Features of various laser cutting/machining techniques for engineering ceramics

Techniques	Advantages	Drawback
Conventional Cutting	<ul style="list-style-type: none"> (1) Complex pattern (2) High machining rate and high Speed (up to 14 mm/s via off-axial nozzle) (3) Employing the conventional laser cutting system and mechanisms (similar with metal cutting) (4) Suitable for 3D cutting 	<ul style="list-style-type: none"> (1) High power intensity requirement (2) Serious HAZ and crack easily initiated causing breakdown (3) Hard to cut thick workpiece (> 10 mm) (4) Relatively low finish quality
Multi-pass Cutting / Machining	<ul style="list-style-type: none"> (1) Complex pattern (2) Employing the conventional laser cutting/machining system and mechanisms (3) Low power requirement and small HAZ resisting crack formation (4) Suitable to machine thick workpiece (up to 9.2 mm) and sharp angle without crack 	<ul style="list-style-type: none"> (1) Low machining rate (2) Deposition and dross degrading the process quality when the target has a melting point (e.g. alumina)
Controlled-Fractal Cutting / Machining	<ul style="list-style-type: none"> (1) High speed (up to 20 mm/s) (2) Low power requirement (3) Almost non-HAZ (4) Suitable to machine thick workpiece (up to 10 mm) 	<ul style="list-style-type: none"> (1) Difficult to control crack propagation (2) Simple pattern machining only (3) Relative complicate cutting/machining systems
Hybrid Cutting / Machining	May have some of above advantages depending on different hybrid methods	<ul style="list-style-type: none"> (1) Complicated cutting/machining systems (2) Multi-operation processes (3) Suitable to specific materials only (4) Limited flexibility

Chapter 3

Fibre Laser Crack-Free Cutting of Thick-Section Alumina

3.1 Introduction

A major challenge in laser fusion cutting of thick-section ceramics is to overcome the thermal-stress induced cracking, which leads to catastrophic breakdown of the material integrity. In order to achieve crack-free cutting of ceramics, it is important to understand the mechanism of the transient temperature field and resulting stress distribution effect on crack formation during laser cutting. In this chapter, both experimental and theoretical investigations are performed to understand crack formation characteristics in fibre laser cutting of thick-section Al₂O₃ ceramics. A three-dimensional (3D) finite element (FE) model for simulation of the transient temperature field and thermal-stress distribution together with material removal in laser cutting was developed. Crack formation characteristics were predicted by the model and validated by experiments. The effects of four process parameters i.e. laser peak power, pulse duration, pulse repetition rate and feed rate on temperature field, resulting stress distribution and potential crack formation were also investigated.

3.2 Experimental Procedure

3.2.1 Laser cutting system setup and process parameters selection

The laser employed in this work was an YLR-1000-SM fibre laser ($M^2=1.1$) manufactured by IPG Photonics GmbH (as Figure 3.1). This is a continuous wave (CW) single mode laser capable of delivering up to 1 kW power at 1075 nm wavelength via an optical fibre with a core diameter of 14 μm . The laser output can be modulated as a pulse train up to 5 kHz. The shortest pulse duration and pulse interval are both 1 ms. A fibre output assembly was mounted on the z-axis Precitec

cutting head, which held the necessary lens and gas nozzle for the fusion cutting. Figure 3.2 schematically shows the experimental setup. In this work, standard rectangular laser pulses were used. The laser beam was focused via a lens of 190.5 mm focal length to give a beam waist diameter of approximately 50 μm . The focal plane was positioned at the half of workpiece thickness below the surface in order to obtain the highest power density throughout the thickness. Based on pilot previous experiments, the range of peak power, pulse width, duty cycle and feed rate selected in this work is listed in Table 3.1. The experimental samples were mounted on a linear motor translation stage to enable the samples to be moved under the laser beam (as Figure 3.2). The cut process is single-pass fusion cutting. In order to obtain reliable and stable experimental results, a straight line passing through the entire workpiece length (50 mm) was applied as the cut path.



Figure 3.1 The IPG YLP-1000-SM fibre laser system

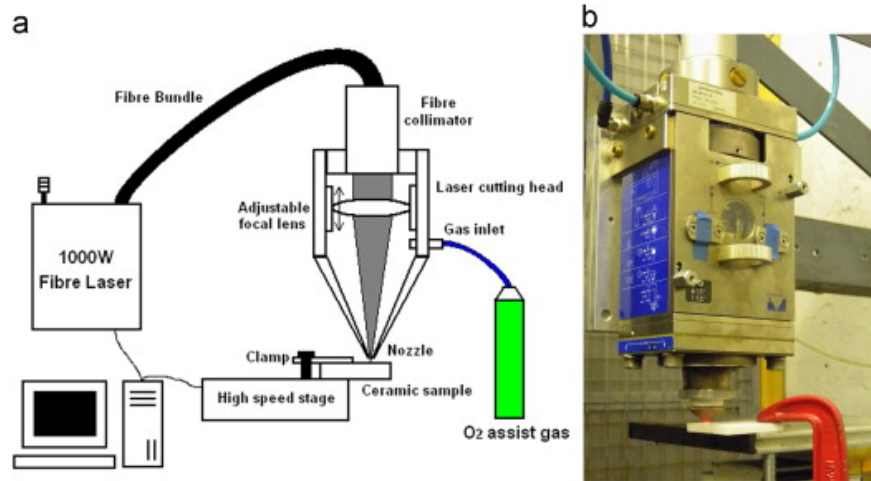


Figure 3.2 Experimental setup incorporating a fibre laser, focusing optics, gas and a high speed linear motor stage. (a) Schematic diagram of the experimental setup. (b) A photograph of the Precitec laser cutting head for the experiments

Table 3.1 Laser cutting parameters employed in this work

Case	Power (W)	Pulse duration (ms)	Pulse repetition rate (Hz)	Cutting speed (mm/s)
1	600	10	20	1
	800	10	20	1
	1000	10	20	1
2	800	5	20	1
	800	10	20	1
	800	20	20	1
3	800	10	50	1
	800	10	20	1
	800	10	10	1
4	800	10	20	0.5
	800	10	20	1
	800	10	20	1.5
5	800	CW	CW	1

In laser cutting, the assist gas serves to protect the optics from the debris and to remove the molten material from the cut kerf more efficiently. In this work, oxygen was selected as the assist gas jetted out from a 1.5 mm nozzle at a pressure of 5 bars with 1 mm stand-off distance between the nozzle tip and the workpiece surface. The reason for choosing oxygen was to reduce the oxygen depletion resulting in alumina discoloration (as Figure 3.3) during laser cutting.

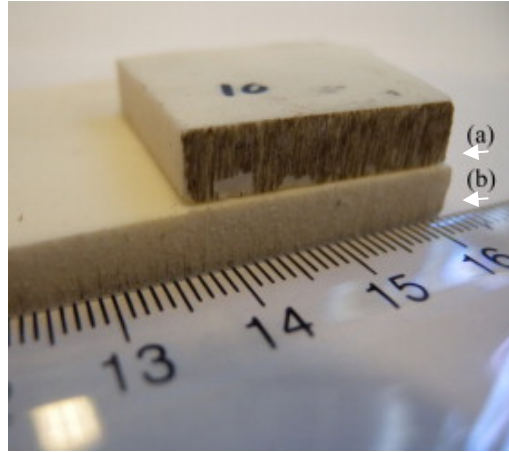


Figure 3.3 Laser cut surfaces using (a) N₂ and (b) O₂ assist gas

The cut samples were then examined by an optical microscope (Polyvar) to capture the crack at cutting edge and the path deviation at the trailing edge. The microstructure of cutting edge was further observed by scanning laser confocal microscopy (Olympus OLS-3100) in order to explore the potential mechanism driving crack formation in laser fusion cutting of thick-section alumina.

3.2.2 Material properties

The dimensions of 95% alumina specimen used in the work were 50 mm×50 mm×6 mm. The major thermal and mechanical properties of the material are listed in Table 3.2, which were obtained from the manufacturer's datasheet.

Table 3.2 Material's properties of 95% alumina used in the work

Properties	Values
Mass density (kg/m ³)	3720
Specific heat (J/kg×K)	880
Thermal conductivity (W/m×K)	35
Elastic module (GPa)	300
Poisson's ratio	0.21
Secant coefficient of thermal expansion (10 ⁻⁶ 1/K)	8.2
Melting point (°C)	2050
Vaporisation point (°C)	2980
Tensile strength (MPa)	220
Compressive strength (MPa)	2600

In particular, the optical properties of alumina are distinct from those of metals with respect to near-infrared (NIR) wavelengths. The absorption of alumina for the 1075 nm wavelength laser can no longer be considered as a surface effect since the distance the light travels in alumina, following the Beer–Lambert Law, is much greater than in metal. Figure 3.4 shows the transmittance and reflectance of 1-mm-thickness alumina for NIR wavelength light, measured by Shimadzu UV-3600 Spectrometer. The values of transmittance and reflectance at 1075 nm are 16.4% and 79.4%, respectively. The attenuation coefficient, α , was thus calculated by [169]

$$P_{out} = P_{in} e^{-\alpha z} = (1 - R) P_0 e^{-\alpha z}$$

$$\Rightarrow \alpha = -\frac{1}{z} \ln \frac{P_{out}}{(1 - R) P_0} = -\frac{1}{z} \ln \frac{T_{light}}{1 - R} \quad (3-1)$$

where P_{out} is the laser power transmitted through the z -thickness-workpiece, P_{in} is the laser power incident into the workpiece and P_0 is the laser power arrives at the workpiece surface. R and T_{light} are the reflectance* and transmittance of the material, respectively, with respect to the specified wavelength. Based on Eq. (3-1), the attenuation coefficient of alumina for 1075 nm wavelength was 228.0 m^{-1} .

* Technical note: The back reflection from the rear surface of alumina workpiece would cause an error in reflectivity measurement. Based on the measured transmissivity, the maximum error for reflectivity was about 4%, this leads to a sum of reflectivity and transmissivity of 103.5% at the 1400 nm spectrum. At 1075 nm, the reflectivity error is lower than 3%. In this work, this measurement error was considered not critical.

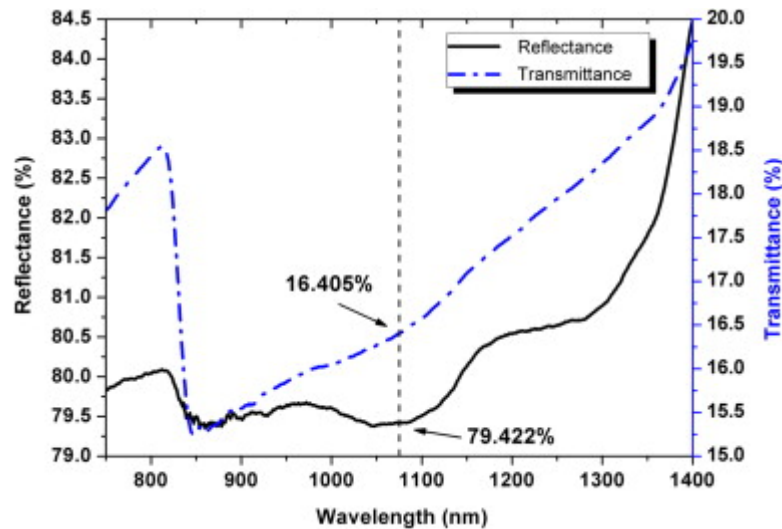


Figure 3.4 Transmittance and reflectance curves of alumina for near infrared wavelength light (750–1400 nm)

3.3 FE Modelling*

3.3.1 FE geometric model

Figure 3.5 shows an overview of the FE semi-model. The qualitative simulation was performed by the entire FE semi-model, in which x -axis represents the laser beam moving direction and z -axis represents the thickness of the specimen. The semi-model was symmetric with respect to x - z plane and the symmetry constraint was applied on this surface. The dimensions of the model were 50 mm×25 mm×6 mm, similar as the semi-sample employed in experimental trials. Another reason to select the semi-model was that this work only focused on thermal-stress generation and crack development rather than cut kerf slot geometry.

* More detail on FE modelling of fibre laser cutting is enclosed in Appendix A

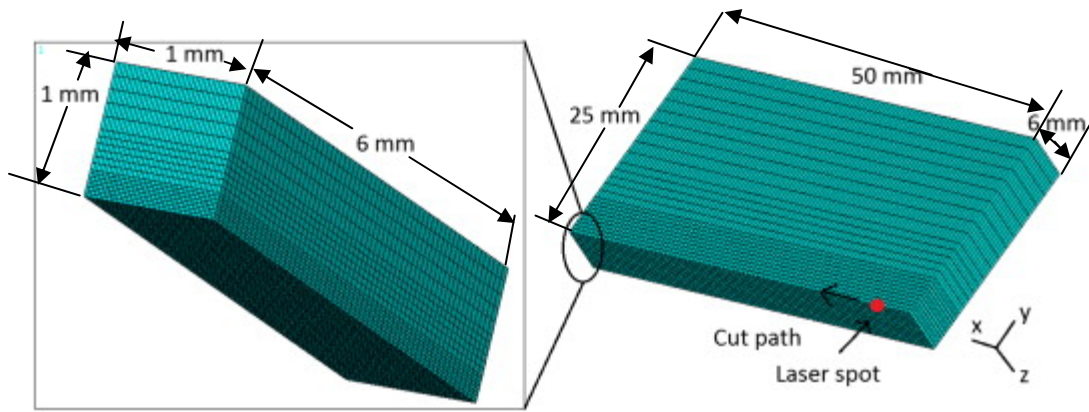


Figure 3.5 Overview of the FE semi-model for numerical simulation (extracted semi-model & entire semi-model)

A local region (1 mm×1 mm×6 mm) at trailing edge was extracted from the entire FE semi-model (as Figure 3.5) in order to quantitatively study the effects of process parameters on temperature and thermal-stress with a high simulation accuracy (according to the fine mesh size). The selection of the region at trailing edge was due to the high magnitudes of the thermal-stresses generated near the edge of the sheet, which would induce cracking and path deviation influencing the final cut quality [124, 135]. Therefore, the extracted semi-model at the trailing edge was employed as a stricter criterion to study the stress distribution. Based on previous study, the region with 1 mm×1 mm×6 mm was found to be sufficient to model the local process without significant modification of the temperature boundary conditions on the outside surfaces of the specimen. From the model, it was expected to obtain a trend in change of temperature gradient and thermal-stress distribution under various process parameters and to understand of the mechanism of crack formation.

3.3.2 Material properties and laser heat load for FE modelling

In numerical simulation, a major problem is the lack of realistic material property data. In order to improve the simulation accuracy, every attempt was made to use the realistic material properties in this work. Although most of essential material properties for modelling are listed in Table 3.2, temperature-dependent thermal conductivity and specific heat are still necessary (as listed in Table 3.3) to generate a

model close to reality. In addition, the material mechanical properties related to thermal-stress development and crack initiation are also listed in Table 3.3. Unlike metals, ceramics are generally considered as elastic materials. Their elastic behaviour can be retained at the elevated temperatures (e.g. 1800 °C for alumina), which is close to their melt points (e.g. 2050 °C for alumina). Moreover, plastic deformation around the cutting edge was not observed in the experiments during laser cutting of alumina. Therefore, the plastic deformation in laser cutting of alumina was ignored in this work.

Table 3.3 Alumina material properties used for FE analysis [12, 170]

Properties	Values
Mass density (kg/m ³)	3720
Specific heat (J/kg×K, to 1773K)	$1044.6 + 1742 \times 10^{-4} \times T - 2796 \times 10^{-4} \times T^{-2}$
Thermal conductivity (W/m×K, 300 – 1573 K)	$5.5 + 34.5e^{[-0.0033 \times (T-273)]}$
Elastic module (GPa)	300
Poisson's ratio	0.21
Secant coefficient of thermal expansion (10 ⁻⁶ 1/K)	8.2
Melting point (°C)	2050
Vaporisation point (°C)	2980
Tensile strength (MPa)	220
Compressive strength (MPa)	2600
Open shear transfer Coefficient	0.5
Close shear Transfer Coefficient	0.9

As discussed above, volumetric absorption was the major form of alumina absorbing laser energy at 1075 nm wavelength. Therefore, the incident laser was considered as a volumetric heat source in the FE model. The heat generation rate, $Q(x,y,z,t)$, caused by the volumetric absorption for a Gaussian laser beam moving along x -direction with velocity, v , can be expressed as [171]

$$\begin{cases} Q(x,y,z,t) = \frac{(1-R) \times P_0 \times e^{(-\alpha z)}}{\pi r^2(z)} \times \alpha \times e^{-\left(\frac{(x-vt)^2 + y^2}{r^2(z)}\right)} \\ r(z) = r_0 \sqrt{1 + \left(\frac{\lambda(z + fpp)}{\pi r_0^2}\right)^2} \end{cases} \quad (3-2)$$

where it was assumed that the laser energy absorbed in material was entirely converted into heat energy. The laser beam propagates along the z -axis. $r(z)$ is laser spot radius at position z . r_0 is the spot radius at the focal plane position, λ is the laser wavelength, and fpp is the position of the focal plane. The positive fpp means the focal plane was above the surface of workpiece and the negative one indicated it was in the workpiece.

3.3.3 Thermal analysis and thermal-stress analysis in FE model

The temperature field simulation was first performed, in which the 3D elements SOLID70 with 8 nodes were employed for the transient thermal analysis. The ‘element death’ methodology (available in ANSYS) was applied to simulate material removal in cutting. When the temperature of an element exceeded the melting point of alumina, the element was removed from the model and had no effect in subsequent analyses. The cut kerf was in turn formed and the incident laser energy was no longer absorbed within the kerf. The boundary condition for thermal analysis was convection heat losses. The air convection coefficient and ambient temperature were taken as $50 \text{ W}/(\text{m}^2 \text{ K})$ and $27 \text{ }^\circ\text{C}$, respectively, in this work.

Based on the calculated temperature field, thermal-stress simulation without cracking was performed. The model with element SOLID70 for thermal analysis was transformed into the SOLID65 used for structural analysis. The boundary condition of the FE model for structural analysis is traction-free for all surfaces except the x - z surface, on which the symmetric boundary was applied to constrain displacement at y -direction. Nevertheless, the removed elements in thermal analysis were still inactive during the thermal-stress simulation. The temperature field calculated by above thermal analysis was applied as a heat load on the structural model and the thermal-stress simulation was then performed in ANSYS.

3.3.4 Fracture criterion and crack prediction in FE model

Prediction of crack generation and propagation was performed following the thermal-stress analysis. The thermal-stress caused by temperature gradient was generally considered as the main reason of crack initiation and propagation in brittle materials [172]. However, the prediction of crack initiation and propagation in 3D finite volume is still a cutting-edge topic in structural mechanics and fracture mechanics. ANSYS software provides a 3D crack simulation based on the current knowledge of crack behaviour in concrete [173]. Generally, some material properties of ceramic are very similar to those of concrete since both are multi-crystal and multi-phase non-metallic materials and are hard and brittle in nature. Therefore, the simulation of 3D crack in concrete was referred to in this work for prediction of crack generation and propagation in alumina during laser fusion cutting.

The element SOLID65 has the capability for simulation of 3D concrete structural responses and crack behaviours governed by stress. Thus the crack simulation in this work was performed after the thermal-stress analysis. Although the solution of crack simulation has been supplied by ANSYS, correct and accurate prediction of 3D crack is still difficult since the proper fracture theory should be chosen and fracture parameters are needed from fracture tests. In brittle materials, the main mechanism causing crack formation was considered to follow the 1st strength theory [174]. The material failure and crack formation were caused by the 1st principal stress when higher than the tensile strength or compressive strength. Therefore, the 1st strength theory was selected in this work as the fracture criterion. The tensile and compressive strength for material failure (as listed in Table 3.3) was set in the material model in ANSYS. Stress relaxation after cracking was also considered by applying an existed function in ANSYS to the FE model, in order to simulate the crack propagation more accurately. When the fracture criterion and material properties on crack formation were set up in material model, the crack simulation can be automatically performed in ANSYS. After simulation, the crack plane in each element was plotted by a red circle (i.e. a vector) indicating the cracking direction [173]. The crack formation in the FE model was therefore demonstrated by all the cracking vectors.

3.3.5 Assumptions

Although the FE model was established to represent the realistic process of laser cutting, some factors had to be ignored for simplification of the model as there are some complicated and uncertain variables in laser cutting, such as anisotropic material properties, phase transition, recoil pressure, melting, evaporation, plasma, etc. For example, in a previous study [175], alumina liquid was formed at 2327 K and remained at the liquid phase until 3500 K. When the liquid temperature is above 3250 K, dissociation yields different species such as $\text{AlO}(\text{g})$, $\text{Al}(\text{l})$, $\text{Al}(\text{g})$ and $\text{Al}_2\text{O}(\text{g})$. At the temperature above 5000 K, dissociation is complete and aluminium vapour and atomic oxygen are formed. These complicated processes were ignored in this work. The assumptions applied to the FE model include:

- (a) The specimen was considered to be homogenous and isotropic.
- (b) The molten and evaporated material removal expelled by assist gas was simplified in the FE model as the region was eliminated when the temperature exceeded the material melting point.
- (c) Chemical dissociation, phase transition, plasma and interaction of laser beam with melt and/or vapour were ignored.
- (d) Beam scattering inside the cut kerf and the multi-reflection effect were ignored.
- (e) The effect of convection in cut kerf was ignored.
- (f) The stress–strain relationship of alumina was considered to be elastic at the whole temperature range and the plastic strain at crack-tips was ignored.

3.4 Results and Discussion *

3.4.1 Initial results

The Case 5 (Table 3.1) was selected as the process parameters for the entire FE model. The model simulation was used for qualitative analysis of the temperature field, thermal-stress distribution and crack formation in laser cutting. The simulated temperature field and the 1st principal stress distribution are shown as Figure 3.6. It

* More information on simulated temperature related to thermal-stress is enclosed in Appendix A

can be found that the thermal-stress concentrated on the region near the cut front, where the crack tended to be formed.

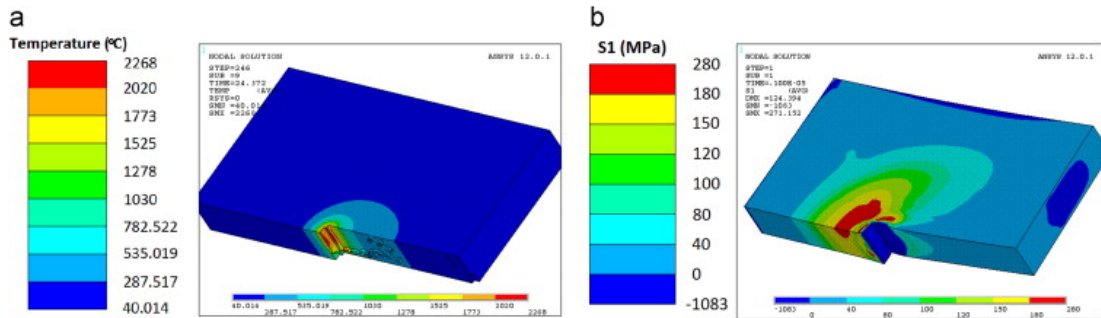


Figure 3.6 Temperature and stress distribution during laser cutting of 6-mm-thick alumina. (a) Temperature field and (b) the 1st principal stress distribution

Figure 3.7 shows the x -component and y -component stress distribution, which implies potential crack propagation. Based on the 1st strength theory, the x -component stress (as Figure 3.7(a)) generally caused the crack propagating along the y -direction (as arrow in Figure 3.7(a)), whereas the y -component stress (as Figure 3.7(b)) induced the crack propagation along the x -direction (as arrow in Figure 3.7(b)).

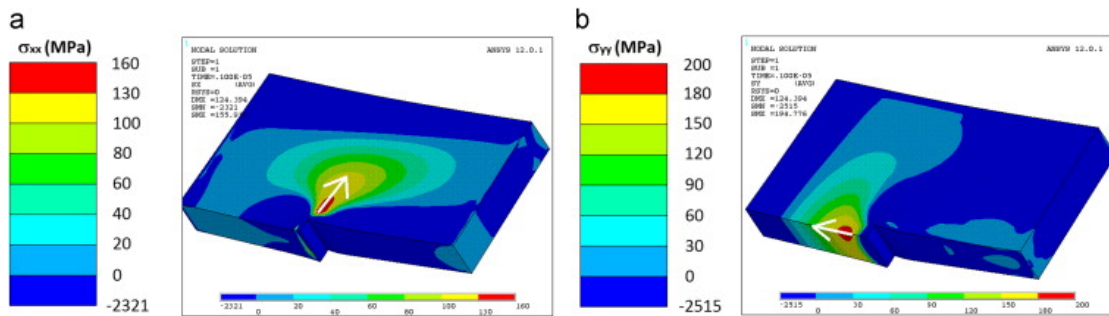


Figure 3.7 Component stress distributions during laser cutting of 6-mm-thick alumina. (a) x -component stress distribution (σ_{xx}) and (b) y -component stress distribution (σ_{yy})

Based on the above thermal-stress distribution, crack propagation was simulated as shown in Figure 3.8 (the red marks), which illustrates that the crack would probably

initiate from the cut front and propagate into the base material. The direction of the maximum crack growth was along a specific angle between x - and y -directions (i.e. 51.62°) due to the resultant vector effect of x - and y -component stresses.

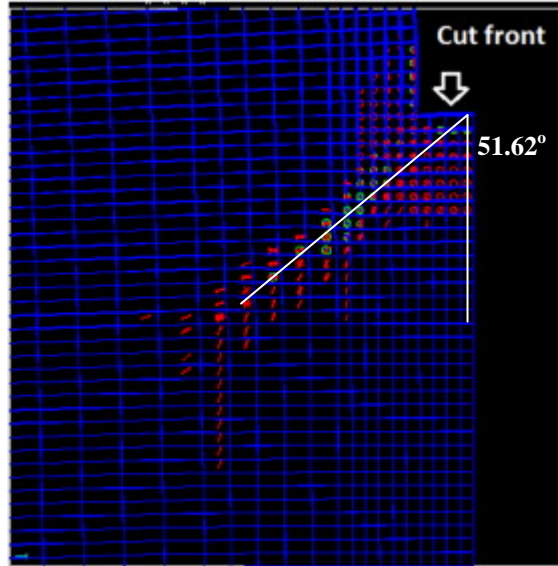


Figure 3.8 Crack formation and propagation from cut front in laser cutting of 6-mm-thick alumina.

An experimental trial was performed as well using the same process parameters (as Case 5 in Table 3.1) to validate the crack prediction by the FE model. The crack was captured as shown in Figure 3.9(a). The characteristic of crack formation and the angle of the micro-crack (i.e. 52.67° with respect to the cutting edge) were in agreement with the FE numerical prediction. Figure 3.9(b) further shows the microstructure of the cutting edge. The crystalline grains that were partially melted and resolidified as glassy phase showed the HAZ existing in alumina. It can be found that the HAZ was very large ($>75\ \mu\text{m}$) during CW laser cutting. The transcrystalline cracking appeared in the large HAZ. The experimental result indicated that the size of HAZ may be the main reason causing the crack formation in alumina. Therefore, the process parameters should be studied and optimised to reduce the HAZ around the cutting edge.

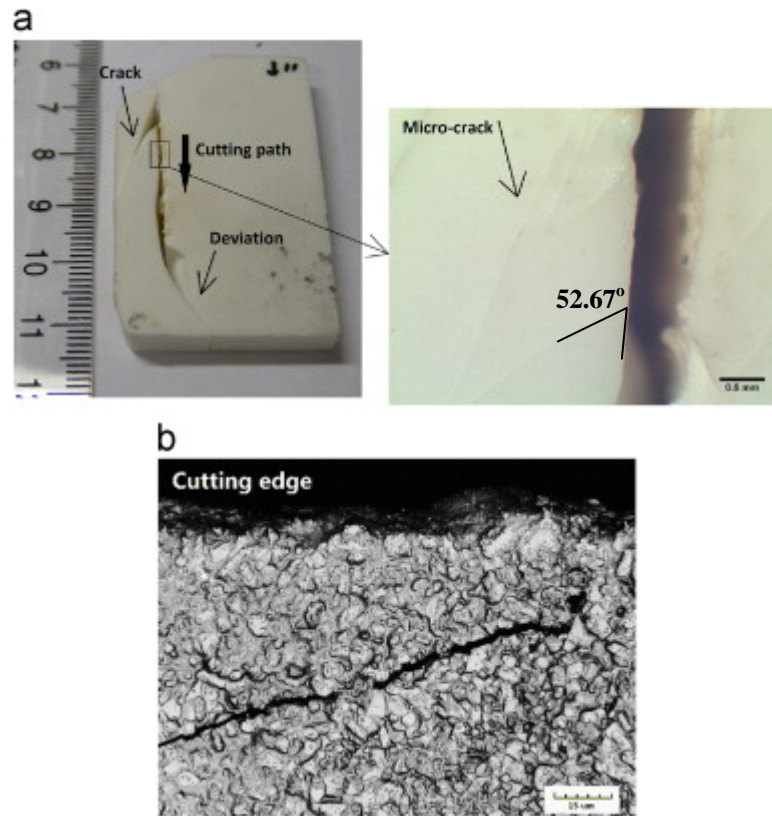


Figure 3.9 The experimental result of 6-mm-thick alumina cut by 800 W CW laser with feed rate of 1 mm/s. (a) Optical micrograph of the cracks and (b) micro-structure of the cutting edge

3.4.2 Laser peak power effect

The effect of laser peak power on temperature and stress distribution was studied using Case 1 in Table 3.1. Figure 3.10 shows the temperature and the corresponding thermal-stress distributions along the x - and y -directions at different laser peak powers. It was found the higher laser peak power generated a steeper temperature gradient for both x - and y -directions, which generated a smaller HAZ (as Figures 3.10(a) and (c)). The stress distributions caused by the temperature gradients highlighted the steeper temperature gradient generated the lower peak tensile stresses along x - and y -directions (as Figures 3.10(b) and (d)). Both the stress distributions along the two directions complied with the tendency as from compressive stresses to tensile stresses. When the tensile stress was low enough (typically lower than the tensile strength), this stress distribution could resist the cracking from the cut front.

Therefore, a high laser peak power was recommended to reduce the HAZ size and thermal tensile stress to resist crack formation during cutting.

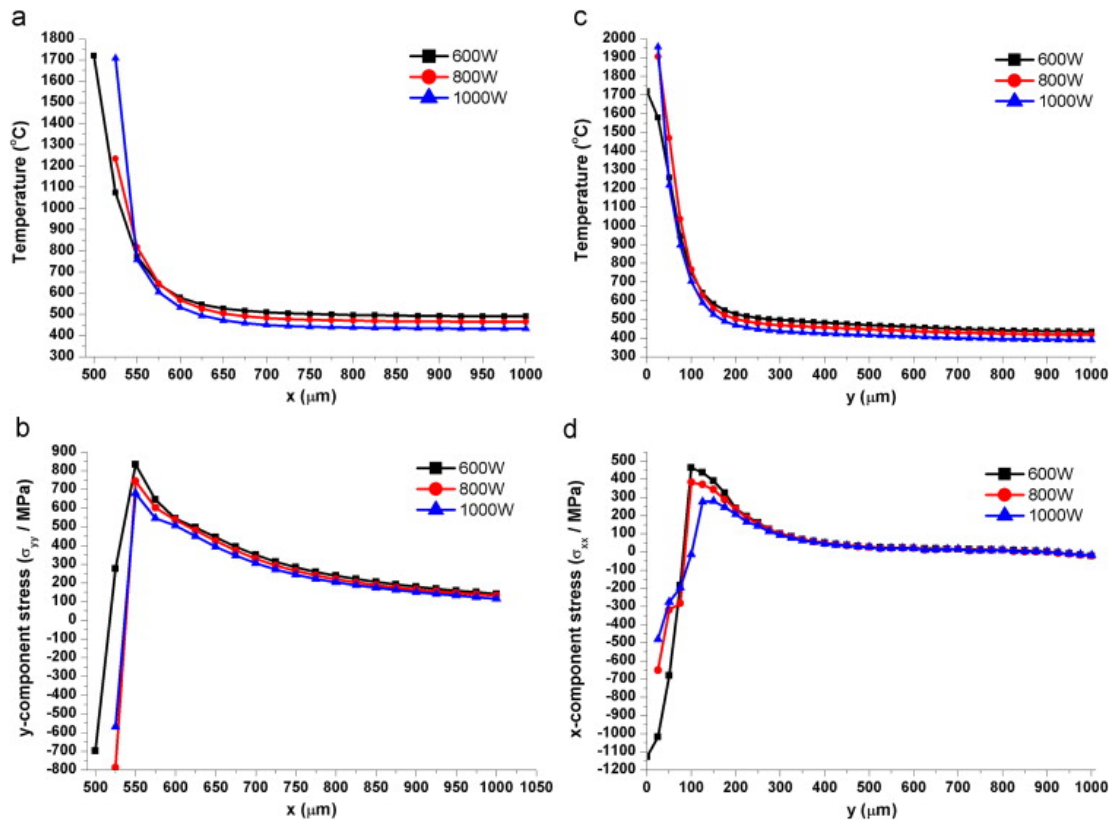


Figure 3.10 Temperature and resulting stress distributions at the cut front on the top surface of the workpiece at various laser peak powers. (a) Temperature along x-direction (T_x), (b) y-component stress along x-direction (σ_{yy}), (c) temperature along y-direction (T_y) and (d) x-component stress along y-direction (σ_{xx})

Figure 3.11 showed the cracking at cutting edge and the path deviation at trailing edge of cut path varying with the laser peak power in experiments. The high laser peak power (1000 W) generated a crack-free cutting edge and generated smaller path deviation at trailing edge, which was in agreement with the prediction in the FE model.

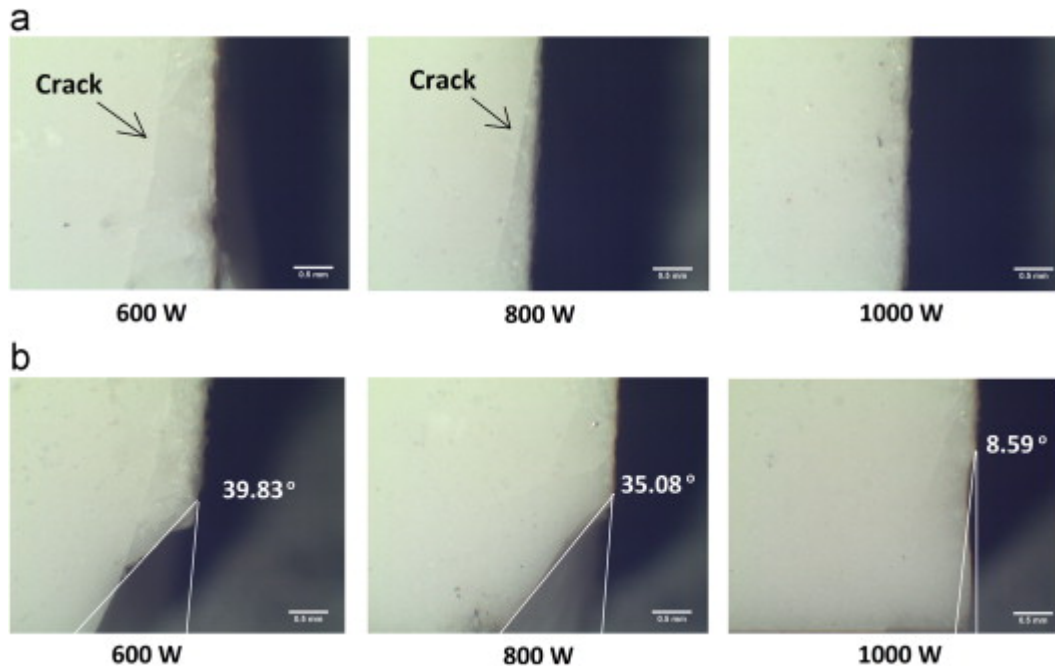


Figure 3.11 Optical photographs of the cutting edge (a) at middle point and (b) at trailing edge of cut path by various laser peak powers

3.4.3 Pulse duration effect

The effect of laser pulse duration was investigated using Case 2 in Table 3.1. The simulated temperature and the resulting thermal-stress distributions along the x - and y -directions at various pulse durations are shown in Figure 3.12. It highlights that shorter pulse durations produce a steeper temperature gradient (i.e. smaller HAZ size) for both x - and y -directions (as Figures 3.12(a) and (c)), and hence the peak tensile stresses along x - and y -directions were reduced (as Figures 3.12(b) and (d)). The basic tendency of thermal-stress was also from compressive stresses to tensile stresses. An exception appeared at 20 ms pulse duration that made the σ_{yy} greater than zero at the cut front. It illustrated that the crack was more easily produced at this pulse duration. Based on the simulated results, the short pulse duration was suitable for resisting crack formation in cutting of thick-section alumina.

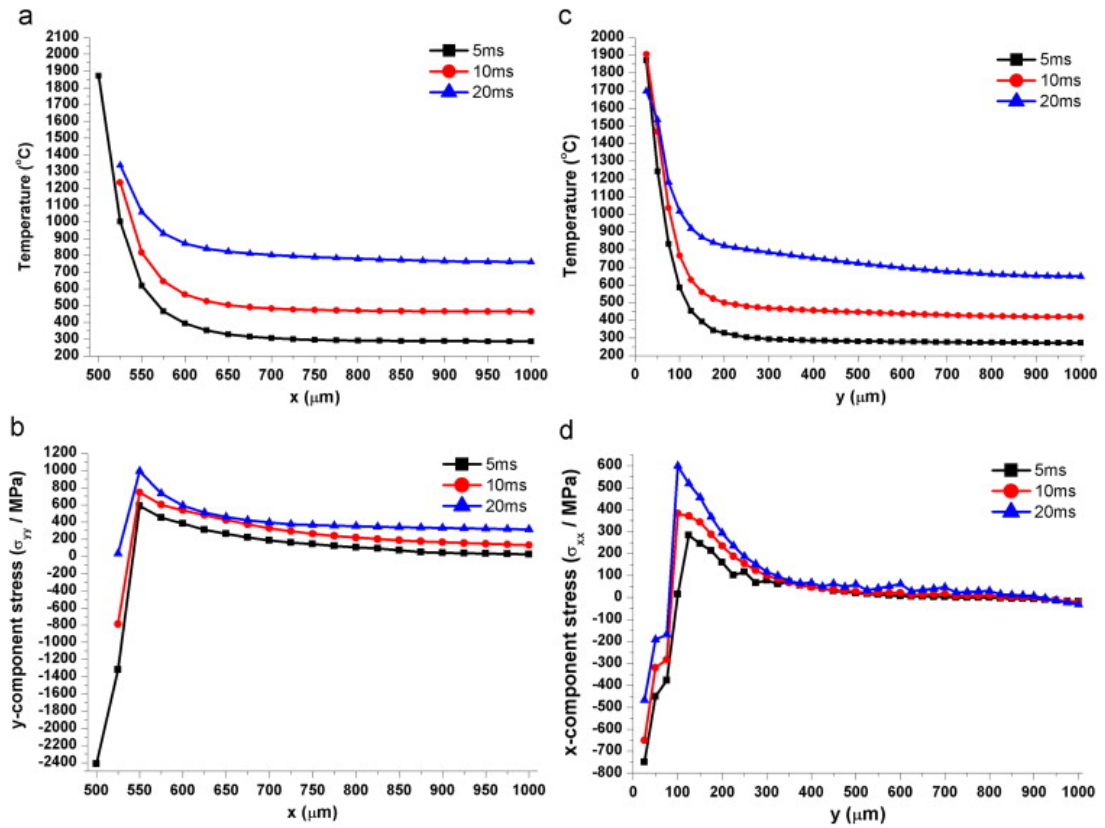


Figure 3.12 Temperature and resulting stress distributions at the cut front on the top surface of the workpiece at various pulse durations. (a) Temperature along x -direction (T_x), (b) y -component stress along x -direction (σ_{yy}), (c) temperature along y -direction (T_y) and (d) x -component stress along y -direction (σ_{xx})

Figure 3.13 shows the cracking at cutting edge and the path deviation at trailing edge of cut path varying with the pulse duration in experiments. It can be found that the short pulse duration (5 ms) generated a crack-free cutting edge and smaller path deviation at trailing edge, which was in agreement with the FE model prediction.

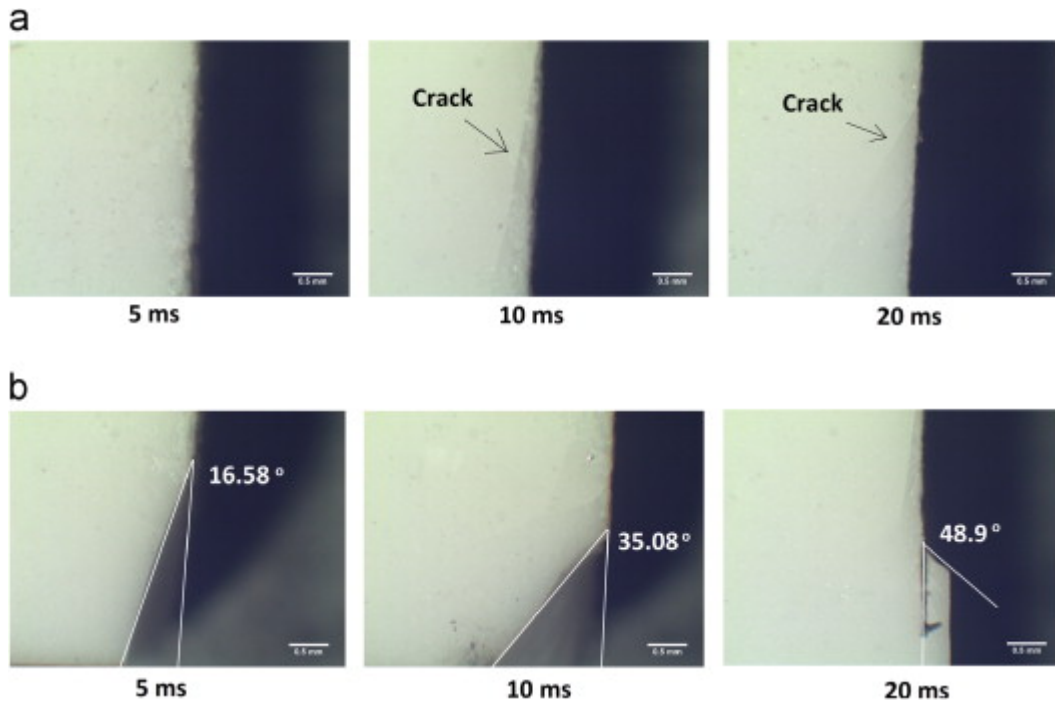


Figure 3.13 Optical photographs of the cutting edge (a) at middle point and (b) at trailing edge of cut path by various pulse durations

3.4.4 Pulse repetition rate effect

The effect of pulse repetition rate on temperature and thermal-stress distribution was studied using Case 3 in Table 3.1. The temperature and the corresponding thermal-stress distributions along the x - and y -directions at various pulse repetitions are shown in Figure 3.14. It illustrates that the lower pulse repetition rate produced a steeper temperature gradient (i.e. smaller HAZ size) for both x - and y -directions (as Figures 3.14(a) and (c)) due to the longer pulse interval for cooling, by which the peak tensile stresses along x - and y -directions were reduced (as Figures 3.14(b) and (d)). The basic tendency of thermal-stress was also from compressive to tensile except the pulse repetition rate of 50 Hz, which led to σ_{yy} and σ_{xx} becoming tensile stresses at the cut front. Therefore, cracking was more likely produced from the cut front at this pulse repetition rate. Based on the simulated results as shown in Figure 3.14, the low pulse repetition rate was desirable for resisting crack formation in laser cutting.

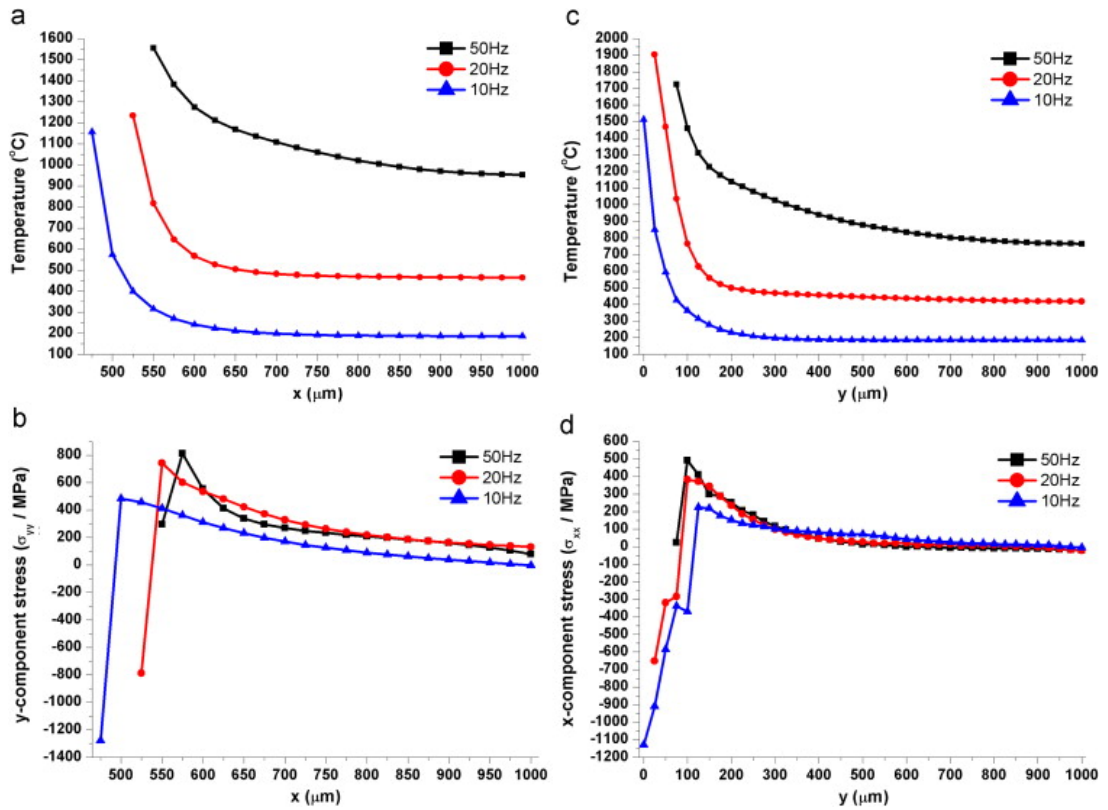


Figure 3.14 Temperature and resulting stress distributions at the cut front on the top surface of the workpiece at various pulse repetition rates. (a) Temperature along x -direction (T_x), (b) y -component stress along x -direction (σ_{yy}), (c) temperature along y -direction (T_y) and (d) x -component stress along y -direction (σ_{xx})

Figure 3.15 shows the crack formation at cutting edge and the path deviation at trailing edge of cut path varying with the pulse repetition rate. The low pulse repetition rate (10 Hz) generated a crack-free cutting edge and smaller angle deviation at trailing edge. The experimental result was in agreement with the FE simulated result.

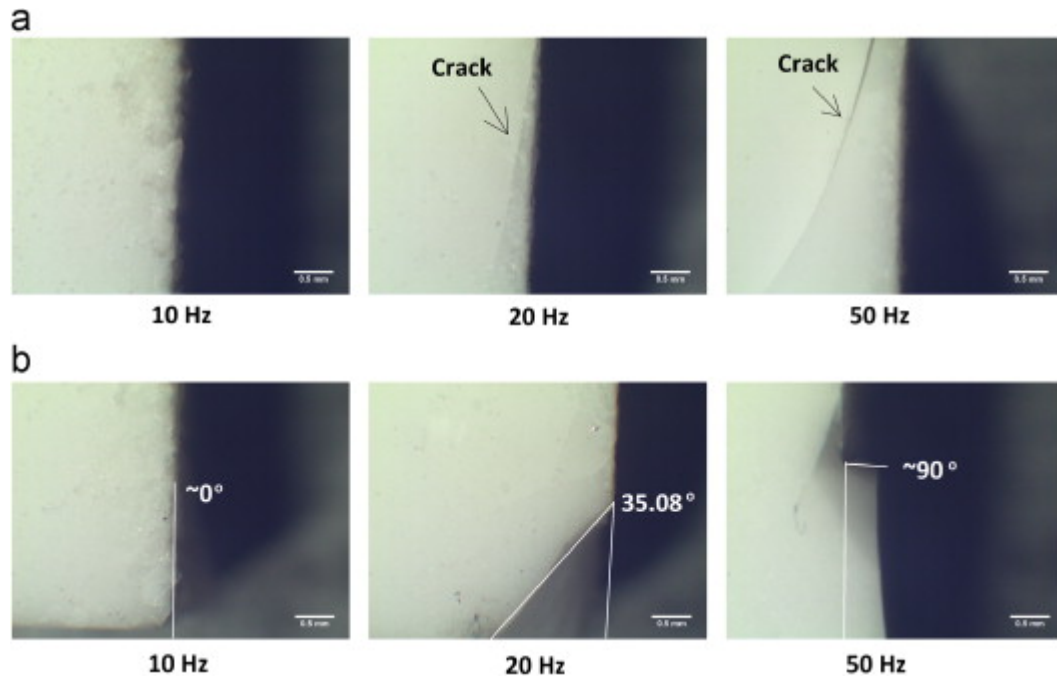


Figure 3.15 Optical photographs of the cutting edge (a) at middle point and (b) at trailing edge of cut path by various pulse repetition rates

3.4.5 Feed rate effect

The effect of feed rate was simulated and compared with experiment using the parameters as Case 4 in Table 3.1. The temperature and the corresponding thermal-stress distributions along the x - and y -directions at various feed rates are shown in Figure 3.16. It can be seen that the higher feed rate produced a steeper temperature gradient, i.e. smaller HAZ size (as Figures 3.16(a) and (c)), by which the peak tensile stresses along x - and y -directions were reduced (as Figures 3.16(b) and (d)) due to the low energy delivered into the base material per unit length. The basic tendency of thermal-stress was also from compressive to tensile except the feed rate of 0.5 mm/s, which made σ_{yy} above zero at cut front. It can be deduced that the crack was produced more easily at the cut front along x -direction by this feed rate.

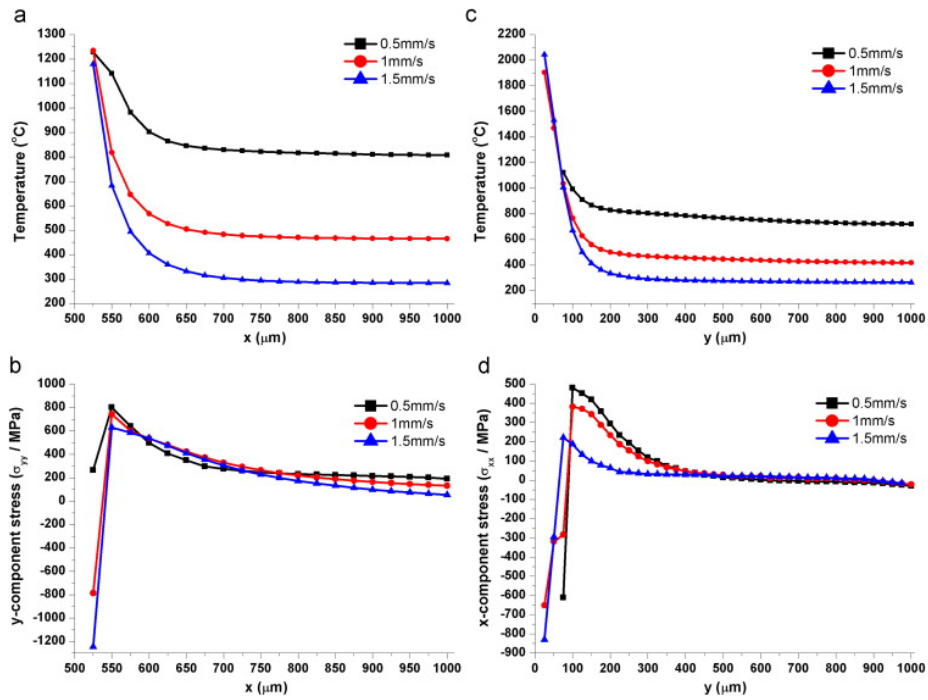


Figure 3.16 Temperature and corresponding stress distributions at the cut front on the top surface of the workpiece at various feed rates. (a) Temperature along x -direction (T_x), (b) y -component stress along x -direction (σ_{yy}), (c) temperature along y -direction (T_y) and (d) x -component stress along y -direction (σ_{xx})

Figure 3.17 shows the cracking at cutting edge and the path deviation at trailing edge of cut path varying with the feed rate. The high and the low feed rate (i.e. 0.5 mm/s and 1.5 mm/s) both generated small angle deviations (i.e. 28.25° and 24.92° , respectively). The difference between the experiment and the simulation was due to the ignored assist gas cooling effect in cut kerf during FE simulation. At low feed rate, there has a long time per unit length for assist gas cooling the workpiece and hence the size of HAZ was reduced to avoid the material strength falling at high temperature. Therefore, the low feed rate may also achieve cut quality as good as high feed rate in experimental trials, depending on the cooling effectiveness of assist gas. For thick-section workpiece, the assist gas is a significant parameter for material removal and specimen chilling. Thus in some circumstances, a low feed rate was necessary to substantially remove molten material and chill cut kerf to avoid the serious thermal damage, whereas the process efficiency was reduced at the same time.

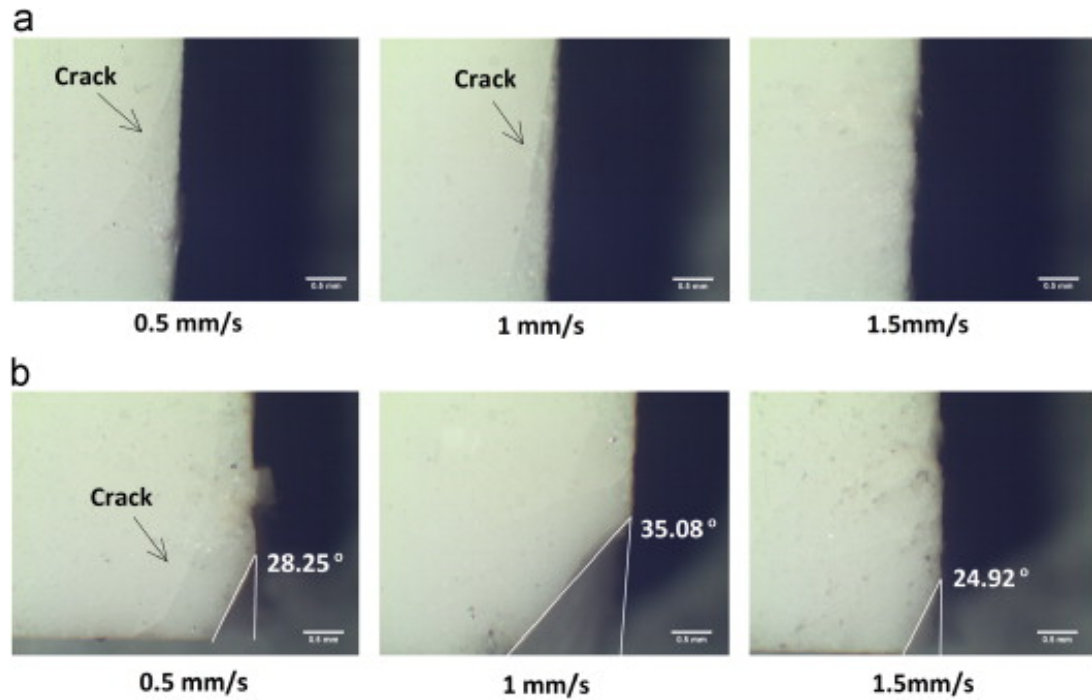


Figure 3.17 Optical photographs of the cutting edge (a) at middle point and (b) at trailing edge of cut path by various feed rates

Therefore, the feed rate should be carefully chosen to balance the cooling effectiveness of assist gas and inherent laser irradiation caused thermal damage. Based on the experimental results shown in Figure 3.17, the high feed rate (i.e. 1.5 mm/s) was recommended in this work since the cracking was formed at the cutting edge and trailing edge under the low feed rate (0.5 mm/s).

3.4.6 Optimisation of process parameters *

Based on above discussion, the process parameters for 1 kW fibre laser crack-free cutting of thick-section alumina (6-mm thickness) were reselected by the developed FE model and the corresponding experiments. The parameters are listed in Table 3.4 and the cut result is demonstrated in Figure 3.18. It is clearly seen that there is no crack at cutting edge and no significant deviation at trailing edge of the cut path. The

* The procedure for optimisation of process parameters is discussed in Appendix A

size of HAZ was $\sim 15 \mu\text{m}$ (as Figure 3.18(c)), which was much smaller than by CW laser cutting as shown in Figure 3.9(b).

Table 3.4 The optimal parameters for crack-free cutting of 6-mm-thick alumina

Power (W)	Pulse duration (ms)	Pulse repetition frequency (Hz)	Speed (mm/s)
1000	5	30	1.5

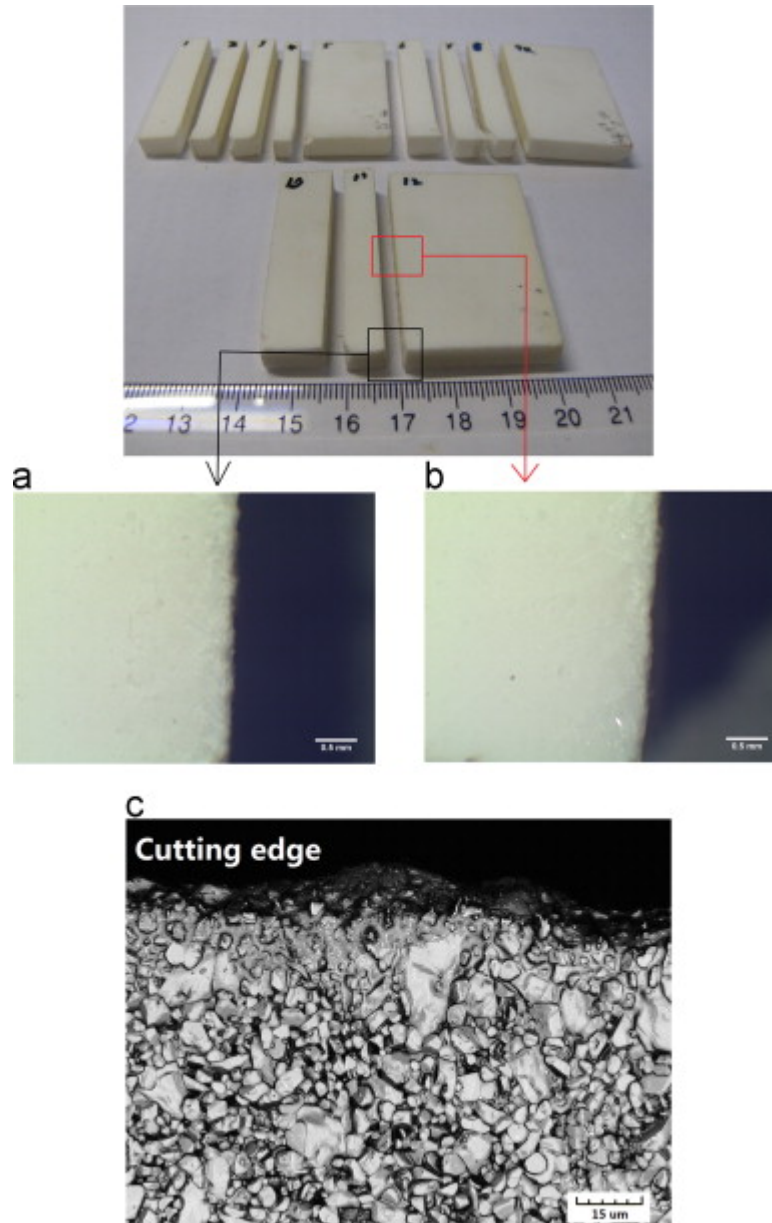


Figure 3.18 6-mm-thick alumina cut by the optimised process parameters. Optical micrographs of the cutting edge (a) at trailing edge and (b) at middle point of cut path. (c) Micro-structure of the cutting edge

3.5 Conclusions

In this chapter, fibre laser cutting of thick-section (6-mm thickness) alumina was investigated. The numerical and experimental study indicated that the single-pass crack-free cutting can be achieved using high laser peak power, short pulse duration and low pulse repetition rate, whereas the feed rate had dual effects depending on the assist gas efficiency. The work shows that due to the transitions from compressive to tensile stress at particular laser cutting parameter, it is possible to identify a threshold of process parameters for crack-free cutting. Based on the numerical and experimental results, a set of improved process parameters for crack-free cutting was proposed. For the 1 kW fibre laser used in this study, a high laser peak power (1 kW), a short pulse duration (5 ms) and a modest pulse repetition frequency (30 Hz) were reselected to achieve crack-free cutting with the feed rate up to 1.5 mm/s. The study of this work highlighted the importance of heat input control in laser crack-free cutting of brittle materials.

Chapter 4

CO₂ Laser Underwater Machining of Deep Cavities in Alumina

4.1 Introduction

In this chapter, a method for crack-free machining of deep cavities in alumina is demonstrated using a low-cost CO₂ continuous wave (CW) laser. Finite Element (FE) modelling and Smooth Particle Hydrodynamic (SPH) modelling techniques were employed in this work to understand the effect of water on crack resistance and debris removal during underwater machining. The microstructures of machined region were studied to reveal different heating and cooling processes during laser machining in water and in air. The experimental trials were also carried out to investigate the effects of machining parameters on kerf width and depth. Finally, some mm-deep polygon cavities machined underwater with the optimised process parameters were demonstrated.

4.2 Experimental Procedure

Figure 4.1 shows the experimental setup of the CO₂ laser underwater machining system, which includes a Spectron CO₂ CW laser ($M^2 < 1.2$) with a maximum laser power of 100 W, an x - y galvanometer beam scanner, a focal lens with a focal length of 300 mm and a sample container with water. The specimen is 95% alumina ceramic with a thickness of 8 mm. The major thermal and mechanical properties of the material are listed in Table 4.1. The sample was submerged in water at room temperature. The focused laser beam with selected process parameters was delivered onto the workpiece through the water layer. The focal plane position was set on the surface of the workpiece giving a spot size of 0.5 mm. A computer aided design program was used to set the scanning pattern and process parameters.

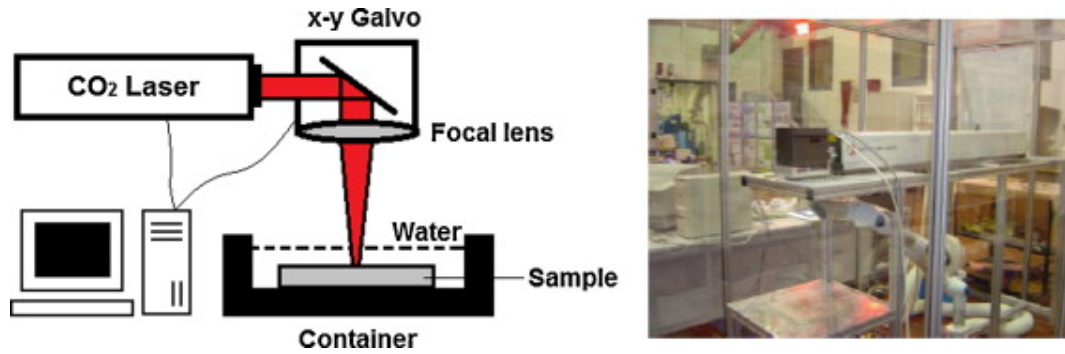


Figure 4.1 Schematic diagram of experimental setup for underwater machining of alumina. The sample was submerged into the water at room temperature

Table 4.1 Material properties of 95% alumina used in the work [12]

Properties	Values
Mass density (kg/m ³)	3720
Specific heat (J/kg×K, to 1773K)	880
Thermal conductivity (W/m×K, to 1573 K)	$1044.6 + 1742 \times 10^{-4} \times T - 2796 \times 10^4 \times T^{-2}$
Elastic module (GPa)	35
Poisson's ratio	$5.5 + 34.5e^{[-0.0033 \times (T-273)]}$
Secant coefficient of thermal expansion (10 ⁻⁶ 1/K)	300
Melting point (°C)	0.21
Vaporisation point (°C)	8.2
Tensile strength (MPa)	2050
Compressive strength (MPa)	2980
	220
	2600

In this work, the effects of water layer thickness and scanning pass number were investigated to understand the mechanism of underwater machining. Based on the initial experiments, it was found that a 2 mm stationary water layer was necessary to wet the alumina surface during machining. Laser machining in air was also performed as a reference sample for comparison. Two machining modes were used in this work. The 30 mm straight lines by multi-pass scanning were performed (as Figure 4.2(a)) to study the machining depth and width at different water layer thicknesses and pass numbers. Figure 4.2(b) shows the mode of laser milling of cavity in alumina to investigate the effect of water on machining quality including recast layers and cracks. The scanning interval between machining lines was set as

0.25 mm, which is equal to the radius of laser focused spot. Optical microscopy (Polyvar) was employed to examine the surface morphology after laser machining and to measure the machined kerf width and depth for the quantitative study. Scanning electron microscopy (SEM, Hitachi S-3400) was used to capture the microstructure of laser machined region. The roughness of machined surface was measured by a Wyko NT1100 white light interferometer. The size distribution of the particles suspended in water during machining was measured by confocal laser scanning microscopy (Olympus OLS-3100) after the suspension was dispersed and dried on a glass substrate.

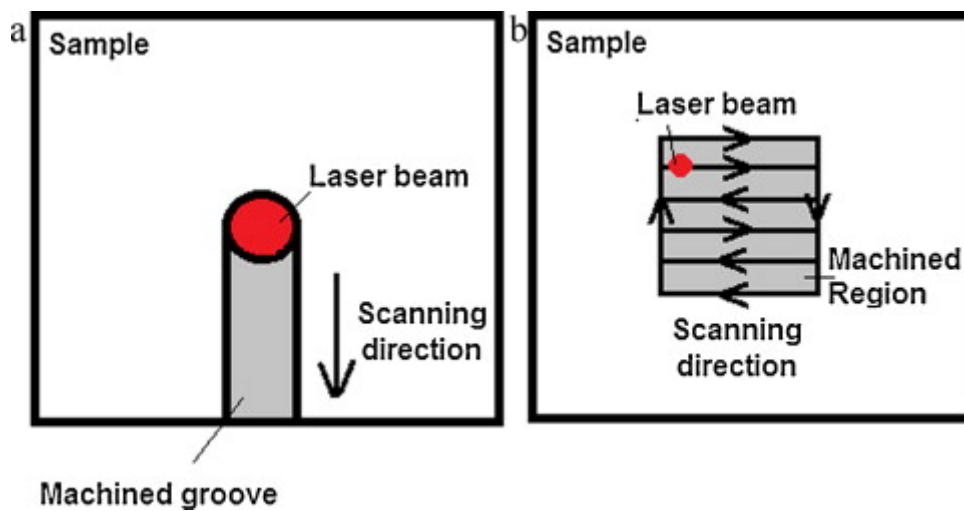


Figure 4.2 Machining modes employed in this work. (a) Straight line grooves by multi-pass scanning and (b) laser milling of rectangular cavities

4.3 Modelling Approaches

In order to understand the effect of water cooling on the thermal behaviour in the machining process, a 3D finite element model was developed to simulate the temperature field and resulting stress characteristics during laser machining in air and in water. ANSYS software was employed to solve this transient problem. For the FE transient thermal analysis, it was assumed that the differences between the thermal behaviours for laser machining in air and in water were predominantly governed by the different heat convection coefficients. The heat convection coefficient of water (500–10,000 W/m²•K) is 2–3 orders higher than that of air (10–

100 W/m²•K) [160]. In this work, the heat convection coefficient of water was set as 1000 W/m²•K, whereas the heat convection coefficient of air was set as 100 W/m²•K. The heat convection was applied on all the surfaces of the model as a boundary condition. The convection heat loss follows [176]:

$$k(T) \frac{\partial T}{\partial n'} = -h(T - T_0) \quad (4-1)$$

where T_0 and h denote the room temperature and heat convection coefficient, respectively, and n' is the normal vector point outward from the surface. The ambient temperatures for air and water were both taken as 27°C.

The CO₂ laser beam was assumed to have a TEM₀₀ mode and the material phase changes during machining were ignored. The FE transient thermal analysis was performed using the same process parameters as in the experiment. The surface heat flux distribution, $I(x, y)$, applied on the surface of workpiece was expressed as

$$I(x, y) = \frac{P_0}{\pi r_0^2} \times e^{-\left(\frac{x^2 + y^2}{r_0^2}\right)} \quad (4-2)$$

where r_0 is the radius of laser spot at focal plane position which was set as 0.5 mm, and P_0 is the laser power arriving at the workpiece surface. Although the 10.6 μm wavelength laser has a static absorption coefficient of about 500 cm⁻¹ in water [177], Beer-Lambert's law was not used to calculate the value of transmitted laser intensity on workpiece underwater due to complex photo thermal interactions of the laser, water and the workpiece during machining [160]. In the FE model, P_0 was assumed as the laser output power. Considering the translational laser beam with a velocity, v , along the $x+$ direction, Eq. (4-2) is rewritten as

$$I(x, y, t) = \frac{P_0}{\pi r_0^2} \times e^{-\left(\frac{(x-vt)^2 + y^2}{r_0^2}\right)} \quad (4-3)$$

The governing equation for the simulation of temperature fields has been established by the following heat diffusion equation [1]:

$$\begin{cases} K(T) \left(\frac{\partial^2 T(x, y, z, t)}{\partial x^2} + \frac{\partial^2 T(x, y, z, t)}{\partial y^2} + \frac{\partial^2 T(x, y, z, t)}{\partial z^2} \right) = \rho C(T) \frac{\partial T(x, y, z, t)}{\partial t} \\ -K(T) \left(\frac{\partial T(x, y, 0, t)}{\partial x} + \frac{\partial T(x, y, 0, t)}{\partial y} + \frac{\partial T(x, y, 0, t)}{\partial z} \right) = I(x, y, t) \end{cases} \quad (4-4)$$

where $k(T)$ is the temperature-dependent thermal conductivity, ρ is the material's mass density and $c(T)$ is the temperature-dependent specific heat as listed in Table 4.1. The initial condition for the model was assumed to be an uniform temperature within the bulk material given as $T(x, y, z, 0) = T_0$, where T_0 is the room temperature, 27°C.

Based on the temperature field calculated by the FE transient thermal analysis, thermal-stress simulation was performed. In the thermal-stress simulation, the FE model with element SOLID70 for thermal analysis was transformed into the SOLID185 that was used for structural analysis. The boundaries for structural analysis were assumed to be traction-free for all surfaces. However, the elements with the temperature above the melting point, i.e. 2050°C were eliminated before structural analysis in order to simulate the melt pool size and obtain the accurate stress simulation. The thermal-stress was generally considered as the main reason of crack generation and propagation during laser machining of brittle material [172]. For the brittle material, it was assumed that the main mechanism causing crack formation followed the 1st strength theory, i.e. the tensile stress larger than the tensile strength [174]. Therefore, the 1st strength theory was selected in this work as the fracture criterion.

A SPH model was also developed in this work to study the hydrodynamic behaviour of interactions between water and molten material during underwater machining. Using the SPH method, the computational domain was divided into a set of discrete particles. These particles have a spatial distance, known as the smoothing length, over which their properties are smoothed by a kernel function. Different from the standard FE methods, SPH approximates physical quantities of each particle using the kernel function. The most attractive nature of SPH method is that it eliminates the need of computation termination due to the possible large element distortion inherent in Lagrangian formulation based FE methods [178]. Therefore, it is more suitable to simulating the fluid dynamics than the standard FE method.

The fluid in the SPH model was divided, and the properties of element were associated with its centre, which was then interpreted as a particle. A particle i has a mass m_i , position r_i , density ρ_i and velocity v_i . In SPH, the interpolated value of any

field, A , at position \bar{r} is approximated by [179]:

$$A(\bar{r}) = \sum_i m_i \frac{A_i}{\rho_i} W(\bar{r} - \bar{r}_i, h') \quad (4-5)$$

where W is an interpolating kernel function, h' is the interpolation length and the value of A at \bar{r}_i is denoted by A_i . The sum is over all particles, i with a radius $2h'$ of \bar{r}_i . $W(\bar{r}, h')$ is a spline based interpolation kernel function of radius $2h'$, which is a C^2 function that approximates the shape of a Gaussian function and has a compact support. This allows smoothed approximations to the physical properties of the fluid to be calculated from the particle information. Thus, the particle approximation for each particle j can be approximated by summing the contributions of neighbouring particles i as follows:

$$A(\bar{r}_j) = \sum_i m_i \frac{A_i}{\rho_i} W(\bar{r}_j - \bar{r}_i, h') \quad (4-6)$$

The final discrete forms of governing equations (i.e. mass, momentum, and energy conservation equations) can be expressed as follows [180]:

$$\begin{cases} \frac{d\rho_j}{dt'} = \rho_j \sum_i \frac{m_i}{\rho_i} (v_i^\alpha - v_j^\alpha) \frac{\partial W(x_j - x_i, h')}{\partial x_j^\alpha} \\ \frac{dv_j^\alpha}{dt'} = - \sum_i m_i \left(\frac{\sigma_j^{\alpha\beta}}{\rho_j^2} + \frac{\sigma_i^{\alpha\beta}}{\rho_i^2} \right) \frac{\partial W(x_j - x_i, h')}{\partial x_j^\beta} \\ \frac{dE_j}{dt'} = - \frac{\sigma_j^{\alpha\beta}}{\rho_j^2} \sum_i m_i (v_j^\alpha - v_i^\alpha) \frac{\partial W(x_j - x_i, h')}{\partial x_j^\beta} \end{cases} \quad (4-7)$$

where t' donates the time, x is the spatial coordinate, v^α is the velocity component, $\sigma^{\alpha\beta}$ is the stress tensor component, E is the specific internal energy, and the subscripts α ($\alpha = 1, 2, 3$) and β ($\beta = 1, 2, 3$) are the component indices. Simulation solutions were obtained by solving Eq. (4-7) in conjunction with equations of state, material models and initial and boundary conditions. This problem was solved by commercially available explicit CFD software AUTODYN (issued by ANSYS Inc.).

4.4 Results and Discussion

4.4.1 Effect of water cooling

Based on initial experimental trials, it was found at a laser power of 60 W and scanning speed of 10 mm/s, high quality machining of alumina ceramic can be realised, in which the thermal damage and recast layer were reduced to a low level and the machining rate was relatively high compared with other parameters. Figure 4.3(a) shows the top-view of CO₂ laser machined alumina cavity in air at a power of 60 W, a speed of 10 mm/s and 4 scanning cycles with a dimension of 5 mm × 5 mm. It was found that fracture appeared frequently during machining in air below 10 scanning cycles due to the high thermal-stress caused by the great amount of accumulated heating energy [181]. The discoloured recast layer on the bottom surface indicated the high temperature (>3500 °C) during laser machining in air resulting in the generation of many sub-oxides of aluminium [1]. The micrograph of the recast layer on the bottom surface is shown in Figure 4.3(b). It can be found that micro-cracks appeared in the recast layer and formed a fine crack network, which indicates serious thermal damage.

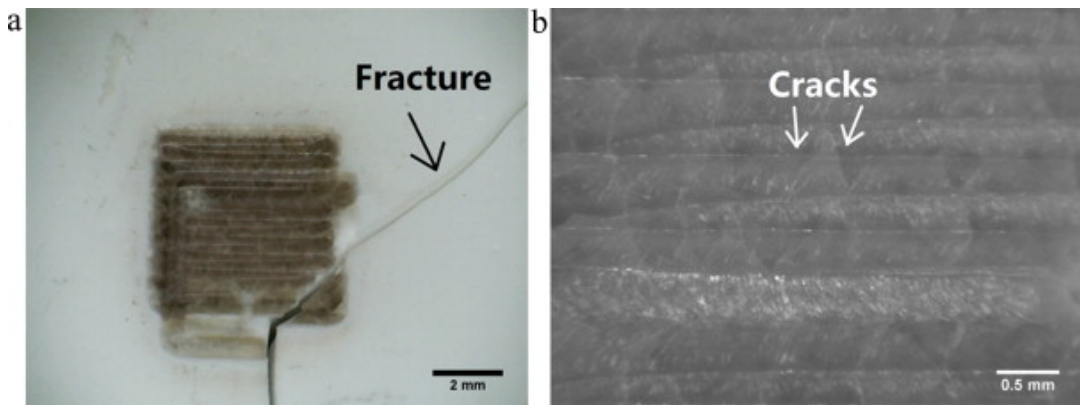


Figure 4.3 The optical micrographs of the alumina cavity machined in air at a laser power of 60 W and a speed of 10 mm/s with drawn dimension of 5 mm × 5 mm, in terms of (a) top view of the cavity and (b) a close-up view of the recast layer on the bottom surface. The fracture appeared at the 4th scanning cycle.

Figure 4.4 shows the cross-section SEM micrographs of the machined cavity in air. It can be found that the recast layer on the bottom of the cavity was significant and a crack propagated into the base material (as Figure 4.4(a)), which could lead to fracture in the workpiece as the side surface indication. Figure 4.4(b) shows the microstructure of recast layer. The alumina grains in the recast layer re-grew to be columnar along the direction of the incident laser, in which the crack propagated along the grain boundary. Figure 4.4(c) shows a smooth recast layer surface on the bottom of the cavity, where the micro-cracks appeared due to the serious thermal damage as the micrograph captured by optical microscopy (as Figure 4.3(b)).

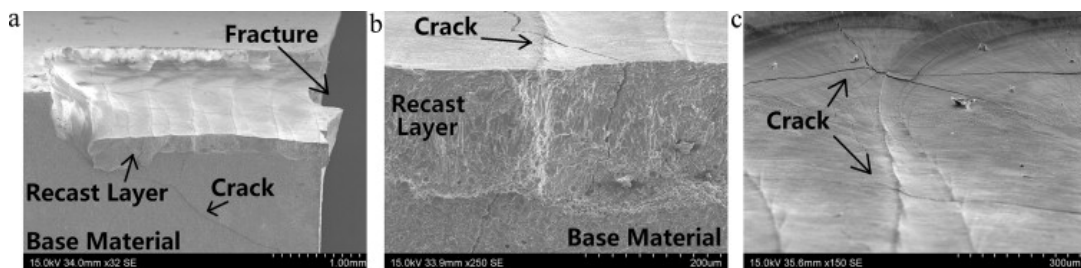


Figure 4.4 The SEM micrographs of the alumina cavity machined in air. (a) An cross-section overview of the cavity, (b) a cross-section close-up view of the recast layer on the bottom of the cavity and (c) a close-up view of the recast layer surface on the bottom of the cavity

The CO₂ laser underwater machined alumina cavity using the same process parameters is shown in Figure 4.5. The thickness of the water layer is about 4 mm above the top surface of workpiece and 50 scanning cycles were applied for the 1-mm deep cavity. Fracture and cracks were suppressed in the underwater machining as shown in Figure 4.5, which demonstrates that the water cooling was beneficial in preventing thermal damage.

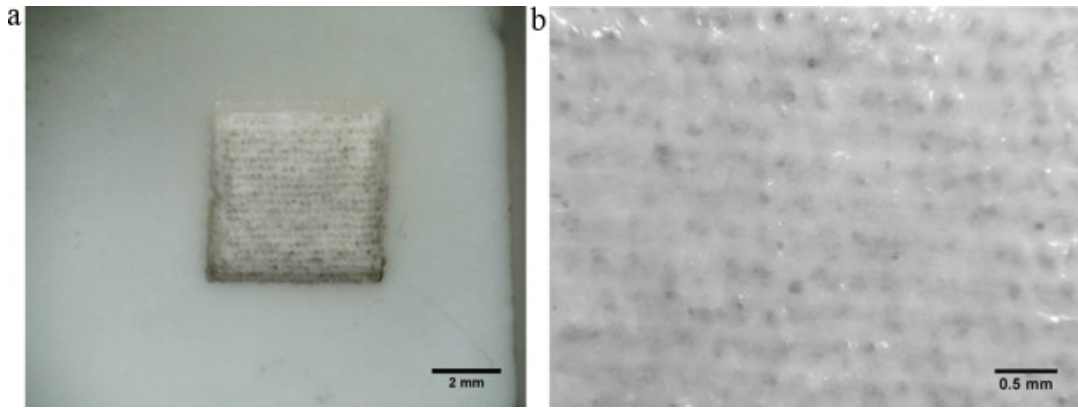


Figure 4.5 The optical micrographs of the alumina cavity machined under water at a power of 60 W, a speed of 10 mm/s and 50 scanning cycles with drawn dimension of 5 mm × 5 mm. (a) Top view of the cavity and (b) a close-up view of the recast layer on the bottom surface. The thickness of water layer is about 4 mm during machining.

Figure 4.6 shows the cross-section SEM micrographs of the machined cavity. It can be found that the recast layer was insignificant and the side wall surface was smooth in underwater machining as shown in Figure 4.6(a). Figure 4.6(b) shows the microstructure of recast layer, in which the alumina grains had no significant change but a porous structure was formed. The porous structure could reduce the strength of the recast layer to the base material, by which the recast layer could be easily removed via mechanical post-processing. Figure 4.6(c) shows the recast layer surface on the bottom of the cavity, where micro-cracks were suppressed but the roughness was increased due to the obvious voids. The difference in the microstructures of recast layer formed by machining in air and in water indicates that the water has a significant effect on chilling of the machined region.

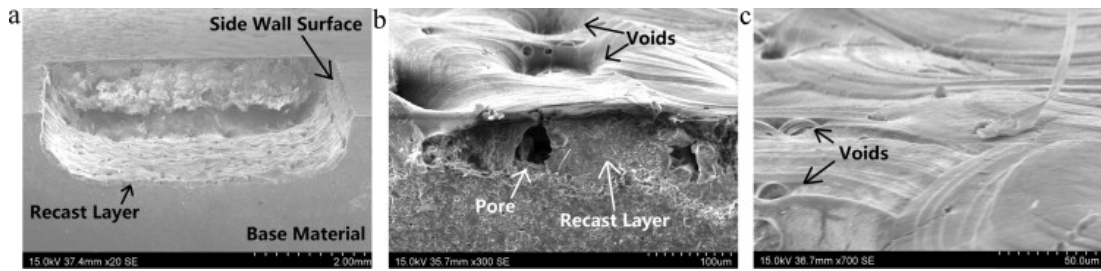


Figure 4.6 The SEM micrographs of the alumina cavity machined under water. (a) An cross-section overview of the cavity, (b) a cross-section close-up view of the recast layer on the bottom of the cavity and (c) a close-up view of the recast layer surface on the bottom of the cavity

In order to understand the difference in thermal behaviour during laser machining in air and in water, an FE thermal and structural analysis was performed. Figure 4.7 shows the difference of temperature and thermal-stress distributions between laser machining in air and in water. It reveals that, with the same process parameters, underwater machining produced a lower maximum temperature and smaller HAZ than machining in air (as Figures 4.7(a) and (b)) and hence the maximum thermal-stress was reduced in underwater machining (as Figures 4.7(c) and (d)), which was in agreement with previous studies using analytical solutions [160, 161]. In order to further investigate the thermal behaviour in different ambient conditions, the FE simulated temperature and thermal-stress distribution along the machining path across the melt pool was plotted as shown in Figure 4.8. It can be found that the melt pool in water was smaller than that in air. The low maximum temperature and steep temperature gradient in water produced a smaller HAZ compared with that in air. Figure 4.8(b) highlights the lower compressive and tensile stress peaks in underwater machining. During machining in air, the two tensile stress peaks near the melt pool are greater than those in water, which implies that cracking in air machining could be more easily initiated than that in underwater machining due to higher heat energy diffused into the base material. The tensile stress in front of the melt pool could induce the crack formation and propagation into the base material causing the fracture as shown in Figure 4.3(a), whereas the tensile stress behind the melt pool induces cracking in recast layer during molten material resolidification (as Figure

4.3(b)). Obviously, the two tensile stress peaks were suppressed in underwater machining (as Figure 4.8(b)).

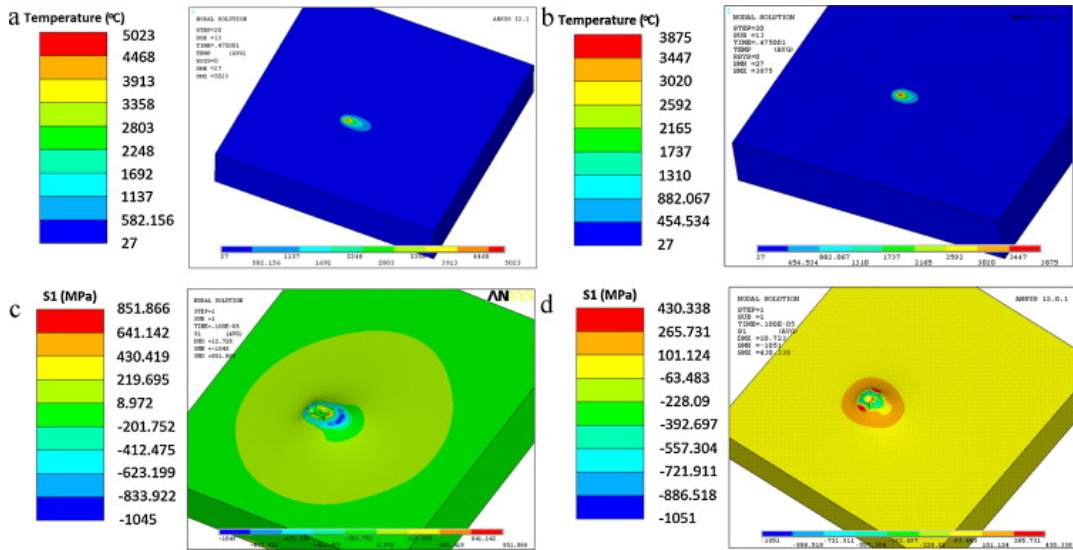


Figure 4.7 Temperature fields and resulting stress distributions during laser machining in different ambient conditions. (a) Temperature field during laser machining in air, (b) temperature field during laser underwater machining, (c) thermal–stress distribution during laser machining in air, and (d) thermal–stress distribution in laser underwater machining

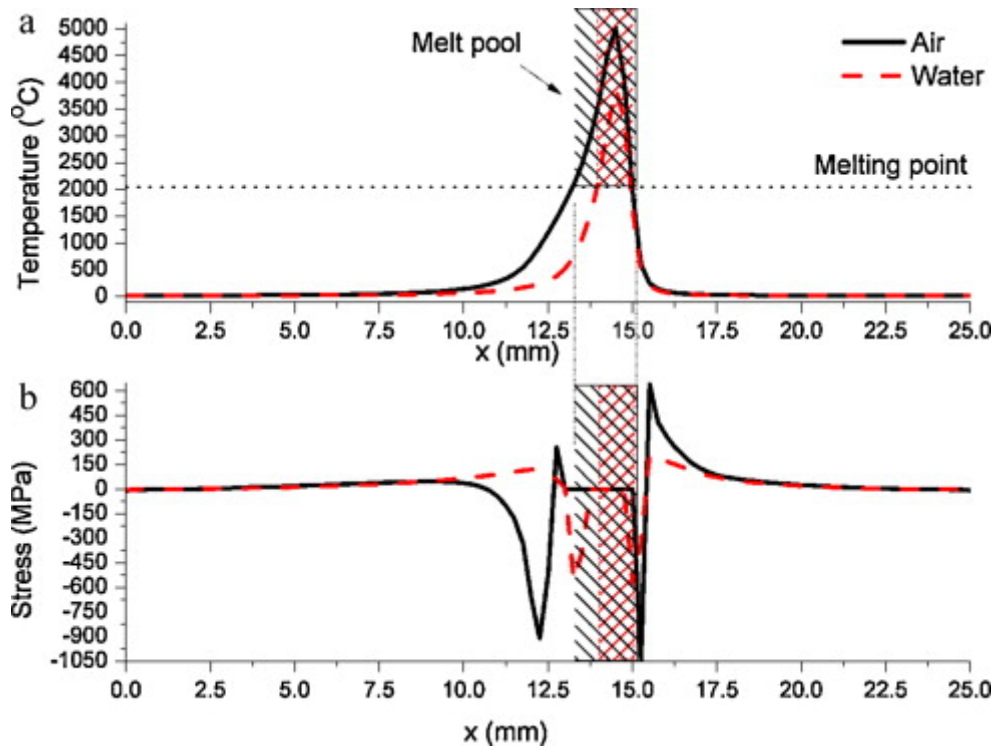


Figure 4.8 (a) Temperature fields and (b) 1st principle stress distributions along machining path during laser machining of alumina in air and in water

4.4.2 Effect of fluid dynamics

Figure 4.9 shows an empirical schematic diagram of interaction between the CO₂ laser beam, water, and the alumina substrate during underwater machining. When the laser was delivered onto the water surface, a portion of the laser energy was absorbed by water, in which a rapid heating and vaporisation process was induced due to the high absorption of the water with respect to the 10.6 μm wavelength CO₂ laser [162]. During this process, many bubbles are generated and a keyhole in water was formed as a channel for the other portion of energy penetrating [182]. The energy delivered onto the surface of alumina was absorbed to melt and/or vaporise the workpiece surface. Then, the molten material was ejected from the machining region into the water by the inherent recoil pressure induced in the keyhole of the workpiece, as well as the water vapour pressure. Finally, the ejected molten particles were removed by the water flow (as shown in Figure 4.9).

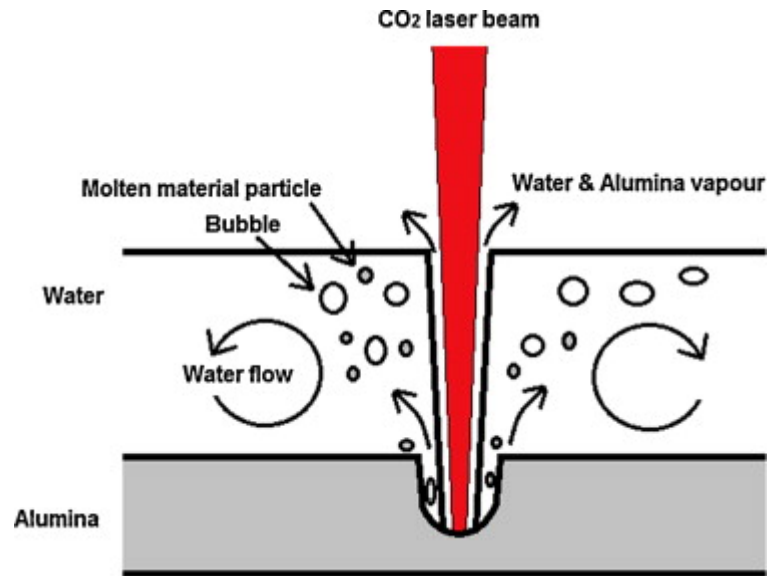


Figure 4.9 Schematic diagram of interaction between the CO₂ laser beam, water, and alumina substrate

Figure 4.10 shows the photographic images of the interaction between laser beam and still water in the experiments. Figure 4.10(a) shows the water wave caused by the water evaporation. It is important for molten particles removal from the machining region. Figure 4.10(b) shows the bubble formation during laser vaporising of water. The mean diameter of these bubbles is about 0.9 mm.

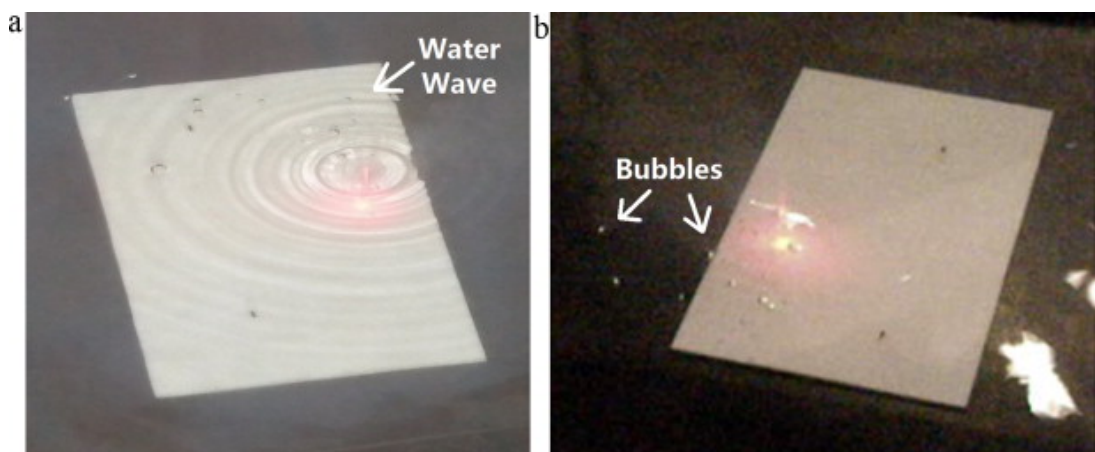


Figure 4.10 Capture of (a) water wave and (b) bubble formation during the interaction between CO₂ laser beam and water

During underwater machining, the velocity of the ejected particles is much lower than that in air due to the presence of viscous fluid, which would prevent debris deposition. Therefore the debris suspends in the water with a relatively long time. The size distribution of the particles generated in laser underwater machining is shown as Figure 4.11, in which the measured particle number is up to 1000 shown in the inserted micrograph. The mean diameter of these particles is 220 nm. The histogram shows that the number of the particles with the diameter up to 500 nm is more than 50% of the total measured particle number. It indicates that the major size distribution of the particles generated in CO₂ laser underwater machining was in sub-microns.

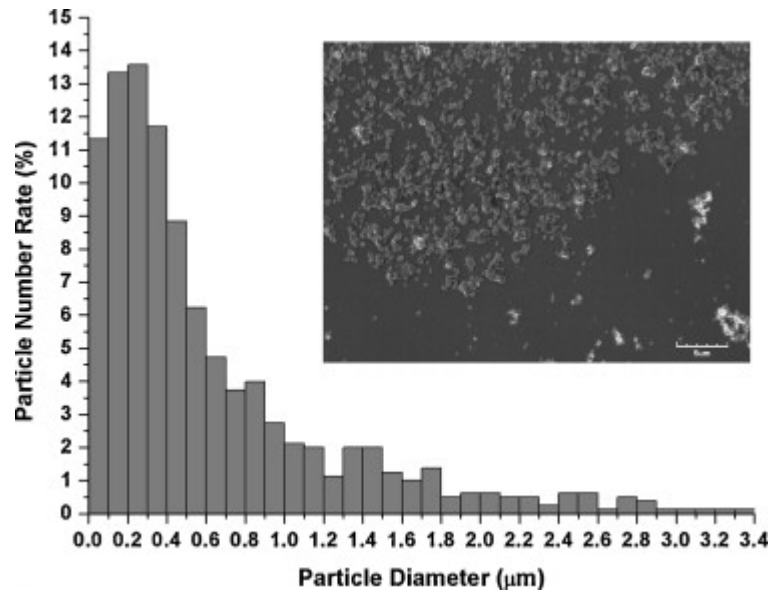


Figure 4.11 Histogram of the size distribution of the particles generated in laser underwater machining

The high recoil pressure caused by water evaporation would also benefit to prevent the recast and dross formation. Figure 4.12 shows the side wall surface of machined groove in air and in water, respectively. Dross was evident on the side wall surface and a significant recast layer was on the bottom of machined groove after machining in air. However, these defects were eliminated in underwater machining (as Figure 4.12(b)), in which the side wall surface was smooth and the recast layer on the bottom of groove was insignificant.

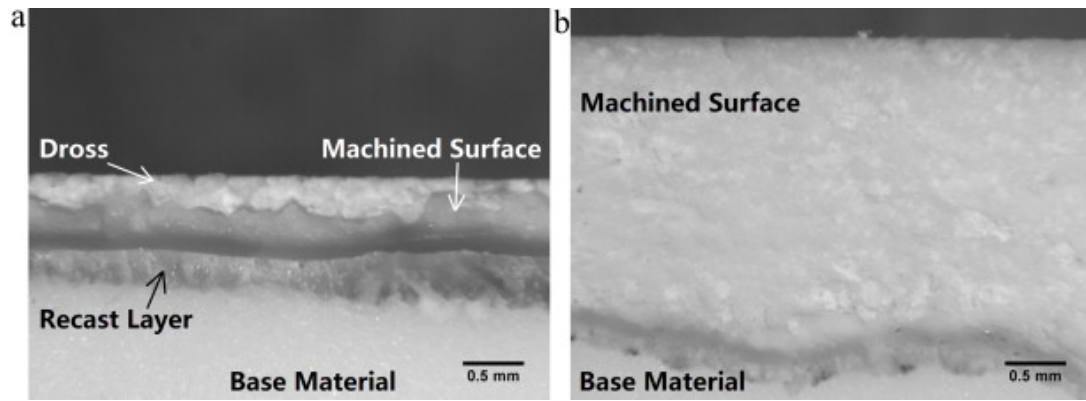


Figure 4.12 Side wall surface of the groove machined (a) in air and (b) in water

Figure 4.13 further shows the microstructure of the side wall surface and the bottom of the machined groove in air and in water, respectively. The grains in dross were mainly glassy phases as shown in Figure 4.13(a), which indicated that the molten material was resolidified on the side wall surface during laser machining in air. During machining in water, the grains on side wall surface were almost same as the base material and a few of grains were melted (as shown in Figure 4.13(b)). This is due to the high recoil pressure produced in water to prevent the molten material resolidification on the side wall surface. Figures 4.13(c) and (d) show the microstructure of recast layer on the bottom of the groove machined in air and in water, respectively. The results were similar as those of machined cavity shown in Figures 4.4 and 4.6, i.e. the significant recast layer with columnar grains formed during machining in air and the porous structure produced in recast layer during underwater machining.

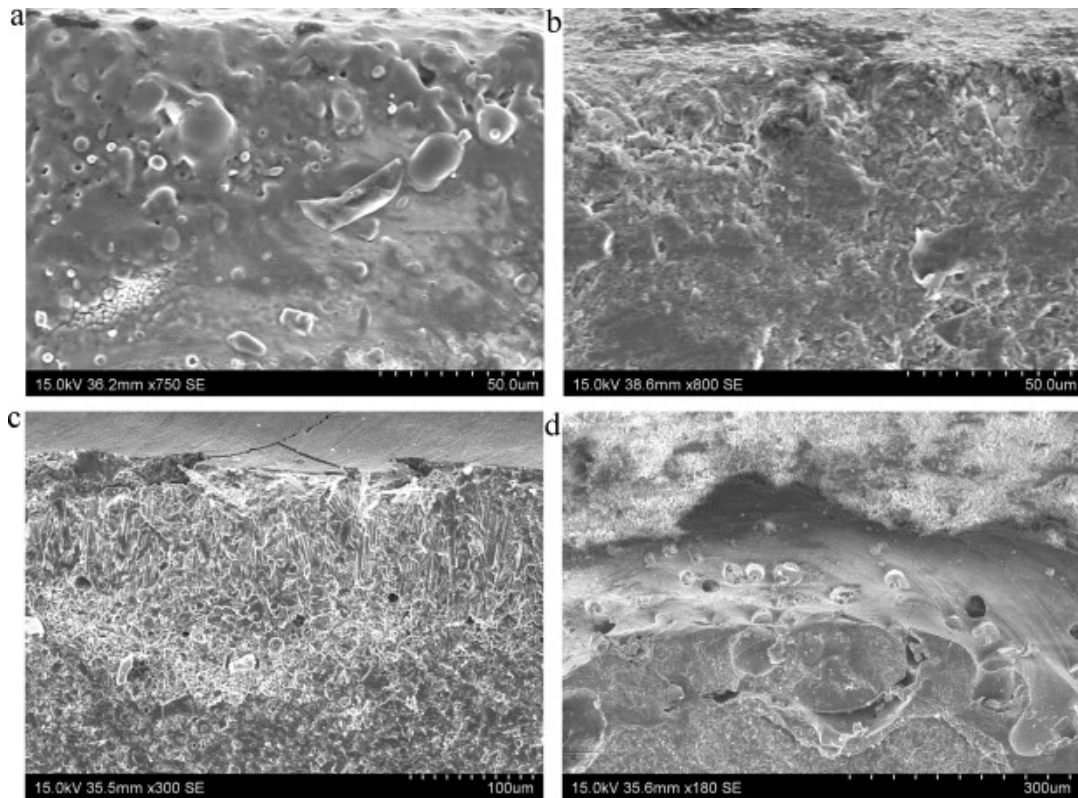


Figure 4.13 Microstructure of dross on the side wall surface of the groove machined (a) in air and (b) in water and cross-section microstructure of recast layer on the bottom of the groove machined (c) in air and (d) in water

Figure 4.14 shows the roughness of the side wall surfaces machined in air and in water. The arithmetical mean roughness (R_a) of the side wall surface machined in air ($R_a = 13.16 \mu\text{m}$) is approximately 1.5 times higher than that of the side wall surface machined in water ($R_a = 5.12 \mu\text{m}$). The average maximum height of the profile (R_z) of the side wall surface machined in air ($R_z = 43.68 \mu\text{m}$) is about double that of the side wall surface machined in water ($R_z = 23.02 \mu\text{m}$). This is due to the dross adhered onto the side wall surface during machining in air. The dross increased the surface roughness as the bulge appeared in roughness plot (as Figure 4.14(a)). The measured surface roughness validated that the underwater machining can prevent dross adhesion and process a smoother side wall surface than that machined in air.

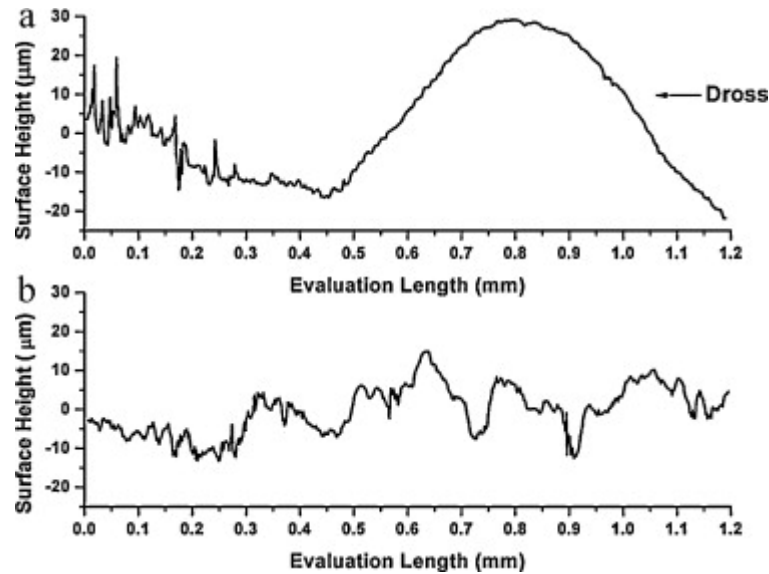


Figure 4.14 Roughness plot of the side wall surface of the groove machined (a) in air ($R_a = 13.16 \mu\text{m}$, $R_z = 43.68 \mu\text{m}$) and (b) in water ($R_a = 5.12 \mu\text{m}$, $R_z = 23.02 \mu\text{m}$)

Figure 4.15 shows the cross-section of the groove machined in air and in water. The crack and fracture appeared after few passes during machining in air (as Figure 4.15(a)). However, the groove machined in water had relatively high quality (as Figure 4.15(b)), demonstrating a high aspect ratio and free of cracks.

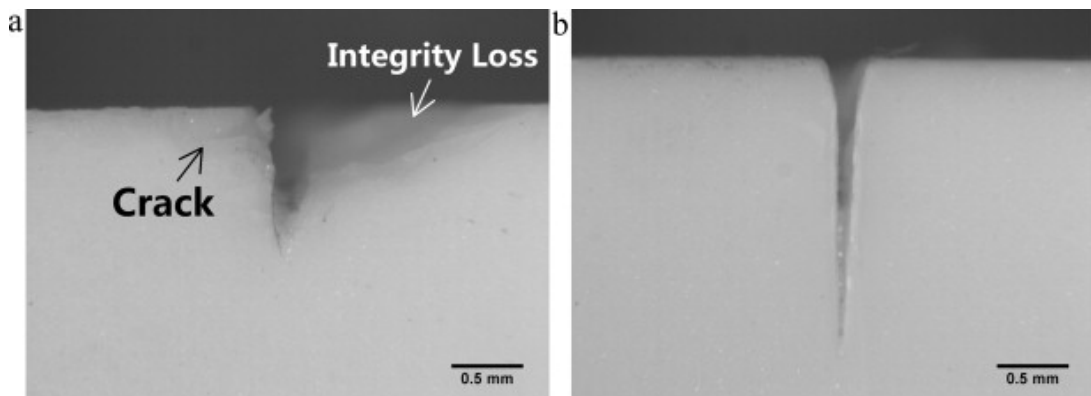


Figure 4.15 Cross-section of the groove machined (a) in air at a power of 60 W and a scanning speed of 10 mm/s for 4 passes and (b) under water at a power of 60 W and a scanning speed of 10 mm/s for 80 passes

In order to further understand the empirical hypothesis of the effect of fluid dynamics (as shown in Figure 4.9), a 2D fluidic transient smooth particle hydrodynamic (SPH) model was developed. Figure 4.16(a) is the setup of the SPH model. The model was simplified to only consider the process of melt ejection rather than the energy absorption and phase transition due to the complicated processes of laser machining and the limitation of the software. It was assumed that the melt pool was formed for the developed model and the molten material was ejected by the recoil pressure in the melt pool. The initial velocity of the melt ejection was set as 20 m/s [183].

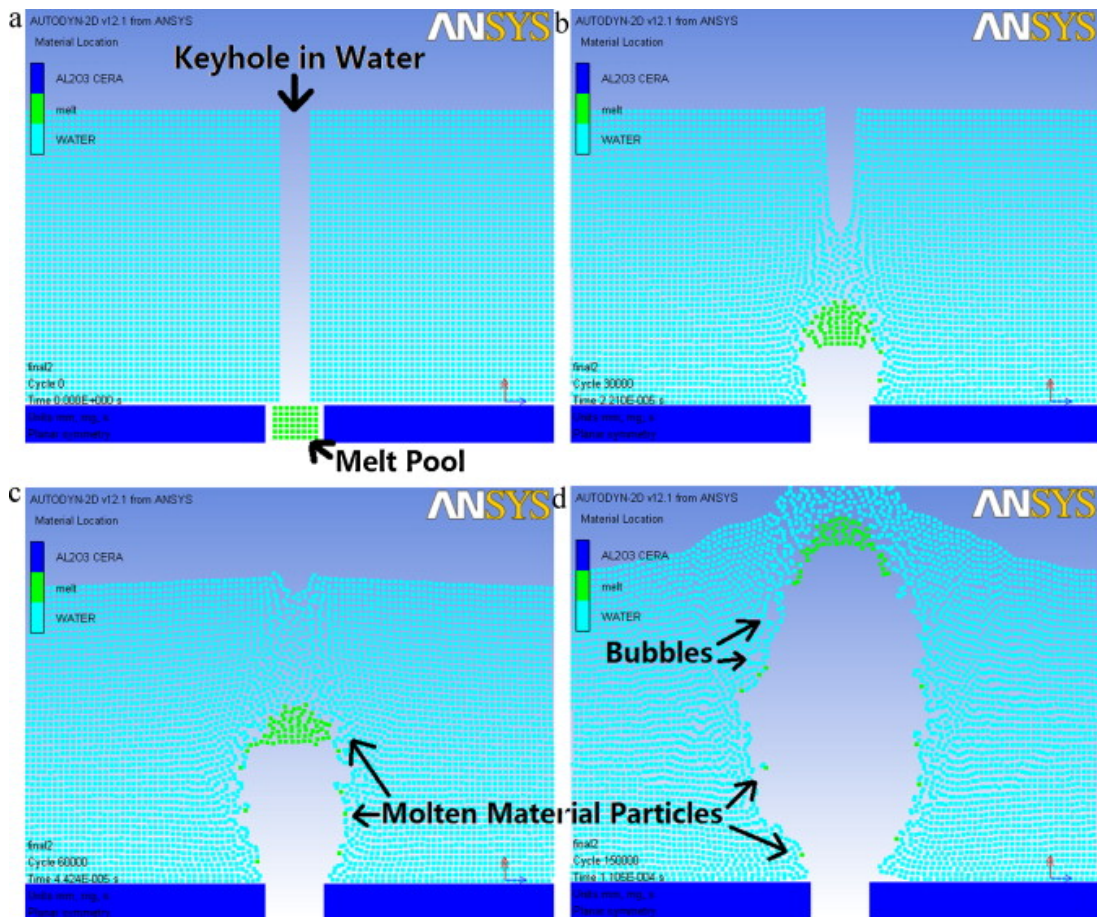


Figure 4.16 Time history of melt ejection during underwater machining at (a) 0 μ s, (b) 22.1 μ s, (c) 51.6 μ s and (d) 110 μ s

Figure 4.16 shows the process of melt ejection from the keyhole during underwater machining. It was found that part of the molten material was injected into the water and the other part was ejected out together with some water (as Figures 4.16(c) and (d)). The bubbles were also formed in water as depicted in Figure 4.16(d). The simulated results implied that the melt ejection perturbed the water and may cause turbulence and laminar flows in water.

Figure 4.17 shows the fluidic velocity caused by melt ejection during underwater machining. It can be found that the maximum velocity was concentrated on the region near the ejecting front and the water was pushed away from the ejecting path as shown in Figure 4.17(a). Figure 4.17(b) to (d) illustrates the details of water flow characteristic under various water depths. The flow vector close to water surface was directed to the normal of the water surface (as Figure 4.17(b)), which indicated that the water in this region would flow to the water surface and hence cause ripples on water surface. The laminar flow appeared at the middle of the water depth (as Figure 4.17(c)), by which the injected molten particles would be carried away from the machined region to resist redeposition. Figure 4.17(d) shows the flow characteristic near the machined region, which demonstrates the initial turbulence formation of the water flow. It was useful to induce the water into the machined groove for chilling. The SPH simulation result indicates the significance of water flow for laser underwater machining and is in agreement with the empirical hypothesis as shown in Figure 4.9.

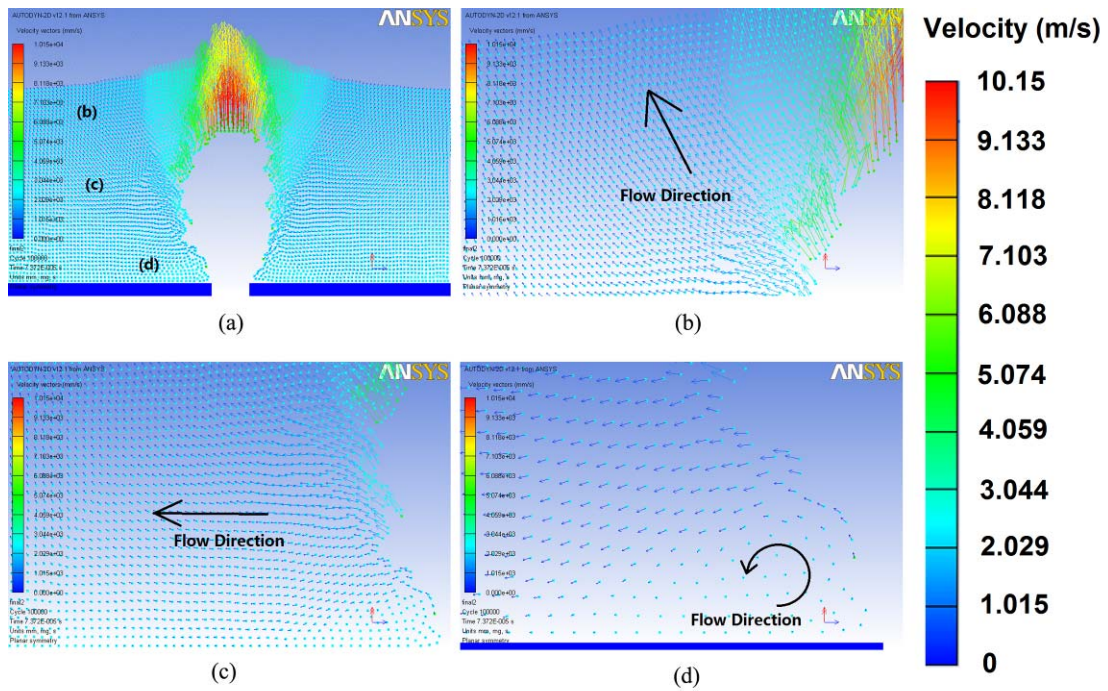


Figure 4.17 Vector plot (a) of water flow during underwater machining and detailed view at the region (b) near the water surface, (c) at the middle of water depth, and (d) near the machined region

4.4.3 Effect of scanning pass number and water layer thickness

The material removal rate of underwater machining depends on the number of laser scanning cycles and the thickness of water layer above the workpiece surface. Figure 4.18 shows the effect of water layer thickness on the machined kerf width and depth in alumina substrate at a fixed 60 W laser power and 10 mm/s scanning speed for 1–100 passes. For the water layer thickness of 2 mm, experiment trials were performed up to 40 passes since cracking appeared for higher number of passes. It can be seen that the kerf depth increases with the pass number but decreases with increasing water layer thickness (as Figure 4.18(a)). The kerf width reduces with the water layer thickening but is similar for different passes at the same water layer thickness (as Figure 4.18(b)). It indicates that the water layer thickness is a significant parameter to determine the machining kerf width due to the laser energy arriving on the workpiece surface varying with the water layer thickness, whereas the number of passes governs the machined depth together with the water layer thickness. Figure

4.19 shows the average machining rate, i.e. depth divided by the number of passes. It reveals that the depth rate exponentially decreases with the number of passes increasing. When the pass number was up to 100, the machining rate approached to a constant that was only determined by the water layer thickness, where the depth rate decreased with increasing water layer thickness.

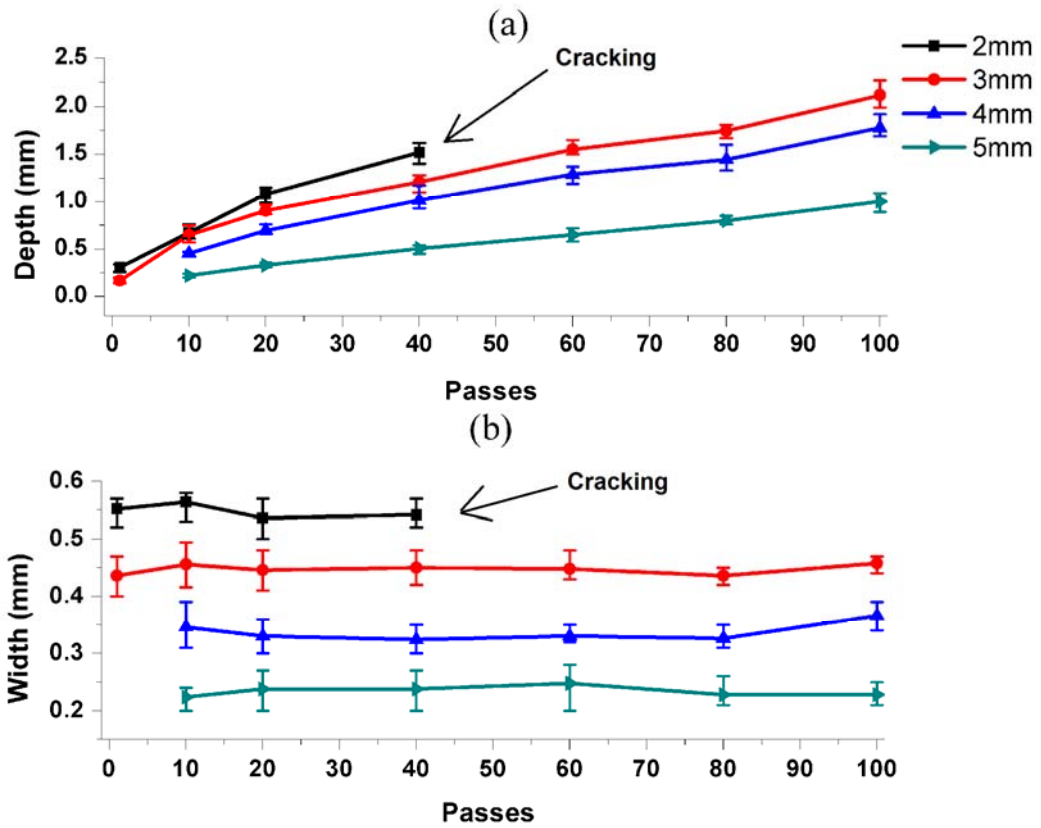


Figure 4.18 The effect of water layer thickness on machining (a) depth and (b) width in alumina substrate at a fixed 60 W laser power and 10 mm/s scanning speed for 1 to 100 passes

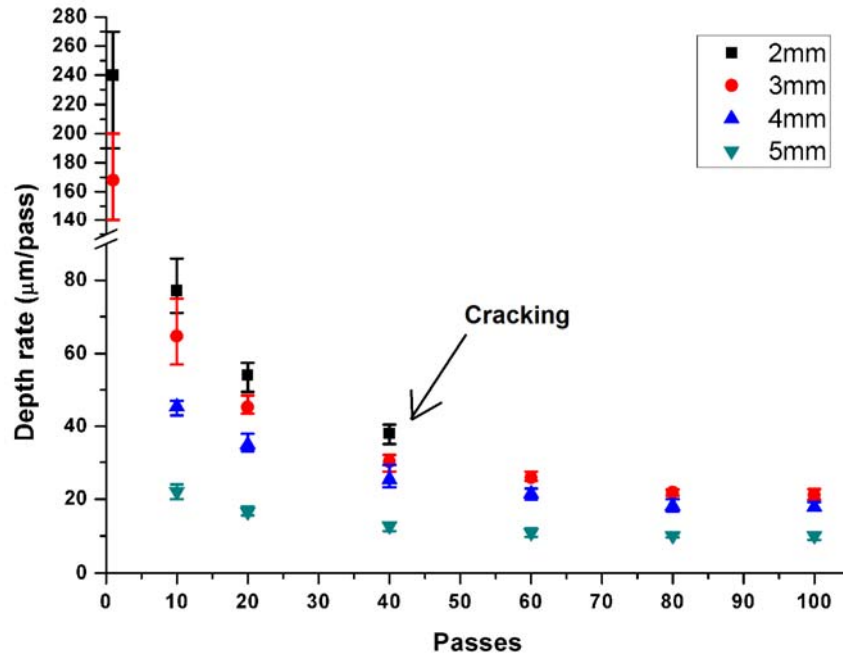


Figure 4.19 The effect of water layer thickness on machining rate for alumina substrate at a fixed 60 W laser power and 10 mm/s scanning speed for 1 to 100 passes

For deep cavity machining, multi-pass is essential and hence the machining rate is mainly determined by the thickness of water layer. For a thin water layer (<2 mm), the water cannot always wet the alumina surface during machining, which could cause a poor cooling effect and induce crack initiation around the machining region. However, when the water layer was greater than 5 mm, the machining rate was below 15 $\mu\text{m}/\text{pass}$ at 60 passes or more, which was undesirable due to the low machining rate. The thickness of water layer is therefore suggested at 3–4 mm in the work, which could balance a good surface cooling effect and a high machining rate. Also the thickness of water layer provided an adequate space to remove molten material particles. As shown in Figure 4.19, the average machining rate for this water layer thickness is always greater than 20 $\mu\text{m}/\text{pass}$ at a 60 W laser power and 10 mm/s scanning speed.

4.4.4 Laser underwater machining of polygon cavities

Based on the parameters discussed above, some polygon cavities were machined underwater at a water layer thickness of 4-mm, a laser power of 60 W and a scanning speed of 10 mm/s for 100 scanning cycles. Figure 4.20 shows the optical micrographs of the CO₂ laser underwater machined alumina polygon cavities. The crack-free machining of polygon cavities in alumina with smooth machined side wall surfaces was achieved by the CO₂ laser underwater machining. The depth of these polygon cavities is up to 2.36 mm. The depth of these polygon cavities is up to 2.36 mm.

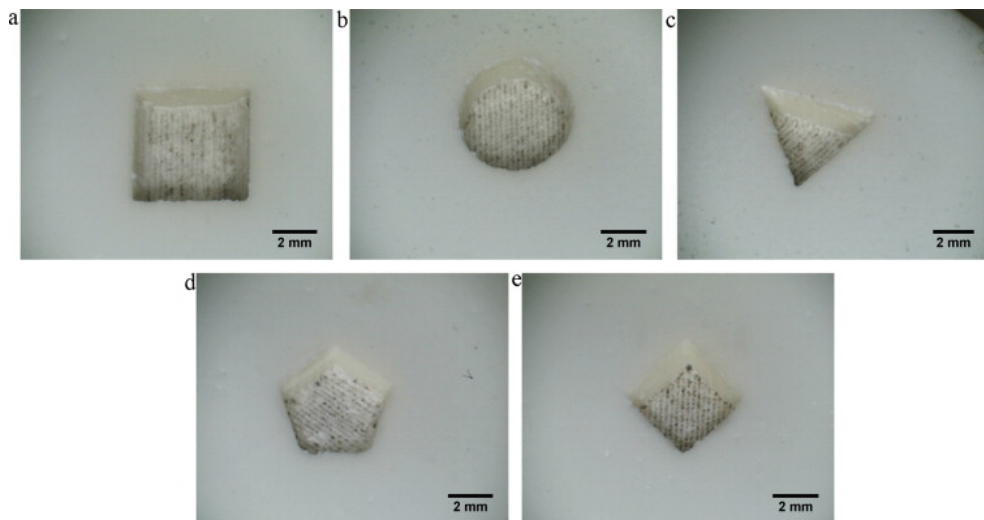


Figure 4.20 Optical micrographs of the CO₂ laser underwater machined polygon cavities including (a) square cavity, (b) circular cavity, (c) triangular cavity, (d) pentagon cavity, and (e) prismatic cavity

The typical machining time for a square cavity with dimension of 5 mm × 5 mm × 2.36 mm was about 30 min. Therefore, the average material removal rate for underwater machining with 60 W laser power and 10 mm/s feed rate at 4 mm thick water layer was 2.95 mm³/min. According to the experimental data shown in Figure 4.19, the material removal rate at the first machining cycle (i.e. the first scanning cycle of the whole cavity pattern) should be 18.75 mm³/min, which is close to pulsed laser machining in air [108]. However, it reduces when the machined depth increases since the water layer becomes thicker as illustrated in Figure 4.21. As a result, the equivalent material removal rate was reduced.

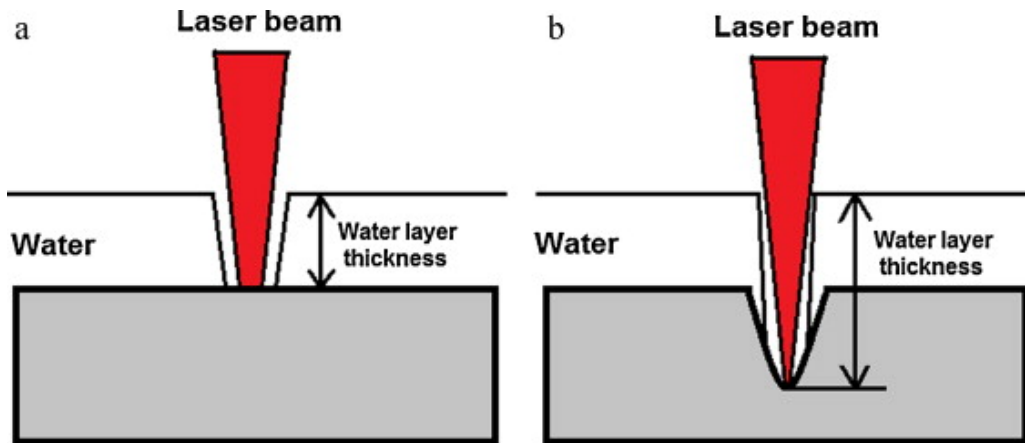


Figure 4.21 Schematic diagram of the change of water layer thickness with increasing of the machining depth. (a) The first pass and (b) the n -th pass

4.4.5 Potential improvements for high machining rate and quality

In order to further improve the machining rate, a substrate position correction technique will be developed in future for consistent water layer thickness with respect to the machining site throughout the machining process. The position of the workpiece should be corrected as the successive passes proceed. However, the maximum machining depth using this method is limited by the thickness of water layer above the workpiece surface, i.e. 4 mm under the current optimised experimental setup. When the machining depth is greater than this value, part of unmachined workpiece surface will be higher than the water surface. Under this condition, the water cannot spontaneously flow into the closed cavities for chilling and thermal damage would occur.

Therefore, the forced water layer formation technique should be developed for machining of deeper closed cavities. The schematic diagram of the process setup is shown in Figure 4.22. A water jet is applied to form a water layer on the top-surface of the workpiece. The layer thickness is primarily determined by the employed water flow rate. This setup can also solve the problem of the suspending particles scatter and absorb the laser light during still-water machining, since the water continuously flows under the high water pressure. A liquid circulation with filtration should also be integrated in the technique. At the same time, the substrate position correction is

applied in order to meet the focal plane position on the machining site. The feasibility of this technique will be verified in our future work.

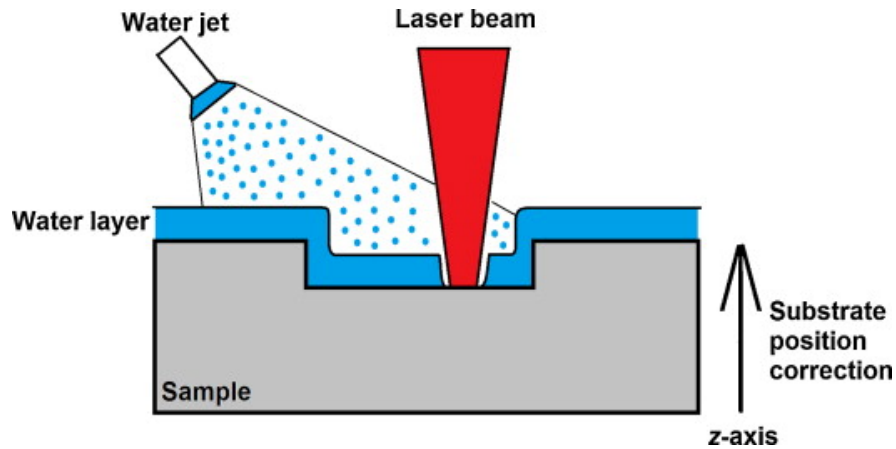


Figure 4.22 Schematic diagram of forced water layer formation technique with substrate position correction.

In addition to the pure water used in this work, other liquids (e.g. salt, basic or acid solutions) have been used in previous studies for chemical-assisted laser machining of hard-to-machined materials. Compared with conventional laser thermal machining, little thermal damage is induced in chemical-assisted laser machining. Alumina ceramic is a compound made up of aluminium atoms and oxygen atoms, which are in a very tight array (i.e. hexagonal atomic structure in grains). Therefore, alumina ceramic has a good corrosion resistance against most of salts, bases and acids. However, the grain boundaries could be easily etched due to the glass phases and inclusions existing [184]. Furthermore, laser activated photo-chemical and thermal-chemical reactions may also occur within the machining site to enhance the etching efficiency. In previous studies, chemical-assisted laser micromachining, involving laser processing within salt solution [184], basic solution [185] and acid solution [186, 187] has been found to be able to produce smoother finished surfaces without any detectable HAZ or recast layer than conventional laser thermal machining. Similar results were also found in laser wet etching of alumina and its composite [185, 186]. In order to introduce these advantages of laser wet etching into high average power laser machining, chemical-assisted laser macro-machining of engineering ceramics will be investigated in our future work.

4.5 Conclusions

The CO₂ laser underwater machining successfully demonstrated crack-free milling of mm-deep cavities in alumina. It was found that the process quality in underwater machining is much better than that in air. Underwater machining has the capability of preventing the crack initiation and reducing thermal damage due to the water cooling effect. ANSYS software was employed to understand the mechanism of crack resistance in underwater machining. The differences in the temperature and resulting stress distributions during laser machining in air and in water were revealed by the FE model. It indicated that the smaller HAZ and the lower thermal stress were produced in laser underwater machining than machining in air. The simulated results were in agreement with the experiments. SPH modelling of interactions between water and molten material ejection shows the behaviour and significance of water flow in the underwater machining process. The machined side wall surface in water was much smoother than in air as the effect of water dynamics produced a high recoil pressure in machining region to eject the molten material from the cavity and prevent recast formation. The effect of water layer thickness and scanning cycle number was also studied in this work. It was found that the kerf width was governed by the water layer thickness whereas the kerf depth was controlled by the scanning cycle number and the water layer thickness. The optimal water layer thickness was proposed to be 3–4 mm above the surface of workpiece to guarantee a sufficient cooling effect and a high material removal rate. Meanwhile, the thickness of water layer provided an adequate space to remove molten material particles. Based on the optimised parameters, several polygon cavities were demonstrated by underwater machining at 100 scanning cycles, 60 W laser power and 10 mm/s scanning speed with a scanning line interval of 0.25 mm. The average machining depth is greater than 2-mm and the machining rate is up to 2.95 mm³/min, similar to picosecond laser machining (< 2.2 mm³/min [112]).

Chapter 5

Nano-Second Pulsed DPSS Nd: YAG Laser Striation-Free Cutting of Alumina Sheets

5.1 Introduction

Lasers are extensively employed in cutting of alumina sheets in the electronic industries. In addition to cracks, another important quality factor in laser cutting is striation (periodical lines) formation on the cut surfaces, which affects the surface roughness and geometry precision of the cut products. The elimination of striation is important for alumina since it is essential for denser circuit patterns and device miniaturisation. The chapter demonstrates striation-free cutting of alumina sheets with 1 mm thickness using a 400 W high repetition rate nano-second pulsed DPSS Nd:YAG laser. The short pulse duration minimises thermal damage. The effects of gas type, gas pressure, nozzle standoff distance, average laser power, cutting speed, and pulse repetition rate on striation characteristics were studied. The specific operating conditions for nano-second pulsed laser striation-free cutting were presented. This work supports one of the existing theories for continuous wave (CW) laser striation-free cutting of metallic materials and further extends it to the pulsed laser striation-free cutting of ceramic materials. A mechanism of pulsed laser striation-free cutting was also proposed, by which a model to predict the operating window for the nano-second pulsed laser striation-free cutting of alumina sheets was developed. The prediction was also validated by the experiment.

5.2 Experimental Procedure

A diode pumped solid state (DPSS) Nd:YAG laser manufactured by Powerlase Photonics was employed in this work. This is a nano-second pulsed laser emitted at 1.06 μm wavelength with high repetition rates of 3–15 kHz and short pulse durations of 30–55 ns. The maximum average laser power nominal output is 400 W. Figure 5.1 shows the experimental setup of the laser cutting system. The raw laser beam (quasi-Gaussian-distribution, $M^2=22$) with a diameter of 8 mm was delivered into a laser cutting head, which held a lens of 83 mm focal length and a gas nozzle with 1.2 mm diameter. The focused laser beam spot size was approximately 300 μm (diameter) and the focal plane position was fixed at 0.5 mm below the nozzle tip. The assist gas flow was coaxial to the laser beam arriving at the workpiece surface. Table 5.1 lists the range of average laser power, pulse repetition rate, cutting speed, nozzle standoff distance, assist gas type, gas pressure, and gas flow rate studied in this work. The average power nominal outputs excited by various diode laser pump voltages at different repetition rates follow the curves plotted in Figure 5.2, where the fixed pulse durations at different repetition rates are also listed. The power loss in optical delivery path is approximately 20%, measured at a pump voltage of 6 V and pulse repetition rate of 15 kHz. In this work, the average laser output power was used as a scale for laser power where possible. However, the pump voltage was also used under special circumstances when the average power was inappropriate in discussion.

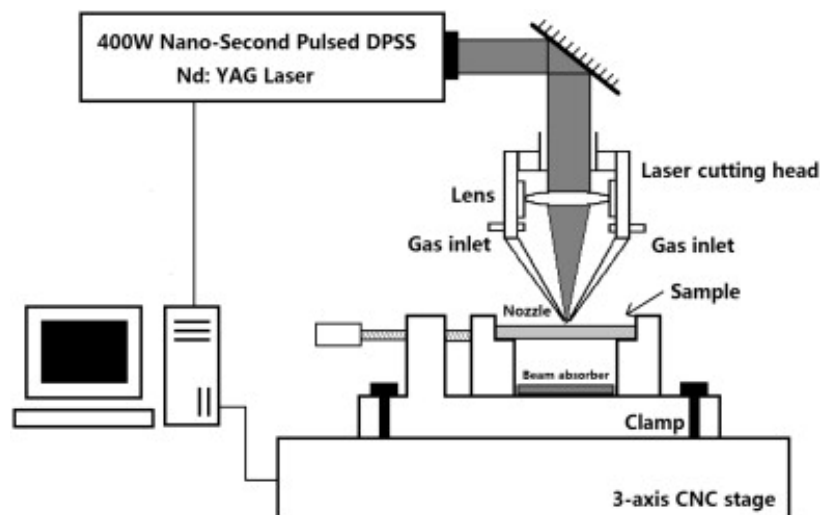


Figure 5.1 Schematic diagram of the experimental setup for nano-second pulsed DPSS Nd:YAG laser cutting of alumina sheets

Table 5.1 Laser cutting conditions used in this work

Parameter	Values
Average power (W)	95-415
Pulse repetition rate (kHz)	3-15
Cutting speed (mm min ⁻¹)	60-360
Nozzle standoff distance (mm)	0.5-3
Assist gas	N ₂ , He, Ar, O ₂ , Air
Gas pressure (bar)	0.5-3
Gas flow rate (L/min)	12-35 (for N ₂ , Ar, O ₂ , and Air at 0.5-3 bar) 45-100 (for He at 0.5-3 bar)

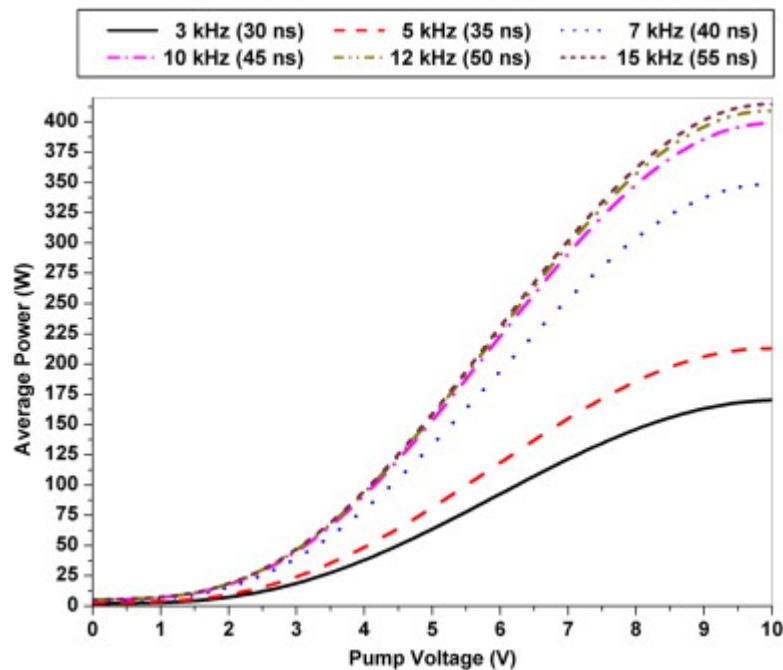


Figure 5.2 Curves of nominal laser average power versus pump voltage at different pulse repetition rates. Pulse durations at different pulse repetition rates are fixed and listed in the legend

The material used in this work was 99.6% alumina sheet with a thickness of 1 mm. The major material properties are listed in Table 5.2. Alumina has a low absorptance with respect to 1.06 μm wavelength laser. The values of reflectance and transmittance of 1-mm-thick alumina sheet at 1.06 μm wavelength were 79.4% and 16.4%, respectively, measured by Shimadzu UV-3600 Spectrometer. Therefore, the absorptance of the alumina sheet was only 4.2% to the DPSS Nd:YAG laser used in

this work at room temperature. The samples were clamped flat on an Aerotech 3-axis CNC stage with a maximum transmitting speed of 200 mm/s. The focused laser beam was delivered onto the workpiece as shown in Figure 5.1. Single pass strategy was used in this study for linear cuts, 20 mm long, and 10 mm outside allowance was applied for the stage acceleration.

Table 5.2 Material properties of 99.6% alumina used in the work [12]

Properties	Values
Mass density (kg/m ³)	3750
Specific heat (J/kg×K, to 1773K)	$1044.6 + 1742 \times 10^{-4} \times T - 2796 \times 10^4 \times T^{-2}$
Thermal conductivity (W/m×K, to 1573 K)	$5.5 + 34.5e^{[-0.0033 \times (T-273)]}$
Melting point (°C)	2072
Latent heat of fusion (10 ⁶ J/kg)	2.53
Boiling point (°C)	2977
Latent heat of vaporisation (10 ⁶ J/kg)	3.91

T: Temperature (K)

The striation pattern on cut surface was captured by three microscopic techniques in order to obtain a reliable demonstration and an accurate evaluation. Optical microscopy (Polyvar) was employed to initially examine the morphology of the cut surface. Then the morphology and roughness of the cut surface were profiled and measured using a white light interferometer (Wyko NT1100), where R_a and R_q were selected as the roughness criteria. Finally, the morphology was further captured using SEM (Hitachi S-3400), by which the effect of light incident angle in optical microscopy on striation capture can be avoided. Also, the cut surface microstructures were examined by SEM, to understand the mechanism of striation formation during laser cutting.

5.3 Results

5.3.1 Demonstration of striation-free cutting

Figures 5.3, 5.4 and 5.5 compare the cut surfaces with and without striations at a 415 W average power and 15 kHz pulse repetition rate under three different cutting speeds. The nozzle standoff distance was 0.5 mm and 1 bar nitrogen gas was used as the assist gas. Figure 5.5 clearly demonstrates that striation-free cutting of alumina sheet has been achieved by the nano-second pulsed laser.

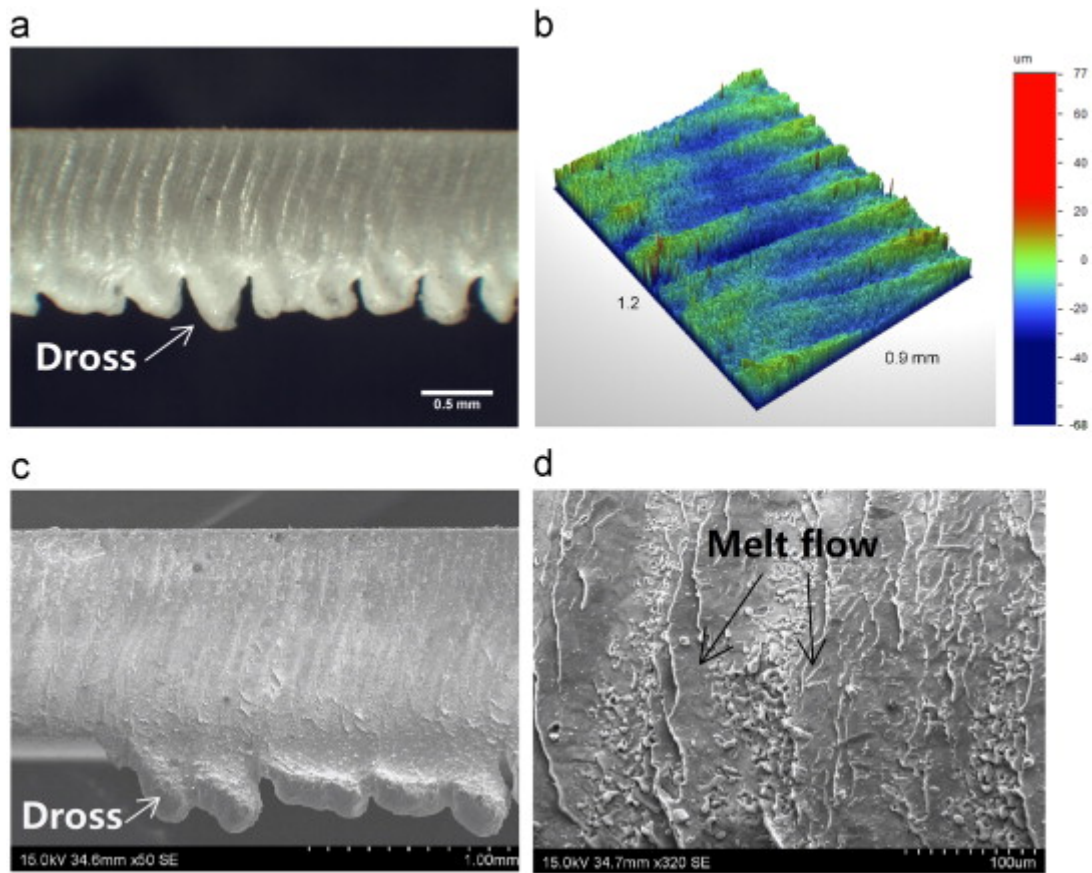


Figure 5.3 Surface profile of a cut with major striations at an average laser power of 415 W, pulse repetition rate of 15 kHz, cutting speed of 360 mm/min, and nozzle stand-off distance of 0.5 mm with 1 bar N₂ assist gas. The micrographs are captured by (a) an optical microscope, (b) white light interferometer ($R_a=8.31 \mu\text{m}$, $R_q=11.22 \mu\text{m}$), and (c) SEM. (d) Close-up view of the cut surface by SEM

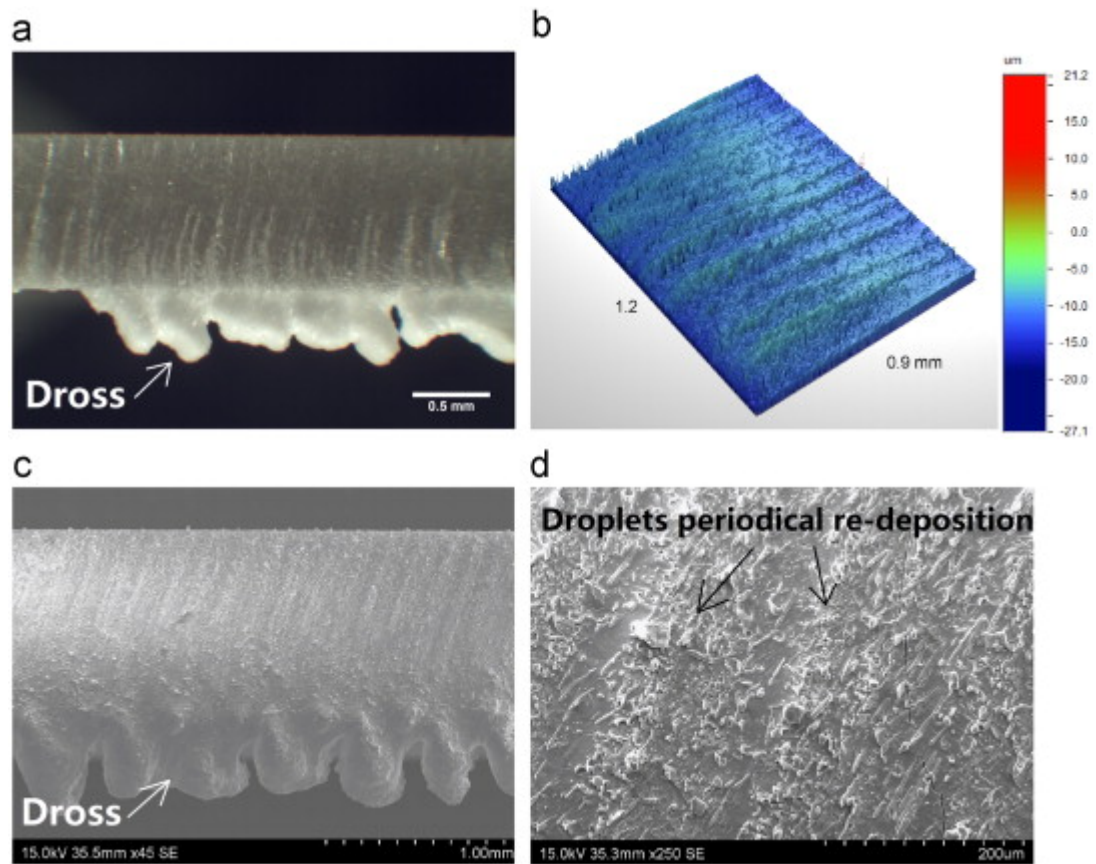


Figure 5.4 Surface profile of a cut with minor striations at an average laser power of 415 W, pulse repetition rate of 15 kHz, cutting speed of 60 mm/min, and nozzle stand-off distance of 0.5 mm with 1 bar N₂ assist gas. The micrographs are captured by (a) an optical microscope, (b) white light interferometer ($R_a=4.09\ \mu\text{m}$, $R_q=5.23\ \mu\text{m}$), and (c) SEM. (d) Close-up view of the cut surface by SEM

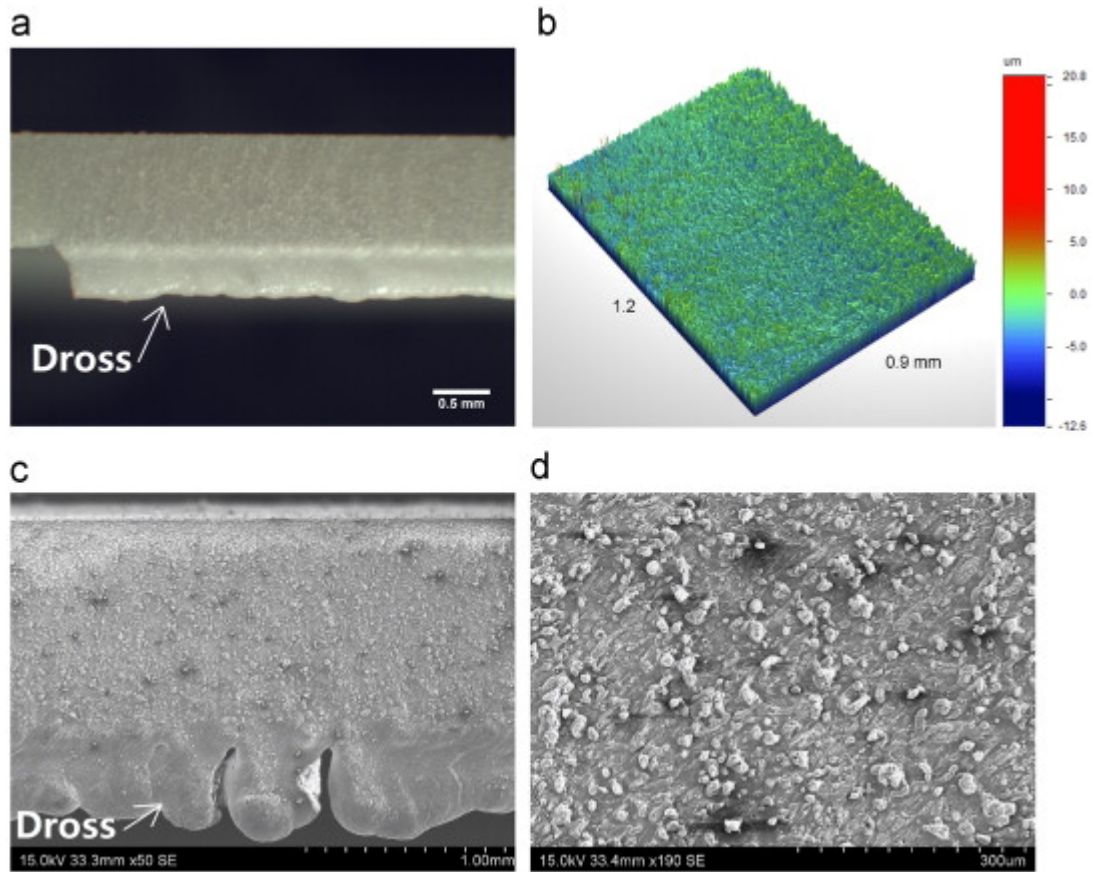


Figure 5.5 Surface profile of a cut with striation free at an average laser power of 415 W, pulse repetition rate of 15 kHz, cutting speed of 186 mm/min, and nozzle stand-off distance of 0.5 mm with 1 bar N₂ assist gas. The micrographs are captured by (a) an optical microscope, (b) white light interferometer ($R_a=2.76 \mu\text{m}$, $R_q=3.47 \mu\text{m}$), and (c) SEM. (d) Close-up view of the cut surface by SEM

At a high cutting speed ($>300 \text{ mm/min}$), striation is clearly seen on the cut surface as shown in Figure 5.3. The material removal at the high cutting speed is dominated by melt flow ejection due to the low energy input per unit length, by which the melt oscillation may occur and thus the striation could appear (as Figure 5.3(d)). The discontinuous dross formation (as Figures 5.3(a) and (c)) further confirmed the melt oscillation during cutting. The R_a and R_q of cut surface at the high cutting speed are 8.31 and 11.22 μm , respectively.

Based on the initial experiments, it was found that striation became gradually shallower as the cutting speed decreased and tended to disappear. When the cutting speed was lower than 120 mm/min, striation appeared again. At a low cutting speed (<120 mm/min), the mechanism of material removal was mainly based on evaporation with little melt on material presence. The contribution of molten material flow to striation formation can be negligible. The droplet was ejected by the vapour pressure and resolidified on the cut surface (as Figure 5.4(d)). However, the low cutting speed caused a discontinuous movement of the cut front, which could induce a discrete ejection and material removal. The less homogeneous cross formation validated this process (as Figures 5.4(a) and (c)). Therefore, the droplets were re-deposited along a periodical distribution as shown in Figure 5.4(d) and hence, formed minor striations on the cut surface (as Figure 5.4(b)). The R_a and R_q of cut surface at low cutting speed are 4.09 and 5.23 μm , respectively, which are lower than roughnesses of the cut surface with major striations.

Between 120 and 270 mm/min cutting speed, the cut surface becomes almost flat and striations are eliminated altogether as shown in Figure 5.5. Figure 5.5(a) shows a homogeneous cross formation, which indicates a continuous process of melt ejection and cut front movement. The melt oscillation and droplets periodical re-deposition were therefore suppressed, leading to a striation-free cut surface. Unfortunately, the re-deposited droplets on the cut surface cannot be eliminated completely (as Figure 5.5(d)). The R_a and R_q values of cut surface at the optimal cutting speed (i.e. 186 mm/min) are 2.76 μm and 3.47 μm , respectively, which are far lower than the roughness values of cut surfaces with striations.

5.3.2 Effect of assist gas type

The above optimal operating conditions (i.e. 415 W average laser power, 15 kHz pulse repetition rate, 186 mm/min cutting speed, and 0.5 mm nozzle standoff distance) were selected to study the effect of assist gas type on the striation characteristics. Figure 5.5 demonstrates the striation-free surface profile of a cut with 1 bar N_2 assist gas, where R_a and R_q are 2.76 and 3.47 μm , respectively. Nitrogen has a medium thermal conductivity for cut kerf chilling, a medium ionisation potential

(15.60 eV) for plasma formation and a medium molecular weight. The experiment shows that it is one of the ideal gases for striation-free laser cutting with low costs.

Figure 5.6 demonstrates the major striation ($R_d=6.69 \mu\text{m}$, $R_q=8.89 \mu\text{m}$) appearing on the cut surface when helium was chosen as the assist gas with 1 bar pressure. Helium has a high thermal conductivity, which can be effective for cooling the workpiece. The high ionisation energy of helium (24.46 eV) suppresses the plasma generation during high peak power pulsed laser cutting, which reduces the laser energy loss by plasma absorption. Figure 5.6(d) illustrates that the molten flow appeared significantly. This is due to the high thermal conductivity of the helium gas cooling the evaporated and molten material excessively. The melt flow was hence formed and melt oscillation occurred. The molten material, resolidified layer by layer, formed striations on the cut surface. The discontinuous dross formation (as Figures 5.6(a) and (c)) further confirmed the melt oscillation during laser cutting. This problem could be solved using a higher power laser or a lower cutting speed in order to have an evaporation driven cut process. However, it will lower the process energy effectiveness. Moreover, the high costs and the high gas flow rate required due to the light molecular weight indicates that helium is not suitable for practical industrial applications in laser cutting of alumina.

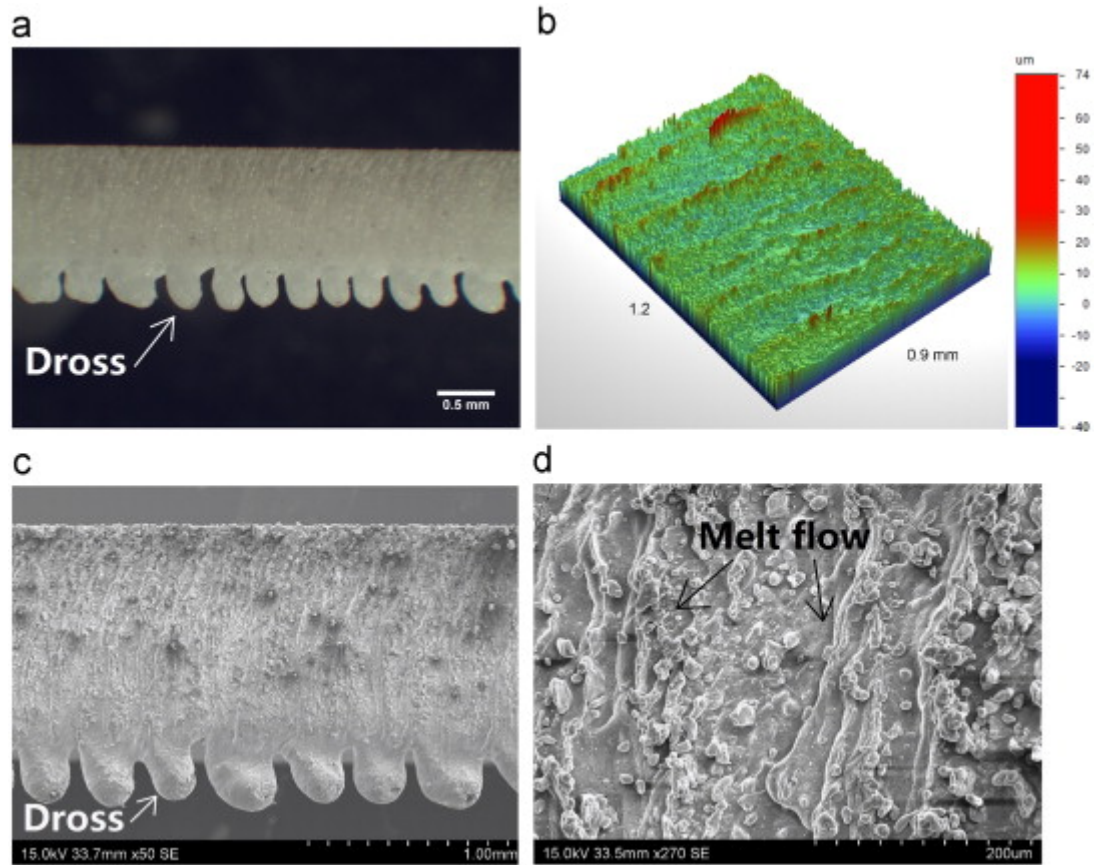


Figure 5.6 Surface profile of a cut with major striations at an average laser power of 415 W, pulse repetition rate of 15 kHz, cutting speed of 186 mm/min, and nozzle stand-off distance of 0.5 mm with 1 bar He assist gas. The micrographs are captured by (a) an optical microscope, (b) white light interferometer ($R_a=6.69 \mu\text{m}$, $R_q=8.89 \mu\text{m}$), and (c) SEM. (d) Close-up view of the cut surface by SEM

Figure 5.7 shows the surface profile of a cut with 1 bar Ar assist gas. Argon has a low thermal conductivity, which cannot effectively cool down the workpiece to reduce thermal damage. However, the medium ionisation potential (15.69 eV) could suppress the plasma generation during cutting. The minor striation appeared on the cut surface as shown in Figure 5.7. Figure 5.7(d) illustrates that droplet re-deposition was the major form of molten material resolidification. This is due to the low thermal conductivity of the assist gas that caused more evaporation and material removal during cutting. Therefore, discontinuous movement of cut front occurred, which induced a discrete ejection (i.e. discontinuous dross adhesion). The droplets

were thereby re-deposited along a periodical distribution and formed minor striations on the cut surface ($R_a=5.20\ \mu\text{m}$, $R_q=7.05\ \mu\text{m}$) as shown in Figures 5-7(b) and (d). Moreover, the operating conditions should be carefully chosen to avoid potential thermal damage when the low thermal conductivity argon assist gas was used, which may further narrow the operating window for crack-free and striation-free cutting of alumina sheets.

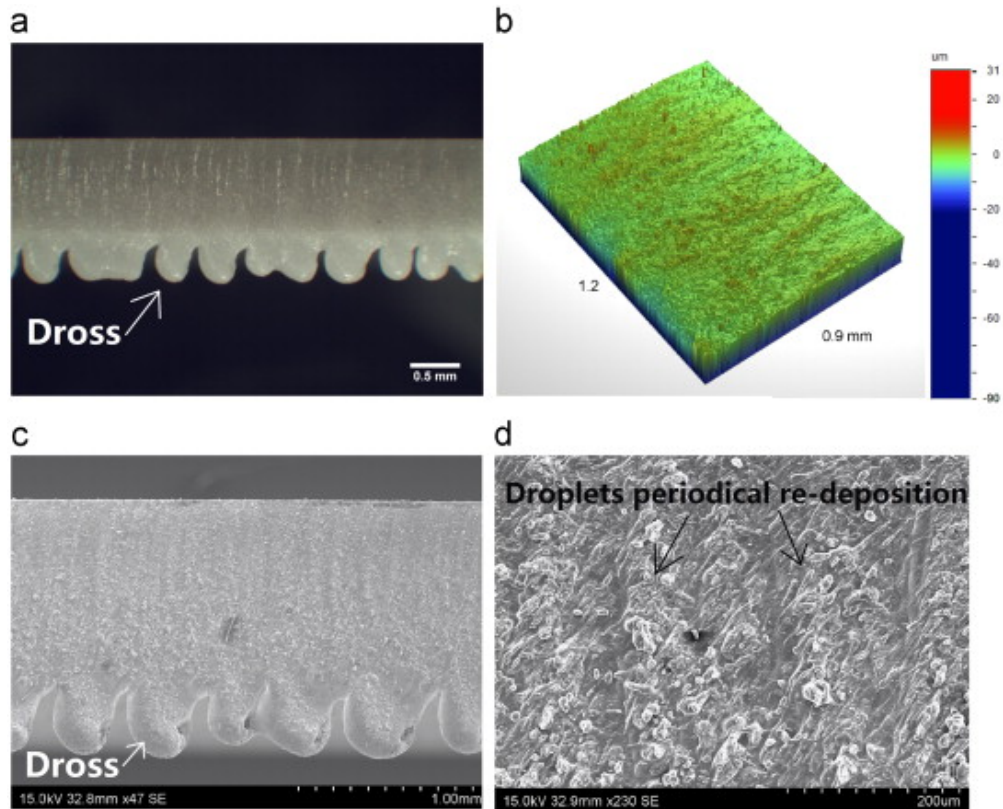


Figure 5.7 Surface profile of a cut with minor striations at an average laser power of 415 W, pulse repetition rate of 15 kHz, cutting speed of 186 mm/min, and nozzle stand-off distance of 0.5 mm with 1 bar Ar assist gas. The micrographs are captured by (a) an optical microscope, (b) white light interferometer ($R_a=5.20\ \mu\text{m}$, $R_q=7.05\ \mu\text{m}$), and (c) SEM. (d) Close-up view of the cut surface by SEM

Figure 5.8 shows the surface profile of a cut with 1 bar O_2 assist gas. The through cuts cannot be obtained due to the low ionisation potential of oxygen (12.50 eV), where the plasma was generated during laser cutting in the experiment. The plasma attenuated laser energy and resisted the laser beam arriving onto the workpiece.

Figures 5.8(a) and (b) illustrate that the molten material was ejected out from the top of the kerf and resolidified as burs on the cut edge due to the blind cut kerf. Figure 5.8(c) indicates the melt ejection direction and the very rough cut surface, of which the roughness values (R_a and R_q) cannot be measured by the white light interferometer. In the previous study, the oxygen assist gas was found to be the most suitable for CW fibre laser striation-free cutting of alumina sheets due to the resistance of discoloured tetragonal alumina formation [83]. However, considering the high tendency to induce plasma generation, oxygen is no longer an ideal assist gas for the high peak power nano-second pulsed laser cutting.

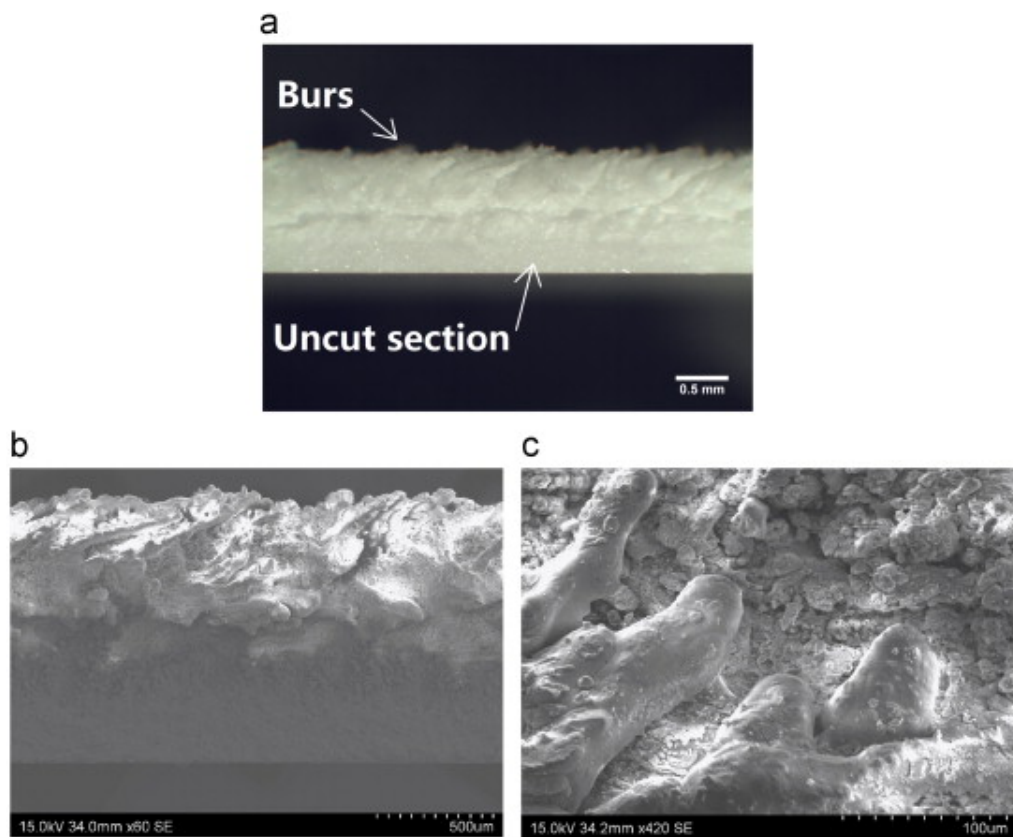


Figure 5.8 Surface profile of a blind cut at an average laser power of 415 W, pulse repetition rate of 15 kHz, cutting speed of 186 mm/min, and nozzle stand-off distance of 0.5 mm with 1 bar O_2 assist gas. The micrographs are captured by (a) an optical microscope and (b) SEM. (c) Close-up view of the cut surface by SEM

Considering the effects of oxygen and nitrogen gases on laser cutting of alumina sheets, compressed air was used in order to combine their advantages. Figure 5.9 shows the surface profile of a cut with 1 bar compressed air assist gas. The plasma was reduced and the through-cuts were achieved. The tetragonal alumina formation was also resisted. Although the dross adhesion was homogenous (as Figure 5.9(a)), significant striations still appeared on cut surface as shown in Figures 5.9(b) and (c), in which the R_a and R_q were 14.05 and 17.35 μm , respectively. This is due to the plasma generated by the oxygen component in air absorbing a portion of the beam energy. The energy arrived on the workpiece was reduced and as a result, the evaporation driven process was converted into the melt governed process. During this process, the melt flow was formed and melt oscillation occurred. The molten material was then resolidified, layer by layer, on the cut surface as major striations (as Figure 5.9(d)). Therefore, compressed air is not suitable for the high peak power nano-second pulsed laser striation-free cutting of alumina sheets.

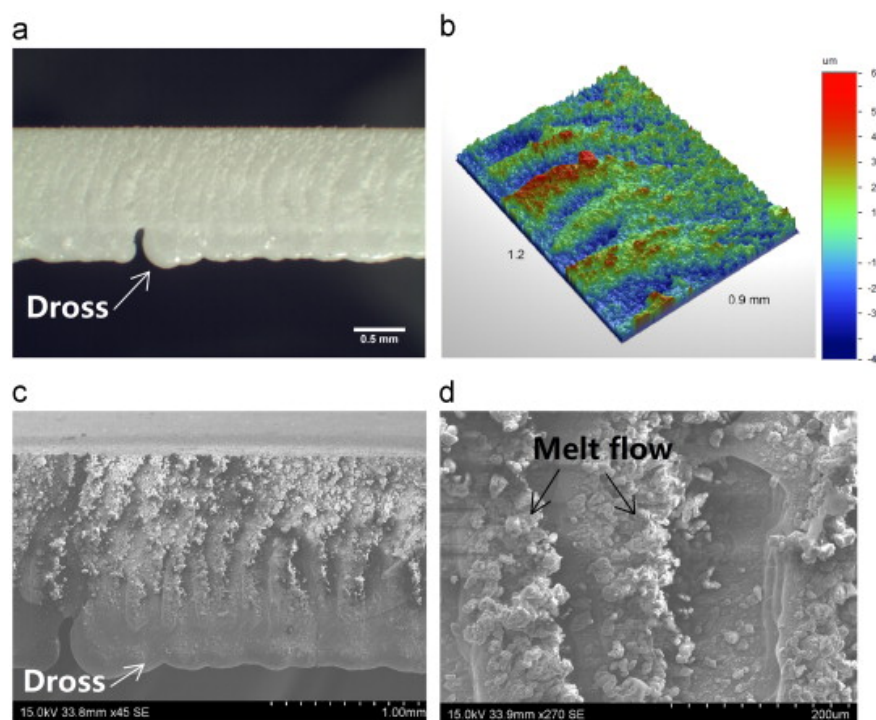


Figure 5.9 Surface profile of a cut with major striations at an average laser power of 415 W, pulse repetition rate of 15 kHz, cutting speed of 186 mm/min, and nozzle stand-off distance of 0.5 mm with 1 bar compressed air assist gas. The micrographs are captured by (a) an optical microscope, (b) white light interferometer ($R_a=14.05 \mu\text{m}$, $R_q=17.35 \mu\text{m}$), and (c) SEM. (d) Close-up view of the cut surface by SEM

Based on the above experiments with different assist gases, it can be found that nitrogen is an ideal gas, due to its good balance of thermal conductivity, ionisation energy, and costs, for high peak power nano-second pulsed laser striation-free cutting of alumina sheets.

5.3.3 Effect of assist gas pressure and nozzle standoff distance

Figure 5.10 shows the effect of assist gas pressure and nozzle standoff distance on the striation characteristics. It indicates that a narrow operating window exists for pulsed laser striation-free cutting. Increasing the standoff distance up to 1 mm can increase the operating window size for assist gas pressure, as a result of a smoother gas flow at this nozzle standoff distance. When the nozzle standoff distance was greater than 1.5 mm, striation-free cutting cannot be achieved. Figure 5.10 clearly demonstrates the high sensitivity of the striation characteristics to gas pressure and nozzle standoff distance. The striation-free cutting can be obtained only at low gas pressures (1.0–1.5 bar), which ensured that the driving force for material removal was the vaporisation while the contribution of assist gas pressure can be negligible. This hypothesis was in agreement with the proposed theory for striation-free cutting of mild steel by Li et al. [69].

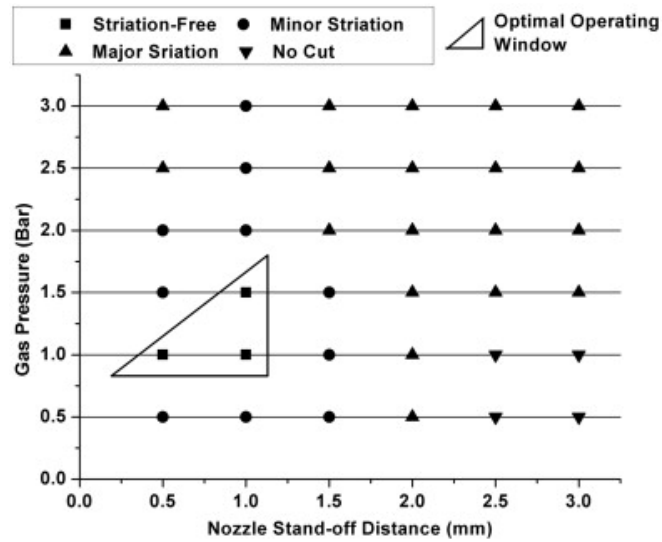


Figure 5.10 Effect of nozzle stand-off distance and gas pressure on striation characteristics at a laser average power of 415 W, pulse repetition rate of 15 kHz, and cutting speed of 186 mm/min with N₂ assist gas

5.3.4 Effect of laser power, pulse repetition rate and cutting speed

Figure 5.11 shows the operating window where striation-free laser cutting can be achieved. A higher average power indicates a higher pulse peak power, which enhances the evaporation process and suppresses melt flow formation during laser cutting as mentioned above. Therefore the cutting speed range for striation-free cutting was enlarged significantly with the increasing average power.

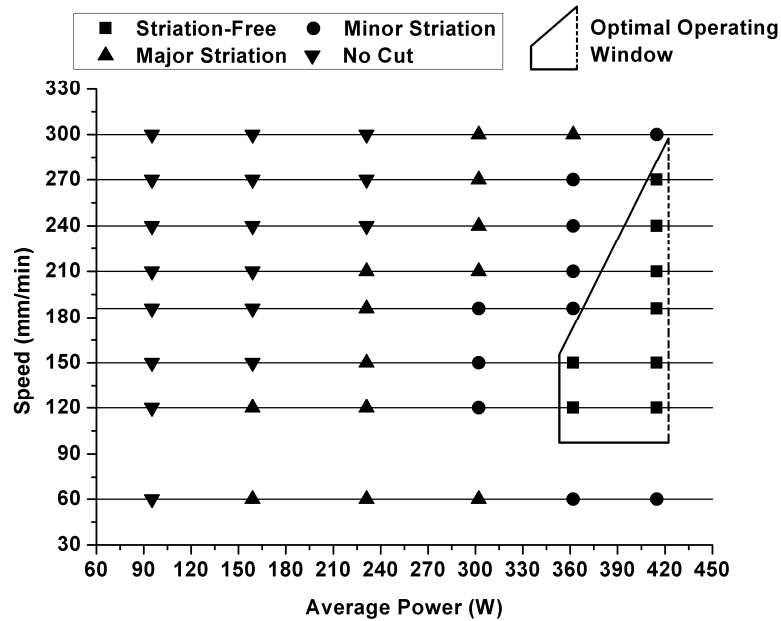


Figure 5.11 Effect of laser average power and cutting speed on striation characteristics at a pulse repetition rate of 15 kHz and nozzle stand-off distance of 0.5 mm with 1 bar N₂ gas pressure (Dash line indicates that the operating window could be extended to a larger area.)

Figure 5.12 shows the effect of cutting speed and pulse repetition rate on striation characteristics. For striation-free cutting, increasing the pulse repetition rate can increase the operating window size for cutting speed. The cut front movement and material removal are discrete in pulsed laser cutting, thus striation formation is normally expected. However, when the pulse repetition rate is high enough and the cutting speed is low enough, the discrete process can be negligible. Based on the experimental results shown in Figure 5.12, it was found that the striation-free cutting could be achieved at the pulses' overlap greater than 99.8%. Otherwise, the striation-free cutting cannot be obtained. Therefore, the cutting speed range for striation-free cutting was enlarged with pulse repetition rate increasing at 12–15 kHz. On the other hand, the excessively low cutting speed (typically <120 mm/min) would lead to a discontinuous movement of cut front due to a larger volume of material removal by heat conduction and potential plasma formation. It could induce a discrete droplet ejection and material removal, by which striation appeared again on the cut surfaces as illustrated in Figure 5.12.

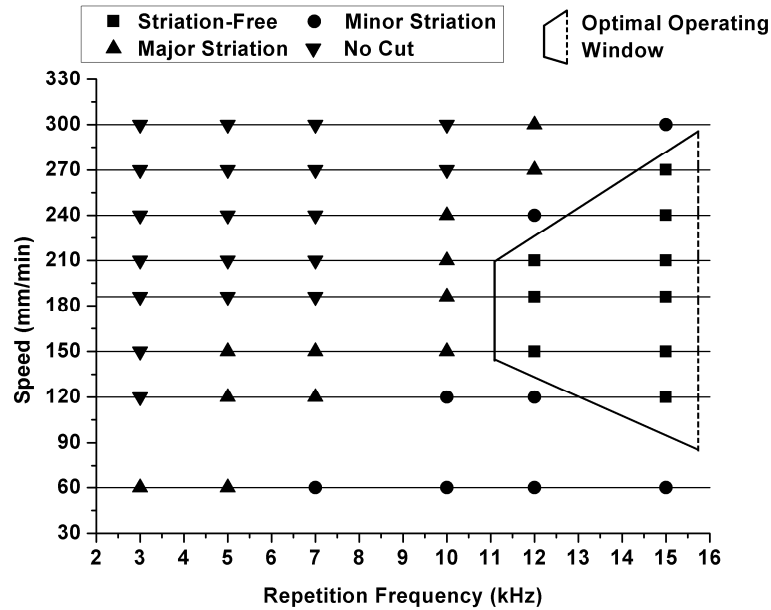


Figure 5.12 Effect of pulse repetition rate and cutting speed on striation characteristics at a diode laser pump voltage of 10 V and nozzle stand-off distance of 0.5 mm with 1 bar N_2 gas pressure (Dash line indicates that the operating window could be extended to a larger area.)

5.4 Discussion

5.4.1 Selection of operating conditions

Based on the experimental results, it was found that pulsed laser striation-free cutting of alumina sheets can be achieved within a specific and narrow operating condition window, which is different from that for standard laser cutting or CW laser striation-free cutting of alumina sheets by CO_2 or YAG lasers, as listed in Table 5.3.

Table 5.3 Comparison between standard laser cutting, CW laser striation-free cutting, and pulsed laser striation-free cutting conditions for alumina sheets

Operating Conditions	Standard Laser Cutting	CW Laser Striation-free Cutting [83]	Pulsed Laser Striation-free Cutting
Average laser power (W)	70-2000	100-1000	360-420
Pulse repetition rate	CW, 10-200 Hz	CW	12-15 kHz
Pulse duration	1-20 ms	-	50-55 ns
Cutting speed (mm/min)	<420	20-350	120-270
Focal plane position	<0	Not presented	0-0.5 mm
Focused spot diameter (μm)	50-500	15	300
Nozzle standoff distance (mm)	1-2	Not presented	0.5-1
Assist gas	Inert gas, O ₂ , Air	N ₂ , O ₂	N ₂
Gas pressure (bar)	3-7	6	1-1.5
Nozzle diameter (mm)	1-2	1.5	1.2

For nano-second pulsed laser cutting, a high average laser power (with a typical pulse peak power of 4.31×10^5 – 6.81×10^5 W, pulse energy of 23.7–34.1 mJ, and fluence of 33.51–48.27 J/cm²) and a high pulse repetition rate are two essential conditions to suppress melt flow formation and stabilise the cut front movement. The corresponding cutting speed should be carefully considered, which must match the average laser power and pulse repetition rate in order to keep a continuous cut process. The positive focal plane position is useful to form a wide cut kerf for material removal. A proper nozzle standoff distance with a large nozzle diameter guarantees a smooth and stable gas flow within the cut kerf. The low gas pressure suppresses eddies and slipstreams avoiding unstable melt oscillation within the cut kerf [58]. Furthermore, nitrogen provides a good balance of thermal conductivity, ionisation energy and costs as the assist gas. Satisfying above conditions, the nano-second pulsed laser striation-free cutting of alumina sheets can be achieved.

5.4.2 Prediction of striation-free laser cutting parameters theoretically

For striation-free laser cutting of alumina sheets with an inert gas, cutting speed is one of the critical factors. The theoretical model developed by Li et al. has been applied to explain this process and predict the cutting speed for striation-free laser cutting. In their theory, the low gas pressure minimised the effect of assist gas on

material removal whereas the vaporisation front advancement in the axial direction (i.e. along the beam down the cut kerf) is considered as the driving force for material removal. Only when the advancement time of the vaporisation front through the depth of the workpiece approximates the time of laser and material interaction within the beam spot, will the melting rate along the depth be equal to the melt removal rate. Under this condition, the melting becomes a continuous process and melt oscillation can be prevented [69]. In practice, this process can be approximately expressed as

$$v_c \approx \frac{D_{drill}}{t_{drill}} \quad (5-1)$$

where v_c is the critical cutting speed at which striation-free cutting occurs, D_{drill} is the average drilled-hole diameter across the depth of the workpiece, and t_{drill} is the threshold time for drilling a through hole.

In order to validate the hypothesis, an experiment for the threshold of drilling a through hole in a 1-mm alumina sheet was performed under the optimum operating conditions (i.e. 415 W average laser power, 15 kHz pulse repetition rate, and 0.5 mm nozzle standoff distance with 1 bar N₂ assist gas). Figure 5.13 shows the time history of the drilling process. It can be found that the threshold time for piercing a hole was about 0.14 s. The average hole diameter across the depth of the workpiece, D_{drill} , was (560+100)/2=330 μm approximately. Therefore, the calculated cutting speed by Eq. (1) for striation-free cutting at the above operating conditions was about 140 mm/min, which was in the optimal operating window illustrated in Figure 5.12 (i.e. 120–270 mm/min).

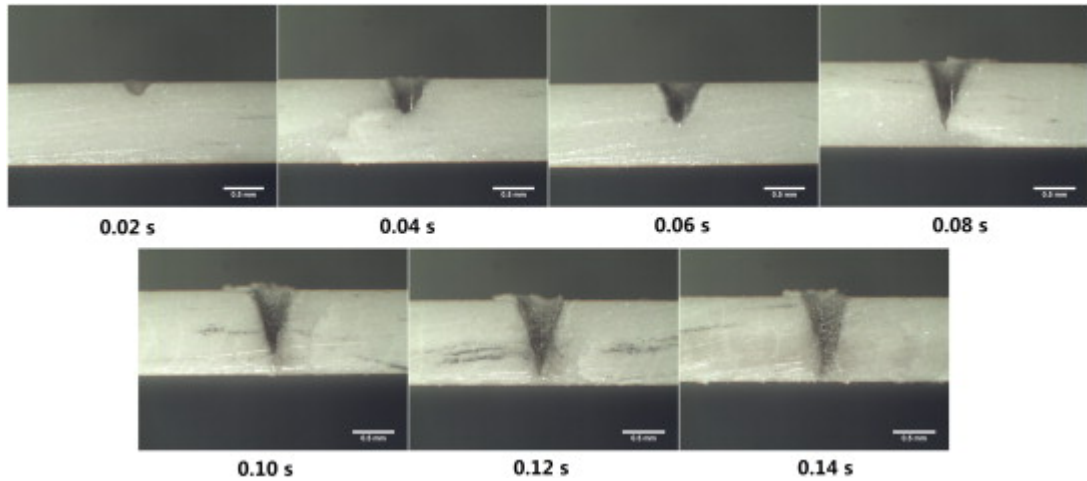


Figure 5.13 Time history for drilling a through hole in a 1-mm alumina sheet using 415 W average laser power, 15 kHz pulse repetition rate, and 0.5 mm nozzle standoff distance with 1 bar N₂ assist gas

5.4.2.1 The upper limit of striation-free cutting speed

In Li's model, the cutting speed (v_c) can be predicted by the following expression [69] and it should be the upper limit, in theory, of cutting speed for striation-free cutting:

$$v_c \approx \frac{A_f (1 + \alpha') FD}{\rho t (L_v + C_p T_b)} \quad (5-2)$$

where A_f is absorptance of the material with respect to the specific wavelength laser beam, F is the laser power density, ρ is the material mass density, L_v is the latent heat of vaporisation, C_p is the thermal capacity, T_b is the boiling temperature, t is the workpiece thickness, D is the average laser spot diameter across the thickness of workpiece, and α' is the proportional contribution of the enthalpy of reaction to the total energy density. In this study, α' was set as zero due to the lack of an exothermic reaction between assist gas and alumina sheet during cutting.

However, the assumption of Li's model is that the cut kerf is larger than beam diameter, generally in CW and/or oxidation-assisted laser cutting. In the nano-second pulsed laser cutting, the typically measured cut kerf was 185 μm on the top surface and 110 μm on bottom surface, which is smaller than the beam diameter on top

surface (300 μm) and on bottom surface (400 μm). The latent heat of fusion L_m and temperature-dependent specific heat $c(T)$ of alumina should also be considered. Hence, the Eq. (5-2) is corrected as

$$v_c \approx \frac{A_f P_0}{\rho D_{cut} h \left(L_v + L_m + \int_{T_0}^{T_b} c(T) dT \right)} \quad (5-3)$$

where P_0 is the laser power arriving on the workpiece, D_{cut} is the average cut kerf width across the depth of the workpiece, T_0 is the room temperature (300 K), $c(T)$ is the temperature-dependent specific heat. The material properties of alumina used in this study are listed in Table 5.1. The workpiece thickness is 1 mm. The typically average cut kerf width $D_{cut}=(185+110)/2=147.5 \mu\text{m}$. Under the operating conditions and power loss ($\sim 20\%$) mentioned above, the P_0 is $415 \times (1-20\%)=332 \text{ W}$. The last parameter is the absorptance, A_f , which is determined by the reflectance and the transmittance at the cut front during laser cutting.

The reflectivity of alumina ceramic is a temperature-dependent function. The temperature of the cut front is above the melting point. Based on the previous study, the reflectivity of alumina ceramic near melting point is about 70% with respect to the near-infrared wavelength (1.15 μm) light [188]. Hence, it was assumed that the absorptance at cut front (A_{front}) for the 1.06 μm wavelength laser was 30%, in this work.

In addition, the cut kerf formation could cause beam energy loss due to portion of laser beam leaking through the cut kerf without interacting with the workpiece. The beam energy loss is dependent upon the angle of inclination of cut front and the taper of the cut kerf. Therefore, assessment of the angle of cut front inclination is critical for estimation of beam energy absorption during cutting.

The angle of cut front inclination can be estimated based on the cut front model developed by Duan et al. [189], which was further simplified as a semi-circular geometric shape across the thickness (i.e. same as the taper of cut kerf). Therefore, the angle of cut front inclination (φ_{in}) can be expressed as

$$\varphi_{in} = \arctan\left(\frac{2t}{D_t - D_b}\right) \quad (5-4)$$

where t is the workpiece thickness (1 mm), D_t is the cut kerf width on the top surface of the workpiece (typically 185 μm), and D_b is the cut kerf width on the bottom surface of the workpiece (typically 110 μm). Hence, the calculated angle of cut front inclination φ_{in} is 87.85°. Figure 5.14 shows the cross-section of cut front under the optimal operating conditions, where the inclination angle of the cut front is about 86.95°. The calculated value is in good agreement with the experimental result.

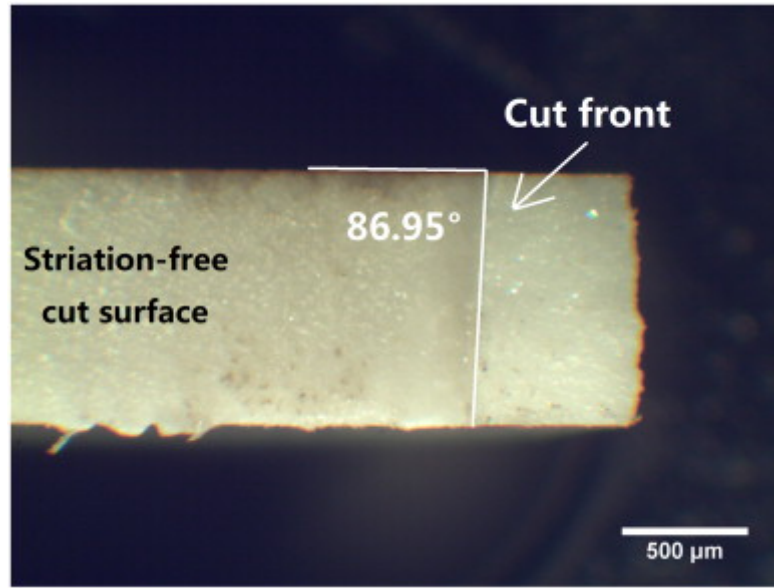


Figure 5.14 Cross-section of cut front under the optimal operating conditions (i.e. an average laser power of 415 W, pulse repetition rate of 15 kHz, cutting speed of 186 mm/min, and nozzle stand-off distance of 0.5 mm with 1 bar N_2 assist gas)

Hence, the beam energy loss from the exit end of the cut kerf L_p can be estimated as

$$L_p = \frac{D_b^2}{D_t^2} \quad (5-5)$$

Further, the laser energy absorbed in the cut kerf was also dependent upon the energy coupled into the cut kerf from the top surface of the workpiece. During the nano-second pulsed laser cutting in this study, the cut kerf width is smaller than the beam diameter across the thickness. Hence, the percentage of coupled beam energy ($A_{coupled}$) into the cut kerf from the top surface can be expressed approximately as

$$A_{coupled} = \frac{D_t^2}{D_{t-spot}^2} \quad (5-6)$$

where D_{t-spot} is the laser spot diameter on the top surface (300 μm).

Therefore, the equivalent absorptance A_f can be expressed as

$$A_f = A_{coupled} \times (1 - L_p) \times A_{front} \quad (5-7)$$

The $A_{coupled}$ calculated by Eq. (5-6) was 38.0%, the L_p calculated by Eq. (5-5) was 36.0%, and A_{front} was 30% as mentioned above. Hence, $A_f=7.30\%$ by Eq. (5-7). Substitution of these values into Eq. (5-3), the upper limit of cutting speed for striation-free cutting was hence calculated, which was 293.4 mm/min.

During pulsed laser striation-free cutting, another crucial process is to keep the molten front stable, i.e. a consistent molten front and continuous movement. Therefore, the pulses must not disturb the molten front, which requires that the pulse overlap area should be large enough (>99.8%) and the pulse advancement should be shorter than the characteristic length of heat conduction caused by the previous pulse in order to smooth the melt front movement. This process can be expressed as

$$\sqrt{\alpha_T t_p} \geq \frac{v}{f} \quad (5-8)$$

where α_T is the material thermal diffusivity ($1.83 \times 10^{-6} \text{ m}^2/\text{s}$ for alumina at average temperature of HAZ, 1040 K), t_p is the pulse duration, and f is the pulse repetition rate. For pulse repetition rate of 15 kHz (55 ns pulse duration), the cutting speed should be lower than 286 mm/min. For 12 kHz (50 ns pulse duration), the cutting speed should be lower than 217 mm/min.

Therefore, the upper limit of cutting speed should be determined by the minimum value of the above two criteria (i.e. Eqs. (3-3) and (3-8)). The upper limit of striation-free cutting speed is 286 mm/min for 15 kHz and 217 mm/min for 12 kHz. The results are very close to the experimental operating window as shown in Figure 5.12.

5.4.2.2 The lower limit of striation-free cutting speed

When the cutting speed is too low, the molten front may escape from the laser spot and the movement would be discontinuous inducing the striation formation on cut surface as shown in Figure 5.4. Therefore, the cutting speed should be higher than a threshold for continuous melt front advancement. The molten front thickness, t_{melt} , can be estimated from [190]

$$t_{melt} = \frac{(T_s - T_m) K_m}{\left(\int_{T_0}^{T_m} c(T) dT + L_m \right) \rho v \sin \phi_{in}} \quad (5-9)$$

where T_s is the melt surface temperature (2977 °C at the interface of melt and vapour), T_m is the melting temperature (2072 °C), K_m is the thermal conductivity of the melt (5.97 W/m K assumed at temperature higher than 1573 K), and v is the cutting speed.

Due to the melt film removal by vapour pressure, the laser beam movement distance during cutting through the workpiece within the beam spot (i.e. $v \times t_{drill}$) should be greater than the melt thickness in order to avoid discontinuous movement of the cut front. This criterion can be expressed as

$$v \times t_{drill} \geq \frac{(T_s - T_m) K_m}{\left(\int_{T_0}^{T_m} c(T) dT + L_m \right) \rho v \sin \phi_{in}} \Rightarrow v \geq \sqrt{\frac{(T_s - T_m) K_m}{\left(\int_{T_0}^{T_m} c(T) dT + L_m \right) \rho t_{drill} \sin \phi_{in}}} \quad (5-10)$$

The calculated result showed that the lower limit of cutting speed for striation-free cutting was 86 mm/min at a 15 kHz pulse repetition rate and 415 W laser power (where $\phi_{in}=87.85^\circ$). This prediction was in agreement with the experimental results as shown in Figure 5.12.

Basically, the developed model in this work can predict the window of operating conditions for nano-second pulsed laser striation-free cutting. It should be noted that, a low gas pressure (≤ 1.5 bar), a high pulse repetition rate (≥ 12 kHz), and a high laser average power (415 W) are three additional required conditions. The three conditions with the critical cutting speed allow the vaporisation driven material removal and

stabilise the cut front movement, by which the melt flow oscillation is prevented and the striation-free cutting can be achieved.

5.4.3 Potential methods for prevention of dross formation

Although the striation on cut surfaces can be avoided completely in this work, the operating conditions window is not for dross-free cutting by comparing with the results from previous studies [191-197]. Under the striation-free cutting conditions, i.e. the positive focal plane position, low gas pressure, relatively low cutting speed, and large focused beam diameter, the dross is likely formed and attached on the bottom surface (as Figure 5.5). The post-mechanical process is still necessary to remove the dross although the low mechanical strength of dross makes them easy removed. In order to further achieve dross-free cutting, some potential assisted techniques without changing the operating conditions of striation-free cutting should be employed in future.

The anti-spatter composite coating (ASCC) method has been successfully used for spatter prevention in laser drilling [198,199]. It could also be applied in laser striation-free cutting for dross prevention. This method is flexible and suitable to profile cuts. Developing a proper composite coating that has a good adherent force to ceramic surface and is removed easily without pollution on the ceramic surface is necessary.

The off-axial assist gas nozzle is another alternative technique to achieve dross-free cutting without changing the major operating conditions. It improves the efficiency of assist gas to remove the molten material and avoid the dross formation [58, 59]. However, this technique needs a de Laval nozzle with a high gas pressure, which is out of the operating condition window mentioned above. Improving the off-axial nozzle to achieve low gas pressure dross-free cutting within the striation-free cutting operating window is essential in future. However, profile cut is still the major challenge to the off-axial nozzle technique, since the gas flow must be aimed at the cut front in real time during cutting.

The water assisted technique can be employed as well to reduce dross formation in laser cutting [200]. In this technique, water flow is introduced only on the bottom surface of the workpiece to reduce the HAZ and dross formation. The operating conditions for striation-free cutting can be retained and profile cuts can be achieved smoothly. However, it is necessary to study the water cooling effect on the cut front, since the water cooling effect may induce some undesired effects such as vapour condensation, melt oscillation, etc. within the cut kerf.

These potential methods for prevention of dross formation in laser striation-free cutting of alumina sheets will be investigated in our future work.

5.5 Conclusions

Striation-free cutting of 1 mm thick alumina sheets has been demonstrated for the first time using a 400 W nano-second pulsed DPSS Nd:YAG laser in this chapter. The experimental results show that nano-second pulsed laser can achieve striation-free cutting but the striation characteristics are very sensitive to the operating conditions. The optimal operating window for striation-free cutting is an average laser power of 360–420 W (with a typical pulse peak power of 4.31×10^5 – 6.81×10^5 W, pulse energy of 23.7–34.1 mJ, and fluence of 33.51–48.27 J/cm²), pulse repetition rate of 12–15 kHz, pulse duration of 50–55 ns, cutting speed of 120–270 mm/min, focal plane position of 0–0.5 mm, and nozzle standoff distance of 0.5–1 mm with 1–1.5 bar nitrogen assist gas. The unusual operating conditions were different from the typically used parameters for standard laser cutting or CW laser striation-free cutting. The high peak laser power enables an evaporation governed cut process, by which the melt oscillation driven striation formation is suppressed. The high pulse repetition rate is to stabilise the cut front movement, which prevents the discontinuous cut process related striation formation. The proper nozzle standoff distance with a low gas pressure guarantees a smooth and stable gas flow within the cut kerf. Compared with other gases, the nitrogen assist gas provides a good balance of thermal conductivity, ionisation energy, and costs for stable cut process avoiding the striation formation. Furthermore, the cutting speed should be carefully chosen, which must match the average laser power and pulse repetition rate to keep a

vaporisation driven and continuous cut process. In order to identify the operating window of cutting speed, a mathematical model modified from the existing theoretical model for vaporisation governed material removal and with the inclusion of pulsed laser characteristics was developed in this work. The predicted operating window by this model was in good agreement with the experimental result. The model allows one to determine the optimum cutting parameters for striation-free cutting of ceramics. Furthermore, the mechanism of nano-second pulsed laser striation-free cutting was pointed out to be the combination of evaporation driven material removal and continuous cut front movement. This work supports the existing theory for CW laser striation-free cutting of metallic materials and further extends it to the pulsed laser striation-free cutting of ceramic materials. One problem remaining to be solved is the dross formation. This problem is associated with the current laser cutting system and the employed parameters. A number of potential approaches are given in this work for potential dross prevention. Further investigation is necessary to avoid dross formation during striation-free cutting.

Chapter 6

Conclusions and Future Recommendations

6.1 Conclusions

An investigation into low-defect laser cutting/machining of engineering alumina ceramics was conducted in this project, in which different laser systems, processing techniques and alumina ceramics with various thicknesses were employed. Crack and surface finishes are identified as the major quality defects in laser cutting/machining of ceramics. The project explored the potential of various lasers in ceramic machining and introduced several novel methods to significantly reduce these quality defects for different laser processing techniques. The present work opens up new opportunities for high-quality laser cutting/machining of engineering ceramics. The main findings and conclusions presented in the thesis are summarised as follows:

6.1.1 Fibre laser crack-free cutting of thick-section alumina

The major challenge in laser fusion cutting of thick-section ceramics is to overcome the thermal-stress induced cracking, which may lead to catastrophic breakdown of the material integrity. In order to improve the cut quality and achieve crack-free cutting of thick-section ceramics, a high-power fibre laser was first employed in this work and main conclusions include:

- The developed three-dimensional (3D) finite element (FE) model was found to have the power to simulate the transient temperature and thermal-stress distribution together with material removal during high-power fibre laser fusion cutting of thick-section alumina. The temperature field and thermal-stress distribution are difficult to be measured experimentally.

- Based on the 1st principal theory, the crack formation during laser fusion cutting can be simulated by the 3D FE model. The predicted crack propagation was in agreement with the experimental result. It opens a new approach to numerically investigate the effect of process parameters on crack formation in laser cutting of ceramics.
- Through numerical simulations and experiments, it has been found that high laser peak power (1 kW), short pulse duration (5 ms) and low pulse repetition rate (10 Hz) are beneficial to single-pass crack-free cutting of thick-section alumina. However, the feed rate (from 0.5 to 1.5 mm/s) has a dual effect (promoting or damaging) depending on the assist gas efficiency.
- A transition from compressive to tensile stresses was found when the laser cutting parameters changed, by which it is possible to identify a threshold of parameters for crack-free cutting. Based on the numerical simulation, the pulse duration shorter than 20 ms and the pulse repetition rate lower than 50 Hz were found to be essential for crack-free cutting of 6 mm thick alumina.
- The process parameters were further optimised based on the present study in order to improve the process efficiency. For the 1 kW fibre laser used in this study, the high laser peak power (1 kW), short pulse duration (5 ms) and modest pulse repetition frequency (30 Hz) was found out to improve the feed rate up to 1.5 mm/s for crack-free cutting of 6 mm thick alumina.

6.1.2 CO₂ laser underwater machining of deep cavities in alumina

Compared with laser cutting, laser machining of engineering ceramics face more challenges due to the further requirement of machine depth control and strict finish quality. In this work, 100 W CO₂ laser crack-free milling mm-deep cavities in alumina was investigated by means of underwater machining. The main findings are summarised as follows:

- CO₂ laser underwater machining has been found to have the capability of reducing substrate defects such as recast layer, dross, cracking and thermal damage that is typically found in air machining.
- The machined side-wall surface in water ($R_a = 5.12 \mu\text{m}$, $R_z = 23.02 \mu\text{m}$) was much smoother than in air ($R_a = 13.16 \mu\text{m}$, $R_z = 43.68 \mu\text{m}$) as the effect of water dynamics produced a high recoil pressure in machining region to eject the molten material from the cavity and prevent recast formation.
- Finite Element (FE) modelling technique and Smooth Particle Hydrodynamic (SPH) modelling technique were employed to understand the effect of water on crack resistance and debris removal during underwater machining. The FE model shows that the temperature field and corresponding thermal-stress distribution is dramatically reduced in underwater machining, which is beneficial for crack resistance. The SPH simulation indicates that the behaviour and significance of water flow in the underwater machining process, in which the water flow carries the ejected molten particles away from the machined region to resist redeposition. Meanwhile, the turbulent water flow near the machined region induces water into the machined groove for chilling, which would reduce the thermal damage. The microstructures of machined region validate the intensive cooling processes during laser machining in water.
- The machined kerf width is strongly affected by the water layer thickness, whereas the kerf depth is controlled by both the laser pass number and water layer thickness.
- The optimal water layer thickness is 3–4 mm above the surface of workpiece to guarantee a sufficient cooling effect and a high material removal rate. Also the thickness of water layer provided an adequate space to remove molten material particles from the machined region.
- Several polygon cavities were demonstrated by CO₂ laser underwater machining with the optimised parameters, i.e. 100 scanning cycles, 60 W laser power and 10 mm/s scanning speed with a scanning line interval of 0.25

mm. The machining depth is greater than 2-mm and the machining rate is up to 2.95 mm³/min.

6.1.3 Nano-second pulsed laser striation-free cutting of alumina sheets

In addition to cracking, striation (periodical lines) formation on cut surface is another major challenge for high-quality laser cutting of ceramic materials. The striation affects the surface roughness and geometry precision of laser cut products. Although high cut quality has been demonstrated by short/ultrashort pulsed lasers, striation formation was still considered as an inherent defect in pulsed laser cutting. In order to further improve the finish quality of laser ceramic cutting for denser circuit patterns and device miniaturisation, this work explores the potential of high-power pulsed laser striation-free cutting of alumina sheets. The main conclusions are summarised as follows:

- Striation-free cutting of 1 mm thick alumina sheets is achieved using a 400 W nano-second pulsed DPSS Nd:YAG laser.
- The mechanism of nano-second pulsed laser striation-free cutting is the combination of evaporation driven material removal and continuous cut front movement.
- The high peak laser power enables an evaporation governed cut process, by which the melt oscillation driven striation formation can be suppressed. The high pulse repetition rate is to stabilise the cut front movement, which prevents the striation formation related with discontinuous cut processes. The proper nozzle standoff distance with a low gas pressure guarantees a smooth and stable gas flow within the cut kerf, in order to prevent the potential striation formation caused by the melt oscillation and droplets periodical re-deposition.
- The cutting speed should be carefully chosen, which must be matched with the average laser power and pulse repetition rate to keep a vaporisation driven and continuous cut process. In order to identify the operating window

of cutting speed, a mathematical model modified from the existing theoretical models for vaporisation governed material removal and with the inclusion of pulsed laser characteristics was developed in this work. The model allows one to determine the optimum cutting parameters for striation-free cutting of ceramics. The prediction was in good agreement with the experimental operating window.

- The optimal operating window for DPSS Nd: YAG nano-second pulsed laser striation-free cutting of alumina sheets is an average laser power of 360–420 W (with a typical pulse peak power of 4.31×10^5 – 6.81×10^5 W, pulse energy of 23.7–34.1 mJ, and fluence of 33.51–48.27 J/cm²), pulse repetition rate of 12–15 kHz, pulse duration of 50–55 ns, cutting speed of 120–270 mm/min, focal plane position of 0–0.5 mm, and nozzle standoff distance of 0.5–1 mm with 1–1.5 bar nitrogen assist gas.

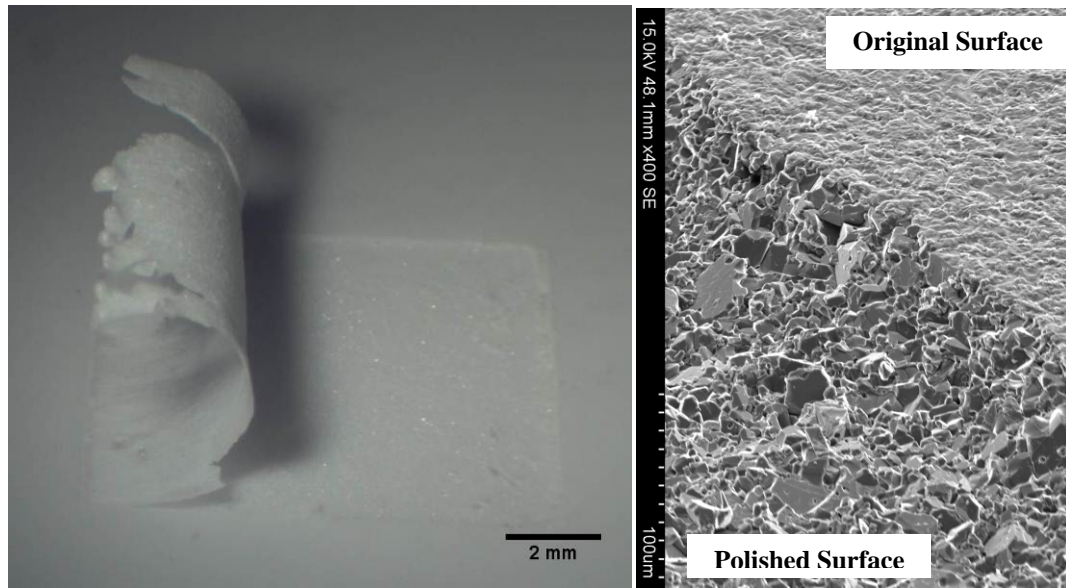
Based on the overall work presented in this thesis, it can be concluded that high-quality cutting/machining of alumina can be achieved by various lasers. The high-power fibre laser (1 kW) can be used to achieve crack-free cutting of 6 mm thick alumina. The low power CW CO₂ laser (100 W) demonstrates the capability of crack-free and high surface finish quality machining of deep cavities in alumina, incorporating with fluid assistance. The high-power nano-second pulsed laser (400 W) demonstrates the feasibility for high-quality precision cutting of alumina sheets, in which striation is eliminated within a narrow operating window. The three parts of the present work reveal the general mechanism and approach to reduce defects in laser cutting/machining of alumina ceramics. It opens up new opportunities for other lasers to achieve high quality cutting/machining of more ceramic materials.

6.2 Future Recommendations

6.2.1 Laser controlled fracture polishing of cut surface

The present study on fibre laser crack-free cutting of thick-section alumina focused on the crack formation during laser cutting. In addition to crack, the recast layer on cut surface is another defect in thick-section ceramic cutting, which degrades the process quality. Although the process parameters can be optimised to reduce the thickness of recast layer, the complete elimination seems to be impossible in laser cutting of thick-section ceramics, especially for those with melt points (e.g. alumina and zirconia). The commonly used method for recast layer removal is diamond grinding after laser cutting. It faces the same challenges as those in mechanical machining of ceramics. Therefore, a dual-step laser machining technique should be developed in future. The first step is laser cutting, in which the process parameters are selected for crack-free cutting regardless of recast layer formation. Then, a process similar to laser controlled fracture milling is performed on the cut surface to remove the recast layer, which can be named the laser controlled fracture polishing technique. In this project, a feasibility of laser peeling of ceramics was studied via a cross-scanning of alumina surface by a 100 W CW CO₂ laser (as Figure 6.1). It can be seen that a chip layer was peeled away from the base material and a relatively smooth subsurface was exposed. As shown in Figure 6.1(b), the roughness of the subsurface was determined by the size of crystalline grains. Figure 6.2 further illustrates the microstructure of the micro-chip, of which the thickness is 70 µm. It can be seen that there are two different microstructures within the micro-chip along thickness. The microstructure in the top half of the micro-chip is similar as the recast layer (as discussed in Chapter 4). It means that the top half was melted and resolidified during scanning. The bottom half of the micro-chip is same as the base material (as Figure 6.1(b)). The experimental result indicates that the formation of the micro-chip should be attributed to controlled fracture during laser scanning of the ceramic surface. The mechanism of controlled fracture polishing is similar as that of controlled fracture milling presented by Tsai et al [140]. Using the novel technique, the cut surface of 6-mm-thick alumina cut by a 1 kW fibre laser was polished as shown in Figure 6.3. The recast layer on cut surface was completely removed

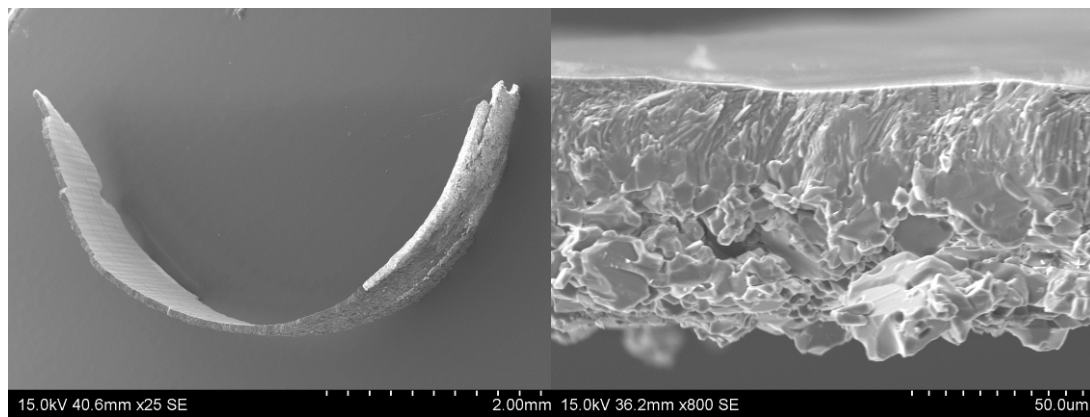
without any thermal damage. The effect of process parameters on polishing quality and efficiency should be investigated in the future work.



(a)

(b)

Figure 6.1 Laser controlled fracture polishing of alumina surface. (a) The Optical photograph after scanning. (b) The microstructure of polished and original surface



(a)

(b)

Figure 6.2 The micrograph of a micro-chip peeled off from the polished surface. (a) The overview and (b) the cross-section microstructure of the micro-chip

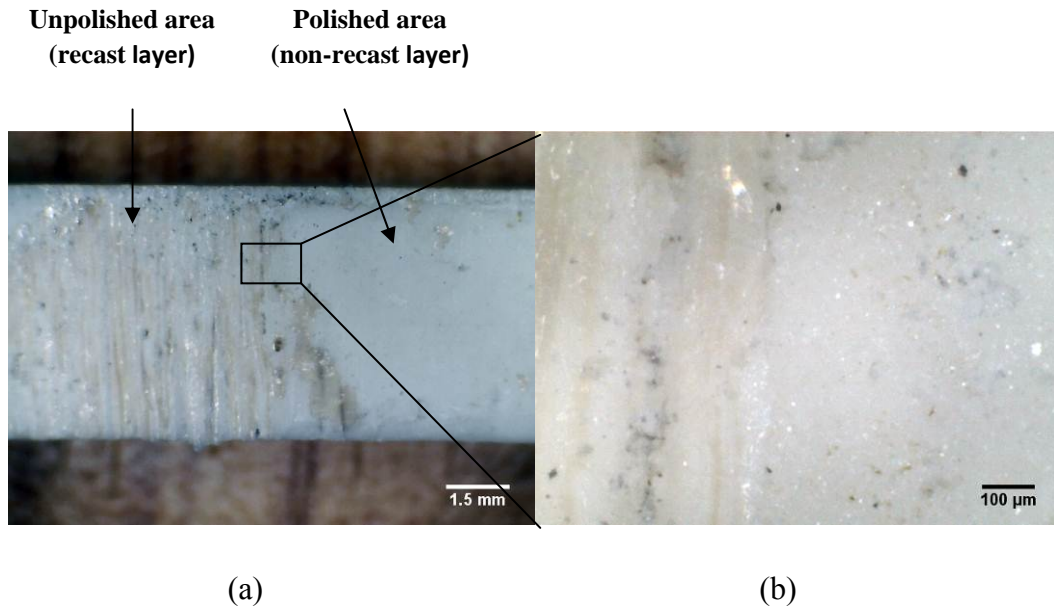


Figure 6.3 (a) An overview of the partially polished 6-mm-thick alumina cut surface and (b) a close-up view of the boundary between unpolished area (left) and polished area (right)

6.2.2 High power pico-second pulsed laser machining

Previous publications have demonstrated the capability of ultra-short pulsed lasers in high-quality micro-cutting/machining of ceramic materials. Nowadays, high power picosecond lasers (up to 400 W of average laser power) are commercially available, which may combine the high quality of ultra-short pulsed laser machining and the high material removal rate of high-power laser machining. A new era would be opened up for ceramic cutting/machining. The major challenges in high-power ultra-short pulsed laser cutting/machining may be the fundamental physical phenomena, such as striation formation, plasma control, nano-sized particles ejection, etc. rather than crack and recast layer formation. Therefore, the future work on high-power ultra-short pulsed laser machining should focus on the interaction of laser pulse with material as well as the physical processes related to the unique finish quality.

6.2.3 Multi-physical numerical simulation of laser cutting/machining

For laser cutting/machining of engineering ceramics, the future work should also include numerical simulation. The hydrodynamic of molten material (and water flow during underwater machining), the aerodynamic of assist gas, the thermal effect of laser irradiating, and their interaction should be investigated by a novel numerical technique, such as the combination of FEM (for thermal and structural simulation) and CFD (for fluid simulation). The behaviours of bulk material, molten/evaporated material in machined area, water/assist gas flow, and their interaction need to be considered and simulated in a multi-physical model. With the development of computational simulation software, the SPH and the ALE (Arbitrary Lagrange-Euler) methods open up new opportunities to simulate the multi-physical processes. The success in the multi-physical model may significantly contribute to the understanding of the mechanisms in laser cutting/machining of ceramic materials.

References

- [1] A.N. Samant, N.B. Dahotre. *Laser machining of structural ceramics – a review*, Journal of the European Ceramic Society **29** (2009) 969-993
- [2] Y. Liang, S.P. Dutta. *Application trend in advanced ceramic technologies*, Technovation **21** (2001) 61-65
- [3] I.P. Tuersley, A. Jawaid, I.R. Pashby. *Review: various methods of machining advanced ceramic materials*, Journal of Material Processing Technology **42** (1994) 377-390
- [4] J.Y. Shen, C.B. Luo, W.M. Zeng, X.P. Xu, Y.S. Gao. *Ceramics grinding under the condition of constant pressure*, Journal of Materials Processing Technology **129** (2002) 176-181
- [5] S. Richlen. *Opportunities for the industrial application of continuous fiber ceramic composites*, Ceramic Engineering and Science Proceedings **11**(7/8) (1990) 576-577
- [6] *Technical and Advanced Structural Ceramics*, BCC Research (2008), available from: <http://www.bccresearch.com/report/advanced-structural-ceramics-avm011c.html>, 26/06/2012
- [7] P. Wray. *Market for structural ceramics to reach \$3.7 billion by 2012*, Copyright@ The American Ceramic Society, available from: <http://ceramics.org/ceramictechtoday/2008/10/31/market-for-structural-ceramics-to-reach-37-billion-by-2012/>, 10/03/2011
- [8] V. Vikulin, I. Kelina, A. Shatalin, L. Rusanova. *Advanced ceramic structural materials*, Refractories and Industrial Ceramics **45** (2004) 383-386
- [9] W. Perrie, A. Rushton, M. Gill, P. Fox, W. O'Neill. *Femtosecond laser microstructuring of alumina ceramic*, Applied Surface Science **248** (2005) 213-217
- [10] R. Riedel. *Handbook of Ceramic Hard Materials*, Weinheim: Wiley-Vch Verlag GmbH (2000)
- [11] R. Morrell. *Handbook of Properties of Technical & Engineering Ceramics – Part 2. Data Reviews, Section I. High-alumina ceramics*, London: Her Majesty's Stationery Office (1987)
- [12] P. Auerkari. *Mechanical and physical properties of engineering alumina ceramics*, Finland: VTT manufacturing Technology (1999)
- [13] A.R. Barron. *Ceramic Processing of Alumina*, Copyright@ Connexions, available from: <http://cnx.org/content/m22376/latest/>, 10/03/2011

- [14] M. Kutz. *Handbook of Materials Selection – Part 2. Major Materials, Section 14. Overview of Ceramics Materials, Designs, and Application*, edited by R.N. Katz, New York: John Wiley & Sons, Inc. (2002)
- [15] *Processing*, Copyright@ Dynamic-Ceramic Ltd., available from: <http://www.dynacer.com/process.htm>, 10/03/2011
- [16] D. Kopeliovich. *Methods of shape forming ceramic powders*, Copyright@ SubsTech (Substances & Technologies), available from: http://www.substech.com/dokuwiki/doku.php?id=methods_of_shape_forming_ceramic_powders, 10/03/2011
- [17] D. Kopeliovich. *Solid state fabrication of Metal Matrix Composites*, Copyright@ SubsTech (Substances & Technologies), available from: http://www.substech.com/dokuwiki/doku.php?id=solid_state_fabrication_of_metal_matrix_composites, 11/03/2011
- [18] *Traditional Ceramics Applications*, Copyright@ Aqualon, available from: [http://www.aqualon.ashland.com/industries/Specialties_Solutions/Applications/Ceramics/Traditional Ceramics and Glazes.aspx](http://www.aqualon.ashland.com/industries/Specialties_Solutions/Applications/Ceramics/Traditional_Ceramics_and_Glazes.aspx), 11/03/2011
- [19] *Tape Casting*, Copyright@ Griff Paper and Film, available from: <http://www.paperandfilm.com/tapecasting.aspx>, 11/03/2011
- [20] *Manufacturing Methods, Step: 2 Green machining*, Copyright@ STC Superior Technical Ceramics Corps, available from: <http://www.ceramics.net/methods/steptwo.html>, 11/03/2011
- [21] K. Imen, S.D. Allen. *Pulsed CO₂ laser drilling of green alumina ceramic*, IEEE Transactions on Advanced Packaging **22**(4) (1999) 620-623
- [22] D. Guo, K. Cai, J. Yang, Y. Huang. *Spatter-free laser drilling of alumina ceramics based on gelcasting technology*, Journal of the European Ceramic Society **23** (2003) 1263-1267
- [23] B.H. Desilets. *Mechanism of cavity formation in unfired ceramic by electron-beam machining*, Journal of Vacuum Science and Technology **15**(3) (1978) 1964-1982
- [24] K. Horio, T. Terabayashi, N. Taniguchi. *Beam defocus effect in electron beam machining of green ceramic sheet*, CIRP Annals – Manufacturing Technology **36**(1) (1987) 95-98
- [25] M.A. Sarfaraz, Y. Yau, N.S. Sabdhu. *Electron beam machining of ceramic green-sheets for multilayer ceramic electronic packaging applications*, Nuclear Instruments and Methods in Physics Research Section B: Beam Interaction with Materials and Atom **82**(1) (1993) 116-120

- [26] *Dimensions and shrinkage*, Copyright@ Brevier Technical Ceramics, available from: http://www.keramverband.de/brevier_engl/4/1/4_1_5.htm, 11/03/2011
- [27] G. Chryssolouris, N. Anifantis, S. Karagiannis. *Laser assisted machining: an overview*, Journal of Manufacturing Science and Engineering **119** (1997) 766-769
- [28] T.B. Thoe, D.K. Aspinwall, M.L.H. Wise. *Review on ultrasonic machining*, International Journal of Machine Tools and Manufacture **38**(4) (1998) 239-255
- [29] J.P. Choi, B.H. Jeon, B.H. Kim. *Chemical-assisted ultrasonic machining of glass*, Journal of Materials Processing Technology **191** (2007) 153-156
- [30] E. Savrun, M. Taya. *Surface characterization of SiC whisker/2124 aluminium of Al₂O₃ composites machined by abrasive water jet*, Journal of Materials Science **23** (1988) 1453-1458
- [31] E. Makino, T. Sato, Y. Yamada. *Photoresist for photochemical machining alumina ceramic*, Precision Engineering **9**(3) (1987) 153-157
- [32] J.M. Park, S.C. Jeong, H.W. Lee, H.D. Jeong, E. Lee. *A study on the chemical mechanical micro-machining (C3M) process and its application*, Journal of Materials Processing Technology **130-131** (2002) 390-395
- [33] T.C. Lee, W.S. Lau. *Some characteristics of electrical discharge machining of conductive ceramics*, Materials and Manufacturing Processing **6**(4) (1991) 635-648
- [34] B. Bhattacharyya, B.N. Doloi, S.K. Sorkhel. *Experimental investigations into electrochemical discharge machining (ECDM) of non-conductive ceramic materials*, Journal of Materials Processing Technology **95** (1999) 145-154
- [35] S.K. Chak, P.V. Rao. *Trepanning of Al₂O₃ by electro-chemical discharge machining (ECDM) process using abrasive electrode with pulsed DC supply*, International Journal of Machine Tools and Manufacture **47** (2007) 2601-2070
- [36] P.C. Pandey, H.S. Shan. *Modern Machining Processes*, New Delhi: McGraw Hill (1980)
- [37] M.U. Islam, G. Campbell. *Laser machining of ceramics: A review*, Material and Manufacturing Processes **8**(6) (1993) 611-630
- [38] W.M. Steen. *Laser material processing – an overview*, Journal of Optics A - Pure and Applied Optics **5** (2003) s3-s7

- [39] *High Power Fibre Lasers for Industrial Applications*, Copyright@ IPG Photonics Corp., available from: http://www.ipgphotonics.com/Collateral/Documents/English-US/HP_Brochure.pdf, 11/03/2011
- [40] G. Chryssolouris. *Laser Machining Theory and Practice*, New York: Springer-Verlag (1991)
- [41] *Laser Cutting*, Copyright@ Rofin-Baasel UK Ltd, available from: http://www.keramverband.de/brevier_engl/4/1/4_1_5.htm, 12/03/2012
- [42] D.A. Belforte, K.H.J. Buschow, W.C. Robert, C.F. Merton, I. Bernard, J.K. Edward, M. Subhash, V. Patrick. *Laser Cutting*, in *Encyclopedia of Materials: Science and Technology*, Oxford: Elsevier (2001)
- [43] K. Li, P. Sheng. *Plane Stress Model for Fracture of Ceramics during Laser Cutting*, *International Journal of Machine Tools and Manufacture* **35**(11) (1995) 1493-1506
- [44] G. Lu, E. Siores, B. Wang. *An empirical equation for crack formation in the laser cutting of ceramic plates*, *Journal of Materials Processing Technology* **88** (1999) 154-158
- [45] S.H. Lee, S.E. Ahn. *A probabilistic Model for Crack Formation in Laser Cutting of Ceramics*, *JSME International Journal Series C* **46**(4) (2003) 1591-1597
- [46] I. Black, K.L. Chua. *Laser cutting of thick ceramic tile*, *Optics and Laser Technology* **29**(4) (1997) 193-205
- [47] C. Durand, M. Ramulu, R.S.T. Pierre, J. Machan. *An experimental analysis of a Nd: YAG laser cutting process for machining silicon nitride*, *International Journal of Product Res* **34**(5) (1996) 1417-1428
- [48] X. Chen, X. Liu. *Short pulsed laser machining: how short is short enough?*, *Journal of Laser Applications* **11**(6) (1999) 268-272
- [49] F. Quintero, J. Pou, F. Lusquinos, M. Boutinguiza, R. Soto, M. Perez-Amor. *Nd: YAG laser cutting of advanced ceramics*, *Proceedings of SPIE* **4419** (2001) 756-760
- [50] M.R.H. Knowles, G. Rutterford, D. Karnakis, A. Ferguson. *Micro-machining of metals, ceramics and polymers using nanosecond lasers*, *International Journal of Advanced Manufacturing Technology* **33** (2007) 95-102

- [51] D.M. Karnakis, M.R.H. Knowles, P.V. Petkov, T. Dobrev, S.S. Dimov. *Surface integrity optimisation in ps-laser milling of advanced engineering materials*, Proceedings of the Fourth International WLT – Conference on Lasers in Manufacturing, Munich (2007)
- [52] X.C. Wang, H.Y. Zheng, P.L. Chu, J.L. Tan, K.M. The, T. Liu, Bryden C.Y. Ang, G.H. Tay. *High quality femtosecond laser cutting of alumina substrates*, Optics and Lasers in Engineering **48** (2010) 657-663
- [53] I. Black, S.A.J. Livingstone, K.L. Chua. *A laser beam machining (LBM) database for the cutting of ceramic tile*, Journal of Materials Processing Technology **84** (1998) 47-55
- [54] J. Pou, F. Quintero, L. Lusquinos, M. Larosi, R. Soto, M. Perez-Amor. *Nd: YAG laser cutting of mullti-alumina*, Proceedings of ICALEO'99, Laser Materials Processing, LIA **87** (1999) c155-c175
- [55] F. Quintero, J. Pou, F. Lusquinos, M. Larosi, R. Soto, M. Perez-Amor. *Cutting of ceramics plates by optical fiber guided Nd: YAG laser*, Journal of Laser Applications **13**(2) (2001) 84-88
- [56] A.N. Samant, N.B. Dahotre. *Differences in physical phenomena governing laser machining of structural ceramics*, Ceramics International **35** (2009) 2093-2097
- [57] W. Perrie, Al Rushton, M. Gill, P. Fox, W. O'Neill. *Femtosecond laser micro-structuring of alumina ceramics*, Applied Surface Science **248** (2005) 213-217
- [58] F. Quintero, J. Pou, F. Lusquinos, M. Boutinguiza, R. Soto, M. Perez-Amor. *Comparative study of the influence of the gas injection system on the Nd: yttrium-aluminum-garnet laser cutting of advanced oxide ceramics*, Review of Scientific Instruments **74**(9) (2003) 4199-4205
- [59] F. Quintero, J. Pou, J.L. Fernandez, A.F. Doval, F. Lusquinos, M. Boutinguiza, R. Soto, M. Oerez-Amor. *Optimization of an off-axis nozzle for assist gas injection in laser fusion cutting*, Optics and Lasers in Engineering **44** (2006) 1158-1171
- [60] O.V. Mazurin, M.V. Streltsina, T.P. Shvaikovskaya. *Handbook of Glass Data, Part A: Silica Glass and Binary Silicate Glasses*, Amsterdam: Elsevier (1983)
- [61] P.F. Paradis, T. Ishikawa. *Surface tension and viscosity measurements of liquid and undercooled alumina by containerless techniques*, Japanese Journal of Applied Physics **44**(7A) (2005) 6082-5085

- [62] A.T. Dinsdale, P.N. Quedsted. *The viscosity of aluminium and its alloys – A review of data and models*, Journal of Materials Science **39**(24) (2003) 7221-7228
- [63] F. Quintero, J. Pou, F. Lusquinos, M. Boutinguiza, R. Soto, M. Oerez-Amor. *Quantitative evaluation of the quality of the cuts performed on mullite-alumina by Nd: YAG laser*, Optics and Lasers in Engineering **42** (2004) 327-340
- [64] F. Quintero, J. Pou, F. Lusquinos, M. Boutinguiza, R. Soto, M. Perez-Amor. *Comprehensive assessment of the CO₂ laser cut quality of ceramics with different assist gas injection systems*, Journal of Laser Applications **16**(4) (2004) 212-220
- [65] A. Riveiro, J. Pou, F. Quintero, F. Lusquinos, R. Comesanan. *Applications of a novel supersonic laser cutting head*, Pacific International Conference on Applications of Lasers and Optics (2008) Invited Paper
- [66] P. Pena, J. Bartolome, J. Requena, J.S. Moya. *Mullite-alumina functionally gradient ceramics*, Journal de physique IV France **03**(C7) (1993) 1261-1266
- [67] E. Kacar, M. Mutlu, E. Akman, A. Demir, L. Candan, T. Canel, V. Gunay, T. Sinmazcelik. *Characterization of the drilling alumina ceramic using Nd: YAG pulsed laser*, Journal of Materials Processing Technology **209** (2009) 2008-2014
- [68] L. Ji, Y. Yan, Y. Bao, Y. Jiang. *Crack-free cutting of thick and dense ceramics with CO₂ laser by single-pass process*, Optics and Lasers in Engineering **46** (2008) 783-790
- [69] L. Li, M. Sobih, P.L. Crouse. *Striation-free Laser Cutting of Mild Steel Sheets*, Annals of the CIRP **56**(1) (2007) 193-196
- [70] A. Invarson, J. Powell, J. Kmalu, C. Magnusson. *The oxidation dynamics of laser cutting of mild steel and the generation of striations on the cut edge*, Journal of Materials Processing Technology **40** (1994) 359-374
- [71] A.F. Kaplan. *An analytical model of metal cutting with a laser beam*, Journal of Applied Physics **79**(5) (1996) 2198-2207
- [72] K. Chen, Y.L. Yao, V. Modi. *Numerical simulation of oxidation effect in laser cutting process*, International Journal of Advanced Manufacturing Technology **15** (1999) 835-842
- [73] L.M. Wee, L. Li. *An analytical model for striation formation in laser cutting*, Applied Surface Science **247** (2005) 277-284

- [74] G.V. Ermolaev, O.B. Kovalev, A.M. Orishich, V.M. Fomin. *Mathematical modelling of striation formation in oxygen laser cutting of mild steel*, Journal of Physics D: Applied Physics **39** (2006) 4236-4244
- [75] D. Schuocker. *Dynamic phenomena in laser cutting and cut quality*, Applied Physics B: Lasers and Optics **40** (1986) 9-14
- [76] M. Vicanech, G. Simon, H.M. Urbassek, I. Decker. *Hydrodynamic instability of melt flow in laser cutting*, Journal of Physics D: Applied Physics **20** (1986) 140-145
- [77] N.K. Makashev. *Gas hydrodynamics of CW laser cutting of metals in inert gas*, Proceedings of SPIE - Industrial Lasers and Laser Material Processing **2257** (1993) 2-9
- [78] F. O. Olsen, L. Alting. *Cutting front formation in laser cutting*, Annals of CIRP – Manufacturing Technology **38**(1) (1989) 215-218
- [79] H. Kaebernick, A. Jeromin, P. Mathew. *Adaptive control for laser cutting using striation frequency analysis*, Annals of CIRP – Manufacturing Technology **41**(1) (1998) 137-140
- [80] M. Sobih, P.L. Crouse, L. Li. *Striation-free fibre laser cutting of mild steel sheets*, Applied Physics A – Materials Science & Processing **90** (2008) 171-174
- [81] M. Sobih, P.L. Crouse, L. Li. *Elimination of striation in laser cutting of mild steel*, Journal of Physics D: Applied Physics **40** (2007) 6908-6916
- [82] L.M. Wee, P.L. Crouse, L. Li. *A statistical analysis of striation formation during laser cutting of ceramics*, International Journal of Advanced Manufacturing Technology **36** (2008) 699-706
- [83] X. Chen, L. Ji, Y. Bao, Y. Jiang. *High Quality Fibre Laser Cutting of Electronic Alumina Ceramics*, Advanced Materials Research **154-155** (2011) 911-922
- [84] N.B. Dahotre, S.P. Harimkar. *Laser fabrication and machining of materials*, New York: Springer (2008)
- [85] Z. Zhang, M.F. Modest. *Temperature-Dependent Absorptance of ceramics for Nd: YAG and CO₂ laser processing applications*, Journal of Heat Transfer **120** (1998) 322-327
- [86] M.W. Chase, C.A. Davies, J.R. Downey, D.J. Frurip, R.A. McDonald, A.N. Syverud. *JANAF Thermochemical Tables*, Washington DC: National Bureau Standards (1985)

- [87] M. Khelkhal, F. Herlemont. *Determination of effective optical constants of infrared CO₂ waveguide laser materials*, Applied Optics **31**(21) (1992) 4175-4181
- [88] A.N. Samant, B. Du, N.B. Dahotre. *In-situ surface absorptivity prediction during 1.06 μm wavelength laser low aspect ratio machining of structural ceramics*, Physica Status Solidi **206**(7) (2009) 1433-1439
- [89] S.Y. Bang, M.F. Modest. *Multiple reflection effects on evaporative cutting with a moving CW laser*, Journal of Heat Transfer **113** (1991) 663-669
- [90] X. Xie, L. Li, X. Wei, W. Hu. *Distribution of the intensity absorbed by evaporative front in laser cutting nonmetallic material*, Optics and Lasers in Engineering **46** (2008) 604-613
- [91] J.G. Andrew, D.R. Atthey. *Hydrodynamic limit penetration of a material by a high-power beam*, Journal of Physics D – Applied Physics **9** (1976) 2181-2194
- [92] J. Mazumdar, W.M. Steen. *Heat transfer model for CW laser material processing*, Journal of Applied Physics **51** (1980) 941-947
- [93] F. Quintero, F. Varas, J. Pou, F. Lusquinos, M. Boutinguiza, R. Soto, M. Perez-Amor. *Theoretical analysis of material removal mechanisms in pulsed laser fusion cutting of ceramics*, Journal of Physics D: Applied Physics **38** (2005) 655-666
- [94] M.F. Modest. *Laser machining of ablating/decomposing materials through cutting and drilling models*, Journal of Laser Applications **9** (1997) 137-145
- [95] S. Roy, M.F. Modest. *CW laser machining of hard ceramics. Part I: effects of three-dimensional conduction variable properties and various laser parameters*, International of Journal of Heat and Mass transfer **36**(14) (1993) 3515-3528
- [96] M.J. Kim, J. Zhang. *Finite element analysis of evaporative cutting with a moving high energy pulsed laser*, Applied Mathematical Modelling **25**(3) (2001) 203-220
- [97] H.K. Tonshoff, H. Kappel. *Surface modification of ceramics by laser machining*, CIRP Annual – Manufacture Technology **47**(1) (1998) 471-474
- [98] C.Y Ho, J.K. Lu. *A closed form solution for laser drilling silicon nitride and alumina ceramics*, Journal of Materials Processing Technology **140** (2003) 260-263

- [99] H. Beyer, W. Ross, R. Rudolph, A. Michaelis, J. Uhlenbusch, W. Wiol. *Interaction of CO₂ laser pulses of microsecond duration with Al₂O₃ ceramic substrates*, Journal of Applied Physics **70**(1) (1991) 75-81
- [100] B.S. Yilbas, C. Karatas, A.F.M. Arif, B.J. Abdul Aleem. *Laser gas assisted nitriding of alumina surfaces*, Surface Engineering **25**(3) (2009) 235-240
- [101] A.S. Kuar, B. Doloi, B. Bhattacharyya. *Modelling and analysis of pulsed Nd: YAG laser machining characteristics during micro-drilling of zirconia (ZrO₂)*, International Journal of Machine tools and Manufacture **46**(12-13) (2006) 1301-1310
- [102] S. Harimkar, N.B. Dahotre. *Laser assisted densification of surface porosity in structural alumina ceramic*, Physical State Solid **204**(4) (2007) 1105-1113
- [103] A.N. Samant, N.B. Dahotre. *Physical effects of multipass two-dimensional laser machining of structural ceramics*, Advanced Engineering Materials **11**(7) (2009) 579-585
- [104] N. Morita, T. Watanbe, T. Yoshida, *Crack-free processing of hot-pressed silicon nitride ceramics using pulse YAG laser (3rd report, analysis of fracture strength and residual stress)*, Transactions of the Japan Society of Mechanical Engineers **57**(537) (1991)
- [105] H. Lei, L. Li. *A study of laser cutting engineering ceramics*, Optics & Laser Technology **31** (1999) 531-538
- [106] F. Quintero, J. Pou, F. Lusquinos, A. Rivero, and M. Perez-Amor. *Single-Pass and Multi-Pass Laser Cutting of Si-SiC: Assessment of the Cut Quality and Microstructure in The Heat Affected Zone*, Journal of Laser Applications **19**(3) (2007) 170-176
- [107] A.N. Samant, N.B. Dahotre. *Three-dimensional laser machining of structural ceramics*, Journal of Manufacturing Processes **12** (2010) 1-7
- [108] C. Wang, X. Zeng. *Study of laser carving three-dimensional structures on ceramics: Quality controlling and mechanisms*, Optics and Laser technology **37** (7) 2007 1400-1405
- [109] X. Wang, J.D. Shephard, F.C. Dear, D.P. Hand. *Optimized nanosecond pulsed laser micromachining of Y-TZP ceramics*, Journal of the American Ceramic Society **91**(2) 2008 391-397
- [110] F.C. Dear, J.D. Shephard, X. Wang, J.D.C Jones, D.P. Hand. *Pulsed laser micromachining of yttria-stabilized zirconia dental ceramic for manufacturing*, International Journal of Applied Ceramic Technology **5**(2) 2008 188-197

- [111] J.P. Parry, J.D. Shephard, F.C. Dear, N. Jones, N. Weston, D.P. Hand. *Nanosecond-laser postprocessing of millisecond-laser-machined zirconia (Y-TZP) surface*, International Journal of Applied Ceramic Technology **5**(3) 2008 249-257
- [112] J.P. Parry, J.D. Shephard, D.P. Hand. *Laser micromachining of zirconia (Y-TZP) ceramics in the picosecond regime and the impact on material strength*, International Journal of Applied Ceramic Technology **8**(1) 2011 163-171
- [113] S. Roy, M.F. Modest. *CW laser machining of hard ceramics – II. Effects of multiple reflections*, International Journal of Heat Mass Transfer **36**(14) (1993) 3529-3540
- [114] L. Hong, L. Li, C. Ju. *Investigation of cutting of engineering ceramics with Q-switched pulse CO₂ laser*, Optics and Laser in Engineering **38** (2002) 279-289
- [115] A.N. Samant, N.B. Dahotre. *Computational predictions in single-dimensional laser machining of alumina*, International Journal of Machine Tools and Manufacture **48** (2008) 1345-1353
- [116] A.N. Samant, N.B. Dahotre. *Absorptivity transition in the 1.06 μm wavelength laser machining of structural ceramics*, International Journal of Applied Ceramic Technology **8**(1) (2011) 137-139
- [117] A.N. Samant, N.B. Dahotre. *Physical effect of multipass two-dimensional laser machining of structural ceramics*, Advanced Engineering Materials **11**(7) (2009) 579-585
- [118] C.H. Tsai, C.J. Chen. *Formation of the breaking surface of alumina in laser cutting with a controlled fracture technique*, Proceedings of the Institution of Mechanical Engineers, Part B: Journal of Engineering Manufacture **247**(4) (2003) 489-497
- [119] R.M. Lumley. *Controlled separation of brittle materials using a laser*, American Ceramic Society Bulletin **48** (1969) 850-854
- [120] A.D. Nurse, N. Paterson, A. Tawn, K. Williams. *On the numerical modeling of laser shearing of glass sheets used to optimize production methods*, Proceedings of the Institution of Mechanical Engineers, Part C (Journal of Mechanical Engineering Science) **218** (2004) 1-11
- [121] M.A. Finucane, I. Black. *CO₂ laser cutting of stained glass*, International Journal of Advanced Manufacturing Technology **12** (1996) 47-59
- [122] C.H. Tsai, B.C. Lin. *Laser cutting with controlled fracture and pre-bending applied to LCD glass separation*, International Journal of Advanced Manufacturing and Technology **32** (2007) 1155-1162

- [123] J. Lin, Y.Z. Wang. *Characterisation of the laser cleaving on glass sheets with a line-shaped laser beam*, Optics and Laser Technology **39** (2006) 892-899
- [124] S. Nisar, M.A. Sheikh, L. Li, S. Safdar. *Effect of thermal stresses on chip-free diode laser cutting of glass*, Optics and Laser Technology **41** (2009) 318-327
- [125] S. Nisar, M.A. Sheikh, L. Lin, S. Safdar. *The effect of material thickness, laser power and cutting speed on cut path deviation in high-power diode laser chip-free cutting of glass*, Optics and Laser Technology **42** (2010) 1022-1031
- [126] S. Nisar, L. Li, M.A. Sheikh, A.J. Pinkerton. *The effect of continuous and pulsed beam modes on cut path deviation in diode laser cutting of glass*, International Journal of Advanced Manufacturing Technology **49** (2010) 167-175
- [127] V.S. Kondratenko. *Method of Splitting Non-metallic Materials*, U.S. Patent (1997) 5609284
- [128] U. Unger, W. Wittenbecher. *The cutting edge of laser technology*, Glass **75** (1998) 101-102
- [129] C.H. Tsai, C.S. Liou. *Fracture Mechanism of Laser Cutting with Controlled Fracture*, Journal of Manufacturing Science and Engineering **125** (2003) 519-528
- [130] C.H. Tsai, C.S. Liou. *Applying an on-line crack detection technique for laser cutting by controlled fracture*, International Journal of Advanced Manufacturing Technology **18** (2001) 724-730
- [131] C.H. Tsai, H.W. Chen. *Laser cutting of thick ceramic substrates by controlled fracture technique*, Journal of Materials Processing Technology **136** (2003) 166-173
- [132] C.H. Tsai, C.J. Chen. *Application of iterative path revision technique for laser cutting with controlled fracture*, Optics and Lasers in Engineering **41** (2004) 189-204
- [133] O. Brugan, G. Cai, R. Akarapu, A.E. Segall. *Controlled-fracture of prescored alumina ceramics using simultaneous CO₂ laser*, Journal of Laser Applications **18**(3) (2006) 236-241
- [134] A.E. Segall, G. Cai, R. Akarapu, A. Romasco, B.Q. Li. *Fracture control of unsupported ceramics during laser machining using a simultaneous prescore*, Journal of Laser Applications **17**(1) (2005) 57-62
- [135] S. Nisar, M.A. Sheikh, L. Li, A.J. Pinkerton, S. Safdar. *The effect of laser beam geometry on cut path deviation in diode laser chip-free cutting of glass*,

- Journal of Manufacturing Science and Engineering **132** (2010) 011002-1-011002-9
- [136] V. Pereles-Santiago, M. Washigton, P. Bruganm, G. Cai, R. Akarapu, S. Pulford, A.E. Segall. *Faster and damage-reduced laser cutting of thick ceramics using a simultaneous prescore approach*, Journal of Laser Applications **17**(4) (2005) 219-224
- [137] A.E. Segall, G. Cai, R. Akarapu. *Studies on the use of offset and angled prescores for fracture control during laser machining of alumina ceramics*, Journal of Laser Applications **18**(4) (2006) 325-329
- [138] R. Akarapu, A.E. Segall. *Active Stressing and the Micromanipulation of Stress-states for Delaying Fracture during Unsupported Laser Cutting*, Journal of Manufacturing Science and Engineering **130** (2008) 061004-1-061004-10
- [139] J. Parry, R. Ahmed, F. Dear, J. Shephard, M. Schmidt, L. Li, D. Hand. *A fiber-laser process for cutting thick Ytria-Stabilized Zirconia: Application and modelling*, International Journal of Applied Ceramic Technology **8**(6) (2010) 1277-1288
- [140] C.H. Tsai, C.H. Ou. *Machining a smooth surface of ceramic material by laser fracture machining technique*, Journal of Materials Processing Technology **155-156** (2004) 1797-1804
- [141] C.H. Tsai, H.W. Chen. *Laser milling of cavity in ceramic substrate by fracture-machining element technique*, Journal of Materials Processing Technology **136** (2003) 158-165
- [142] C.H. Tsai, H.W. Chen. *The laser shaping of ceramic by a fracture machining technique*, International Journal of Advanced Manufacturing Technology **23** (2004) 342-349
- [143] S. Rajagopal. *Laser-assisted machining of tough materials*, Laser Focus with Fiberoptic Technology **18**(3) (1982) 49-54
- [144] Y. Tian, Y.C. Shin. *Thermal Modeling for Laser-Assisted Machining of Silicon Nitride Ceramics with Complex Features*, Journal of Manufacturing Science and Engineering **128**(2) (2006) 425-434
- [145] C.W. Chang, C.P. Kuo. *An investigation of laser-assisted machining of Al_2O_3 ceramics planning*, International Journal of Machine Tools and Manufacture **47** (2007) 452-461

- [146] S. Lei, Y.C. Shin, F.P. Incropera. *Experimental Investigation of Thermo-Mechanical Characteristics in Laser-Assisted Machining of Silicon Nitride Ceramics*, Journal of Manufacturing Science and Engineering **123** (2001) 639-646
- [147] Y. Tian, B. Wu, M. Anderson, Y.C. Shin. *Laser-Assisted Milling of Silicon Nitride Ceramics and Inconel 718*, Journal of Manufacturing Science and Engineering **130**(3) (2008) 031013-1-031013-9
- [148] X. Shen, S. Lei. *Experimental study on operating temperature in laser-assisted milling of silicon nitride ceramics*, International Journal of Advanced Manufacturing Technology **52** (2010) 143-154
- [149] X. Shen, S. Lei. *Thermal Modeling and Experimental Investigation for Laser Assisted Milling of Silicon Nitride Ceramics*, Journal of Manufacturing Science and Engineering **131**(5) (2009) 051007-1-051007-10
- [150] B. Yang, S. Lei. *Laser-Assisted Milling of Silicon Nitride Ceramic: A Machinability Study*, International Journal of Mechatronics and Manufacturing Systems **1**(1) (2008) 116-130
- [151] P. Rebro, Y.C. Shin, F.P. Incropera. *Design of operating conditions for crackfree laser-assisted machining of mullite*, International Journal of Machine Tools and Manufacture **44** (2004) 677-694
- [152] F.E. Pfefferkorn, Y.C. Shin, Y. Tian, F.P. Incropera. *Laser-Assisted Machining of Magnesia-Partially Stabilized Zirconia*, Journal of Manufacturing Science and Engineering **126**(1) (2004) 42-51
- [153] S. Lei, Y.C. Shin, F.P. Incropera. *Deformation mechanisms and constitutive modeling for silicon nitride undergoing laser-assisted machining*, International Journal of Machine tools and Manufacture **40**(15) (2000) 2213-2233
- [154] S. Sun, M. Brandt, M.S. Dargusch. *Thermally enhanced machining of hard-to-machine materials – A review*, International Journal of Machine Tools and Manufacture **50**(8) (2010) 663-680
- [155] A. Kruusing. *Underwater and water-assisted laser processing: Part 1 – general features, steam cleaning and shock processing*, Optics and Laser in Engineering **41**(2) (2004) 307-327
- [156] A. Kruusing. *Underwater and water-assisted laser processing: Part 2 – Etching, cutting and rarely used methods*, Optics and Lasers in Engineering **41**(2) (2004) 329-335
- [157] N. Morita, S. Ishida, Y. Fujimori, K. Ishikawa. *Pulsed laser processing of ceramics in water*, Applied Physical Letters **52**(23) (1988) 1965-1966

- [158] N. Muhammad, D. Whitehead, A. Boor, L. Li. *Comparison of dry and wet fibre laser profile cutting of thin 316L stainless steel tube for medical device applications*, Journal of Materials Processing Technology **210**(15) (2010) 2261-2267
- [159] L. Qi, Y. Wang, L. Yang. *Study of Nd: YAG pulsed laser milling Al₂O₃ ceramic in water and air condition*, International Technology Innovation Conference (2006) 489-493
- [160] C.K. Chung, S.L. Lin. *CO₂ laser micromachined crackless through holes of Pyrex 7740 glass*, International Journal of Machine Tools and Manufacture **50**(11) (2010) 961-968
- [161] C.K. Chung, Y.C. Sung, G.R. Huang, E.J. Hsiao, W.H. Lin, S.L. Lin. *Crackless linear through-wafer etching of Pyrex glass using liquid-assisted CO₂ laser processing*, Applied Physics A – Material Science and Processing **94**(4) (2009) 927-932
- [162] C.H. Tsai, C.C. Li. *Investigation of underwater laser drilling for brittle substrates*, Journal of Materials Processing Technology **209**(6) (2009) 2838-2846
- [163] C. Barnes, P. Shrotriya, P. Molian. *Water-assisted laser thermal shock machining of alumina*, International Journal of Machine Tools and Manufacture **47** (2007) 1864-1874
- [164] D. Kalyanasundaram, P. Shrotriya, P. Molian. *Obtaining a Relationship between Process Parameters and Fracture Characteristics for Hybrid CO₂ Laser/Waterjet Machining of Ceramics*, Journal of Engineering Materials and Technology **131** (2009) 011005-1-011005-10
- [165] C.H. Tsai, J.S. Shiu. *Laser cutting ceramics using an unstable fracture technique*, Journal of Laser Applications **21**(1) (2009) 57-62
- [166] A. Murray. *The Reduction of Microstructural Damage During the Drilling of Ceramics by High Power Laser*, in Department of Mechanical Engineering, Loughborough University: Loughborough (2001)
- [167] J. Pascual-Cosp, A.J. Ramirez del Valle, J. Garcia-Forteza, P.J. Sanchez-Soto. *Laser cutting of high-vitrified ceramic materials: development of a method using a Nd: YAG laser to avoid catastrophic breakdown*, Materials Letters **55** (2002) 274-280
- [168] R.F. Firestone, E.J. Vesely. *High power laser beam machining of structural ceramics*, Proceedings of the ASME symposium on Machining of Advanced Ceramic Materials and Components (1988) 215-227

- [169] B.S. Yilbas, S.Z. Shuja. *Heat transfer analysis of laser heated surfaces—conduction limited case*, Applied Surface Science **108** (1997) 167-175
- [170] S.K. Padmarajaiah, A. Ramaswamy. *A finite element assessment of flexural strength of prestressed concrete beams with fiber reinforcement*, Cement and Concrete Composites **24**(2) (2002) 229-241
- [171] Z. Guan. *Hand Book of Laser Processing*. China Metrology Press, Beijing (1998)
- [172] L.J. Yang, Y. Wang, Z.G. Tian, N. Cai. *YAG laser cutting soda-lime glass with controlled fracture and volumetric heat absorption*, International Journal of Machine Tools and Manufacture **50** (2010) 849–859
- [173] *ANSYS Help Documentation*, Version 12.1, ANSYS Inc., Canonsburg, PA, USA
- [174] S. Govindje, G.J. Kay, J.C. Simo. *Anisotropic modelling and numerical simulation of brittle damage in concrete*, International Journal for Numerical Methods in Engineering **38** (1995) 3611–3633
- [175] P.V. Ananthapadmanabhan, T.K. Thiyagarajan, K.P. Sreekumar, N. Venkatramani. *Formation of nano-sized alumina by in-flight oxidation of aluminium powder in a thermal plasma reactor*, Scripta Materialia **50** (2004) 143–147
- [176] R. Negarestani, M Sundar, M.A. Sheikh, P. Mativenga, L. Li, Z.L. Li, P.L. Chu, C.C. Khin, H.Y. Zheng, G.C. Lim. *Numerical simulation of laser machining of carbon-fibre-reinforced composites*, Proceedings of the Institution of Mechanical Engineers, Part B: Journal of Engineering Manufacture **224** (2010) 1017-1027
- [177] G.M. Hale, M.R. Querry. *Optical constants of water in the 200-nm to 200- μ m wavelength region*, Applied Optics **12** (1973) 555-563
- [178] W. Wang, Y. Huang, M. Grujicic, D.B. Chrisey. *Study of impact-induced mechanical effects in cell direct writing using Smooth Particle Hydrodynamic method*, Journal of Manufacturing Science and Engineering **130** (2008) 021012
- [179] H.A. Joseph, C. Paul, A. Vladimir, N. Thang. *Simulation of die filling in gravity die casting using SPH and MAGMASoft*, Second international conference on CFD in the minerals and process industries, CSIRO, Melbourne, Australia (1999) 423–428
- [180] J.J. Monaghan, R.A. Gingold. *Shock Simulation by the Particle Method SPH*, Journal of Computational Physics **52** (1983) 374-389

- [181] G. Allcock, P.E. Dyer, G. Elliner, H.V. Snelling. *Experimental observations and analysis of CO₂ laser-induced microcracking of glass*, Journal of Applied Physics **78** (1995) 7295-7303
- [182] R.E. Mueller, J. Bird, W.W. Duley. *Laser drilling into an absorbing liquid*, Journal of Applied Physics **71** (1992) 551-556
- [183] K.T. Voisey, S.S. Kudesia, W.S.O. Rodden, D.P. Hand, J.D.C. Jones, T.W. Clyne. *Melt ejection during laser drilling of metals*, Materials Science and Engineering A **356** (2003) 414-424
- [184] L. Li, C. Achara. *Chemical assisted laser machining for the minimisation of recast and heat affected zone*, CIRP Annals – Manufacturing Technology **53** (2004) 175-178
- [185] Y.F. Lu, K.D. Ye. *Laser-induced etching of polycrystalline Al₂O₃TiC in KOH aqueous solution*, Applied Physics A **62** (1996) 43-49
- [186] H. Horisawa, N. Akimoto, H. Ashizawa, N. Yasunaga. *Effects of a quartz beam-guide on high-precision laser-assisted etching of Al₂O₃ ceramics*, Surface and Coatings Technology **112** (1999) 389-393
- [187] R. Nowak, S. Metev, G. Sepold. *Nd: YAG-laser-induced wet chemical etching of titanium and stainless steel*, Sensors and Actuators A **51** (1995) 41-45
- [188] V.A. Petrov. *Abrupt increase of the absorption coefficient of alumina at melting by laser radiation and its decrease at solidification*, International Journal of Thermophysics **30** (2009) 1938–1959
- [189] J. Duan, H.C. Man, T.M. Yue. *Modelling the laser fusion cutting process: I. mathematical modelling of the cut kerf geometry for laser fusion cutting of thick metal*, Journal of Physics D: Applied Physics **34** (2001) 2127-2134
- [190] F.O. Olsen, L. Alting. *Cutting front formation in laser cutting*, Annals of CIRP – Manufacturing Technology **38** (1989) 215-218
- [191] A. Kratky, D. Schuocker, G. Liedl. *Processing with kW fibre lasers: advantages and limits*, Proceedings of SPIE—XVII International Symposium on Gas Flow, Chemical Lasers, and High-Power Lasers **7131** (2008) 71311X
- [192] B.S. Yilbas. *Laser cutting of thick sheet metals: effects of cutting parameters on kerf size variations*, Journal of Materials Processing Technology **201** (2008) 285–290
- [193] H.G. Salem, M.S. Mansour, Y. Badr, W.A. Abbas. *CW Nd:YAG laser cutting of ultra low carbon steel thin sheets using O₂ assist gas*, Journal of Materials Processing Technology **196** (2008) 64–72

- [194] C. Wandera, V. Kujanpaa, A. Salminen. *Laser power requirement for cutting thick-section steel and effects of processing parameters on mild steel cut quality*, Proceedings IMechE Part B—Journal of Engineering Manufacture **225** (2011) 651–661
- [195] C. Wandera, V. Kujanpaa. *Characterization of the melt removal rate in laser cutting of thick-section stainless steel*, Journal of Laser Applications **22** (2010) 62–67
- [196] C. Wandera, A. Salminen, V. Kujanpaa. *Inert gas cutting of thick-section stainless steel and medium-section aluminium using a high power fiber laser*, Journal of Laser Applications **21** (2009) 154-161
- [197] C. Wandera, V. Kujanpaa. *Optimization of parameters for fibre laser cutting of a 10 mm stainless steel plate*, Proceedings of IMechE Part B—Journal of Engineering Manufacture **225** (2011) 641-649
- [198] D.K.Y. Low, L. Li, A.G. Corfe, P.J. Byrd. *Spatter-free laser percussion drilling of closely spaced array holes*, International Journal of Machine Tools and Manufacture **41** (2001) 361-377
- [199] D.K.Y. Low, L. Li, P.J. Byrd. *Spatter prevention during the laser drilling of selected aerospace materials*, Journal of Materials Processing Technology **139** (2003) 71-76
- [200] N. Muhammad, D. Whitehead, A. Boor, L. Li. *Comparison of dry and wet fibre laser profile cutting of thin 316L stainless steel tubes for medical device applications*, Journal of Materials Processing Technology **210** (2010) 2261-2267

Appendix A

Supplement: Modelling on Fibre laser Crack-Free Cutting of Thick-Section Alumina

A.1 FE Geometric Model and Mesh Strategy

In order to gain a better understanding of the effects of process parameters on thermal-stress and insight of mechanisms in crack generation and propagation, a 3D thermally coupled transient FE model was developed using commercially available software ANSYS in Chapter 3. The temperature field, thermal-stress distribution and crack within the bulk material during the laser cutting were simulated. It was expected that the model is useful to optimise the process parameters to achieve minimum thermal-stress distribution and avoid crack initiation. Crack formation and propagation mechanisms were also proposed based on the FE model analysis.

Figure 3.5 shows the overview of the FE semi-model for qualitative simulation of laser cutting. Using the symmetric semi-model, the amount of finite element was reduced by half and the simulated results on cross-section along the cut direction can be inspected. The dimensions of the model were 50 mm × 25 mm × 6 mm, similar as the semi-sample employed in experimental trials. Considering the memory limit space of the computer used in this work, a coarse mesh density ($\geq 500 \mu\text{m}$ mesh size) was applied for this model in order to qualitatively simulate the temperature field, thermal-stress distribution and crack propagation. A local region (1mm × 1mm × 6mm) at trailing edge was extracted from the entire model (as Figure 3.5) in order to study the effects of process parameters on temperature and thermal-stress with a higher precision. From the model, it was expected to obtain a trend in change of temperature gradient and thermal-stress distribution under various process parameters and hence to optimise the process parameters.

In the FE modelling, mesh size is one of crucial factors to control the simulation accuracy. A fine mesh size produces a high-accuracy simulation result but it also

leads to high computation time and computer memory requirement. To strike a balance between accuracy and computational time and memory consumption, the mesh should be constructed with reasonable densities.

There are two factors governing the mesh size. The characteristic length of heat conduction, l , indicates the region of main temperature gradient during laser cutting, which is given by:

$$l = \sqrt{\alpha_T t_p} \quad (\text{A-1})$$

Where α_T is material thermal diffusivity ($1.07 \times 10^{-5} \text{ m}^2/\text{s}$ for alumina) and t_p is the pulse duration ($\geq 1 \text{ ms}$ for the fibre laser employed in this work). Thus the minimum characteristic length of heat conduction was approximately 0.1 mm. It required the mesh size to be shorter than this length in order to correctly represent the temperature gradient.

In addition to the characteristic length of heat conduction, the laser spot radius, r , should also be considered. In order to profile the Gaussian energy distribution of the laser beam, it was supposed that the mesh size within the laser spot should also be smaller than the laser spot radius (25 μm).

In the corresponding numerical experiments, it was found that the simulated temperature generally converged to a limited temperature with finer mesh sizes. When the mesh size is equal to the spot radius, r , the maximum temperature is close to the converged value within 5% error as shown in Figure A.1. Therefore the mesh size, L_{mesh} , was determined by the minimum of heat conduction length ($l=0.1 \text{ mm}$) and laser spot radius ($r=25 \mu\text{m}$) as expressed by Eq. (A-2).

$$L_{mesh} = \min \{l, r\} \quad (\text{A-2})$$

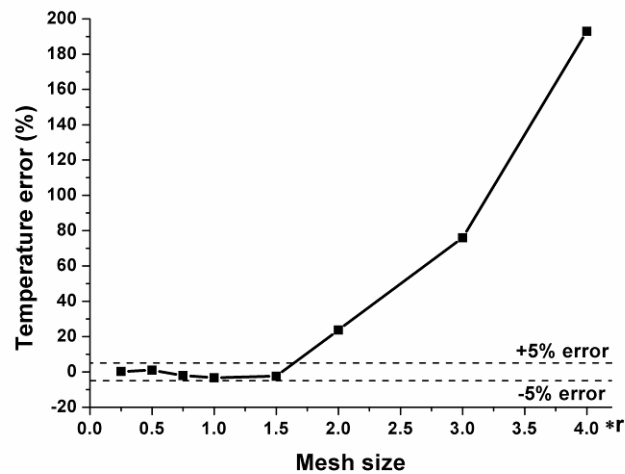


Figure A.1 Error of FE simulated temperature for different mesh sizes at the fixed time-step of 25 ms

However if the extracted model ($1 \text{ mm} \times 1 \text{ mm} \times 6 \text{ mm}$) was all meshed by this element size, it would require a very long computation time and massive memory. Actually, the laser spot and the HAZ are located only within a very small region (typically less than $150 \text{ }\mu\text{m}$ [139]). This means not every region of a spatial simulation domain is of particular importance for the solution. Therefore, it is useful to apply a finer mesh in simulation domains where a high resolution is necessary and a coarse mesh in regions of less importance in order to reduce the memory consumption and computational time. Considering the laser spot size and HAZ, the region-dependent mesh strategy was employed as shown in Figure A.2.

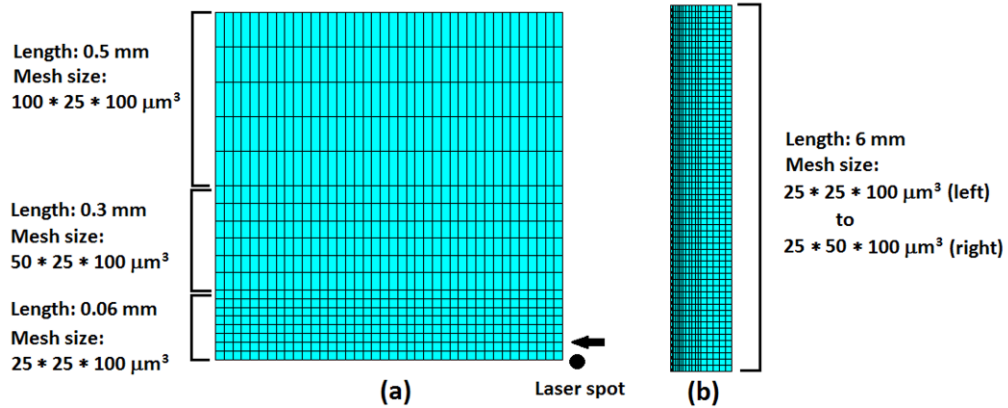


Figure A.2 Mesh strategy for the extracted symmetric semi-model. (a) The top view and (b) the side view

A.2 FE Time-Step Criterion

The computational accuracy of FE modelling is also determined by the time-step in addition to the mesh density. The mesh size and time-step influence two distinct aspects of FE simulation accuracy. The mesh size influences the spatial accuracy, whereas the time-step determines the time accuracy.

In FEM, the continuous physical process is transformed into a series of discrete static ones, which means the laser beam motion is split into a string of static laser irradiations. The size of time-step governs the discrete model to approach to the practical continuous physical process. A short time-step length produces a high-accuracy simulation result due to close to the continuous process, but it is time-consuming for a high calculation frequency in unit length. In order to balance computational accuracy and costs, the time-step should be considered to be a reasonable size.

The shadow regions in Figure A.3 highlight the area error between the continuous laser beam and the discrete laser beam sweeping the same length. Figure A.4 shows the area errors at various time-step sizes, which indicated the time-step length should be shorter than laser beam spot radius r in order to obtain a low area error ($< 5\%$). Furthermore, considering the Gaussian distribution of laser beam, each FE node within the cutting path should be exposed to the peak power density of the Gaussian

beam when the laser beam passed it. Therefore, the laser beam spot radius was considered as the reasonable time-step size in this work.

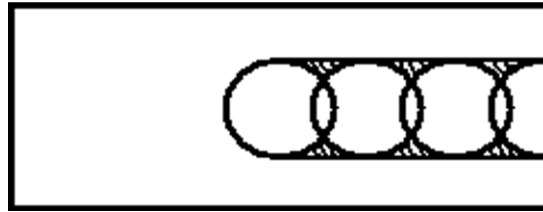


Figure A.3 Continuous laser beam and discrete laser beam sweeping the same length (shadow parts indicates the area error between the two modes)

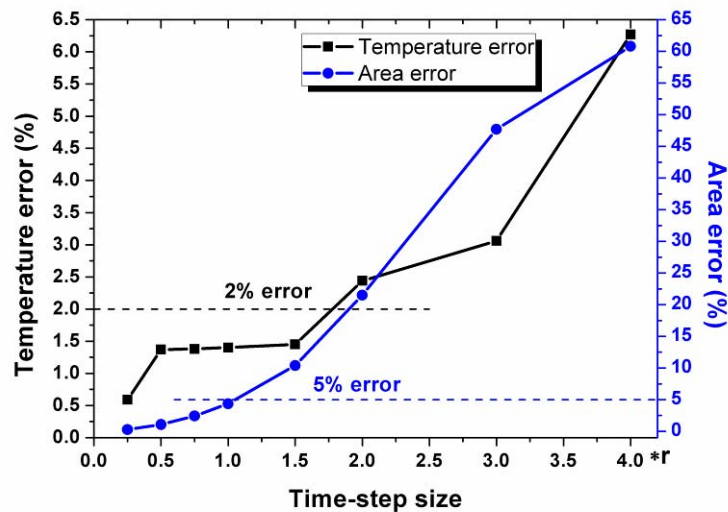


Figure A.4 Error of swept area and simulated temperature in FE model for different time-step sizes at the fixed mesh size of 25 μm

Some numerical simulation trials were also performed in order to determine the effect of time-step length on simulated temperature. It was found that temperature fields were similar at various time-steps, but the maximum temperature generally increased and converged to a limit with finer time-step sizes. Figure A.4 shows that the temperature error was 2% or less when the time-step length was shorter than the laser spot radius. Therefore, the laser spot radius is further validated as an accepted time-step length for the FE simulation with a low temperature error.

Furthermore, for a pulsed laser, the time-step length was also determined by the minimum of the beam spot radius and the beam movement length in each pulse. If the beam spot movement length in each pulse was less than the beam spot radius (i.e. low cutting speed with short pulse duration), the time-step should be set as the pulse duration. If beam spot movement in each pulse was greater than beam spot radius (i.e. high cutting speed with long pulse duration), the time-step was thus determined by the beam spot radius, whereas the pulse duration should be divided into some time-slots that make the beam movement length shorter than the laser spot radius in each time slot. Based on the above discussion, the time-step length selection criterion, $L_{time-step}$, is expressed as

$$L_{time-step} = \min \{ r, vt_p \} \quad (A-3)$$

Considering the process and laser parameters mentioned in Chapter 3, the time-step length selected in this work should be settled by the beam spot radius.

The corresponding time-step selection criterion, $T_{time-step}$, employed in the FE simulation should thus follow

$$T_{time-step} = \frac{L_{time-step}}{v} = \frac{\min \{ r, vt_p \}}{v} \quad (A-4)$$

A.3 Solution Strategy

The governing equation for simulation of temperature field has been established by the following heat diffusion equation [1]:

$$k(T) \left(\frac{\partial^2 T}{\partial x^2} + \frac{\partial^2 T}{\partial y^2} + \frac{\partial^2 T}{\partial z^2} \right) + Q(x, y, z) = \rho c(T) \frac{\partial T}{\partial t} \quad (A-5)$$

Where $K(T)$ is the temperature-dependent thermal conductivity, ρ is the material's mass density, $c(T)$ is the temperature-dependent specific heat and $Q(x,y,z)$ is the heat generation rate. The initial condition for the model was assumed to be an uniform temperature within the workpiece given as $T(x,y,z,0)=T_0$, where T_0 is the room temperature, 27°C.

The boundary condition for thermal analysis was convection caused heat losses. This condition was applied on all surfaces of the model except the x - z surface which had a

surface symmetric boundary due to the semi-model. The convection heat loss on relative surfaces follows [176]:

$$k(T) \frac{\partial T}{\partial n'} = -h(T - T_0) \quad (\text{A-6})$$

Where h denotes heat transfer coefficient, and n' is the normal vector point outward of the surface. The air convection coefficient and ambient temperature were taken as $50 \text{ W}/(\text{m}^2\text{K})$ and 27°C , respectively, in this work.

The cut surface, directly formed by the killed elements after thermal analysis, contained many residual cubes with rectangular angles due to the inherent element shape, which resulted in a very rough cut surface. These small shapes would cause thermal-stress concentration on them and obtain an incorrect simulated result (as Figure A.5). In this work, the elements that induced singular shapes were eliminated before the thermal-stress simulation, by which the problem of stress singularity on cut surface was resolved as shown in Figure A.6.

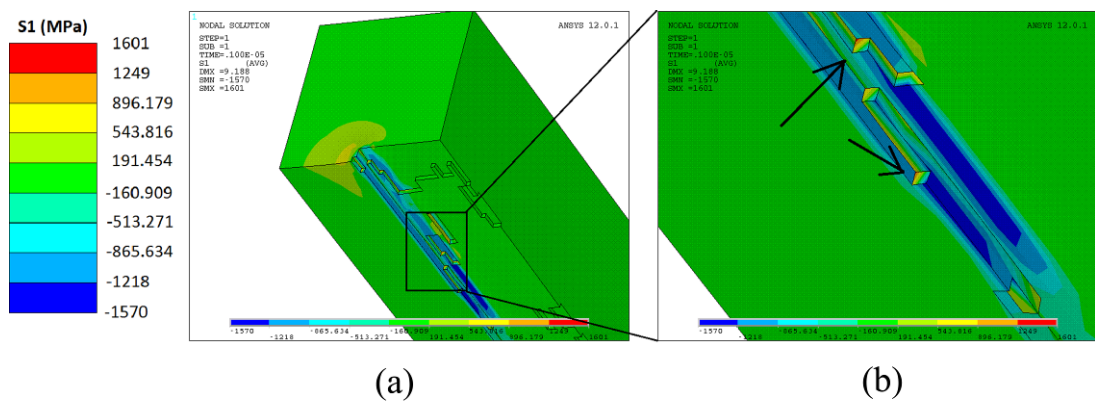


Figure A.5 The thermal-stress concentration on rough cut surface

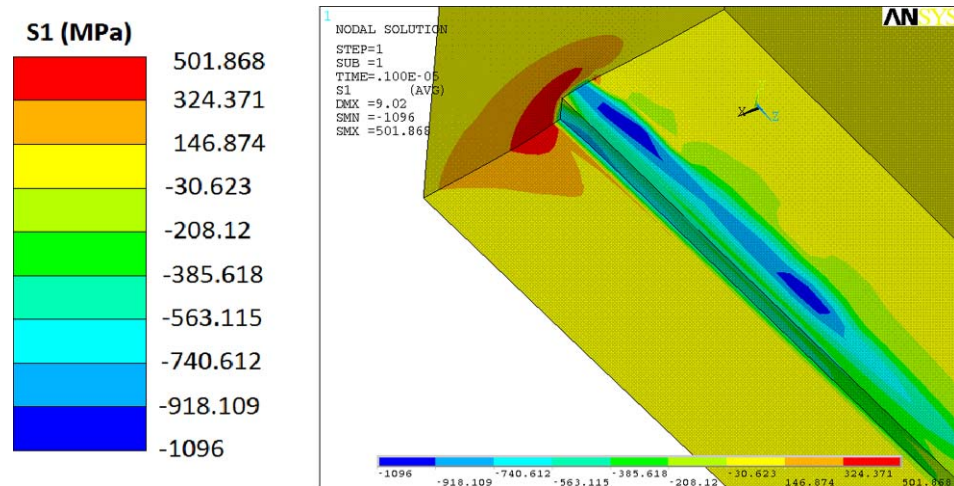


Figure A.6 The thermal-stress on smooth cut surface

A.4 Measurement Strategy in Extracted FE Model

In order to quantitatively study the effect of process parameters on temperature and thermal-stress distribution, the extracted FE model was used for high accuracy simulation. In Chapter 3, laser power, pulse duration, pulse repetition frequency and feed rate were selected to study their effects on temperature and thermal-stress.

The evaluation strategy for temperature and thermal-stress distribution was shown in Figure A.7, where the y -component stress along x -direction and the x -component stress along y -direction were selected together with the corresponding temperature distribution to study the effects of process parameters on temperature field and thermal-stress distribution.

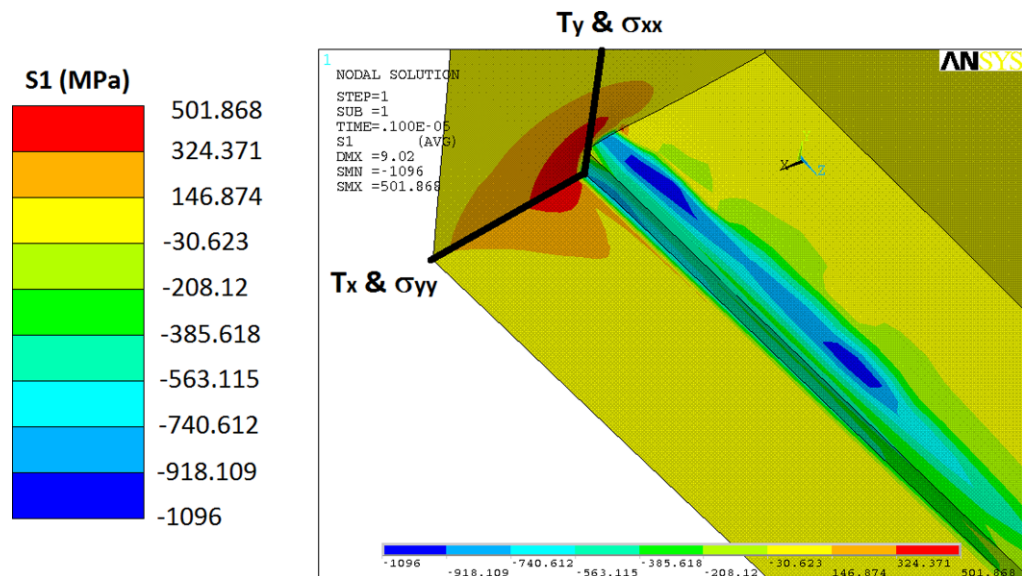


Figure A.7 Measurement strategy for temperatures (T_x and T_y) and resulting stresses (σ_{yy} and σ_{xx}) in the FE model

A.5 Effect of Process Parameters on Temporal Temperature Distribution

Effect of laser peak power

Figure A.8 shows the effect of laser peak power (Case 1 in Table 3.1) on temporal temperature distribution at the middle point of the cut kerf throughout the laser beam passing it. At high temperatures, the strength of alumina was reduced with the increasing of temperature before soften temperature (1500°C) [12, 166]. Figure A.8 indicates that higher laser peak power produces a lower heat effect on the cutting edge, which would cause lower thermal damage in the base material.

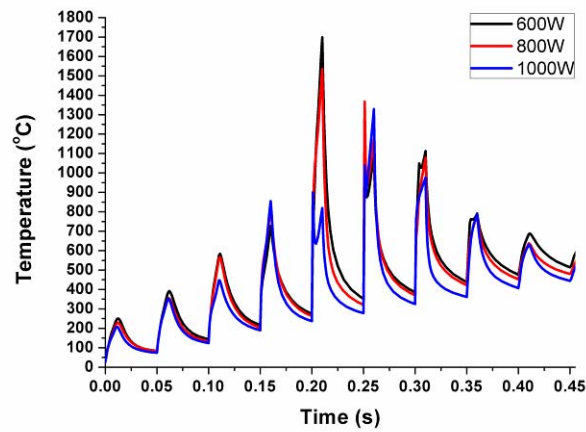


Figure A.8 Temporal distribution of temperature at the middle point of the cut kerf under various laser peak powers

Effect of pulse duration

Figure A.9 shows the effect of pulse duration (Case 2 in Table 3.1) on temporal temperature distribution at the middle point of the cut kerf throughout the laser beam passing it. The simulated result highlights that the shorter pulse duration produces a lower convergent temperature on the cutting edge, which would benefit to resist crack and thermal damage formation.

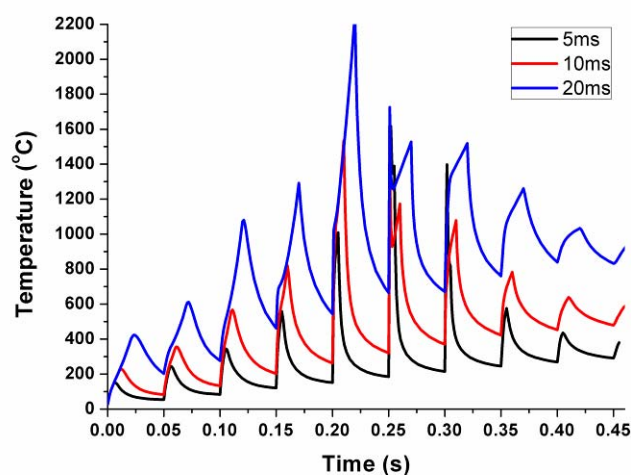


Figure A.9 Temporal distribution of temperature at the middle point of the cut kerf under various pulse durations

Effect of pulse repetition rate

Figure A.10 shows the effect of pulse repetition rate (Case 3 in Table 3.1) on temporal temperature distribution at the middle point of the cut kerf throughout the laser beam passing it. The simulated result indicates that the lower pulse repetition rate produces a lower convergent temperature on the cutting edge, which would be beneficial to suppress cracks and thermal damage.

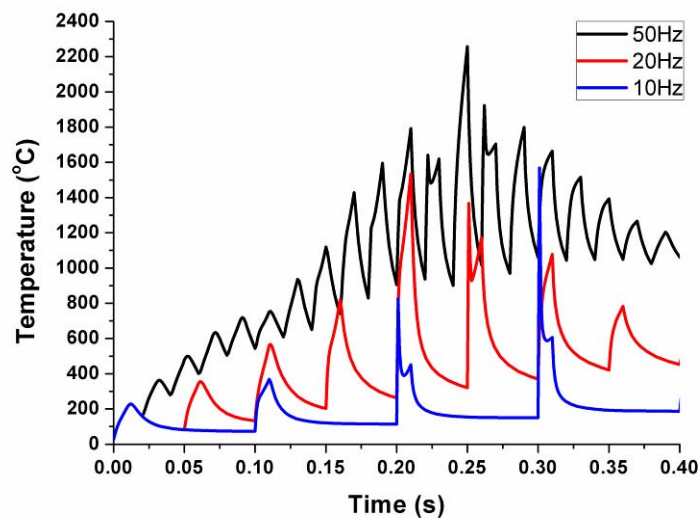


Figure A.10 Temporal distribution of temperature at the middle point of the cut kerf under various pulse repetition rates

Effect of feed rate

Figure A.11 shows the effect of feed rate (Case 4 in Table 3.1) on temporal temperature distribution at the middle point of the cut kerf throughout the laser beam passing it. The simulated result illustrates the higher feed rate produces a lower convergent temperature on the cutting edge, which would resist cracks and thermal damage.

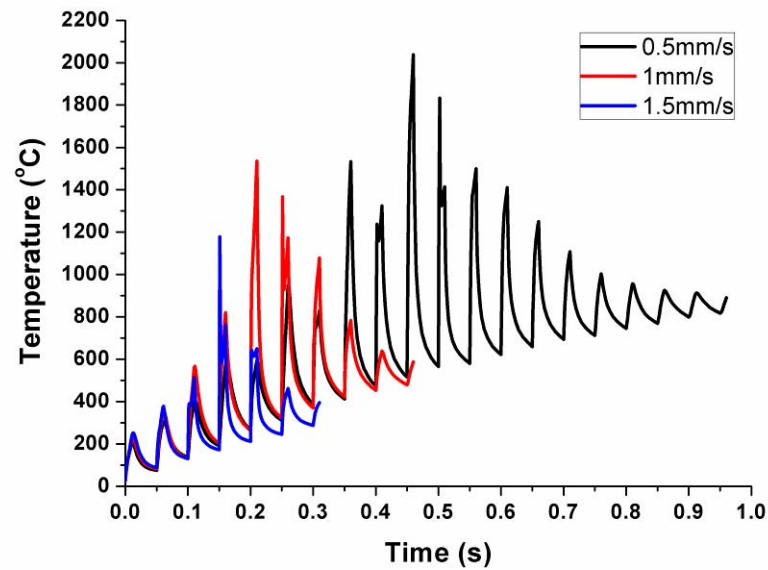


Figure A.11 Temporal distribution of temperature at the middle point of the cut kerf under various feed rates

A.6 Optimisation Procedure for Process Parameters

For laser cutting of thick-section ceramics, it is necessary to find out the process parameters to achieve crack-free cutting. According to the results and discussion in Chapter 3, a simple procedure for optimisation of process parameters to resist crack formation and thermal damage in laser fusion cutting of thick-section alumina was developed, as shown in Figure A.12.

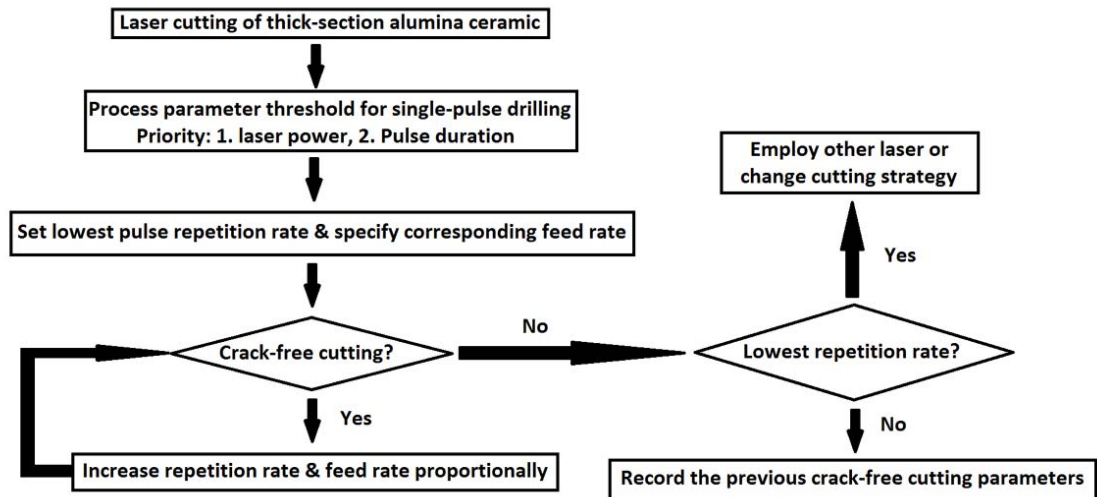


Figure A.12 Stepwise procedure for optimisation of process parameters for crack-free cutting of thick-section ceramics

For a specified laser, the first target for optimising process parameters is to find out the parameter threshold for drilling a through-hole. The maximum power of the laser should be employed and the threshold of pulse duration for drilling a through-hole via single pulse should be determined experimentally. Then the lowest pulse repetition rate is chosen initially in order to ensure the lowest thermal-stress distribution. The feed rate, v , is in turn determined by the pulse repetition rate f and beam spot size d , which is expressed as following:

$$v \leq d \times f \quad (\text{A-7})$$

In order to further improve process efficiency, the pulse repetition rate and feed rate can be proportionally increased obeying Eq. (A-7) and the corresponding experimental trial should be performed to inspect the cut quality. During this process, the pulse duration may need to be increased a bit with the feed rate increasing due to more energy required per pulse for material removal. When the feed rate and pulse repetition rate are proportionally increased until cracks are formed in experiments, the previous parameter set is the optimal selection, i.e. the highest feed rate for crack-free cutting.

Based on the above procedure, the process parameters for 1 kW fibre laser cutting of thick-section alumina (6-mm thickness) were optimised. The optimised parameters are listed in Table 3.4.

(This page is intentionally left blank)